FINITE ELEMENT MODELLING AND

ELASTO-PLASTIC ANALYSIS OF RHS

DOUBLE AND SINGLE CHORD T-JOINTS

by

ATIF AHMED AHMED SHEHATA, B.Sc., M.Sc.

A Thesis

Submitted to the School of Graduate Studies

in Partial Fulfilment of the Requirements

for the Degree

Doctor of Philosophy

McMaster University

© April 1983

ELASTO-PLASTIC MODELLING

OF RHS T-JOINTS

DOCTOR OF PHILOSOPHY   (1983)   McMASTER UNIVERSITY

(Civil Engineering)   Hamilton, Ontario

TITLE: Finite Element Modelling and Elasto-Plastic Analysis of RHS.

         Double and Single Chord T-Joints

AUTHOR: Atif Ahmed Ahmed Shehata, B.Sc. (Cairo University)

                              M.Sc. (University of Texas at Austin)

SUPERVISORS: Dr. Robert M. Korol and Dr. Farooque A. Mirza

NUMBER OF PAGES: xx, 258

To my Mother

and to my Wife

ABSTRACT

A research program is presented to investigate the behaviour of rectangular hollow section (RHS) T-joints in the elasto-plastic range of loading. The study includes the determination of both rotational and punching shear stiffnesses and strengths of the RHS T-joints due to branch moment or punching shear or a combination of both. The determined joint characteristics are then incorporated into an elasto-plastic analysis of Vierendeel trusses composed of RHS members.

Two different joint types have been analyzed, the double chord T-joint and the single chord type. In both cases, the joint is modelled by the chord top flange treated as a thin plate loaded on the perimeter of a rigid inclusion, and restrained by coupled translational and rotational springs along its longitudinal edges. These springs simulate the restraining effect of the side walls and connecting bottom flange. Transverse edges, some distance from the joint, are taken as simply supported.

The proposed finite element formulation incorporates rectangular plate, beam and boundary spring elements. The formulation considers both bending and in-plane actions. Material nonlinearities of the joint are assumed to be adequately represented by the Von-Mises yield criterion and the associated flow rule. While geometric nonlinearities have been neglected, this assumption is reasonable for the range of deformations deemed important in this study.

A parametric analysis has been undertaken for each of the double chord and single chord joints under either branch moment or punching shear. Each analysis considers the effect of each of five non-dimensional geometric parameters. One of the parameters, considered, is used to study the stiffening effect of a reinforcing flange plate. Results of the analysis are presented in the form of non-dimensionalized load-deformation ($M-\phi$ and $P-\delta$) curves.

A standardization procedure has been used to develop generalized $M-\phi$ and $P-\delta$ formulae, based on the parametric analyses. In addition, formulae for the joint stiffness and strength, in terms of its geometry, are presented for each case.

When the joints are analyzed under combined loading, the branch moment and punching shear are applied in different ratios. The results are presented in the form of interaction equations.

Next, the joint characteristics have been incorporated in an elasto-plastic finite element analysis of Vierendeel trusses. The effect of the joint flexibility on the truss behaviour is investigated. Also considered is a comparison between trusses possessing single chords and those possessing double chords.

Another aspect of this investigation is to predict upper bound capacities for the double chord joints due to branch moment or punching shear. The yield line theory has been utilized for this purpose.

The experimental part of the study involves the testing of ten double chord joints. Results of these tests along with other available experimental data are used in examining the validity of the analytical models that have been developed.

ACKNOWLEDGEMENTS

TABLE OF CONTENTS

LIST OF FIGURES

LIST OF TABLES

LIST OF SYMBOLS

b_o, h_o, t_o = width, height and wall thickness of single chord member (Fig. 2.3)

b_1, h_1, t_1 = width, height and wall thickness of branch member (Fig. 2.3)

b_s, h_s, t_s = width, length and thickness of flange stiffening plate (Fig. 2.3).

D = plate flexural rigidity

E = modulus of elasticity

E_T = tangent modulus

M = branch moment on joint (Fig. 3.3)

M_m = theoretical moment capacity under combined loading

M_{pc}, M_{pb} = Plastic moment of chord and branch members, respectively

$M_u, M_u^*, \bar{M}_u$ = theoretical (present solution), upper bound and experimental joint capacities under branch moment

P = punching shear on joint (Fig. 3.3)

P_m = theoretical punching shear capacity under combined loading

$P_u, P_u^*, \bar{P}_u$ = theoretical (present solution), upper bound and experimental joint capacities under punching shear

R = non-dimensional standardization factor for joint behaviour under branch moment

$\bar{R}$ = non-dimensional standardization factor for joint behaviour under punching shear

r_1, r_2, r_3, r_4, r_5 = non-dimensional geometric parameters

$u_i, v_i, w_i, \Theta_{x_i}, \Theta_{y_i}$ = displacements at nodal point i (Fig. 3.4)

$W_u^{\ f}, W_u^{*f}$ = theoretical (present solution) and upper bound load capacities of Vierendeel trusses with flexible joints

$W_u^{\ r}, W_u^{*r}$ = theoretical (present solution) and upper bound load capacities of Vierendeel trusses with rigid joints

φ = rotation of rigid inclusion due to branch moment

δ = deflection of rigid inclusion due to punching shear

ν = Poisson's ratio

ε_Y = yield strain

ε_{ST} = strain hardening strain

σ_Y = yield strength

$[B]$ = strain matrix

$[D]$ = elastic compliance matrix

$[D_{ep}]$ = elasto-plastic compliance matrix

$[K^e]$ = plate element stiffness matrix

$[K_s]$ = matrix of spring coefficients

$[K_s^e]$ = boundary spring stiffness matrix

$[N]$ = shape functions matrix

$\{R\}$ = load vector

$\{\varepsilon\}$ = strain vector

$\{\sigma\}$ = stress vector

$\{\delta^e\}$ = nodal displacement vector

CHAPTER 1

INTRODUCTION

1.1   Do not. General

The use of hollow structural sections (HSS) in Vierendeel
trusses and other framed structures has gained wide acceptability in
recent years. This is attributed mainly to the extensive research in
the past fifteen years which has allowed a better understanding of the
joint characteristics in HSS construction.

Hollow structural sections have many advantages over other
conventional sections. Their geometrical shape effectively resists
torsion and out-of-plane forces; the exposed surface area is much less
than that of other shapes, thus reducing the cost of protective coat-
ings; their clean lines and smooth surfaces permit architects to
visually integrate the structure with interior building decor or with
exterior landscapes.

Structures utilizing rectangular hollow sections (RHS) have the
added advantage of ease of fabrication. Straight end cuts and simple
fillet welding are normally sufficient for attaching connecting members
together and are performed at low cost. In fact, Vierendeel girders are
particularly attractive both from the point of view of fabrication and
appearance.

The most common type of RHS construction utilizes single chord joints. However, a major disadvantage of this concept is that direct welding of the branch's end to the flat flange of the chord produces a flexible and weak joint unless the framing sections are of approximately equal size. Another constraint in using single chord HSS is the practical aspect of connecting the branch to the chord. When welded connections are used the web member should be 25 to 50 mm narrower in width than the chord so that fillet welds can be used. If the web and chord members are of the same width, a difficult butt weld would be required resulting in a higher cost detail. In heavily loaded trusses, some form of joint reinforcement is often necessary to develop the full strength of the web members and stiffer joints.

In Canada, the largest size of RHS produced is 304.8 × 304.8 × 12.7 mm which imposes a major restriction on the maximum unsupported span. For example, roof trusses with normal span to depth ratios of 8 to 10, and subject to normal loads, cannot be expected to span more than 30 metres. However, longer spans would give greater interior design flexibility within buildings and improve the competetiveness of HSS. Such appears to be the potential for the double chord HSS trusses utilizing T or K joints. This concept involves the use of two square or rectangular chord members placed back-to-back and detailing the connections as for the single chord case.

There appears to be a number of advantages to using such a joint configuration. It provides for ease and economy of fabrication and has the potential for efficient joint design. A large portion of the branch

member forces, as will be shown, are transferred directly to the inner webs of the double chords, whereas the connecting flange of the chord member must transfer these forces in the case of the single chord. Consequently, the double chord will be shown to provide a much stiffer and stronger joint than a single chord of equivalent properties. In addition, the double chord would require less, if any, lateral bracing due to its inherent lateral rigidity.

However, before double chord truss systems can be employed in general use, research must be undertaken on the behaviour of the joints through which the member forces must be transferred. The investigation described in this thesis, therefore, focusses on the connections, rather than the members.

1.2   Literature Review

A considerable amount of research has been accomplished on single chord HSS connections using circular or rectangular HSS. The following presentation will deal only with connections having T config- uration and in which the chord and branch members are made of rectangu- lar or square HSS.

Research on HSS welded joints began at Sheffield University in the early 1960s. Mee [3] undertook research on the strength of T-joints under punching shear and tested 18 specimens with varying branch-to- chord width ratio. He found that the joint strength and stiffness increased considerably with higher width ratios. He also carried out a
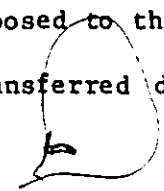
theoretical analysis of the elastic punching shear characteristics of the joint by treating the connecting chord face as a laterally loaded thin plate and analyzing it using the finite difference method. Redwood [2, 15] was the first to propose a theoretical model of the joint in which he assumed the inclusion between the branch and the connecting chord face to be rigid. The elastic rotational supports along the longitudinal edges of the loaded plate, provided by the two walls of the tube, were accounted for through an empirical formula established by Jubb et al. [11]. Mansour [16] improved upon Redwood's model by introducing uncoupled elastic springs along the longitudinal edges of the plate. His evaluation of the spring coefficients was based on the flexibility analysis of a simplified model. Most recently, El-Hifnawy [22] proposed an elasto-plastic finite element model which incorporates coupled boundary springs. However, she assumed these springs to remain elastic throughout the analysis.

Patel et al. [5] reported test results for eighteen single chord T-joints under direct punching shear. They concluded that less than full-width joints are undesirable for heavily loaded systems due to the large displacements associated with ultimate joint capacity thus rendering an inefficient structure. Extensive experimental data on T-joints under branch moments have also been reported by Korol et al. [1], Mang [4], Brady [10] and Kantani et al. [14]. It is concluded in reference [14] that the flexural failure of the chord flange governs the joint strength when the ratio of branch width to width of flat portion of the chord flange is less than 1.0. If this ratio is larger than 1.0, failure will be either due to web crippling of the chord member or

flange buckling of the branch member depending on the relative slender-
ness of the two members.

Mouty [12] worked out theoretical formulae for the calculation
of the ultimate strength of single chord T-joints due to branch moment
or punching shear. Based on experimental results, he proposed a simple
yield line model for both cases. Using the upper bound limit theorem,
he obtained a failure mechanism and calculated the ultimate capacity as
a function of the dimensions of the chord and the inclusion for a given
yield strength. Acceptable correlations with experimental joint
strengths at small deformations were obtained. Korol, Mitri and Mirza
[23] extended Mouty's work to include plate reinforced T-joints. They
concluded that the optimum plate size is obtained if its width is equal
to the width of the flat portion of the chord flange and its length is
twice the chord width. No work has been reported on the interaction
between the branch moment and punching shear and the joint behaviour
when both types of loading are present.

The concept of double chord RHS T-joint was first proposed by
Chidiac and Korol [7], who tested four double chord RHS T-joints as part
of an experimental investigation. They concluded that greatly improved
connection strength and stiffness characteristics could be achieved if
two chords placed back-to-back were welded together along their adjacent
corner edges for a short distance from the centre line of the joint.
The improvement in performance may be explained by the fact that, as
opposed to the single chord joint, a large portion of the branch load is
transferred directly through membrane action to the inner webs of the

chord members. No analytical work on this joint type appears to have been undertaken.

1.3   Objectives and Scope

This study is concerned with investigating the behavioural characteristics of double chord and single chord RHS T-joints. Three types of loading, namely branch moment or punching shear or a combination of the two, are considered. A theoretical analysis scheme involving elasto-plastic finite element modelling of the two joint types is developed and verified. In addition to experimental data available in the literature, a total of ten double chord T-joints were tested. The strength and stiffness of the joints are compared with experimental and yield line results in order to examine the validity and accuracy of the finite element models.

The following is the organization of the material presented in this dissertation. Chapter 2 contains detailed descriptions of analytical modelling of the joints and loads. The finite element formulation of the models is presented in Chapter 3 along with the solution technique employed in solving the system of non-linear equations. A description of the experiments on double chord joints and test results are given in Chapter 4. Chapters 5 and 6 present parametric analyses of double chord and single chord joints respectively, in which five geometric non-dimensional parameters are identifed. The effect of each parameter on the joint behavior under moment or punching shear is described by a set of load-deformation curves. In addition, analyses of

joint behaviour under combined loading are also given. Yield line solutions for moment and punching shear capacities of double chord connections are presented in Chapter 5.

A standardization scheme of joint characteristics is introduced in Chapter 7. Analytical formulae employing this scheme and the parametric analysis results of Chapters 5 and 6 are used to describe the joint stiffness and strength in terms of its geometric and material properties. Validity of these formulae is tested by comparison with experimental and yield line results.

The above-mentioned standardized formulae are then incorporated into an elasto-plastic finite element model for Vierendeel trusses that takes into account the flexible RHS T-connections. The model developed for this purpose is outlined in Chapter 8. Included also are case studies of a number of single and double chord trusses.

Finally, Chapter 9 provides a summary of the results from the present investigation with a presentation of the overall conclusions and recommendations for future research.

CHAPTER 2

ANALYTICAL MODELLING OF T-JOINTS

2.1   Introduction

Analytical models for both double chord and single chord RHS T-
joints are presented in this chapter.   In both cases, the joint can be
unreinforced or reinforced by a chord flange plate, as shown in Figs.
2.1 and 2.2.   In double chord joints (Fig. 2.1), the chord member is
composed of two back-to-back rectangular tubes which may be welded
together along their adjacent edges for a central distance.

A properly designed joint should be capable of transferring the
maximum branch forces to the chord without excessive localized deforma-
tions or failure.   In order to satisfy this design criterion, and
whether the joints ought or not to be reinforced, it is necessary to
understand the behavioural characteristics of such joints.   For this
reason, the analytical modelling is attempted and presented here.

Clearly an "exact" analysis for determining the stiffness and
strength characteristics of the above-described joints would involve a
three-dimensional analysis.   It would necessitate a large storage
requirement and a major allocation of computer time.   Consequently, such
an approach was not undertaken.

In this study, the joint behaviour is simulated by a two-dimensional model. The top flanges of the double chord member are treated as a thin plate supported on sets of coupled translational and rotational springs along the longitudinal direction. These springs represent the restraining effect of the remainder of the chord section on the top flanges. The branch loads are modelled by line forces acting along the perimeter of a rigid inclusion representing the intersection area of the top flange and the branch member.

In all joint analyses, material is assumed linearly elastic up to yield and plastic beyond the yield point. Furthermore, the deformations are assumed small and hence, the geometric nonlinearities are neglected. This latter assumption is believed to be very reasonable as the models to be presented are not meant to simulate failure mechanisms.

2.2   Model of Double Chord T-Joints

The geometry of a typical double chord T-joint is defined in Fig. 2.3. The chord and branch members are assumed to be fabricated from two RHS of dimensions $h_0 \times b_0 \times t_0$ and one RHS of dimensions $h_1 \times b_1 \times t_1$, respectively. Geometry of the stiffening plate, if present, is defined by its length h_s, width b_s, and thickness t_s.

Idealization of the joint in the transverse direction is indicated in Fig. 2.4. It involves treating the flat portion of the chord's top flange as a thin plate supported along the longitudinal edges (A' &

F' in Fig. 2.4) by coupled springs. These edge springs (two transla-
tional and one rotational along each edge) simulate the restraining
effect of the remaining section (frame ABCDEF) on the top plate.
Because of the localized nature of the joint behaviour, it is necessary
to eliminate the effect of overall bending of the chord member in the
longitudinal direction. Thus, in order to eliminate contributions to
the vertical displacement and rotation of the joint arising from overall
bending, rollers R are introduced at points D as shown in Fig. 2.4. It
should be noted that the chosen locations of rollers R are symmetric
about the joint centreline due to symmetry of the joint geometry and
loading in the transverse direction. The choice of placing the rollers
underneath the centerline of the inner webs is based on the fact that
these webs are very stiff in their planes and, under membrane forces,
will behave as deep beams without any significant out-of-plane deforma-
tions. It was also observed that additional rollers at points C (Fig.
2.4) have no significant effect on the joint behaviour. The area of the
top flanges inscribed by the branch member is modelled as a rigid inclu-
sion having the outer dimensions of the branch cross section. Rigidity
of the inclusion is achieved by taking its thickness as, say, 1000 times
the flange thickness.

It is readily seen that the connection is symmetric about both
vertical, longitudinal and transverse planes when analyzed under punch-
ing shear. It is also symmetric about the longitudinal vertical plane
and anti-symmetric about the transverse vertical plane when analyzed
under branch moment. Therefore, only one-quarter of the joint needs to
be modelled under either type of loading. Evidently, there is only one

plane of symmetry (transverse vertical) when a combined loading is considered, and hence one-half of the joint is analyzed in this case. Under any of the loading conditions discussed above, transverse symmetry exists and, therefore, only one-half of the joint cross section is considered in the model.

The right half of the idealized cross section is shown in Fig. 2.5. Both membrane and bending actions are considered in the analysis of the top flange plate. The edge springs supporting the top flange plate correspond to in-plane degree of freedom (DOF) v, and out-of-plane DOF's w and θ as indicated in Fig. 2.5. Superscripts r and ℓ denote right and left edges respectively. The spring coefficients per unit length are then determined through stiffness analysis of the plane frame ABCDEF made of the top rounded corners, two webs, and bottom flange. Centreline of this frame coincides with the centreline of the RHS and has a unit length perpendicular to its plane. Because material non-linearities are incorporated in the analysis, the tangential stiffness of the frame (and thus of the springs) shall be determined by numerical integration. This is accomplished by dividing the frame into a number of beam-column elements. It has been idealized by eighteen elements with three DOF's at each node. The distribution of elements and their lengths are chosen according to expected stress levels in different parts of the frame.

The frame stiffness matrix (54 × 54) can be obtained in terms of geometric and material properties of the hollow sections; the task then reduces to incorporating the proper boundary conditions for the frame so

that it will appropriately model the influence of the remaining section on the top plate. The six by six spring coefficients matrix sought can then be obtained from the overall frame stiffness matrix (54 × 54) in the following manner.

(1)   Apply the appropriate boundary conditions, as will be explained later.

(2)   Set degree of freedom (DOF) 1 (Fig. 2.5) equal to unity while restraining DOF's 2 to 6.

(3)   Eliminate DOF's 7 to 54 through matrix condensation and solve for the holding forces along DOF's 1 to 6. These forces represent the first column in the required matrix of spring coefficients.

(4)   Repeat steps (2) and (3) for DOF's 2 to 6, one at a time, to obtain columns 2 to 6 of the matrix.

This procedure will be explained further in Section 3.3.

Boundary conditions for modelling the double chord RHS member are presented below.

(1)   Set the displacement at DOF 32 (roller R) equal to zero.

(2)   Restrain DOF 31 (horizontal movement at D) if the two chord members are welded at the bottom.

(3)   Restrain DOF 52 (horizontal movement at E) if the two chord members are welded at the top.

(4)   Restrain DOF's 31 and 52 if the two chord members are welded at

both top and bottom.

It is worth noting that different constraint conditions can be imposed along the connection length as necessitated by the amount and type of weldment applied. In order to account for the plate action, the frame element flexural rigidity, EI per unit length, is then replaced by the plate flexural rigidity $D = \dfrac{Et_0^3}{12(1 - \nu^2)}$, t_0 being the chord thickness, E the modulus of elasticity and ν Poisson's ratio.

At this stage, it is obvious that one would obtain a coupled six by six edge spring stiffness matrix in contrast to the simplified models of uncoupled flexibility coefficients used by Redwood [2] and Korol and Mansour [6]. In all the test cases studied, it was observed that many of the off-diagonal terms in the matrix were either of the same order or larger than the corresponding diagonal terms. Some numerical examples of the edge spring stiffness matrix are reported in reference [25]. This, of course, confirms the existence of strong coupling among the spring stiffnesses.

A schematic representation of the top flange plate and boundary springs presented above is shown in Fig. 2.6. Only one-quarter of the connection is modelled. A plate length of five times the branch height ($= 5h_1$) is used. This has been found to be the minimum length necessary to make the end conditions of little significance on the joint behaviour. Therefore, the transverse edges of the plate are assumed simply supported. Also shown in Fig. 2.6 is a typical boundary spring element

ABCD. The function of this newly-developed element is to incorporate the stiffnesses of the edge springs into the joint's overall stiffness matrix. Derivation of this element is based on the principle of virtual work. The displacement fields of the plate elements adjacent to edges AB and CD are also employed in formulating the boundary spring elements. This helps maintain the same compatability as employed for the plate elements. It can be observed that the boundary spring elements bridge across the plate edges in a wrap-around fashion. Detailed derivations of the different elements employed in the current investigation are presented in Chapter 3.

2.3 Degeneration of Double Chord to Single Chord T-Joint Model

Geometry of a single chord T-joint is defined in Fig. 2.7. The chord and branch members are assumed to be fabricated from RHS having dimensions $h_0 \times b_0 \times t_0$ and $h_1 \times b_1 \times t_1$, respectively. Geometry of the stiffening plate, if provided, is symmetrically positioned on the flange plate having dimensions h_s, b_s and t_s. These connections can be model-led in exactly the same manner as was described in Sec. 2.2 for double chord T-joints.

The idealized cross section of a single chord T-joint is shown in Fig. 2.8. Again, it involves treating the top flange as a thin plate supported along the longitudinal edges by coupled translational and rotational springs as shown. The tangential spring coefficients at any load level are determined through stiffness analysis of the U-shaped frame ABCDEF of unit width. Rollers R are introduced at points C and D

to eliminate contributions to the vertical displacement and rotation of the joint due to overall deflection of the chord. As for the double chord joint only one-quarter of the joint needs to be analyzed when either moment or punching shear loading is considered. The right half of the idealized cross section is shown in Fig. 2.9. In order to pre-serve symmetry, zero rotation and horizontal displacements are imposed at point G, the middle point of the bottom flange. Frame ABCG of Fig. 2.9 is modelled by 10 beam-column elements and 11 nodes with 3 DOF's per node.

It may be observed that a close similarity exists between the models of double chord and single chord joints. In fact, the finite element formulation of the former can be easily degenerated to allow analysis of the latter. This has been done in the present study as will be demonstrated in Chapter 3. It may also be pointed out that the frame for double chord joints (Fig. 2.5) can also be used to determine the spring stiffness coefficient matrix of single chord joints after apply-ing the appropriate boundary conditions. The disadvantage of this approach is the need to analyze one-half, rather than one-quarter, of the connection. Following the procedure of Sec. 2.2, the three by three spring coefficient matrix can be obtained from the overall frame stiffness matrix (33 × 33) as follows.

(1)   Apply the appropriate boundary conditions, as will be explained later.

(2)   Set DOF 1 (Fig. 2.9) equal to unity while restraining DOF's 2 and 3.

(3)   Eliminate DOF's 4 to 33 through matrix condensation and solve
        for the holding forces along DOF's 1 to 3.   These forces
        represent the first column in the required matrix of spring
        coefficients.

(4)   Repeat steps (2) and (3) for DOF's 2 and 3, one at a time, to
        obtain columns 2 and 3 of the matrix.

Boundary conditions for modelling the RHS chord member are
presented below.

(1)   Set the displacement at DOF 26 (roller R) equal to zero.

(2)   Set the horizontal displacement and rotation at point G (DOF's
        31 and 33) equal to zero.

Again, strong coupling amongst the spring stiffness coefficients was
observed in all test cases, as reported in reference [25].

Clearly, the schematic representation of the double chord model,
as shown in Fig. 2.6, is also valid for the single chord model described
above with modifications.   The edge springs in the latter model act
along edge CD only. Detailed derivation of the boundary spring elements
is presented in Chapter 3.

2.4   Modelling of Material Properties

In this study, material used for the joints is structural carbon
steel. The material properties, which are very important from a joint

behaviour point of view can be obtained from a tension or compression test on a small coupon of the material from which the chord members are made. Such a test furnishes stress–strain curves. Typical curves for structural carbon steel may be idealized by a tri-linear curve as shown in Fig. 2.10. In this curve, the stress is proportional to strain with slope E up to the yield stress σ_Y following which the curve exhibits a pronounced plastic plateau until a strain ε_{ST} is attained. Subsequently, strain hardening behaviour develops with strain-hardening modulus E_{ST}.

However, in the interests of a more simplified model, the stress–strain curve will be simplified to bi-linear behaviour consisting of the elastic line of slope E and the strain-hardening line of slope E_T, the tangent modulus (Fig. 2.10).

Galambos [17] has suggested the following values for structural steel:

$$\varepsilon_{ST} = 12\,\varepsilon_Y \qquad , \qquad E_{ST} = 0.04\,E \qquad ,$$

If the maximum strain is taken as $\varepsilon_{max} = 30\,\varepsilon_Y$, then

$$E_T = 0.025\,E$$

The following numerical values of the material constants have been assumed in the analysis.

$E = 200,000$ MPa, $E_T = 5,000$ MPa, $\sigma_Y = 345$ MPa, and Poisson's ratio, $\nu = 0.30$.

Furthermore, the joint material is assumed isotropic; its elasto-plastic stress-strain relations are characterized by the Von-Mises yield criterion and its associated flow rule. These assumptions are usually made for metallic materials [8].

BRANCH

CHORD

a. Unreinforced Connection

STIFFENING
PLATE
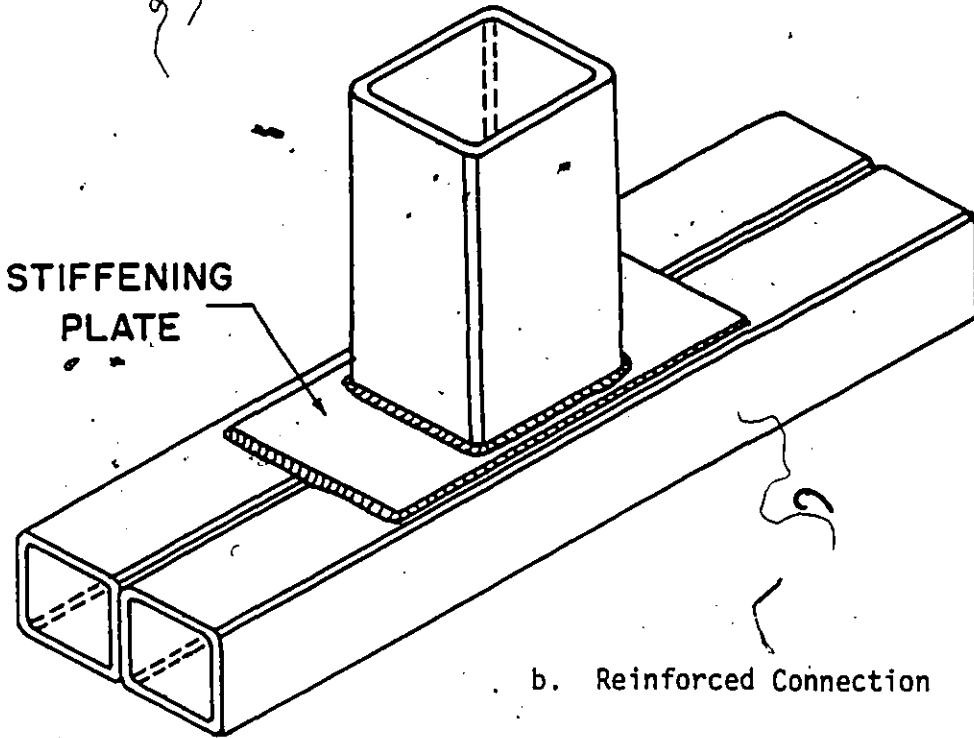
b. Reinforced Connection

FIG. 2.1   DOUBLE CHORD RHS T-JOINTS
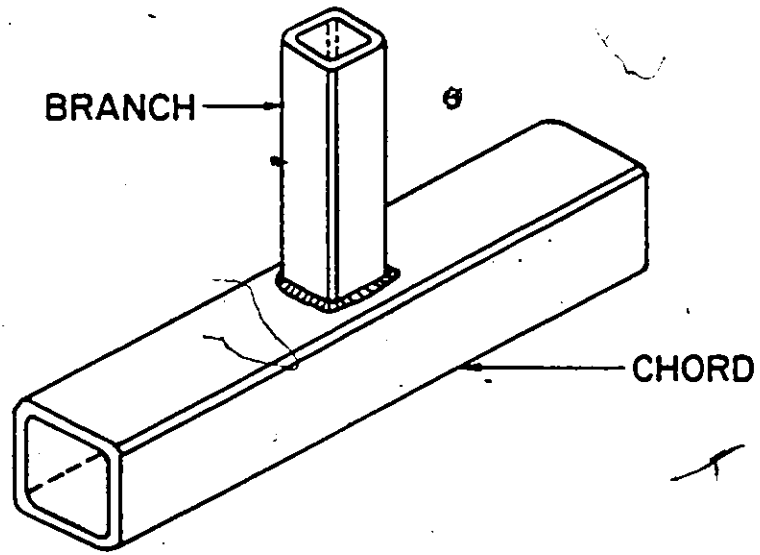
a.   Unreinforced Connection
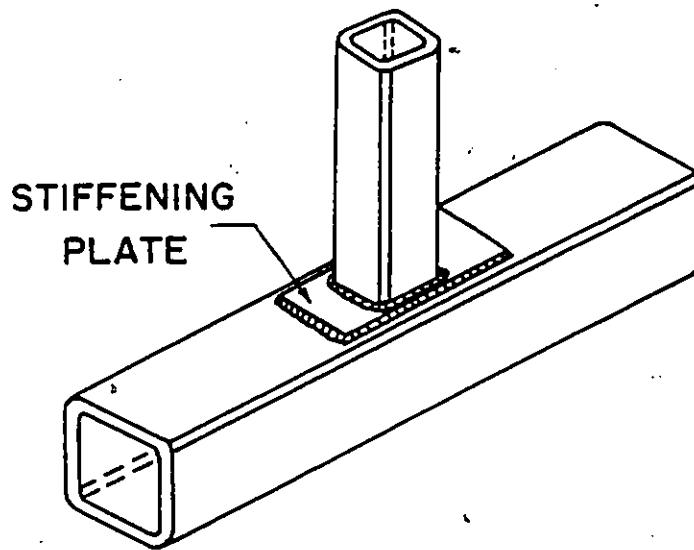
b.   Reinforced Connection

FIG. 2.2   SINGLE CHORD RHS T-JOINTS
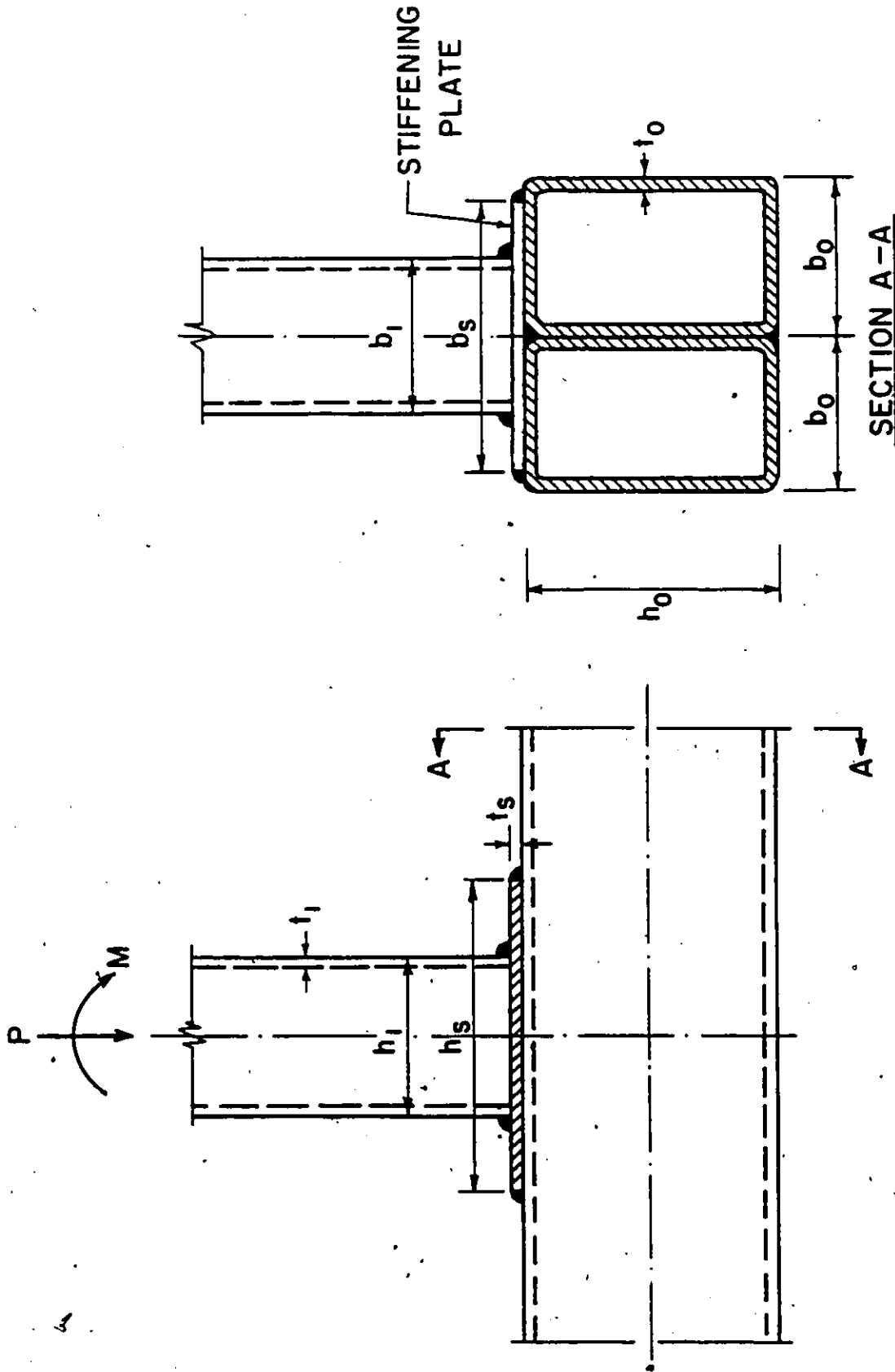
FIG. 2,3   GEOMETRY OF DOUBLE CHORD JOINTS
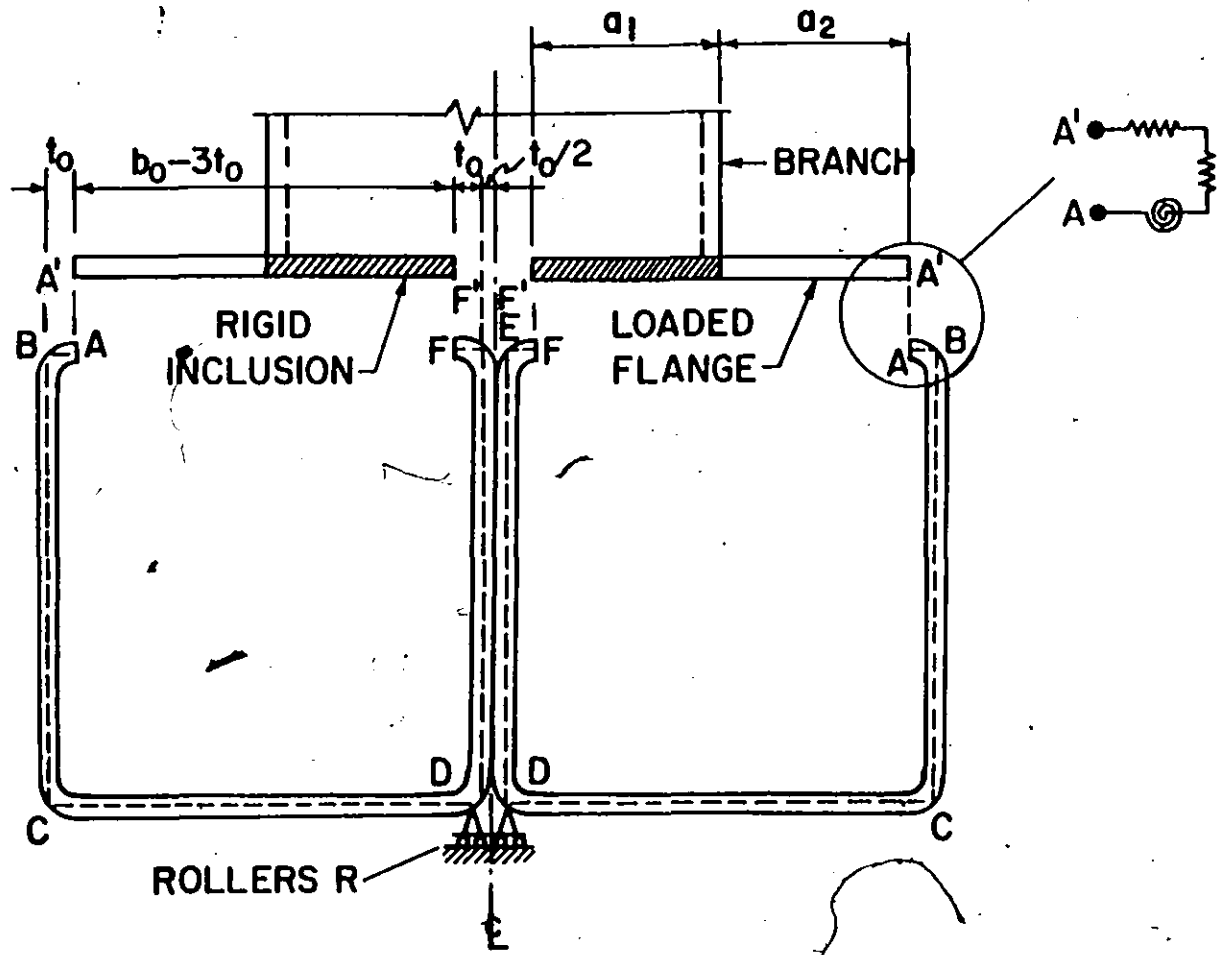
FIG. 2.4   IDEALIZATION OF DOUBLE CHORD JOINTS
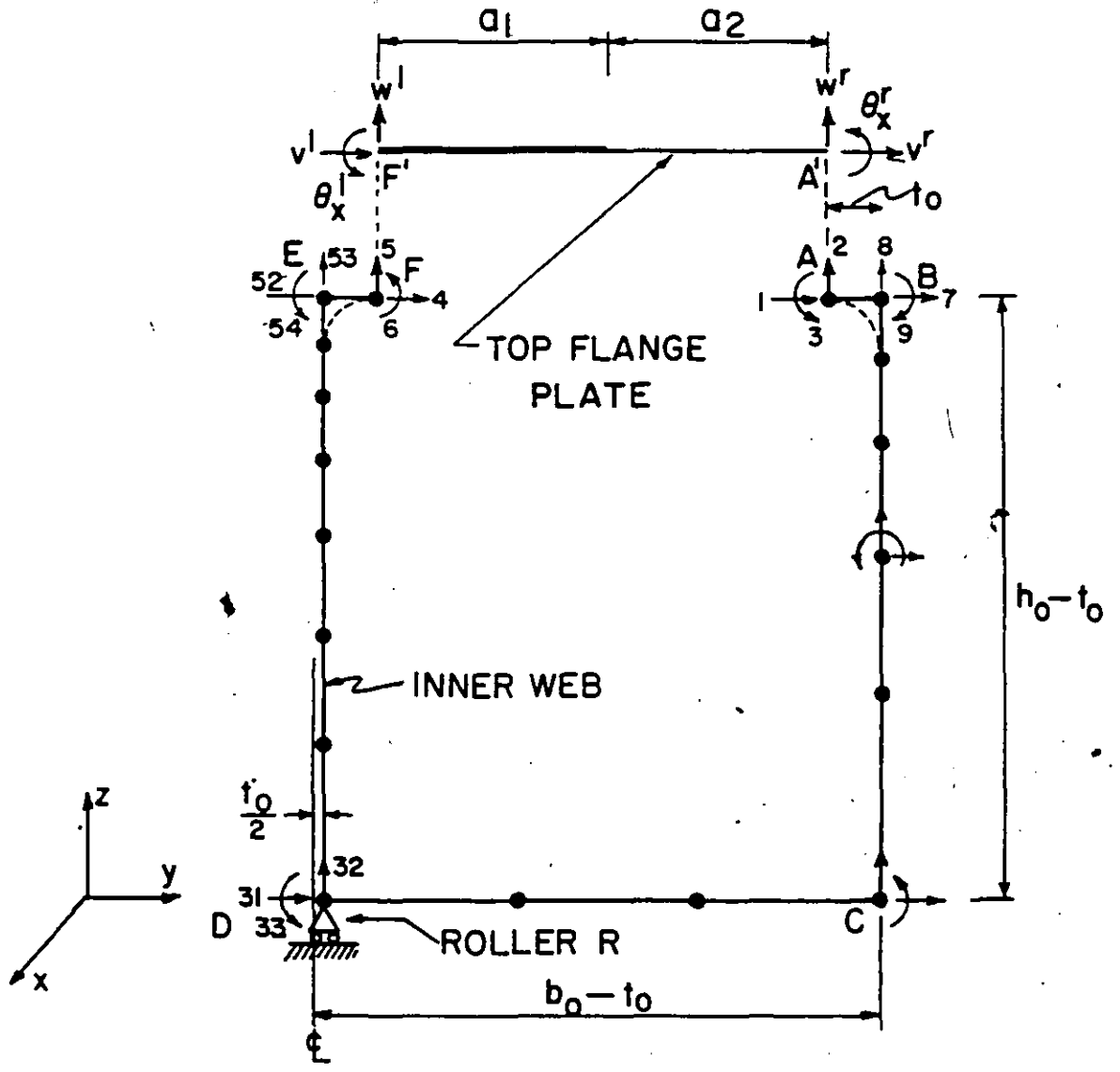
FIG. 2.5 MODEL OF THE CROSS SECTION OF DOUBLE CHORD JOINTS
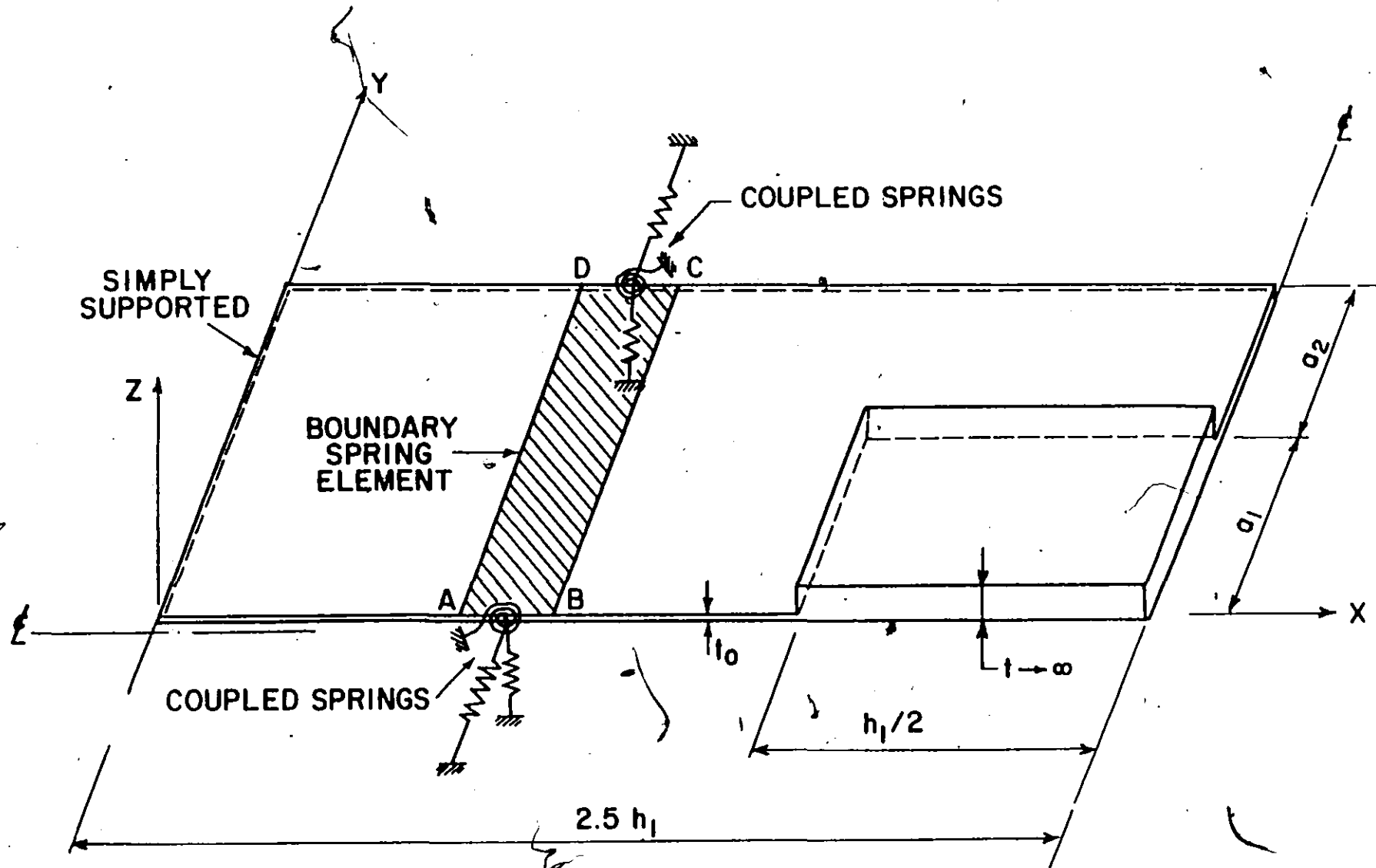
FIG. 2.6 SCHEMATIC REPRESENTATION OF DOUBLE CHORD MODEL
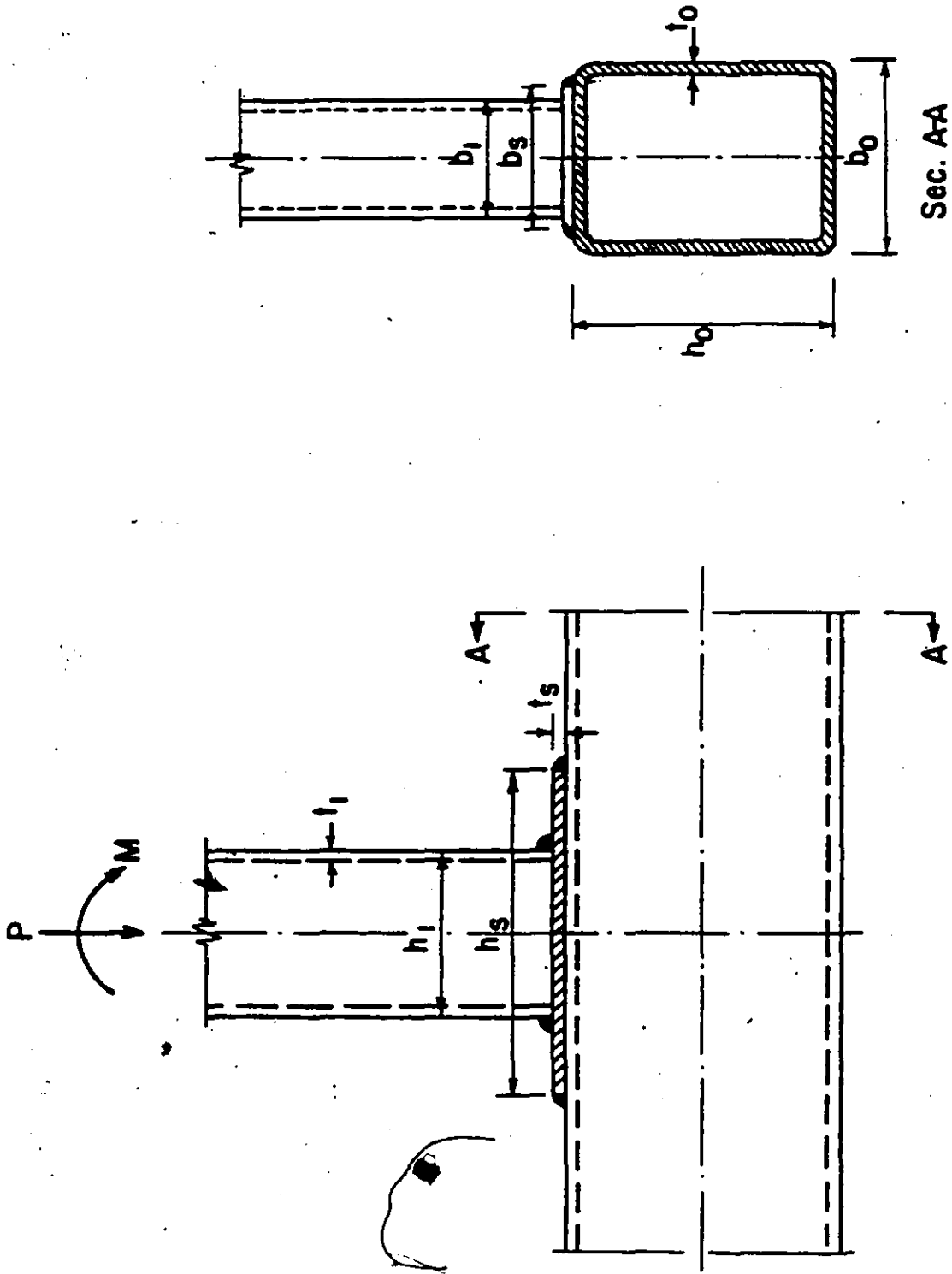
FIG. 2.7 GEOMETRY OF SINGLE CHORD JOINTS
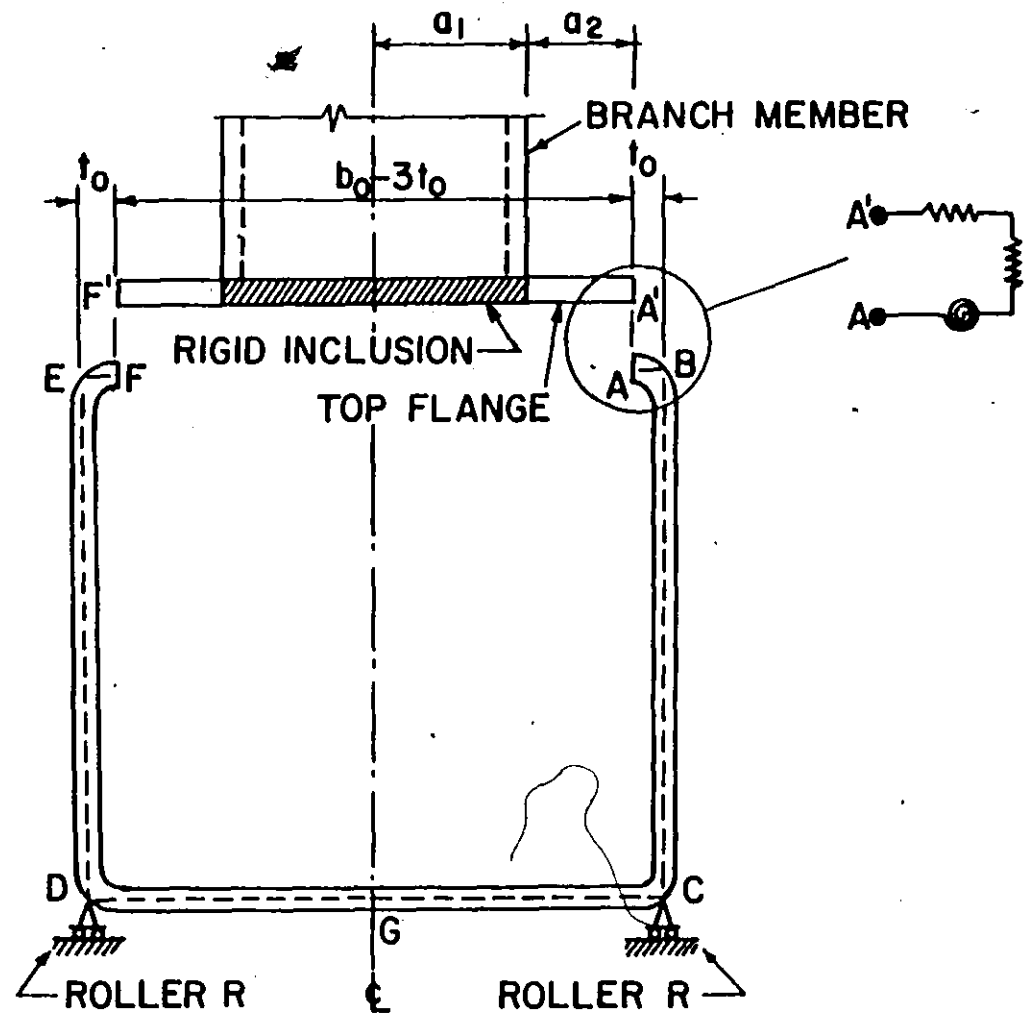
FIG. 2.8   IDEALIZATION OF SINGLE CHORD JOINTS
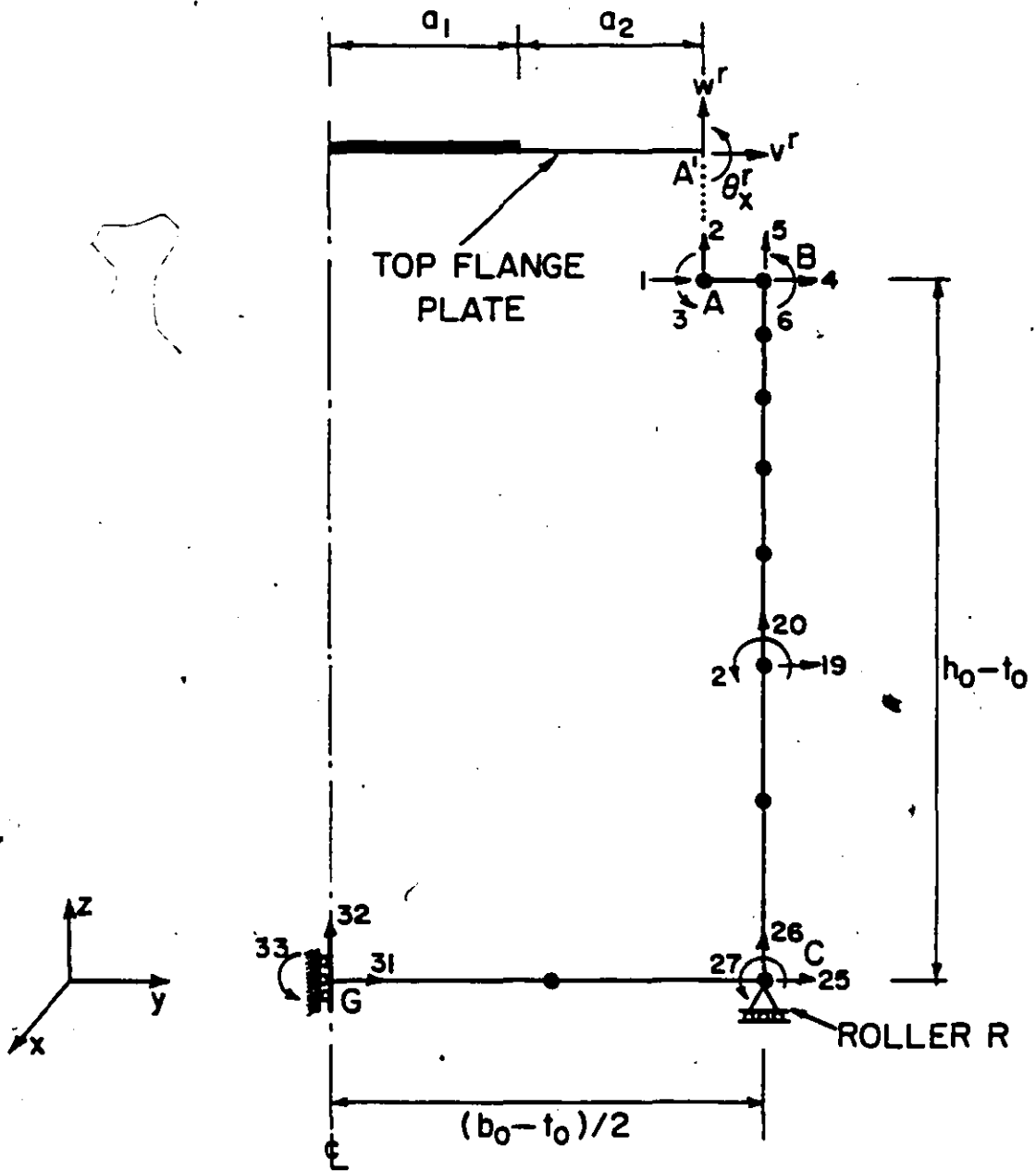
FIG. 2.9 MODEL OF THE CROSS SECTION OF SINGLE CHORD JOINTS
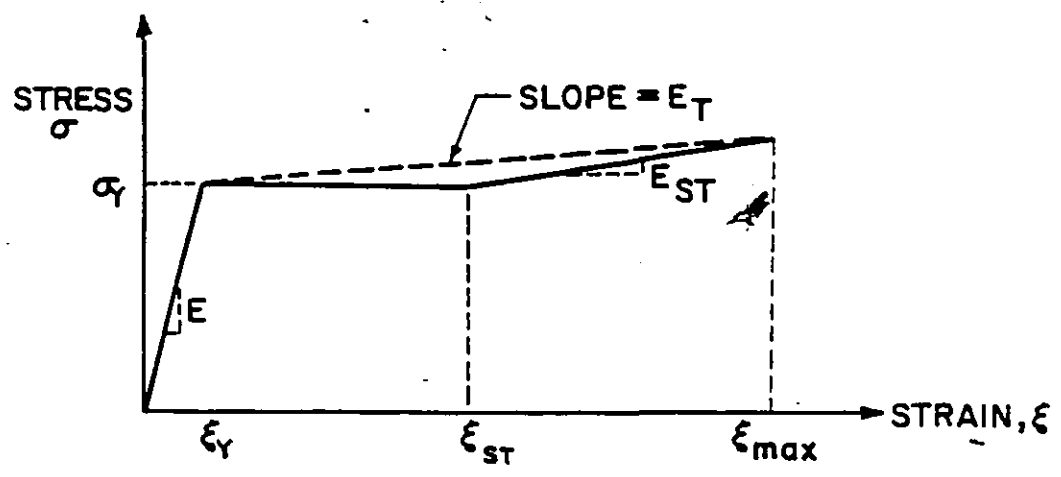
FIG. 2.10   IDEALIZED STRESS-STRAIN CURVE

CHAPTER 3

FINITE ELEMENT FORMULATION OF JOINT MODELS AND

NONLINEAR SOLUTION TECHNIQUES

3.1   Introduction

The finite element method is a convenient and powerful tool for analysis of problems in continuum mechanics with complicated boundary conditions and loads. Since its development during the late-fifties and early sixties, the method has been applied to a wide variety of problems with excellent success. One of the greatest virtues of the method is its capability of handling complicated geometries and varying material properties. While analyses of linear problems are relatively straight-forward, the nonlinear problems are considerably more difficult and require intelligently thought out numerical algorithms for nonlinear analysis which are beyond just the finite element discretizations of such problems.

The basis of the analysis to be presented in this chapter is the modelling of the top flange plates of the chords by an assemblage of rectangular finite elements which incorporate both membrane and plate bending actions. The eight degrees of freedom, rectangular plane stress element and the twelve degrees of freedom, non-conforming rectangular plate bending element [8], [19] are employed. The resulting element has

five degrees of freedom $(u, v, w, \theta_x = \frac{\partial w}{\partial y}, \theta_y = -\frac{\partial w}{\partial x})$ per node. The first two are displacements in the x and y directions due to membrane action while the other three are displacement in the z direction and rotations about the x and y axes due to plate bending action, respectively.

Boundary spring elements are developed to incorporate the restraining effect of the remainder of the chord section on the connecting top flange plate. To maintain compatibility along the longitudinal edges of the chord, interpolation functions of the plate elements adjacent to the edges are used in formulating the stiffnesses of the boundary spring elements. Three different approaches for formulation of these elements will be examined.

Due to the presence of material nonlinearities, the discretized equations of equilibrium have been developed in an incremental form using the principle of virtual work. For each load increment the Newton-Raphson iterative method is used to solve for the nodal displacement increments as well as strain and stress increments at the integration points of both the top flange and the rest of the double or single chord section.

3.2   Finite Element Idealization of Top Flange Plate

Analytical models of the top flange plate for double and single chord HSS T-joints were presented in Sections 2.2 and 2.3, respectively.

Finite element discretization of both models is shown in Fig. 3.1. One-quarter of the top flange plate is modelled by a mesh of 8 × 13 rectangular elements of the type described in Section 3.1. The mesh gradually becomes coarser farther away from the zone of high stress gradients adjacent to the branch inclusion. The plate thickness within the branch inclusion is taken as one thousand times the HSS thickness to represent a relatively much larger stiffness for rigid plate action. Overall dimensions of the plate have been defined in Section 2.2. Other characteristics of the finite element model are as shown in Fig. 3.1.

The boundary conditions that should be incorporated in the finite element model vary according to the type of joint and loading. Boundary conditions corresponding to the branch moment or punching shear are listed in Table 3.1 for a double chord HSS T-joint. When these joints are analyzed under combinations of moment and punching shear, symmetry or anti-symmetry of the joint behaviour in the longitudinal direction is no longer present. Hence, one-half of the joint must be modelled when combined loads are considered. The finite element mesh employed for this analysis consists of 8 × 14 elements as shown in Fig. 3.2. Characteristics of the mesh are similar to those of the former mesh. Its boundary conditions are given in Table 3.2. Evidently, the mesh of Fig. 3.2 is about twice as coarse as that of Fig. 3.1.

When a double chord joint is analyzed under a branch moment, its behaviour is to be characterized by a moment-rotation (M-ϕ) diagram, where ϕ is rotation of the rigid inclusion as indicated in Fig. 3.3(a). On the other hand, the joint behaviour under punching-shear is deter-

mined by the load-deflection (P-δ) diagram where δ is the transverse displacement of the inclusion as indicated in Fig. 3.3(b). Both branch moments and punching shears are idealized by line loads acting along the inclusion perimeter as shown in Fig. 3.3. The equivalent nodal forces in the form of a consistent load vector are then calculated from these line loads using the principle of virtual displacement.

The eight degrees of freedom (DOF) rectangular plane stress elements and the twelve DOF, non-conforming, rectangular plate bending elements [19] have been used to model the top flange plate. Thus, there are twenty generalized parameters which can be determined in terms of the nodal DOF. After solving for the generalized parameters in the polynomial approximations in terms of the nodal DOF, and back substituting into the polynomials, the following equations result.

$$u(\xi, \eta) = \sum_{i=1}^{4} N_{p_i}(\xi, \eta)u_i \qquad (3.1(a))$$

$$v(\xi, \eta) = \sum_{i=1}^{4} N_{p_i}(\xi, \eta)v_i \qquad (3.1(b))$$

$$w(\xi, \eta) = \sum_{i=1}^{12} N_{b_i}(\xi, \eta)\delta_{b_i} \qquad (3.2)$$

The coordinates ξ and η are nondimensional with origin at the lower left corner of the element as shown in Fig. 3.4. $N_{p_i}(\xi, \eta)$ and $N_{b_i}(\xi, \eta)$ are the shape functions for in-plane and out-of-plane displacements,

respectively. These are listed in Appendix A. u_i and v_i are the in-plane displacements and δ_{b_i} are the out-of-plane displacement and rotation degrees of freedom. Equations 3.1 and 3.2 can be written in the following matrix form

$$
\begin{Bmatrix} u(\xi, \eta) \\ v(\xi, \eta) \\ w(\xi, \eta) \end{Bmatrix} = [N(\xi, \eta)] \quad \{\delta_e\} \tag{3.3}
$$

where the shape functions matrix $[N]$ is given by

$$
[N] = \begin{bmatrix}
N_{p_1} & 0 & 0 & 0 & 0 & N_{p_2} & 0 & 0 & 0 & 0 \\
0 & N_{p_1} & 0 & 0 & 0 & 0 & N_{p_2} & 0 & 0 & 0 \\
0 & 0 & N_{b_1} & N_{b_2} & N_{b_3} & 0 & 0 & N_{b_4} & N_{b_5} & N_{b_6} \\
N_{p_3} & 0 & 0 & 0 & 0 & N_{p_4} & 0 & 0 & 0 & 0 \\
0 & N_{p_3} & 0 & 0 & 0 & 0 & N_{p_4} & 0 & 0 & 0 \\
0 & 0 & N_{b_7} & N_{b_8} & N_{b_9} & 0 & 0 & N_{b_{10}} & N_{b_{11}} & N_{b_{12}}
\end{bmatrix} \tag{3.4}
$$

and the displacement vector $\{\delta_e\}$ is as follows:

$$
\{\delta_e\}^T = \langle u_1 \ v_1 \ w_1 \ \theta_{x_1} \ \theta_{y_1} \ | \ u_2 \ v_2 \ w_2 \ \theta_{x_2} \ \theta_{y_2} \ | \ \cdots \ \theta_{y_4} \rangle \tag{3.5}
$$

The strains at any point within the element are related to

displacements by the following equation;

$$\{\varepsilon\} = \left\{ \begin{array}{c} \varepsilon_{xx} \\ \varepsilon_{yy} \\ \gamma_{xy} \end{array} \right\} = \left[\begin{array}{ccc} \dfrac{\partial}{\partial x} & 0 & -z\dfrac{\partial^2}{\partial x^2} \\ 0 & \dfrac{\partial}{\partial y} & -z\dfrac{\partial^2}{\partial y^2} \\ \dfrac{\partial}{\partial y} & \dfrac{\partial}{\partial x} & -2z\dfrac{\partial^2}{\partial x\partial y} \end{array} \right] \left\{ \begin{array}{c} u \\ v \\ w \end{array} \right\} = [L] \left\{ \begin{array}{c} u \\ v \\ w \end{array} \right\} \quad (3.6)$$

where $\{\varepsilon\}$ is the column matrix of strains. Substituting Equation 3.3 into Equation 3.6 yields

$$\{\varepsilon\} = [L] \quad [N] \quad \{\delta_e\} = [B] \quad \{\delta_e\} \tag{3.7}$$

where [B] is called the strain matrix. The element stiffness matrix $[k^e]$ is given as

$$[k^e] = \int_V [B]^T [D] [B] \, dV \tag{3.8}$$

where integration is performed over the element volume. The compliance matrix [D] is defined in Section 3.4. Since the formulation is nonlinear, $[k^e]$ is evaluated numerically. It can be shown that the 3-point Gauss quadrature numerical integration, applied in each of the three directions ξ, η and z, suffices to evaluate Equation 3.8 exactly in the elastic range [8],[19]. Hence, using the coordinates of Fig. 3.4, Equation 3.8 is integrated numerically in the following manner.

$$[k^e] = \frac{a}{2} \cdot \frac{b}{2} \cdot \frac{t}{2} \sum_{i=1}^{3} \sum_{j=1}^{3} \sum_{k=1}^{3} \{W_i W_j W_k [B(\xi_i, \eta_j, z_k)]^T [D]_{ijk}$$

(20×20)   (20×3)   (3×3)

$$[B(\xi_i, \eta_j, z_k]\}$$ (3.9)

(3×20)

and the weighting functions and numerical integration points are as defined below.

$$\{W\}^T = \left\langle \frac{5}{9} \quad \frac{8}{9} \quad \frac{5}{9} \right\rangle$$ (3.10(a))

$$\{\xi\}^T = \{\eta\}^T = \langle (0.5 - \sqrt{0.15}) \quad 0.5 \quad (0.5 + \sqrt{0.15}) \rangle$$ (3.10(b))

$$\{z\}^T = \langle -t\sqrt{0.15} \quad 0 \quad t\sqrt{0.15} \rangle$$ (3.10(c))

It may be noted that the strain matrix [B] at an integration point (ξ_i, η_j, z_k) remains constant throughout the analysis since the geometric nonlinearities are neglected. As a result, the [B] matrix is calculated at each of the 27 integration points only once at the initial formulation of the problem. However, the compliance matrix [D], on the other hand, is updated for every iteration during the load increments when one or more integration points are subject to stress levels past the elastic limit. This is explained in Section 3.5 when dealing with nonlinear finite element analysis.

3.3 Finite Element Idealization of Webs and Bottom Flange –

Boundary Spring Elements

Modelling the restraining effect of the rest of the section (webs and bottom flange) by boundary springs has been presented in Sections 2.2 and 2.3 for double chord and single chord T-joints, respectively. The finite element idealizations of these models, are presented in this section.

The finite element idealization of the analytical model is explained for the double chord T-joint. The degeneration of the double chord model to a single chord T-joint will be pointed out at appropriate stages. Consider the double chord model indicated in Figs. 2.5 and 2.6. The stiffness matrix $[S]$ of frame ABCDEF is of size (54×54). The six by six matrix of spring coefficients $[k_s]$ can be obtained from $[S]$ in the following manner.

(1)   Apply the appropriate boundary conditions to $[S]$ as described in Section 2.2.

(2)   Express the frame equations of equilibrium in the form

$$\left\{ \begin{array}{c} f_1 \\ (6 \times 1) \\ f_2 \\ (48 \times 1) \end{array} \right\} = \left[\begin{array}{cc} S_{11} & S_{12} \\ (6 \times 6) & (6 \times 48) \\ S_{21} & S_{22} \\ (48 \times 6) & (48 \times 48) \end{array} \right] \left\{ \begin{array}{c} \delta_1 \\ (6 \times 1) \\ \delta_2 \\ (48 \times 1) \end{array} \right\} \qquad (3.11)$$

where forces $\{f_1\}$ and displacements $\{\delta_1\}$ refer to DOF's 1 to 6 while $\{f_2\}$ and $\{\delta_2\}$ refer to DOF's 7 to 54 (Fig. 2.5).

(3)   Eliminate DOF's 7 to 54 by keeping the corresponding forces $\{f_2\}$ at zero. This condensation process leads to

$$\{f_1\} = ([S_{11}] - [S_{12}] [S_{22}]^{-1} [S_{12}]^T) \; \{\delta_1\}. \tag{3.12}$$

(4)   The holding forces $\{f_1\}$ given by Equation 3.12 represents column "i" of the required stiffness matrix $[k_s]$ when $\{\delta_1\}$ consists of unit displacement at DOF "i" and zeros for the other five DOF's. Hence, this procedure is repeated six times to obtain all six columns.

The procedure above is also valid in the elasto-plastic range in which [S] represents the tangential stiffness of appropriate members of the frame which are subject to forces beyond the proportional range. The resulting $[k_s]$ matrix can be written in the following form.

$$[k_s] = \begin{bmatrix} [k_{rr}] & [k_{r\ell}] \\ (3\times3) & (3\times3) \\ [k_{\ell r}] & [k_{\ell\ell}] \\ (3\times3) & (3\times3) \end{bmatrix} \tag{3.13}$$

This is a symmetric matrix and its positive definiteness can be easily verified from the boundary conditions imposed on the frame in Fig. 2.5. Coefficients of the submatrices $[k_{rr}]$ or $[k_{\ell\ell}]$ represent the forces that

would be required on the right or left parts of the frame if the dis-
placements v, w or θ_x (1, 2, or 3) at right or (4, 5, or 6) at left were
given unit displacements, taken one at a time, while maintaining the
other five displacements at zero.   Similarly, the off-diagonal sub-
matrices $[k_{r\ell}]$ and $[k_{\ell r}]$ represent the forces that would be required on
the right part due to a unit displacement imposed on a degree of freedom
on the left part, and vice versa.

The elastic strain energy, U_B, due to displacements of the
boundary springs is

$$
U_B = \frac{1}{2} \int_{\ell_e} \left\{ \begin{array}{c} \delta_B^r \\ \\ \delta_B^\ell \end{array} \right\}^T \left[\begin{array}{cc} k_{rr} & k_{r\ell} \\ \\ k_{\ell r} & k_{\ell\ell} \end{array} \right] \left\{ \begin{array}{c} \delta_B^r \\ \\ \delta_B^\ell \end{array} \right\} dx \tag{3.14}
$$

where ℓ_e is the length AB or CD of the boundary spring element indicated
by the shaded area in Fig. 2.6 or Fig. 3.1 and

$$
\left\{ \delta_B^r \right\}^T = \langle v^r \quad w^r \quad \theta_x^r \rangle \tag{3.15(a)}
$$

$$
\left\{ \delta_B^\ell \right\}^T = \langle v^\ell \quad w^\ell \quad \theta_x^\ell \rangle \tag{3.15(b)}
$$

Due to coupling of the boundary springs across edges AB and CD, computa-
tion of the strain energy involves displacements along both edges. The
shaded area ABCD, thus, represents the boundary spring element joining

edge AB to edge CD. Of course, it will be connected to the rectangular elements across the band ABCD, used for discretizing the top plate, at edges AB and CD. The finite element approximations for v^r, w^r, θ_x^r and v^ℓ, w^ℓ, θ_x^ℓ, are so chosen such that these preserve the same continuity of displacements as used for the rectangular plate-elements. This can be accomplished by simply taking the corresponding finite element displacement fields along edges CD or 3-4 and AB or 1-2 for elements R and L in Fig. 3.1, respectively. Thus, the shape functions for both v and w along the right and left edges are identical, i.e. linear and cubic, respectively. Thus

$$v^r = \xi \, v_3^r + (1 - \xi) \, v_4^r \qquad\qquad (3.16(a))$$

$$v^\ell = (1 - \xi) \, v_1^\ell + \xi \, v_2^\ell \qquad\qquad (3.16(b))$$

$$w^r = [\xi^2(3 - 2\xi)] \, w_3^r + [- a\xi^2(1 - \xi)]\theta_{y_3}^r + [1 - \xi^2(3 - 2\xi)]w_4^r$$

$$\qquad + [a\xi (1 - \xi)^2]\theta_{y_4}^r \qquad\qquad (3.16(c))$$

$$w^\ell = [1 - \xi^2(3 - 2\xi)]w_1^\ell + [a\xi (1 - \xi)^2]\theta_{y_1}^\ell + [\xi^2 (3 - 2\xi)]w_2^\ell$$

$$\qquad + [- a\xi^2 (1 - \xi)]\theta_{y_2}^\ell . \qquad\qquad (3.16(d))$$

, where $\xi = x/a$ is the non-dimensional coordinate along the local x-axis

of the plate element and, a, is the length AB or CD. Using the expressions of Equations 3.16 to define the u and w displacements in Equations 3.15 will ensure continuity of these DOF along the edges.

However, the lack of continuity of the normal slopes along the plate edges and its dependence on DOF of the interior nodes causes some complications. For example, θ_x^ℓ along edge 1-2 of element L in Fig. 3.1 is given as:

$$\theta_x^\ell = [\frac{1}{b_\ell} \{\xi - \xi^2(3 - 2\xi)\}]w_1^\ell + [1 - \xi]\theta_{x_1}^\ell + [\frac{a}{b_\ell} \xi (1 - \xi^2)]\theta_{y_1}^\ell$$

$$+ [\frac{1}{b_\ell} \{\xi^2(3 - 2\xi) - \xi\}]w_2^\ell + [\xi]\theta_{x_2}^\ell + [-\frac{a}{b_\ell} \xi^2(1 - \xi)]\theta_{y_2}^\ell$$

$$+ [\frac{1}{b_\ell} \{\xi - \xi^2(3 - 2\xi)\}]w_3^\ell + [\frac{a}{b_\ell} \xi^2(1 - \xi)]\theta_{y_3}^\ell$$

$$+ [\frac{1}{b_\ell} \{\xi^2(3 - 2\xi) - \xi\}]w_4^\ell + [-\frac{a}{b_\ell} \xi(1 - \xi)^2]\theta_{y_4}^\ell . \qquad (3.16(e))$$

Note that θ_x^ℓ does not depend on $\theta_{x_3}^\ell$ and $\theta_{x_4}^\ell$. An exact mirror image exists for element R. Because of discontinuity of the slopes normal to the edges of nonconforming plate elements already employed, one can incorporate further simplifications thus rendering the following three options.

(1)   Use linear interpolations for approximation of the normal slopes, i.e.

$$\theta_x^m = [1 - \xi]\theta_{x_1}^m + [\xi]\theta_{x_2}^m; \quad m = r \text{ or } \ell \qquad (3.16(f))$$

Linear approximation of θ_x instead of the cubic in Equation 3.16(e) implies a stiffer boundary spring finite element model.

(2)   Use a single element across the top plate width, i.e. $b_\ell = a_1 + a_2$ (Fig. 3.1) in Equation 3.16(e). This will allow a cubic variation in θ_x and eliminate its dependence on DOF of the internal nodes. This option is expected to yield a more flex-ible model than option (1).

(3)   Approximate the normal slope θ_x within both elements R and L using full Equation 3.16(e). This, of course, would yield the most flexible boundary spring model because of its ability to deform more readily than the previous two options.

Obviously, options (1) and (2) yield a stiffness matrix of size 16 × 16 for the boundary spring element whereas option (3) yields a 24 × 24 matrix.

Option (3) has been used for formulating the boundary spring finite elements employed in the analysis to be reported. After substitution of Equations 3.16(a) to 3.16(e), Equation 3.15 becomes

$$\{\delta_B^r\} = [N_r] \quad \{\delta_B^{er}\} \tag{3.17(a)}$$
$$(3\times1) \quad (3\times12) \quad (12\times1)$$

$$\{\delta_B^\ell\} = [N_\ell] \quad \{\delta_B^{e\ell}\} \tag{3.17(b)}$$
$$(3\times1) \quad (3\times12) \quad (12\times1)$$

where $[N_r]$ and $[N_\ell]$ contain the appropriate shape functions for v, w and θ_x on the right and left edges, respectively. $\{\delta_B^{er}\}$ and $\{\delta_B^{e\ell}\}$ are vectors of active nodal DOF for elements R and L, respectively; i.e.

$$\{\delta_B^{er}\}^T = \langle v_1^r \ w_1^r \ \theta_{x_1}^r \ \theta_{y_1}^r \quad v_2^r \ w_2^r \ \theta_{x_2}^r \ \theta_{y_2}^r \quad w_3^r \ \theta_{y_3}^r \ w_4^r \ \theta_{y_4}^r \rangle \tag{3.18}$$

The required stiffness matrix, denoted $[k_s^e]$, for the boundary spring element is derived using Equations 3.14 and 3.17 as

$$[k_s^e] = a \int_0^1 \begin{bmatrix} [N_r]^T & [0] \\ [0] & [N_\ell]^T \end{bmatrix} \begin{bmatrix} k_{rr} & k_{r\ell} \\ k_{\ell r} & k_{\ell\ell} \end{bmatrix} \begin{bmatrix} [N_r] & [0] \\ [0] & [N_\ell] \end{bmatrix} d\xi. \tag{3.19}$$
$$(24\times24) \qquad (24\times6) \qquad (6\times6) \qquad (6\times24)$$

The stiffness matrix $[k_s^e]$ above enables one to incorporate the restraining effect of the rest of the section (webs and bottom flanges) on the top flange in the present finite element modelling of double chord RHS T-joints.

Precisely the same procedure can be used to derive the equiva-

lent $[k_s^e]$ stiffness matrix for a single chord RHS T-joint. The model for this case involves boundary springs in the directions of v^r, w^r and θ_x^r only (Fig. 2.9) and, of course, the proper boundary conditions. Hence, it can be easily shown that the stiffness matrix of the boundary spring element for the single chord model is given by

$$[k_s^e] = a \int_0^1 [N_r]^T [k_{rr}] [N_r] \, d\xi. \qquad (3.20)$$

$(12{\times}12) \qquad (12{\times}3) \ (3{\times}3) \ (3{\times}12)$

In both cases, the matrix $[k_s^e]$ is computed using numerical integration.

It should be mentioned that the formulation of $[k_s^e]$ as given above is valid in the elastic as well as the elasto-plastic range of loading. Material nonlinearities at any load level are incorporated in the formulation through using the tangential stiffnesses of the edge springs in $[k_s]$. Furthermore, the in-plane and the out-of-plane actions of the top flange plate are uncoupled without the boundary springs. However, incorporation of the coupled edge springs results in the coupling of the two actions prior to onset of plasticity.

3.4   Compliance Relationship for Elasto-Plastic Analysis

The joint material (steel) is assumed isotropic, linear elastic up to the yield limit, and linear strain-hardening thereafter. The Von-Mises yield criterion and the associated flow rule have been

employed here. According to this yield criterion for plane stress problems, yielding begins when the effective stress $\bar{\sigma}$ exceeds a certain limit, where [18], [27]

$$\bar{\sigma} = (\sigma_x^2 + \sigma_y^2 - \sigma_x \sigma_y + 3\tau_{xy}^2)^{\frac{1}{2}}. \qquad (3.21)$$

Differentiation of both sides of Equation 3.21 and substitution of the deviatoric stresses

$$\sigma_x' = \frac{1}{3}(2\sigma_x - \sigma_y), \; \sigma_y' = \frac{1}{3}(2\sigma_y - \sigma_x), \; \tau_{xy}' = \tau_{xy} \qquad (3.22)$$

leads to the following

$$d\bar{\sigma} = \left\langle \frac{3\sigma_x'}{2\bar{\sigma}} \; \frac{3\sigma_y'}{2\bar{\sigma}} \; \frac{3\tau_{xy}'}{\bar{\sigma}} \right\rangle \begin{Bmatrix} d\sigma_x \\ d\sigma_y \\ d\tau_{xy} \end{Bmatrix} = \left\{ \frac{\partial \bar{\sigma}}{\partial \sigma} \right\}^T \{d\sigma\} \qquad (3.23)$$

The Prandtl-Reuss relations state that

$$\{d\epsilon^P\} = \left\langle d\epsilon_x^P \; d\epsilon_y^P \; d\gamma_{xy}^P \right\rangle = \left\{ \frac{\partial \bar{\sigma}}{\partial \sigma} \right\} d\bar{\epsilon}^P \qquad (3.24)$$

thus defining the three plastic strain increments that result when the effective plastic strain increment $d\bar{\epsilon}^P$ occurs under a known state of stress.

Since this strain increment $\{d\varepsilon\}$ is the sum of its elastic component $\{d\varepsilon^e\}$ and its plastic component $\{d\varepsilon^P\}$, one can apply Hooke's law to obtain

$$\{d\sigma\} = [D]\{d\varepsilon^e\} = [D]\ (\{d\varepsilon\} - \{d\varepsilon^P\}) \tag{3.25}$$

where $[D]$ is the elastic compliance matrix.

A relation that yields $d\bar{\varepsilon}^P$ from the total strain increment $\{d\varepsilon\}$ is obtained by substituting Equation 3.24 into Equation 3.25, i.e.

$$d\bar{\varepsilon}^P = \frac{\left\{\frac{\partial\bar{\sigma}}{\partial\sigma}\right\}^T [D]}{H' + \left\{\frac{\partial\bar{\sigma}}{\partial\sigma}\right\}^T [D] \left\{\frac{\partial\bar{\sigma}}{\partial\sigma}\right\}}\ \{d\varepsilon\} = \langle w \rangle \{d\varepsilon\} \tag{3.26}$$

where H' is the strain hardening modulus, i.e., the slope of the $\bar{\sigma} - \bar{\varepsilon}^P$ curve, and is given by

$$H' = \frac{d\bar{\sigma}}{d\bar{\varepsilon}^P} = \frac{\left\{\frac{\partial\bar{\sigma}}{\partial\sigma}\right\}^T \{d\sigma\}}{d\bar{\varepsilon}^P} = \frac{E\ E_T}{E - E_T} \tag{3.27}$$

where E_T is the tangent modulus.

An incremental stress-strain relationship, analagous to Hooke's law but valid beyond the proportional limit, is obtained by substitution of Equation 3.26 in Equation 3.24 and the result into Equation 3.25.

This relationship is given by

$$\{d\sigma\} = ([D] - [D] \left\{\frac{\partial \bar{\sigma}}{\partial \sigma}\right\} \langle w \rangle) \{d\epsilon\} = [D_{ep}]\{d\epsilon\} \qquad (3.28)$$

where $[D_{ep}]$ is the elasto-plastic compliance matrix. For plane stress problems, Equation 3.28 becomes [18]

$$\left\{\begin{matrix} d\sigma_x \\ d\sigma_y \\ d\tau_{xy} \end{matrix}\right\} = \left[\begin{matrix} [\frac{E}{1-\nu^2} - \frac{S_1^2}{S}] & & \text{symm.} \\ [\frac{\nu E}{1-\nu^2} - \frac{S_1 S_2}{S}] & [\frac{E}{1-\nu^2} - \frac{S_2^2}{S}] & \\ [-\frac{S_1 S_3}{S}] & [-\frac{S_2 S_3}{S}] & [\frac{E}{2(1+\nu)} - \frac{S_3^2}{S}] \end{matrix}\right] \left\{\begin{matrix} d\epsilon_x \\ d\epsilon_y \\ d\gamma_{xy} \end{matrix}\right\} \quad (3.29)$$

or

$$\{d\sigma\} = [D_{ep}]\{d\epsilon\}$$

where

$$S = \frac{4}{9} H' \bar{\sigma}^2 + S_1 \sigma_x' + S_2 \sigma_y' + 2S_3 \tau_{xy} \qquad (3.30(a))$$

$$S_1 = \frac{E}{(1-\nu^2)} (\sigma_x' + \nu\sigma_y') \qquad (3.30(b))$$

$$S_2 = \frac{E}{(1-\nu^2)} (\sigma_y' + \nu\sigma_x') \qquad (3.30(c))$$

$$S_3 = \frac{E}{(1 + \nu)} \tau_{xy} \qquad\qquad (3.30(d))$$

In the elastic range, S becomes infinite and $[D_{ep}]$, as given above, reduces to the more familiar elastic compliance matrix $[D]$. Furthermore, for plastic yielding ($E_T = 0$), the matrix of Equation 3.29 renders no numerical problems and has been used for elasto-plastic analysis of the T-joints in conjunction with the Newton-Raphson method presented in the next section.

3.5   Nonlinear Finite Element Analysis

Nonlinear analysis involves establishing the finite element equilibrium equations through virtual work for each load increment. These are then solved for the incremental displacements, strains and stresses. Since the displacement finite element method is used, the principle of virtual displacement has been employed to express equilibrium. Using the analytical models for the double and single chord T-joints and their finite element formulations, the discretized equations of equilibrium after the nth load increment can be expressed in the following form [8].

$$\{\Psi(\delta_n)\} = \int_V [B]^T \{\sigma_n\} dV - \{R_n\} = 0 \qquad\qquad (3.31)$$

The vector $\{R_n\}$ represents the consistent load vector due to surface tractions (line loads along the branch inclusion perimeter). For incre-

mental load analysis, Equation 3.31 takes the following form

$$\int_V [B]^T \{\Delta\sigma_n\} dV - \{\Delta R_n\} = 0 \qquad (3.32)$$

Obviously Equation 3.31 is not satisfied exactly after performing a limited number of iterations and there are undesired residual forces present. In order to minimize these residual forces and prevent drifting of the solution, the Newton-Raphson method is employed and iterations are carried out within each load increment. Hence, during the nth load increment and the mth iteration, the residual forces are computed in the following manner.

$$\{\Psi_n^m\} = \int_V [B]^T \{\sigma_n^m\} dV - \{R_n\} \qquad (3.33)$$

The iterative Newton-Raphson equation can be written as

$$\{\Psi_n^{m+1}\} = \{\Psi_n^m\} + [K_T(\underline{\sigma}_n^m)] \{\Delta\delta_n^m\} = \{0\} \qquad (3.34)$$

where the tangential stiffness matrix $[K_T(\underline{\sigma}_n^m)]$ has been computed by assembling the individual stiffness matrices of all elements. It is important to note that an individual stiffness matrix is computed through numerical integration by using twenty-seven integration points for the state of stress $\underline{\sigma}_n^m$. Proper $[D_n^m]$, elastic or elasto-plastic matrix, is used depending on the stress level and the tangent modulus at each integration point. It may very well happen that within the same

element some integration points can be within the elastic range and others past the proportional limit. The residual load vector in Equation 3.33, which can be controlled by specifying a certain tolerance, is added to the next load increment $\{\Delta R_n\}$ at the beginning of m iterations. This prevents any further drifting of the solution.

The incremental displacements are computed as

$$\{\Delta \delta_n^m\} = - [K_T(\underline{\sigma}_n^m)]^{-1} \{\Psi_n^m\} \qquad (3.35)$$

and the incremental total strains and stresses at any point within an element are given by

$$\{\Delta \epsilon_{ne}^m\} = [B] \{\Delta \delta_{ne}^m\} \qquad (3.36)$$

$$\{\Delta \underline{\sigma}_{ne}^m\} = [D_n^m] \{\Delta \epsilon_{ne}^m\} \qquad (3.37)$$

where $\{\Delta \delta_{ne}^m\}$, $\{\Delta \epsilon_{ne}^m\}$ and $\{\Delta \sigma_{ne}^m\}$ are the element nodal displacements, strains and stresses at the chosen point, respectively.

The strain matrix [B] and the updated elastic or elasto-plastic matrix $[D_n^m]$ are functions of space (i.e., x, y and z or ξ, η and $\tilde{z}$) and must be evaluated at the point where the strain and the stress increments are required to be computed. The updated element stiffness matrix $[k_T^e(\underline{\sigma}_n^m)]$ is evaluated by using Equation 3.9 and $[D_n^m]$, the elastic

or elasto-plastic compliance matrix determined for stress level σ_{-n}^{m}.

The Newton-Raphson iterative scheme above is illustrated graphically in Fig. 3.5 for a single degree of freedom system. However, it is equally applicable to a multi-degree of freedom system. A brief description of the steps followed in the finite element computer program is as follows.

Suppose that at a load level $\{R_n\}$, the displacement vector $\{\delta_n^0\}$ and the stiffness matrix $[k_T(\sigma_{-n}^0)]$ of the system are known. Apply the next load increment $\{\Delta R_n\}$ which brings the load level up to $\{R_{n+1}\}$. The resulting displacement increment $\{\Delta\delta_n\}$ is computed in the following manner.

(1) After the Newton-Raphson iterative procedure has converged (within the specified tolerance) for the $(n-1)^{th}$ load increment after m iterations, assume that the residual forces are given by $\{\Psi_{n-1}^m\}$ according to Equation 3.33. The displacement increment due to first iteration for the nth load increment can be computed from the following equation:

$$[k_T(\sigma_{-n}^0)] \{\Delta\delta_n^0\} = -\{\Psi_{n-1}^m\} + \{\Delta R_n\} = -\{\Psi_n^0\} + \{\Delta R_n\}$$

where $\{\Psi_n^0\} = \{\Psi_{n-1}^m\}$ and $\{\Delta R_n\}$ is the $(n+1)^{th}$ load increment.

(2)   The displacement vector is updated in the following manner.

$$\{\delta_n^1\} = \{\delta_n^0\} + \{\Delta\delta_n^0\}$$

(3)   For each plate element, do the following:

(i)   Extract the element incremental nodal displacements $\{\Delta\delta_{ne}^0\}$ from $\{\Delta\delta_n^0\}$ just computed.

(ii)   At each integration (sampling) point (ξ_i, η_i, z_i):

- calculate the incremental strains via Equation 3.36

$$\{\Delta\varepsilon_n^0\}_i = [B(\xi_i, \eta_i, z_i)] \{\Delta\delta_{ne}^0\} \quad (i, j, k = 1, 2, 3);$$

- calculate the incremental stresses via Equation 3.37,

$$\{\Delta\sigma_n^0\}_i = [D_n^0]_i \{\Delta\varepsilon_n^0\}_i$$

where the elasto-plastic compliance matrix $[D_n^0]_i$ is determined for the stress levels $(\underline{\sigma}_n^0)$ at point i with local coordinates (ξ_i, η_i, z_i);

- update the stresses at each integration point;

$$\{\sigma_{n+1}^1\}_i = \{\sigma_n^0\}_i + \{\Delta\sigma_n^0\}_i$$

- check for the compliance matrix.

$$[D_n^1]_1 = [D_{e\ell}]_1 \quad \text{if} \quad \bar{\sigma}_1 < \sigma_Y$$

$$[D_n^1]_1 = [D_{epn}^1]_1 \quad \text{if} \quad \bar{\sigma}_1 > \sigma_Y$$

where $\bar{\sigma}_1$ is the effective stress at point i defined in Equation 3.21.

(iii) If $\bar{\sigma}_1 > \sigma_Y$ at one or more integration points, update the element stiffness matrix $[k^e]$ using Equation 3.9.

(iv) Calculate the residual forces for a single element using Equation 3.33 and numerical integration.

$$\{\Psi_{ne}^1\} = \int_{V_e} [B]^T \{\sigma_n^1\} dV - \{R_{ne}^1\}.$$

(4) For each boundary spring element, do the following.

(i) Extract the incremental nodal displacements for the elements L and R which have common edges AB and CD, respectively, with the longitudinal boundaries (Fig. 3.1(a)). The twelve relevant DOF are used for each element to express $\{\Delta\delta_{Bn}^{\ell 0}\}$ and $\{\Delta\delta_{Bn}^{r0}\}$ in Equations 3.17 in the incremental form.

(ii) Recall the coupled edge springs stiffness matrix $[k_s]$

described in Section 3.3 in which the stiffness coeffi-
cients are defined per unit length. Knowing the incremen-
tal displacements $\{\Delta\delta_{Bn}^{\ell 0}\}$ and $\{\Delta\delta_{Bn}^{r0}\}$ and using the interpol-
ations in Equations 3.16, the displacement and rotation
increments can be determined at the three integration
points (six per integration point, i.e. $\{\Delta\delta_{1,n}^{0}\}_i$) along the
edges AB and CD, respectively, but have been taken as con-
stant in the analyses to be presented in this theses.
Hence, a constant $[k_s]$ matrix is required along edges AB
and CD.

(iii) Nine integration points are taken for evaluating the stiff-
ness matrices for beam-column elements for the U-shaped
frame of Fig. 2.5 to represent stiffness of the rest of the
section. The previous [S] matrix (i.e. $[S_n^{0}]$), with fifty-
four DOF's in Equation 3.11, is of course known. Using
this and knowing the incremental displacements at DOF's one
to six, the incremental displacements are determined for
the rest of DOF's (forty-eight altogether) in the following
manner.

$$\{\Delta\delta_{2,n}^{0}\}_i = - [S_{22n}^{0}]_i^{-1} [S_{21n}^{0}]_i \{\Delta\delta_{1,n}^{0}\}_i$$
$$\quad (48\times1) \qquad (48\times48) \quad (48\times6) \quad (6\times1)$$

This permits carrying out the incremental elasto-plastic
analysis of the U-shaped frame in Fig. 2.5.

(iv) Knowing $\{\Delta\delta_{2,n}^{0}\}_i$, step (3) for the plate element is
repeated for the beam-column element of the frame. This

is much simpler than the procedure followed for the plate element (i.e. instead of using $[D_{e\ell}]_i$ or $[D_{epn}^1]_i$, the elastic modulus E or the tangent modulus E_T are used).

(v) Once the incremental quantities have been updated, for the new stress levels, one forms the updated $[S_{n+1}^1]_i$ at all i integration points. Following the procedure for determining the $[k_s]$ matrix in Section 3.3, the matrices $[k_s^1]_i$ are obtained for use in formulation of the updated boundary spring element matrices.

(vi) Use the following equation (numerical integration of Equation 3.19) to formulate the updated boundary spring element matrix.

$$[k_{sn}^{e1}] = a \sum_{i=1}^{3} W_i [\tilde{N}]_i^T [k_{sn}^1]_i [\tilde{N}]_i$$

Note $[\tilde{N}]_i = \begin{bmatrix} [N_r] & [0] \\ [0] & [N_\ell] \end{bmatrix}_i$ is evaluated at the ith

integration point ξ_i where ξ_i and W_i are the same as defined in Equations 3.10.

(vii) Calculate the boundary spring element residual forces

$$\{\Psi_{ns}^1\} = a \sum_{i=1}^{3} W_i [\tilde{N}]_i^T \{f_{1,n+1}^1\}_i$$

where $\{f_{1,n+1}^1\}_i$ are the internal forces (at the present

load level) that correspond to the U-frame nodal displace-
ments in Equation 3.18.

(5) Assemble the global tangential stiffness matrix $[k_T(\sigma_{-n}^1)]$ and the
global residual force vector $\{\Psi_n^1\}$ using both, the plate and the
boundary spring elements.

(6) Solve the following equation to determine the next incremental
displacement vector.

$$[K_T(\sigma_{-n}^1)] \{\Delta\delta_n^1\} = - \{\Psi_n^1\}$$

(7) Repeat steps (2) to (6) until the incremental solution for
displacements is within the specified percentage tolerance γ
which is calculated in the following manner.

$$\gamma = 100 \times \frac{Det[K_T(\sigma_{-n}^m)] - Det[K_T(\sigma_{-n}^{m-1})]}{Det[K_T(\sigma_{-n}^{m-1})]}$$

(8) If the percentage tolerance is within the prescribed value,
apply the next load increment and repeat steps (1) to (7).

The iterative procedure outlined above is commenced by formulat-
ing the system elastic stiffness matrix and applying an arbitrary magni-
tude of the loads. The system is then solved for displacements, strains
and stresses. The yield limit is determined by scaling the applied

loads such that $\bar{\sigma}$ at the most stressed point in the model (top flange and frame) exceeds the yield limit σ_Y. The same scaling factor is applied to the calculated displacements, strains and stresses. Additional loads are then applied in increments as a percentage of the yield load until stiffness of the joint reduces significantly in comparison with its initial value where stiffness is defined as the slope of either the P-δ diagram or the M-ϕ diagram.

The Newton-Raphson procedure outlined in this section requires a complete reanalysis of the system for every iteration. However, it allows application of the loads in relatively large increments. Furthermore, the method converges in about two to three iterations for each load increment. For equal load increments, the number of iterations required for convergence starts increasing rather quickly as the P-δ or M-ϕ curve becomes flatter or the stiffness changes rapidly. This is usually a signal to decrease the load increments in this range to help reduce the number of iterations as would be expected in any nonlinear problem.

3.6   Test Example

A square plate, simply supported on all four sides, under uniform pressure is analyzed to verify the elasto-plastic modelling. One quarter of the ten inch square plate (thickness = 0.4 in.) has been modelled by nine square elements as indicated in Fig. 3.6(b). The plate is uniformly loaded well into the inelastic range. The modulus of elasticity E is 10^4 ksi, tangent modulus $E_T = 10^3$ ksi, Poisson's ratio ν

= 0.5 and the yield stress σ_Y is 30 ksi. The data above conforms with that used by Stanton and Schmit [13] so that the results from the present analysis could be compared. Fig. 3.6(a) indicates very good agreement for the uniform pressure versus the central deflection response. It sould be pointed out that the use of bicubic Hermite displacement functions render a rectangular, conforming plate bending element; bicubic splines provided the curvature continuity. Overall, the element used in [13] is stiffer than that used in the present analysis. Progression of yield zones at various pressure levels appears in Fig. 3.7 and seems very reasonable.

TABLE 3.1 Boundary Conditions for Finite Element Model of Fig. 3.1.

Boundary Conditions

Nodes No.	Bending	Punching Shear
1 to 9	$w = \theta_x = 0$	$w = \theta_x = 0$
Inclusion Nodes	$u = v = \theta_x = 0$	$u = v = \theta_x = \theta_y = 0$
118, 120, 122, 124, 126	$u = v = w = \theta_x = 0$	$u = v = \theta_x = \theta_y = 0$
119, 121, 123, 125	$u = w = \theta_x = 0$	$u = \theta_x = \theta_y = 0$

TABLE 3.2 Boundary Conditions for Finite Element Model of Fig. 3.2.

Boundary Conditions

Nodes No.	Bending	Punching Shear
1 to 9, 127 to 135	$w = \theta_x = 0$	$w = \theta_x = 0$
Inclusion Nodes	$u = v = \theta_x = 0$	$v = u = \theta_x = \theta_y = 0$
65, 67, 69, 71	$u = 0$	$u = 0$
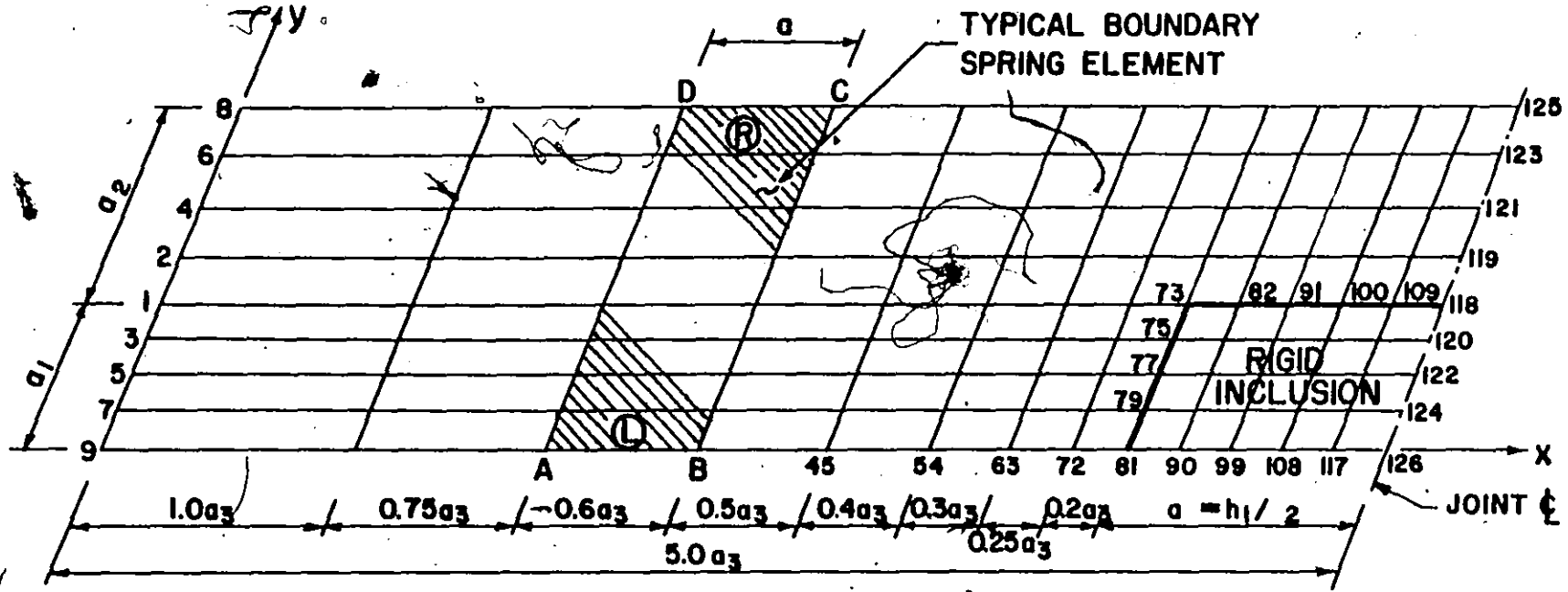
a. Finite Element Mesh

Properties of the Mesh:

No. of Nodes = 126
No. of Rec. Elements = 104
No. of Boundary Spring Elements = 13
No. of DOF's = 630
No. of Unknowns = 510
Half Band Width = 64
Size of Global Stiffness
Matrix = 33,150
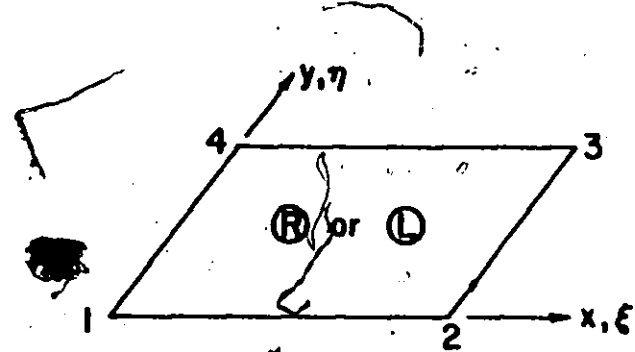
b. Typical Rectangular Plate Element

FIG. 3.1   FINITE ELEMENT IDEALIZATION OF ONE-QUARTER OF RHS T-JOINTS

- 59 -
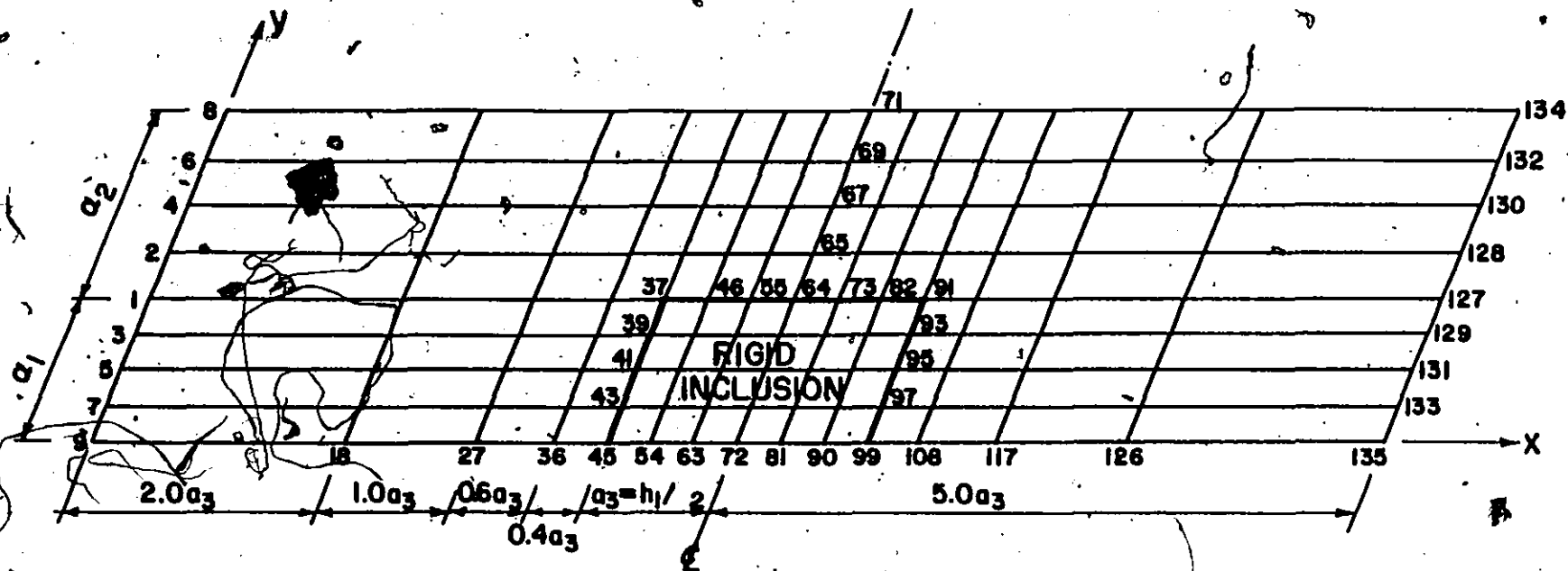
Properties of the Mesh:

No. of Nodes = 135
No. of Rec. Elements = 112
No. of Boundary Spring Elements = 14
No. of DOF's = 675
No. of Unknowns = 530
Half Band Width = 64
Size of Global Stiffness Matrix = 34,450

FIG. 3.2 FINITE ELEMENT IDEALIZATION OF ONE-HALF OF RHS T-JOINTS

- 09 -

$$N_a = \frac{P}{2(b_1 + h_1)}$$

$$N_b = \frac{3M}{h_1(3b_1 + h_1)}$$
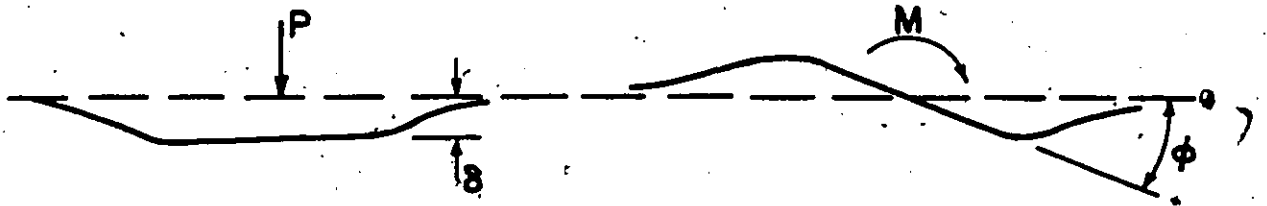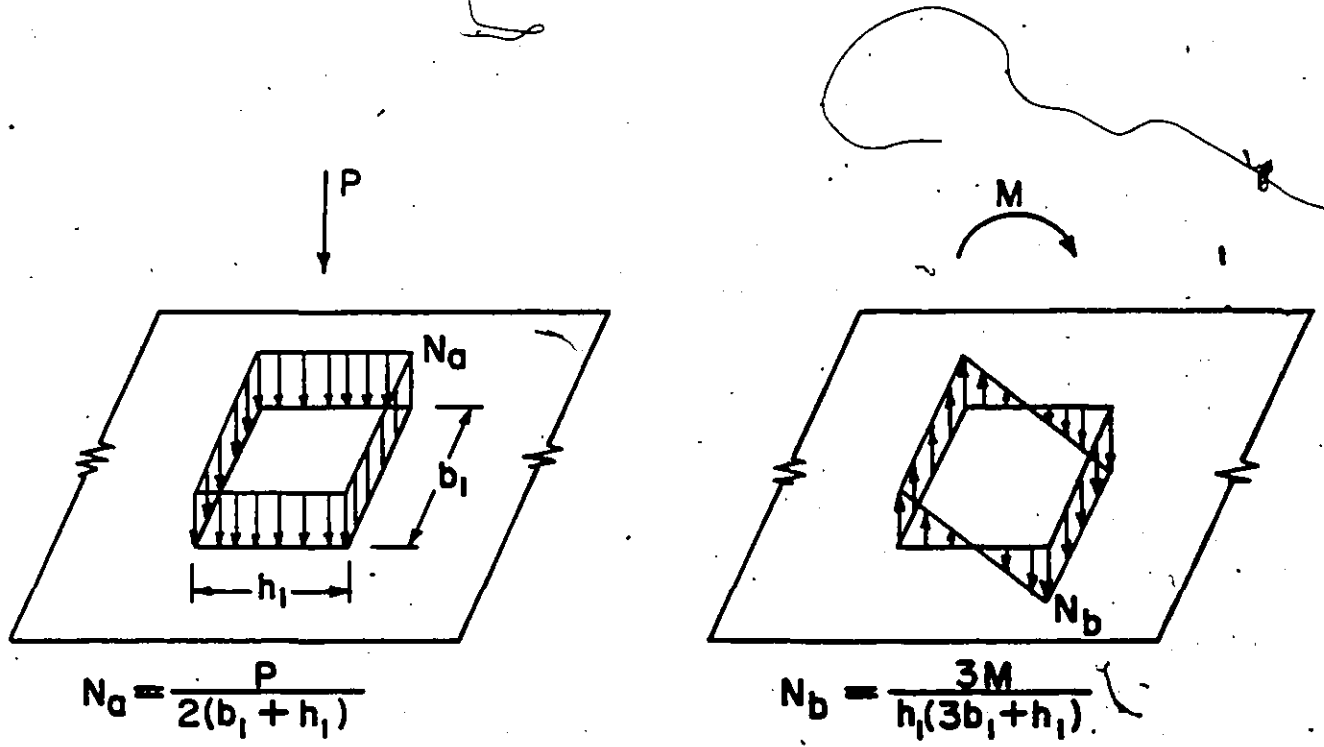
b. PUNCHING SHEAR   a. BENDING MOMENT

FIG 3.3   DEFINITION OF JOINT LOADS AND DEFORMATIONS
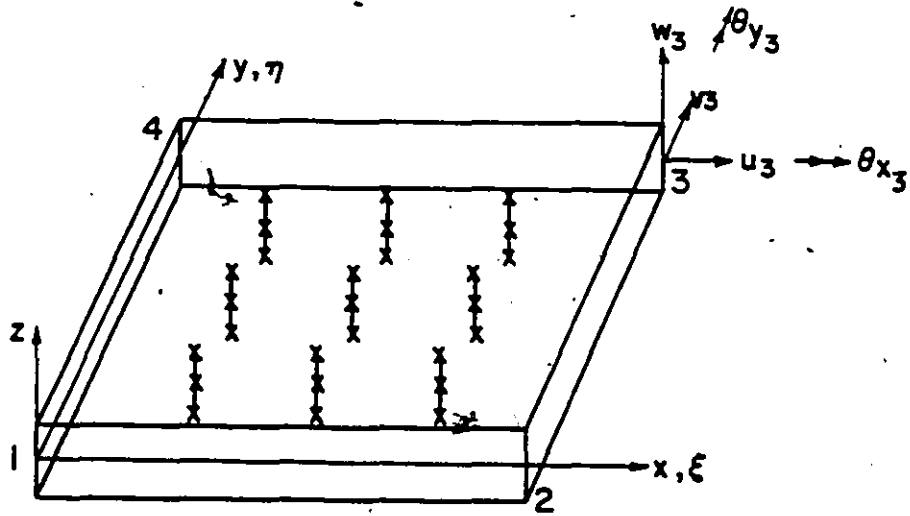
x — INTEGRATION POINT

FIG. 3.4 RECTANGULAR PLATE ELEMENT
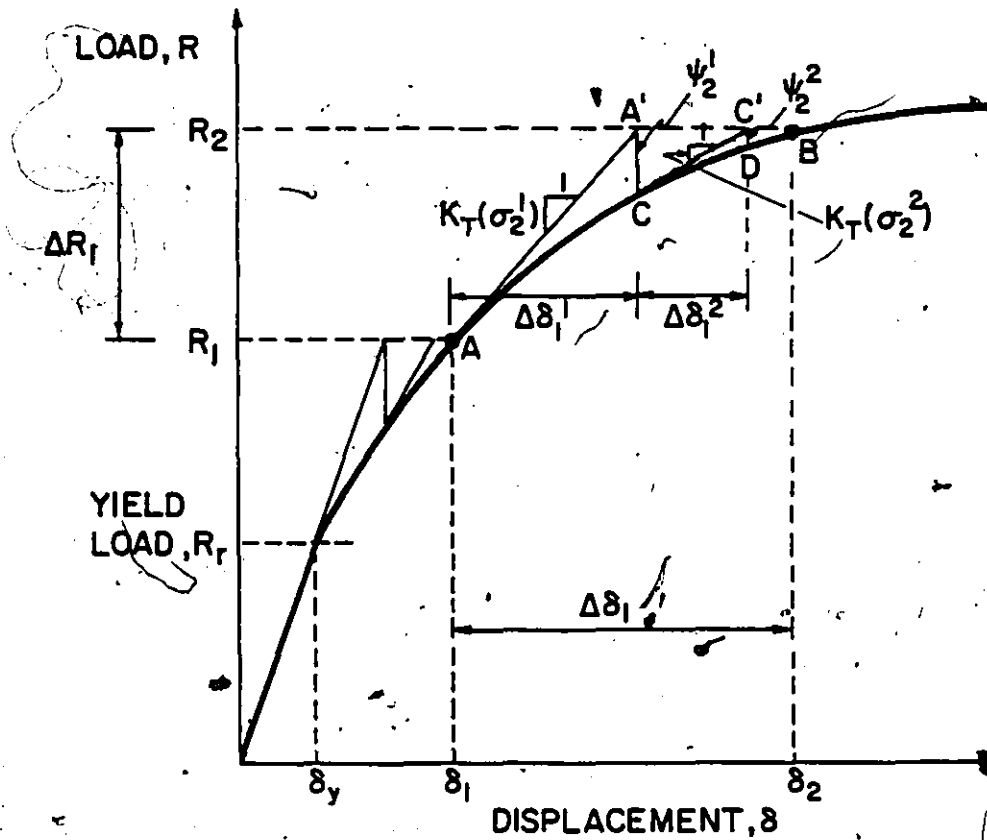
FIG. 3.5 NEWTON-RAPHSON ITERATIVE METHOD
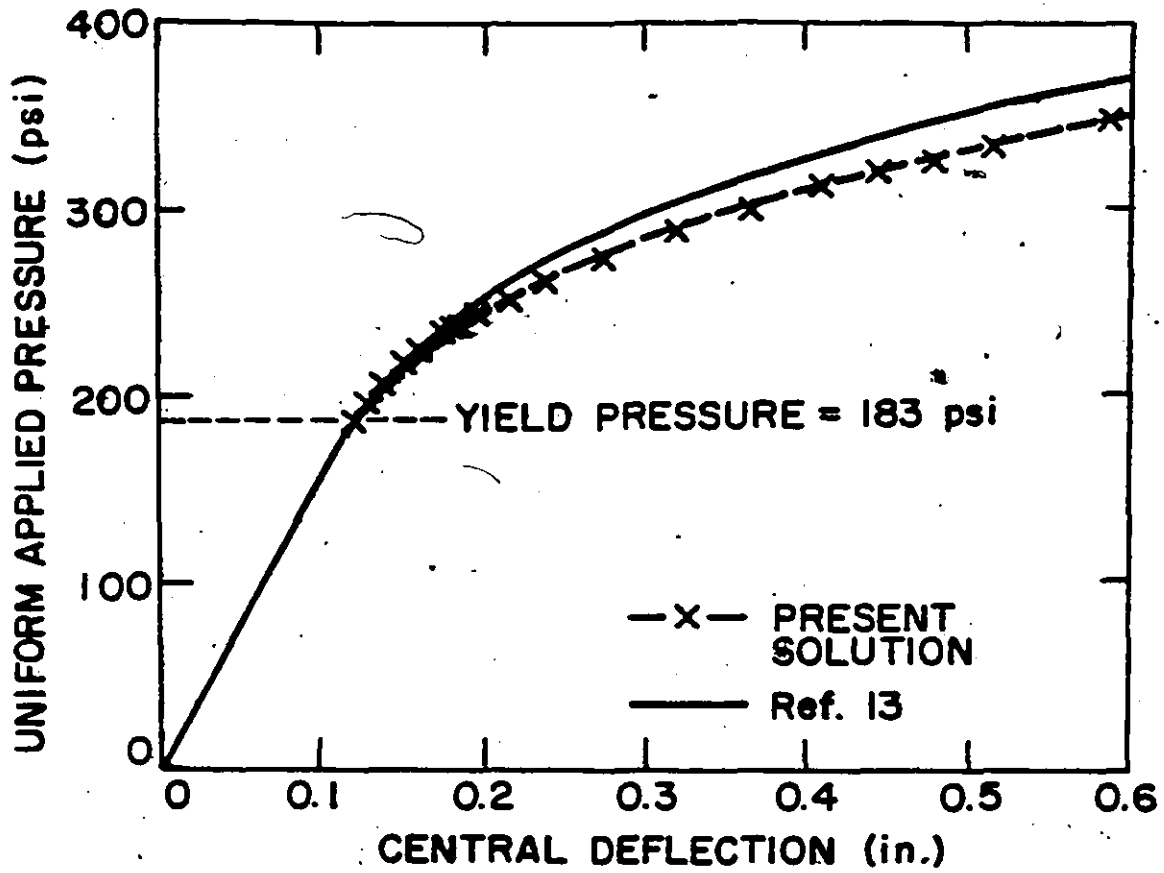
(a) LOAD-CENTRAL DEFLECTION
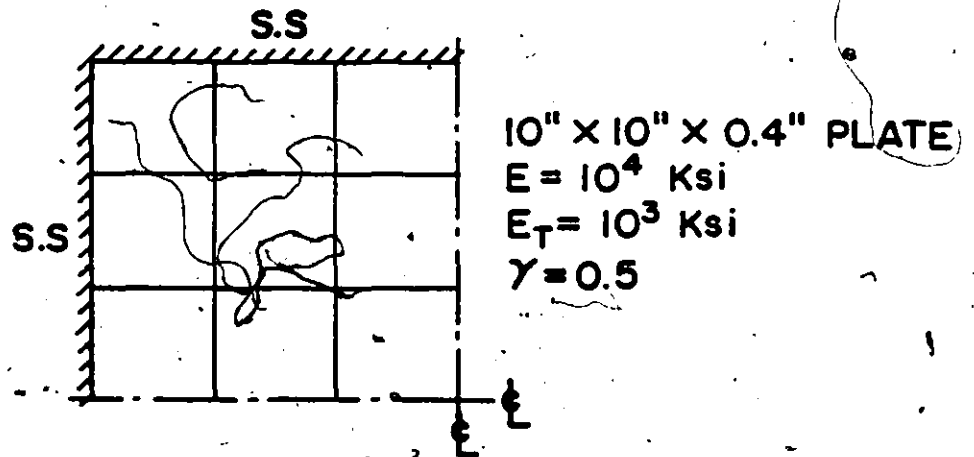
(b) F. E. MESH (ONE-QUARTER)

FIG. 3.6 UNIFORMLY LOADED SIMPLY SUPPORTED PLATE
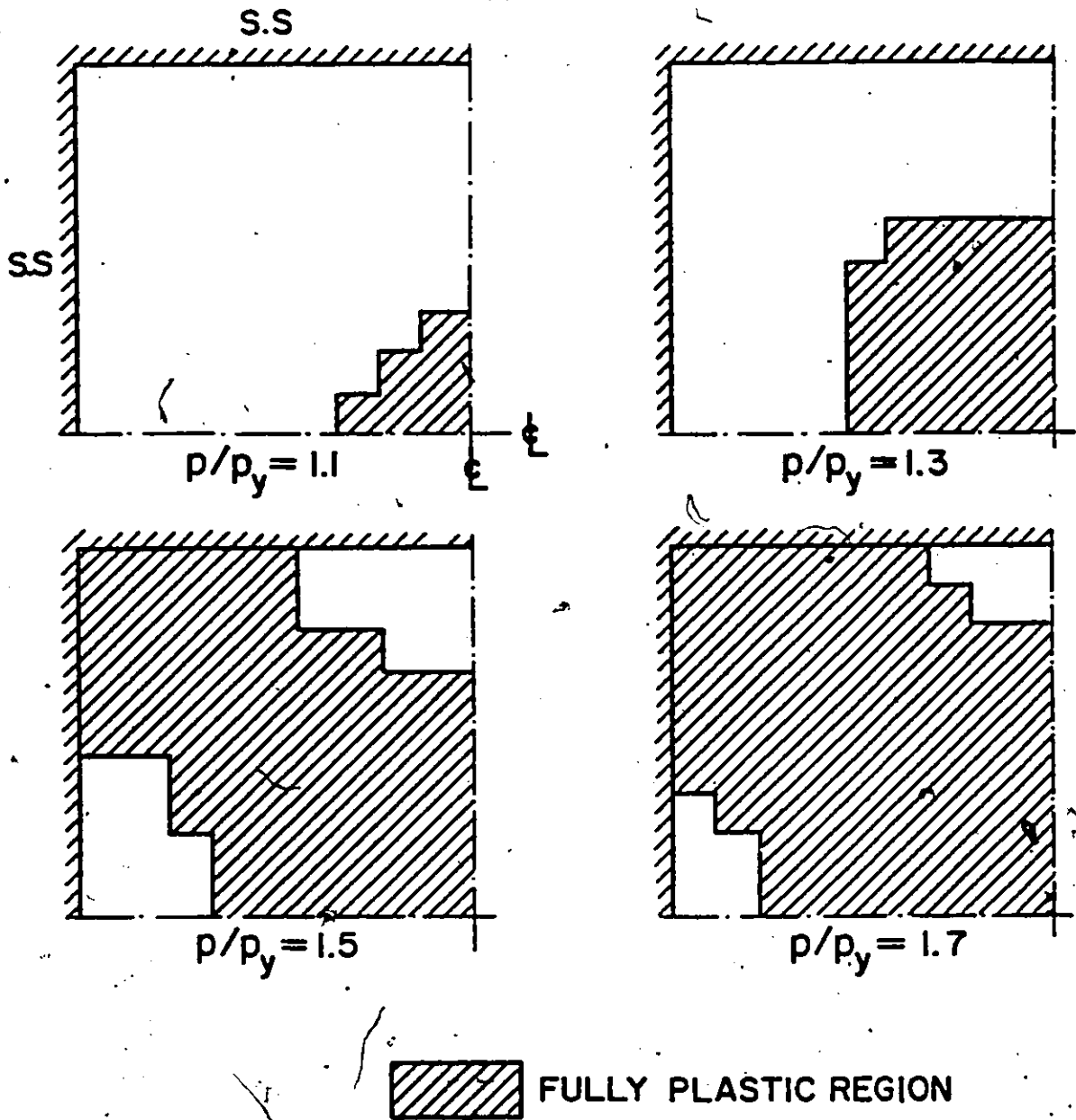
FIG. 3.7   PROGRESSION OF PLASTIC REGION IN A UNIFORMLY LOADED
SIMPLY SUPPORTED PLATE

CHAPTER 4

EXPERIMENTAL WORK ON DOUBLE CHORD T-JOINTS

4.1   Introduction

The purpose of the experimental program was primarily to assess the adequacy of the theoretical model of the double chord RHS T-joints under bending or punching shear loading and then, to formulate the load transfer mechanism for this type of joint in Vierendeel trusses.

Four bending and six punching shear tests were undertaken in this study. The effect of inter-chord welding was investigated under punching shear only, since a similar study was conducted by Chidiac and Korol [7] on moment connections.

4.2   Specimen Details

Details of the bending specimens, M-1 to M-4, are given in Table 4.1. Each specimen consisted of a 1220 mm long single RHS branch, fillet welded to a 2130 mm long double RHS chord. Configurations of the joints were chosen to include a practical range of each of width ratio, $b_1/2b_0$, the branch aspect ratio, b_1/h, and the branch width-to-chord thickness ratio, b_1/t_0. These parameters have also been considered in the theoretical parametric analysis of the joint behaviour. In all four specimens, the inter-chord weld length was 305 mm at both top and bot-

tom.

Details of the punching shear specimens, A-1 to A-6, are presented in Table 4.2. Each specimen consisted of a 381 mm long single chord branch, fillet welded to a 762 mm long double RHS chord. Specimens with similar geometries (A-1 and A-2, or A-3 and A-4) were identical to each other except for the length of weldments connecting the chord members at both top and bottom. The length of weld for specimens A-1 and A-3 was 76 mm but was 305 mm for the others. The branch member was filled with concrete to guard against its premature local buckling. The computed branch yield loads as given in Table 4.2 are based on the equivalent steel area of the concrete-filled section and a nominal 350 MPa yield strength. The assumed modular ratio was taken as 15.

4.3   Material Properties

The steel used for the HSS specimen was CSA grade 40.21-M, Class H, cold formed. Upon completion of the tests, coupons from each chord member were subjected to standard tensile tests in accordance with ASTM specifications. The yield stresses obtained are listed in Tables 4.1 and 4.2.

4.4   Setup for Moment Tests

The four moment tests were conducted with the apparatus shown in Fig. 4.1. The chord was supported at both ends on wide flange beams bolted to the laboratory floor as shown in Fig. 4.2. The end tending to

uplift was held down by a channel section and two 63.5 mm diameter bolts. To prevent displacement in the longitudinal direction, an end plate was welded to the flange beam. In addition, sideways movement was prevented by angle cleats welded to the flange beams.

The load was applied to the branch member by a hydraulic jack used in conjunction with a 225 KN capacity load cell. Also, there was provision for horizontal adjustment to the loading system to ensure that the load was applied centrally to the branch member in all cases. To account for rotation at the load contact point on the branch member, a 38 mm diameter bar was inserted in the recesses of plates welded to the member's webs. The bar rested in a recessed plate positioned against the bearing surface of the load cell.

To determine the displacements of the top flanges of the chord member, four dial gauges were positioned at prescribed locations. Four additional gauges were mounted to record displacements of the bottom flanges. These were employed to assess the rotation of the chord member at the joint. Branch tip displacement was monitored by a dial gauge mounted at the level of the applied load, while an additional gauge was placed at the base to record the chord member displacement parallel to loading. Arrangement of the gauges is shown in Fig. 4.2.

4.5   Setup for Punching Shear Tests

The six punching shear specimens were tested in a 2500 KN capacity RIEHLE Standard Testing Machine. A photograph of the testing

apparatus is shown in Fig. 4.3. The chord member was supported on rollers at both ends as illustrated in Fig. 4.4.

The direct punching load was applied through a stiff plate placed on top of the branch member. The load was increased in equal increments of about 5% of the predicted maximum load. Readings were taken at smaller increments once yielding was observed.

Four dial gauges, arranged as shown in Fig. 4.4, recorded displacements of the top flanges of the chord member. One additional gauge measured displacement of the bottom flange near the joint's centroid. A sixth gauge recorded the displacement of the machine's top plate in the direction of loading.

4.6   Results of Moment Tests

Chidiac and Korol [7] reported some improvement of overall joint stiffness and strength due to the presence of interchord welds. Such specimens were found to have capacities higher by about 15% than those not so treated. Consequently, only welded chord specimens were fabricated for the bending tests in this study.

Plots of lateral deflection as a function of the moment for the four specimens are presented in Fig. 4.5. The moment, M, has been calculated as the lateral load multiplied by the moment arm of 1118 mm. The lateral deflection is given by the difference in readings of dials 10 and 9 (see Fig. 4.2). From the plots, it is evident that all speci-

mens exhibited some non-linear behaviour at an early stage of loading. There was no well-defined yield point, which as will be seen is characteristic of the spread of yield zones.

All four specimens failed by inner web tearing. As is evident from Table 4.3, the specimens with stocky branch members and relatively large width ratios, M-2 and M-4, reached ultimate moments that were considerably less than the nominal fully plastic moment, M_p, based on a 350 MPa yield stress. The other two specimens, M-1 and M-3, performed much better, attaining 110% and 104% of their nominal M_p values, respectively. The higher relative capacities of these latter specimens may be explained by the fact that branch member thicknesses were less than those of the chords. Inner chord web tearing is essentially governed by the chord thickness and the geometry of the rounded corners. Consequently, an increase in branch thickness would not be expected to improve joint strength appreciably. It is noted that the chord yield strengths of specimens M-1 and M-3 were also considerably higher than the nominal 350 MPa value.

The results suggest that it is unlikely that the full plastic moment of the branch can be developed if $t_1/t_0 > 1.0$. Also of significance is the width ratio. In the tests, a $b_1/2b_0$ ratio greater than 0.5 resulted in less than a desired capacity. These two parameters influence the strength and stiffness of unreinforced joints. Stress coat was applied to the loaded chord surface of specimen M-2 to determine the strain distribution in the joint with load. Because of the nature of its brittle properties, the normal and tangential directions of the

developing cracks tend to coincide with the minimum principal stress directions at a given point. From visual observations it was evident that local yielding of the top chord surface adjacent to the branch's tension face spread from the inner web junction to an extensive domain around the periphery of the branch. Further loading of the specimen resulted in failure by tearing of the parent metal of the chord's inner web on the tension side of the branch member. Once tearing was initiated, cracks began to propagate in the chord member's top flanges along their intersection with the branch member. This can be seen in Fig. 4.6 for specimen M-1. Similar observations were made for the other specimens. It is interesting to note that the stress distribution pattern, indicated by cracks in the stress coat, is similar to the theoretically predicted pattern (see Fig. 5.6).

4.7   Results of Punching Shear Tests

Plots of deflection, δ, as a function of the punching load, P, for individual specimens are given in Fig. 4.7. It can be seen that the P-δ curves are approximately bi-linear in character with the elastic portion extending to about 2/3 of the maximum load. However, there is no well-defined yield point on the curves. The initial strength of the joint is provided mainly by the inner webs of the chord which act as a short column under the punching load. Once the membrane stresses in the inner webs reach the yield point, the joint's stiffness and strength deteriorate rapidly until failure occurs. It may be mentioned here that a yield line solution (Section 5.6) indicates that the inner webs contribute about 80% of the joint's capacity, which is consistent with

experimental observations.

The provision of adequate inter-chord welds has a beneficial effect on the joint behaviour, as observed from Fig. 4.7 and Table 4.4. Specimens with similar geometries (A-1 and A-2 or A-3 and A-4) possessed significantly higher stiffness and strength for the longer inter-chord welds. Table 4.4 indicates also that specimens A-1 and A-2 attained 83% and 97% of the branch yield load. The other four specimens reached ultimate punching loads that were considerably less than the branch yield load. Based on this limited number of tests, it is noted that joints having $t_1/t_0 > 1.0$ and $b_1/2b_0 > 0.67$ did not develop the full yield load of the branch.

After a significant amount of yielding two modes of failure were observed for the six specimens. Both A-1 and A-3 exhibited distortion and separation of the chord members on both sides of the inter-chord welds. In contrast, the other specimens, with longer inter-chord welds, failed by punching shear of the chord top flanges with little distortion or separation. The "dishing" effect was clearly observed along the periphery of the branch member accompanied with visible in-plane plastic deformations in the inner webs, as is clear from Fig. 4.8(a) and (b) for specimen A-5. Note the deflected shape of the seam line of the inner webs in Fig. 4.8(b).

From this experimental investigation of punching shear joints, it is recommended that the chord members should be welded together for a central length not less than the branch depth, h_1, to guard against

premature failure due to excessive distortion and separation.

TABLE 4.1   DETAILS OF MOMENT TEST SPECIMENS

Specimen No.	Chord Member 2RHS ($h_0 \times b_0 \times t_0$) (mm)	Branch Member RHS($h_1 \times b_1 \times t_1$) (mm)	$b_1/2b_0$	b_1/h_1	b_1/t_0	t_1/t_0	Chord Yield Strength (MPa)	Branch Plastic Moment [a] M_p(kN-m)
M-1	152.4×152.4×9.53	152.4×152.4×6.35	0.50	1.0	16.0	0.67	438	69.0
M-2	152.4×152.4×6.35	254.0×254.0×9.53	0.83	1.0	40.0	1.50	302	290.0
M-3	152.4×152.4×9.53	203.2×152.4×6.35	0.50	0.75	16.0	0.67	393	103.6
M-4	152.4×152.4×9.53	203.2×203.2×9.53	0.67	1.0	21.3	1.00	393	181.0

[a]   Computed value based on nominal 350 MPa yield strength.
Note: Weld length between chords = 305 mm for all specimens.

TABLE 4.2 DETAILS OF PUNCHING SHEAR TEST SPECIMENS

Specimen No.	Chord Member RHS $(h_0 \times b_0 \times t_0)$ (mm)	Branch Member RHS $(h_1 \times b_1 \times t_1)$ (mm)	$b_1/2b_0$	b_1/h_1	b_1/t_0	t_1/t_0	Chord Yield Strength (MPa)	Branch Yield Load[a] (KN)	Weld Length Between Chords (mm)
A-1	152.4×152.4×9.53	152.4×152.4×6.35	0.50	1.0	16.0	0.67	423	1719	76
A-2	152.4×152.4×9.53	152.4×152.4×6.35	0.50	1.0	16.0	0.67	393	1719	305
A-3	152.4×152.4×6.35	203.2×152.4×6.35	0.50	0.75	24.0	1.00	302	2108	76
A-4	152.4×152.4×6.35	203.2×152.4×6.35	0.50	0.75	24.0	1.00	302	2108	305
A-5	152.4×152.4×6.35	254.0×254.0×6.35	0.83	1.0	40.0	1.00	406	3525	305
A-6	152.4×152.4×6.35	203.2×203.2×6.35	0.67	1.0	32.0	1.00	380	2562	305

[a] Computed value based on nominal 350 MPa yield strength of composite section.

TABLE 4.3   RESULTS OF MOMENT TESTS

Specimen No.	Ultimate Moment M_u (KN-m)	Ultimate Moment as % of Branch Plastic Moment	Failure Mode
M-1	76.0	110	Inner chord web tearing
M-2	107.3	37[a]	Inner chord web tearing
M-3	107.5	104	Inner chord web tearing
M-4	125.8	70[a]	Inner chord web tearing

[a]   Stocky branch members used (see Table 4.1).

TABLE 4.4   RESULTS OF PUNCHING SHEAR TESTS

Specimen No.	Ultimate Punching Load P_u (KN)	Ultimate Punching Load as % of Branch Yield Load	Failure Mode
A-1	1412	82	Chord separation and distortion
A-2	1637	95	Punching shear
A-3	858	41	Chord separation and distortion
A-4	1255	60	Punching shear
A-5	1528	43	Punching shear
A-6	1465	57	Punching shear

FIG. 4.1: TEST APPARATUS FOR MOMENT SPECIMENS

SECTION I-I   ELEVATION
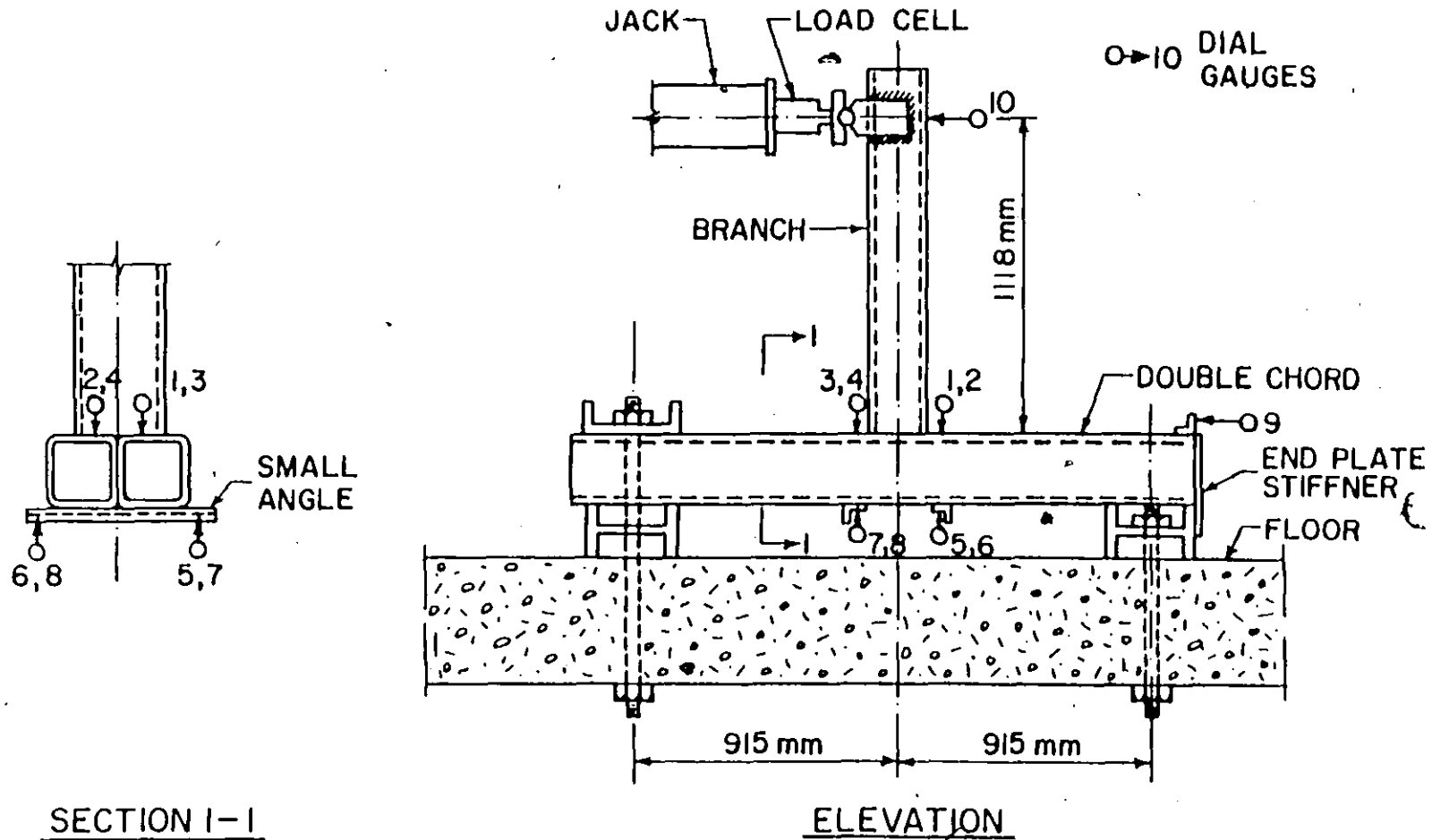
FIG. 4.2   LOADING AND SUPPORT SYSTEM WITH DIAL GAUGE ARRANGEMENT FOR BRANCH MOMENT TESTS
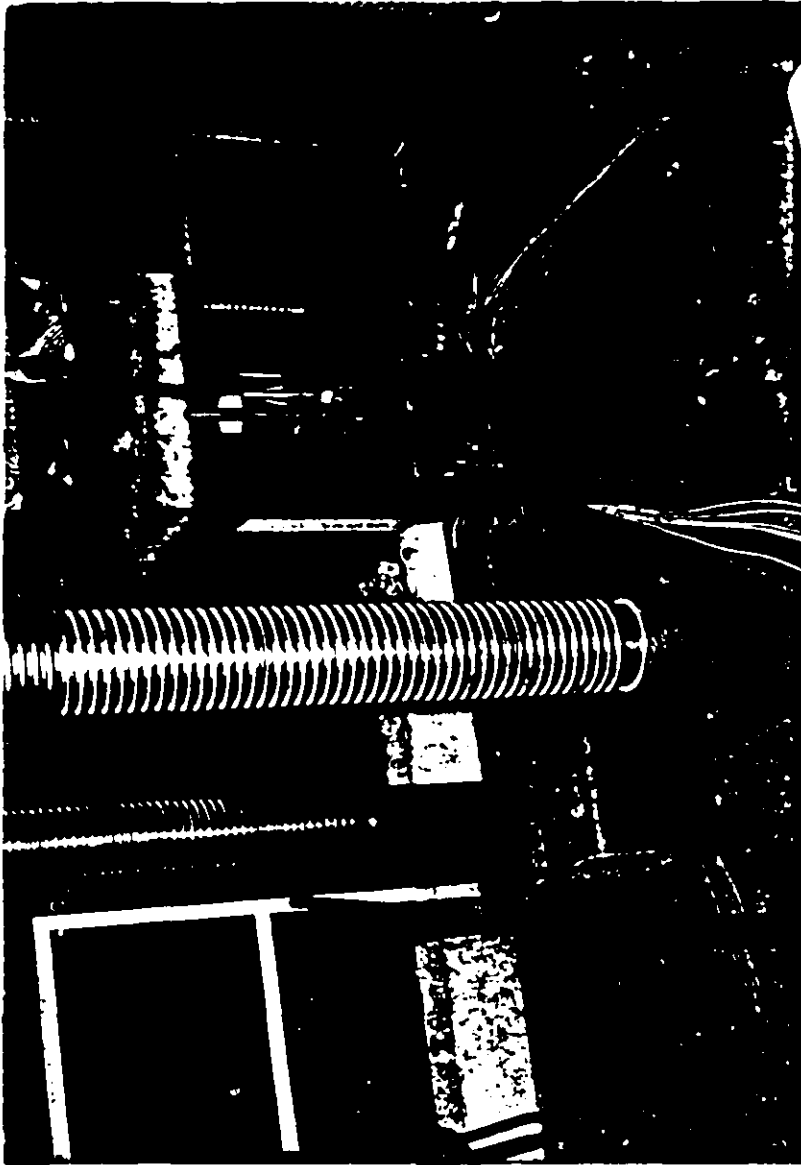
FIG. 4.3   TEST APPARATUS FOR PUNCHING SHEAR SPECIMENS

SECTION I-I   ELEVATION
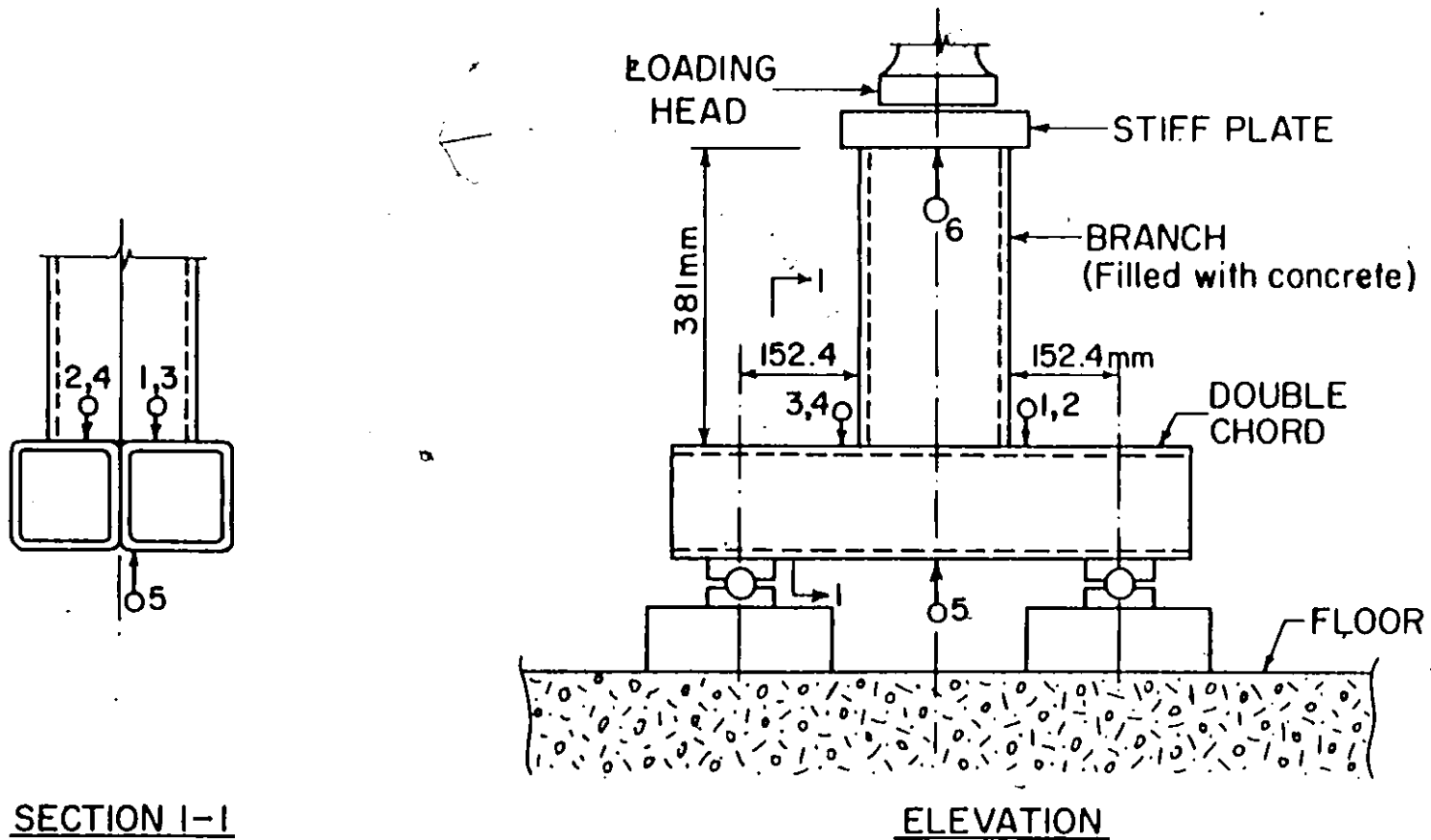
FIG: 4.4   LOADING AND SUPPORT SYSTEM WITH DIAL GAUGE ARRANGEMENT FOR PUNCHING SHEAR TESTS
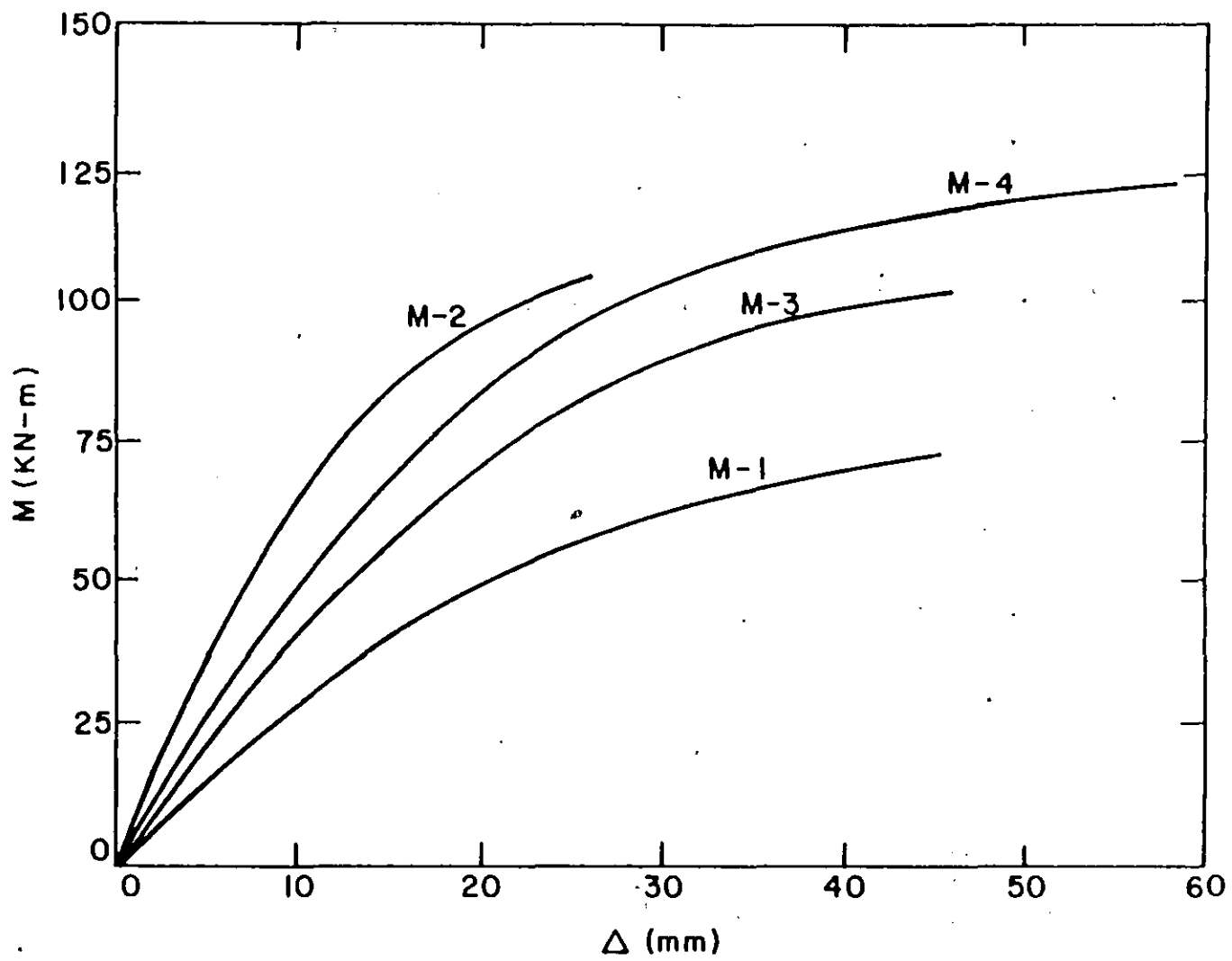
FIG. 4.5   EXPERIMENTAL BRANCH MOMENT - TIP DISPLACEMENT CURVES

FIG. 4.6   FAILURE MODE FOR SPECIMEN M-1
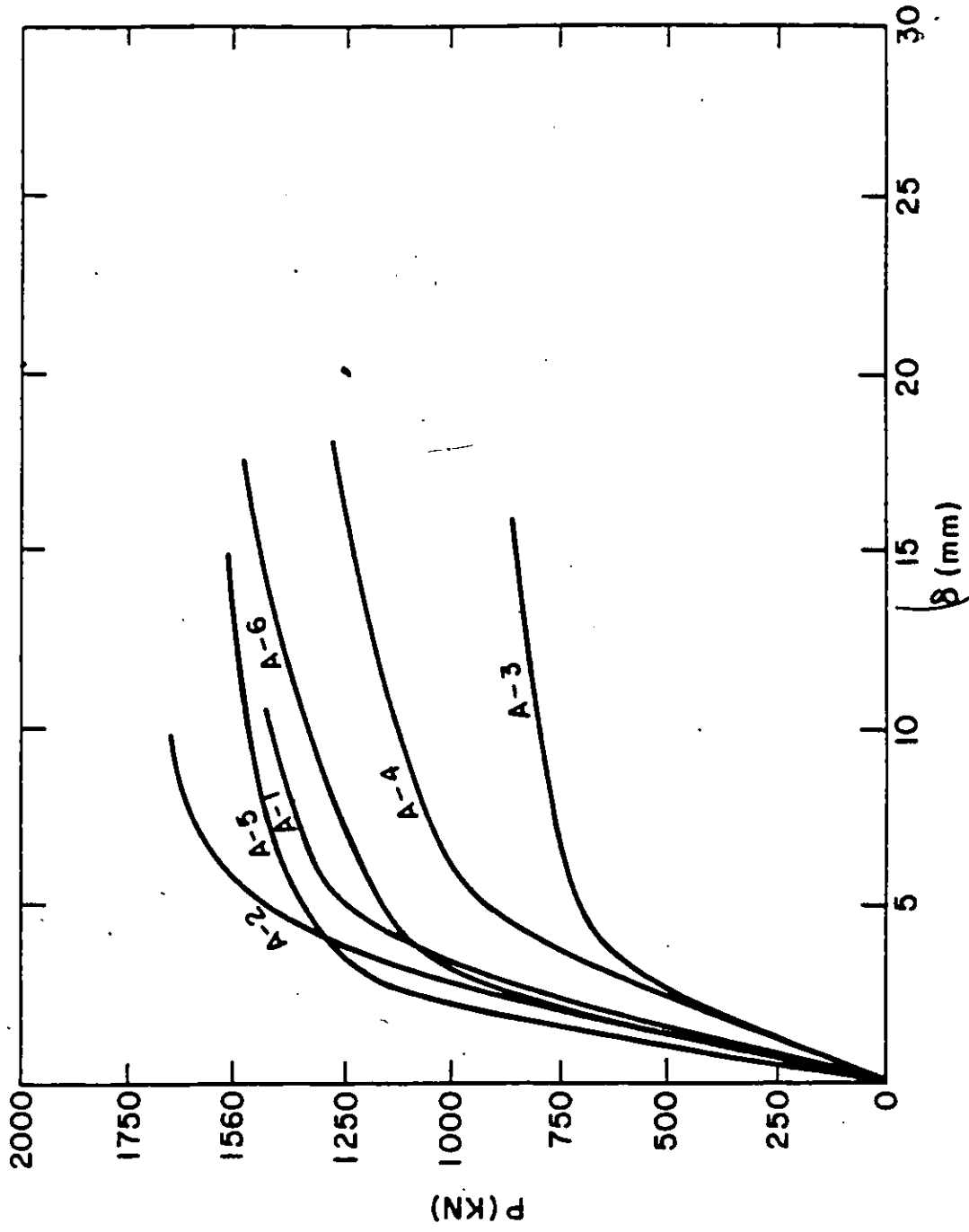
FIG. 4.7 EXPERIMENTAL PUNCHING SHEAR-DEFLECTION CURVES
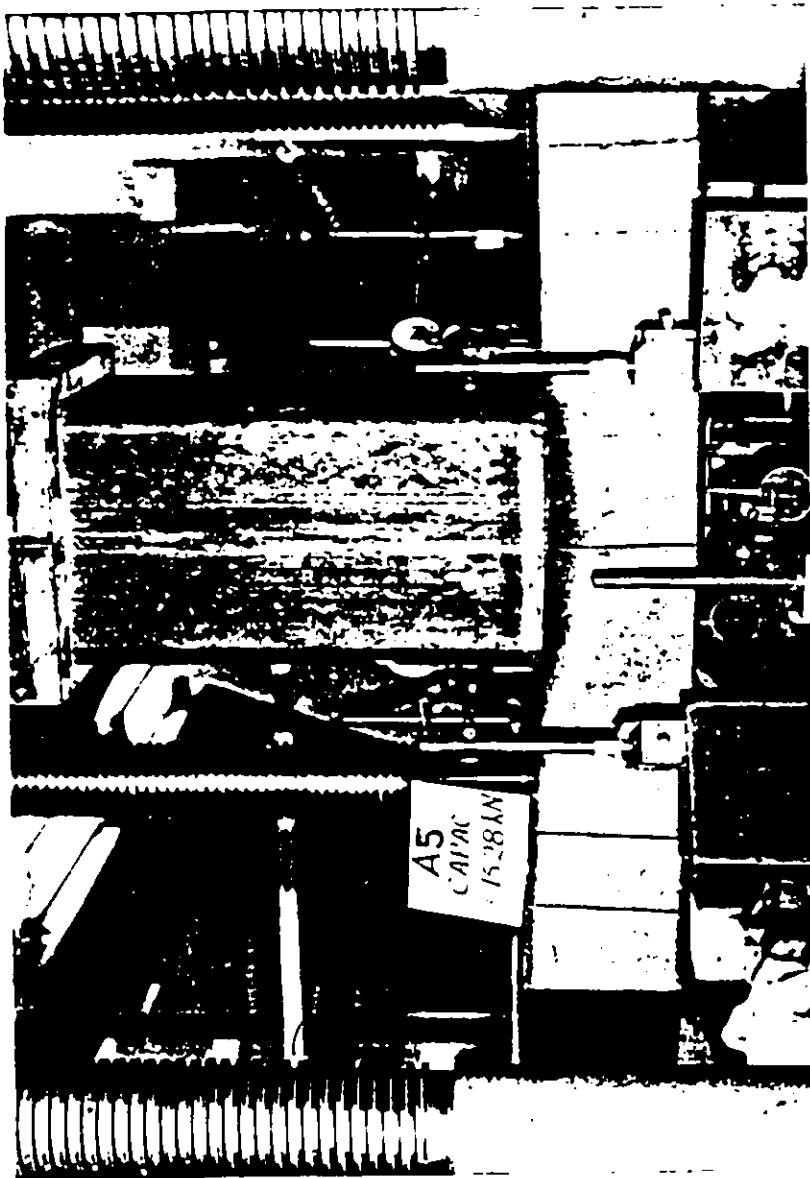
FIG. 4.8(a)   FAILURE MODE OF SPECIMEN A-5

CAPAC.
=1528kN
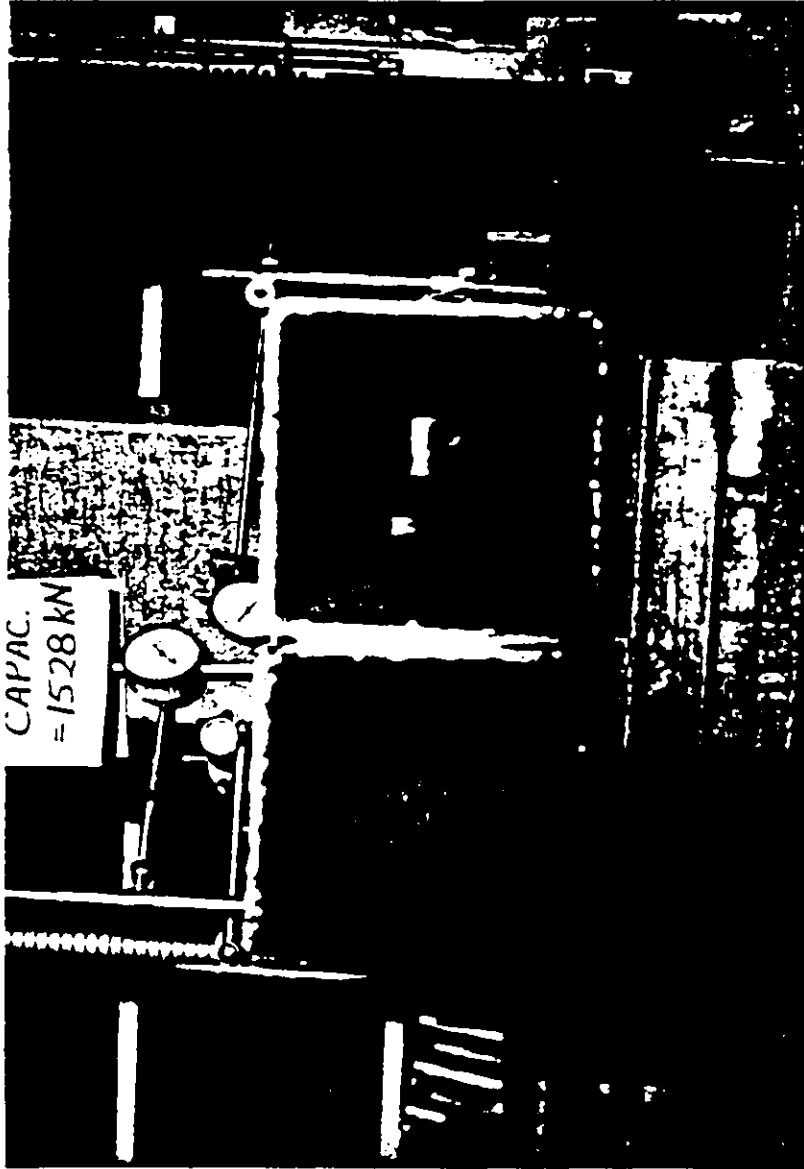
FIG. 4.8(b)   FAILURE MODE OF SPECIMEN A-5

CHAPTER 5

ANALYSIS OF DOUBLE CHORD RHS T-JOINTS

5.1   Introduction.

Analysis of Vierendeel trusses and other framed structures, which utilize double chord RHS T-joints, requires prior knowledge of the joint behaviour. These joints are generally not rigid and, therefore, their stiffness and strengths have a profound effect on the overall behaviour of a structure. The stiffness of such joints is defined by certain nonlinear relationships between the applied load (branch moment or punching shear) and the relative displacement or rotation of the connecting chord at a joint.

Finite element analyses of double chord T-joints under different loading conditions are to be presented in this chapter. Initially, the joints were analyzed under branch moment or punching shear using the finite element grid for one-quarter of the joint shown in Fig. 3.1. It consisted of 104 rectangular plate elements and 13 boundary spring elements. The grid is finer in the region of high stress gradients adjacent to the branch inclusion and becomes coarser away from this region.

In order to gain some insight into the joint characteristics under branch moment or punching shear, a number of cases have been analyzed. The joint geometry has been varied to study the influence of the

joint configuration on its performance. Five nondimensional parameters have been chosen to express configurations of different joints. These are defined as follows (see Fig. 2.3).

Width ratio; $\qquad r_1 = b_1/2b_0$

Branch aspect ratio; $\qquad r_2 = b_1/h_1$

Chord aspect ratio; $\qquad r_3 = b_0/h_0$

Branch width-to-chord thickness ratio; $\quad r_4 = b_1/t_0$

Stiffening plate parameter; $\qquad r_5 = 1 + t_s/t_0.$

In order to reduce the number of parameters, the length and width of the stiffening plate, if present, will be taken as dependent variables. Hence, the plate width b_s is assumed equal to $(2b_0 - 4t_0)$ and its length h_s is assumed as twice the branch height h_1. Such a value for h_s is approximately equal to the length of the yielded region at maximum load as determined from analyses of unstiffened connections (see Figs. 5.6 and 5.12).

The two rectangular hollow sections forming the chord member are considered to have been welded at top and bottom along the middle 305 mm. of the joint. This weld length had been used in the tests on double chord T-joints reported in reference [7].

In addition to analyses of double chord T-joints subject to either only the branch moment or puching shear, the joint behaviour was also investigated under various combinations of branch moments and punching shears. The finite element grid of Fig. 3.2, for one-half of

the joint, has been used and the results are presented in the form of an interaction envelope.

Analysis of double chord connections was carried out by first determining the yield load from an elastic analysis. Additional loads were then applied in equal increments of twenty-percent of the yield load for determining the nonlinear response. The yield load is defined as the load level at which the most highly stressed sampling point just reaches the yield stress. This load increment size was determined through various analyses and found to be the most suitable and efficient for the Newton-Raphson iterative procedure outlined in Chapter 3.

The results from the finite element analyses presented in this chapter are subsequently used in Chapter 7 to develop empirical formulae to aid in design of double chord T-joints. These formulae will then be incorporated in an elasto-plastic analysis of Vierendeel trusses which employ such connections (Chapter 8). Yield line solutions for the double chord T-joint capacity, under branch moment or punching shear, are also presented. Results from the finite element analyses will be compared with those obtained experimentally and by those predicted from the proposed yield line solutions.

5.2   Behaviour Under Branch Moment

A parametric study was carried out by analyzing fourteen double chord T-joints under branch moments. These are designated DB-1 to DB-14 where "DB" is the abbreviation for "Double-Bending". Dimensions of the

double chords and branch members of all fourteen joints as well as numerical values of the associated parameters are given in Table 5.1. Fourteen joints are categorized into five groups and each group is used to study the influence of a single parameter on the joint behaviour. The groups are indicated by underlined values of the corresponding parameter. An attempt was made to vary only one parameter in each group (with the exception of the group for r_1) while the other parameters are held constant. In the group for r_1, both parameters r_1 and r_4 vary and thus some provision must be made to determine the influence of r_1 alone as will be explained in Chapter 7. The chosen values of each parameter cover the practical range of its variation. Each joint has been loaded well into the plastic range. Convergence of the incremental solution to within the prescribed tolerance usually occurred after one or two iterations during the first twenty moment increments. Beyond this, up to five iterations were required due to more rapid yielding of the joint. A prescribed tolerance of the determinant condition of one percent was used as the convergence criterion. Loading was terminated when the joint rotation reached fifty times the yield rotation. It is assumed that geometric nonlinearities would thence become significant and hence the adopted theory of small deformations would not be valid. Furthermore, the tangential stiffness of the joint reduces to about three percent of the elastic stiffness.

Normalized moment-rotation curves for the double chord T-joints from finite element analyses were plotted in five groups, each representing variation of a single parameter, as shown in Figs. 5.1 to 5.5. Flexural rigidity D of the combined chord top flange and the stiffening

plate, if present, has been used to normalize moments.

It can be observed from the figures that with the exception of chord aspect ratio r_3, all other geometric parameters have a significant effect on the joint stiffness and strength. The $M/D-\phi$ curves of Fig. 5.3 show that the depth of the chord member has very little influence on the behaviour. The computed values of yield moments M_Y, yield rotations ϕ_Y and moments M_u at $\phi = 50\phi_Y$ are given in Table 5.2. The joint flexural stiffness J is the slope of the $M-\phi$ curve at any load level. Values of the elastic stiffness J_{EL} and the tangential stiffness J_T at the limiting rotation are also given in Table 5.2. One can observe from Figs. 5.1 to 5.5 and Table 5.2 that the double chord T-joints start to yield at an early stage of loading. However, they are able to sustain moments about six times the yield moment values before developing an extensive loss of stiffness.

Progression of the plastic regions in the top flanges and inner webs of the chord member is illustrated in Fig. 5.6 for one-quarter of joint DB-6. The progression is indicated by successive contour lines which represent boundaries of the yielded zone at a given moment ratio $\frac{M}{M_Y}$. The area encompassed by two consecutive contours is the zone which has yielded due to the additional branch moment given by the difference in moment ratios represented by the two contours. Because of membrane action present in the top flange and a single integration point taken for the boundary element formulation, calculated stresses at adjacent points on the flange and web are different and explains the disconti-

nuity of contour lines along the intersection between the two plates.
A better continuity would be obtained if three integration points (same
as for the top flange plate bending elements) had also been used for the
boundary spring elements.

The loading on joint DB-6 was continued well beyond M_u until a
very large number of interations was required for convergence. Some
important observations regarding the yield pattern of the double chord
T-joint can be made in Fig. 5.6. Yielding initates simultaneously in
the top flanges and the inner webs at the points adjacent to the branch
inclusion and above the inner webs. Subsequent yielding takes an ellip-
tical pattern about these points in both the flanges and inner webs.
The joint stiffness becomes very small as soon as yielding spreads to
the outer webs of the chord member.

5.3   Behaviour Under Punching Shear

The behaviour of double chord T-joints under punching shear was
investigated through analyses of fourteen joints. These are designated
DA-1 to DA-14 where "DA" is the abbreviation for "Double-Axial". Geom-
etry of each DA joint is identical to that of the DB joint with the same
number. Dimensions of the chord and branch members for each joint as
well as numerical values of the five geometric parameters r_1 to r_5 are
presented in Table 5.1. The parametric study was carried out in the
same manner as for the branch moment case in the previous section.

Each joint was loaded incrementally well into the plastic range.

Convergence of the incremental solution to within the prescribed toler-
ance of one percent usually occurred in a couple of iterations for the
first fifteen load increments of twenty percent of the yield load.
Additional load increments required up to five iterations due to more
rapid plastification of the joint.

Preliminary runs indicated that the joint can be considered to
have reached its capacity when the deflection has reached fifty times
the yield deflection. Beyond this level of deformation, geometric non-
linearities are presumed to introduce signficant errors. Furthermore,
tangential stiffness of the joint at that load level reduces to about
three percent of the elastic stiffness and convergence is slowed down
considerably. The normalized load-deflection curves for the joints
analyzed were plotted in five groups, each representing the variation of
a simple parameter as shown in Figs. 5.7 to 5.11. The ratio D/b_0 was
used to normalize loads whereas deflections are normalized by the total
thickness ($t = t_0 + t_s$) of the top flange and the stiffening plate, if
present.

It can be observed in Figs. 5.7 to 5.11 that all of the parame-
ters considered, with the exception of r_3, have a significant influence
on the joint stiffness and strength under punching shear. The load-
deflection curves in Fig. 5.9 confirm that the chord aspect ratio r_3 has
very little influence on the joint behaviour. Larger depths of the
chord members decrease the joint strength slightly as the stiffness
contribution due to the vertical faces decreases. This, in turn,
reduces the end restraints of the load-receiving face of the chord

member. However, this influence is rather small and can be neglected. Table 5.3 summarizes the analytical results for punching shear P_Y and deflection δ_Y at yielding and the ultimate punching shear P_U at a deflection equal to fifty times δ_Y. The joint axial stiffness C is the slope of the P–δ curve at any load level. The elastic stiffness C_{EL} and the tangential stiffness C_T at $\delta = 50\ \delta_Y$ are also tabulated. One can conclude from these results that the joints start to yield at an early stage of loading and sustain loads of about five times the yield load before an extensive loss of stiffness occurs.

Development of the plastic zones for this case is illustrated in Fig. 5.12 for one-quarter of joint DA-6. The progression of yielding is identified by boundaries of the yielded zone at a given load level P/P_Y. The area enclosed by two consecutive contours is the zone which has yielded due to the additional punching shear. Once again, the calculated stresses at adjacent points on the flange and web are different for the same reasons as have been mentioned for the branch moment case presented in the previous section.

Joint DA-6 was loaded beyond P_u until convergence of the incremental solution became very slow. Some important observations, with regard to the yield pattern of the joint, can be summarized. In Fig. 5.12, yielding initiates simultaneously in the top flanges and inner webs at the points adjacent to the branch inclusion and above the inner webs. Subsequent yielding of the flanges takes an elliptical pattern about these points. Boundaries of the yielded region in the inner webs are approximately parallel to the inclusion under the branch member.

The joint stiffness becomes very small as soon as yielding spreads to the outer webs of the chord member.

5.4   Behaviour Under Combined Loading

In a Vierendeel truss, joints are normally subjected to both branch moments and punching shears. The task here is to study the behaviour of double chord RHS T-joints under different combinations of these two types of loadings. However, it is assumed that the proportion of the two types, acting on a single joint, remains constant throughout the loading history. Nine cases, designated DAB-1 to DAB-9, have been analyzed. Different load combinations, ranging from pure moment on DAB-1 to pure shear on DAB-9, were used by varying the stress ratio N_a/N_b, where N_a and N_b are as defined in Fig. 3.3. Table 5.4 indicates the load combinations for each case. The joint geometry in all cases was based on that of joint DB-6 (or DA-6) i.e., 2RHS 152.4 × 152.4 × 6.35 mm chord members and an RHS 254.0 × 152.4 mm branch inclusion. The finite element mesh of Fig. 3.2 for one-half of the joint has been employed throughout the analysis.

Loading was terminated when rotations ϕ (or deflection δ in case of DAB-9) reached fifty times the yield value. The normalized moment-rotation curves are shown in Fig. 5.13. The ultimate moment M_u for case DAB-1 (pure moment) was used to normalize branch moments. Obviously, the presence of punching shears reduces the moment capacity and vice-versa for the joint. Results from the analyses are summarized in Table 5.5. Here the results for DAB-1 and DAB-9 are not the same as those for

DB-6 and DA-6, respectively. This is because of the coarser finite element mesh that has been employed in the present analysis. It should be pointed out here that symmetry exists only about the longitudinal vertical plane which necessitates analysis of half the problem instead of a quarter. The predicted ultimate moments and punching shears under combined loading are designated M_m and P_m, respectively. The ratios M_m/M_u and P_m/P_u are also listed in Table 5.5 for all cases.

The relationship between the ultimate moment and the ultimate punching shear carried by a joint can be described by an interaction envelope as shown in Fig. 5.14. This interaction relationship is approximated by the following equations.

$$\left(\frac{P_m}{P_u}\right)^{5/3} + \left(\frac{M_m}{M_u}\right)^{5/3} = 1.0 \quad ; \quad \frac{P_m}{P_u} < 0.80 \tag{5.1}$$

$$\frac{P_m}{P_u} + 0.40 \frac{M_m}{M_u} = 1.0 \quad ; \quad \frac{P_m}{P_u} > 0.80. \tag{5.2}$$

Analytical expressions for M_u and P_u will be presented in Chapter 7. Knowing M_u and P_u for a given double chord joint geometry, Equations 5.1 and 5.2 can be used to predict the joint capacity in the presence of both branch moment and punching shear.

5.5   Yield Line Solution for Branch Moment Capacity

An upper bound solution for the moment capacity of double chord

T-joints is presented here. This solution is based on the yield line theory and assumes, the joint material to be rigid-plastic with no strain-hardening.

The assumed failure mechanism is schematized in Fig. 5.15. Tensile or compresive forces in the inner webs are assumed to cause the webs to yield in their planes by stretching or indenting. Applying the principle of virtual work to the mechanism indicated in Fig. 5.15 and denoting the predicted joint capacity by M_u^*, the external work W_E is given by

$$W_E = M_u^* \cdot \phi = M_u^* \cdot \frac{w}{v}.$$ (5.3)

The internal work due to the top flanges W_{If} is given by

$$W_{If} = \frac{t_o^2 \cdot \sigma_Y}{4} \left\{ \frac{8w}{x} (v + x \cdot \tan \alpha) + \frac{4w \cdot a}{x \cdot \tan \alpha} + \frac{2a \cdot w}{v} \right\}$$ (5.4)

and that due to the inner webs W_{Iw} by

$$W_{Iw} = (2t_0)\sigma_Y \{ w(v + x \cdot \tan \alpha) \}$$ (5.5)

Derivation of Equations 5.4 and 5.5 is given in Appendix B. Now, equating the external work and the internal work yields

$$M_u^* = t_0^2 \cdot v \cdot \sigma_Y \left\{ \frac{2(x + t_0)}{x \cdot t_0} (v + x \cdot \tan \alpha) + \frac{a}{x \cdot \tan \alpha} + \frac{a}{2v} \right\}. \quad (5.6)$$

Applying the condition for minimum virtual work, i.e. $\dfrac{dM_u^*}{d\alpha} = 0$, leads to

$$\tan \alpha = \sqrt{\frac{a \cdot t_0}{2x(x + t_0)}}. \quad (5.7)$$

Upon substitution of Equation 5.7 into Equation 5.6 and replacing u, v and x by the respective joint dimensions, the following expression for M_u^* is obtained;

$$M_u^* = t_0 \cdot h_1 \cdot \sigma_Y \left\{ \frac{h_1}{2} \left(1 + \frac{2t_0}{a - b_1}\right) + \frac{a \cdot t_0}{2h_1} + \sqrt{2a \cdot t_0 \left(1 + \frac{2t_0}{a - b_1}\right)} \right\}. \quad (5.8)$$

where $a = 2b_0 - t_0$.

The joint capacity, as given by Equation 5.8, can be split into two parts: contribution from the flanges M_{uf}^* and contribution from the inner webs M_{uw}^* where

$$M_{uf}^* = t_0^2 \cdot h_1 \cdot \sigma_Y \left\{ \frac{h_1}{a - b_1} + \frac{a}{2h_1} + \sqrt{\frac{4a}{a - b_1} + \frac{a(a - b_1)}{2t_0(a - b_1 + 2t_0)}} \right\} \quad (5.9)$$

$$M_{uw}^{*} = t_0 \cdot h_1 \cdot \sigma_Y \left\{ \frac{h_1}{2} + \sqrt{\frac{a \cdot t_0 (a-b_1)}{2(a-b_1+2t_0)}} \right\} . \qquad (5.10)$$

The values of M_{uf}^{*}, M_{uw}^{*} and M_{u}^{*} for joints DB-1 to DB-11 have been calculated and presented in Table 5.6. It may be noted that the inner webs contribute about seventy percent of the total strength of the joints. The moment capacities, as predicted by the yield line solution presented here, have been compared with the finite element results of Section 5.2. It can be observed from Table 5.6 that the yield line results are always higher on the average by about twenty percent with a standard deviation of about ten percent. Despite the fact that the two approaches are based on different theories, correlation between their results is apparent in the test cases.

5.6   Yield Line Solution for Punching Shear Capacity

The failure mechanism due to punching shear is sketched in Fig. 5.16. It is assumed that failure of the inner webs is caused by in-plane yielding without bulging.

Applying the principle of virtual work on the basis of the mechanism indicated in Fig. 5.16, and denoting the predicted ultimate load by P_u^{*}, then the external virtual work W_E is given by

$$W_E = P_u^{*} \cdot \delta \qquad (5.11)$$

The interal work contributed by the top flanges W_{If} is given by

$$W_{If} = \frac{t_0^2 \cdot \sigma_Y}{4} \left\{ \frac{8\delta}{x} (v + x \cdot \tan \alpha) + \frac{4a \cdot \delta}{x \cdot \tan \alpha} \right\} \qquad (5.12)$$

while that contributed by the inner webs W_{Iw} is

$$W_{Iw} = (2t_0)\sigma_Y \left\{ 2v \cdot \delta + x \cdot \delta \cdot \tan \alpha \right\}. \qquad (5.13)$$

The derivation of Equations 5.12 and 5.13 is presented in Appendix B. Now, equating the external and internal work yields

$$P_u^* = t_0^2 \cdot \sigma_Y \left\{ \frac{2v}{x} + 2 \tan \alpha + \frac{a}{x \cdot \tan \alpha} \right\}$$

$$+ 2t_0 \cdot \sigma_Y \left\{ 2v + x \cdot \tan \alpha \right\}. \qquad (5.14)$$

Applying the condition for minimum virtual work, i.e. $\frac{dP_u^*}{d\alpha} = 0$, to Equation 5.14 produces the same expression as in Equation 5.7. Upon substitution of Equation 5.7 into Equation 5.14 and replacing u, v, x by the respective joint dimensions, the following expression for P_u^* is obtained;

$$P_u^* = 2t_0 \cdot \sigma_Y \left\{ h_1 (1 + \frac{t_0}{a-b_1}) + \sqrt{2a \cdot t_0 (1 + \frac{2t_0}{a-b_1})} \right\} \qquad (5.15)$$

where $a = 2b_0 - t_0$.

The joint capacity, as given by Equation 5.15, can be split into two parts: contribution of the flanges P_{uf}^* and contribution of the inner webs P_{uw}^* where

$$P_{uf}^* = 2t_0^2 \cdot \sigma_Y \left\{ \frac{h_1}{a-b_1} + \sqrt{\frac{4a}{a-b_1} + \frac{a(a-b_1)}{2t_0(a-b_1+2t_0)}} \right\} \qquad (5.16)$$

$$P_{uw}^* = 2t_0 \cdot \sigma_Y \left\{ h_1 + \sqrt{\frac{a \cdot t_0(a-b_1)}{2(a-b_1+2t_0)}} \right\}. \qquad (5.17)$$

The values of P_{uf}^*, P_{uw}^* and P_u^* for joints DA-1 to DA-11 have been calculated and presented in Table 5.7. It may be noted that the inner webs again contribute about eighty percent of the total strength of the joints. The load capacities, as predicted by the yield line solution presented here, have been compared with the finite element results of Section 5.3. It can be observed from Table 5.7 that the yield line results are about six percent higher on average, with a standard deviation of about eight percent. The correlation between results from two approaches is once again apparent in the test cases. The improved results obtained for the punching shear case, using the yield line theory, can be attributed to a more appropriate mechanism used for this case compared to that of branch moment.

TABLE 5.1   PROPERTIES OF ANALYZED DOUBLE CHORD T-JOINTS

Joint No.	Chord (2RHS) $(h_0 \times b_0 \times t_0)$ (mm)	Branch (RHS) $(h_1 \times b_1)$ (mm)	t_s (mm)	$r_1 = b_1/2b_0$	$r_2 = b_1/h_1$	$r_3 = b_0/h_0$	$r_4 = b_1/t_0$	$r_5 = 1 + \frac{t_s}{t_0}$	D^* (KN-m)
DB-1	152.4×152.4×6.53	254.0×254.0	—	0.833	1.00	1.00	40.00	1.00	4.688
DB-2	152.4×152.4×6.35	203.2×203.2	—	0.667	1.00	1.00	32.00	1.00	4.688
DB-3	152.4×152.4×6.35	177.8×177.8	—	0.583	1.00	1.00	28.00	1.00	4.688
DB-4	152.4×152.4×6.35	152.4×152.4	—	0.500	1.00	1.00	24.00	1.00	4.688
DB-5	152.4×152.4×6.35	203.2×152.4	—	0.500	0.75	1.00	24.00	1.00	4.688
DB-6	152.4×152.4×6.35	254.0×152.4	—	0.500	0.60	1.00	24.00	1.00	4.688
DB-7	203.2×152.4×6.35	203.2×203.2	—	0.667	1.00	0.75	32.00	1.00	4.688
DB-8	254.0×152.4×6.35	203.2×203.2	—	0.667	1.00	0.60	32.00	1.00	4.688
DB-9	152.4×152.4×4.67	203.2×203.2	—	0.667	1.00	1.00	42.67	1.00	1.978
DB-10	152.4×152.4×7.94	203.2×203.2	—	0.667	1.00	1.00	25.60	1.00	9.157
DB-11	152.4×152.4×9.53	203.2×203.2	—	0.667	1.00	1.00	21.33	1.00	15.827
DB-12	152.4×152.4×6.35	177.8×177.8	6.35	0.583	1.00	1.00	28.00	2.00	37.516
DB-13	152.4×152.4×6.35	177.8×177.8	9.53	0.583	1.00	1.00	28.00	2.50	73.274
DB-14	152.4×152.4×6.35	177.8×177.8	12.07	0.583	1.00	1.00	28.00	3.00	126.620

$$^*D = \frac{Et^3}{12(1-\nu^2)}; \quad t = t_0 + t_s, \quad E = 200,000 \text{ MPa}, \quad \nu = 0.30$$

TABLE 5.2 ANALYTICAL RESULTS FOR DOUBLE CHORD T-JOINTS UNDER BRANCH
MOMENT

Joint No.	Yield Values			Values at $\phi=50\phi_Y$		$\dfrac{M_u}{M_Y}$	$\dfrac{J_T}{J_{EL}}$
	M_Y (KN-m)	ϕ_Y $\times 10^{-4}$(rad.)	$J_{EL}\times 10^3$ (KN-m/rad)	M_u (KN-m)	$J_T\times 10^2$ (KN-m/rad.)		
DB-1	17.61	6.269	2.809	103.14	0.922	5.86	0.033
DB-2	11.90	7.836	1.519	67.76	0.467	5.69	0.031
DB-3	9.61	8.958	1.073	58.08	0.356	6.04	0.033
DB-4	6.04	9.105	0.633	34.96	0.203	5.79	0.032
DB-5	10.21	6.952	1.469	65.54	0.455	6.42	0.031
DB-6	14.76	5.475	2.696	85.32	0.917	5.78	0.034
DB-7	11.74	9.805	1.197	70.08	0.386	5.97	0.032
DB-8	11.65	11.658	0.993	71.00	0.295	6.09	0.030
DB-9	8.48	7.527	1.127	52.11	0.401	6.15	0.036
DB-10	15.65	8.137	1.923	84.22	0.537	5.38	0.028
DB-11	19.94	8.430	2.365	108.40	0.814	5.44	0.034
DB-12	13.63	8.962	1.521	82.65	0.574	6.06	0.038
DB-13	16.12	8.961	1.800	97.75	0.690	6.06	0.038
DB-14	18.49	8.775	2.107	113.75	0.735	6.15	0.035

1 KN-m = 8.851 Kip-in.

TABLE 5.3 ANALYTICAL RESULTS FOR DOUBLE CHORD T-JOINTS UNDER PUNCHING SHEAR

Joint	Yield Values			Values at $\phi=50\phi_Y$		$\dfrac{P_u}{P_Y}$	$\dfrac{C_T}{C_{EL}}$
No.	P_Y (KN)	$\delta_Y \times 10^{-2}$ (mm)	$C_{EL} \times 10^3$ (KN/mm)	P_u (KN)	$C_T \times 10^2$ (KN/mm)		
DA-1	304.6	7.06	4.31	1401	1.14	4.60	0.027
DA-2	249.3	7.29	3.42	1152	0.94	4.62	0.028
DA-3	224.3	7.48	3.00	1091	1.13	4.86	0.027
DA-4	174.6	7.54	2.32	838	0.63	4.80	0.027
DA-5	226.8	6.77	3.35	1127	1.24	4.97	0.037
DA-6	271.5	6.48	4.19	1246	1.42	4.59	0.034
DA-7	248.5	8.89	2.80	1165	0.74	4.69	0.026
DA-8	248.4	10.28	2.42	1178	0.63	4.74	0.026
DA-9	182.5	6.88	2.65	909	0.69	4.98	0.026
DA-10	318.4	7.44	4.28	1326	0.95	4.16	0.022
DA-11	395.5	8.14	4.86	1756	1.34	4.44	0.028
DA-12	248.8	7.26	3.43	1304	1.16	5.24	0.034
DA-13	261.6	7.17	3.65	1412	1.32	5.40	0.036
DA-14	273.6	7.09	3.86	1509	1.38	5.51	0.036

1 KN = 0.2248 Kips

1 KN/mm = 5.710 K/in.

TABLE 5.4   LOAD COMBINATIONS FOR DOUBLE CHORD T-JOINTS
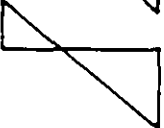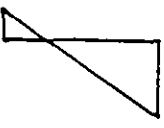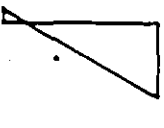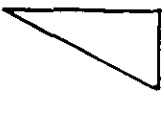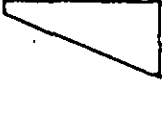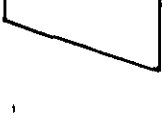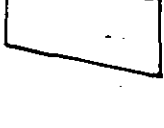
Case No.	Chord (2RHS) $(h_0 \times b_0 \times t_0)$ (mm)	Branch (RHS) $(h_1 \times b_1)$ (mm)	N_a/N_b	Loading	Remarks
DAB-1	152.4×152.4×6.35	254.0×152.4	0.00		Pure moment
DAB-2	"	"	0.25		
DAB-3	"	"	0.50		
DAB-4	"	"	0.80		
DAB-5	"	"	1.00		
DAB-6	"	"	1.25		
DAB-7	"	"	2.00		
DAB-8	"	"	4.00		
DAB-9	"	"	∞		Pure Punching Shear

TABLE 5.5 ANALYTICAL RESULTS FOR DOUBLE CHORD T-JOINTS UNDER COMBINED
LOADING

Case	Yield Values			Values at $\phi=50\phi_Y$ or $\delta=50\delta_Y$			
No.	M_Y (KN-m)	ϕ_Y $\times 10^{-4}$ (rad.)	P_Y (KN)	M_m (KN-m)	P_m (KN)	$\dfrac{M_m}{M_u}$	$\dfrac{P_m}{P_u}$
DAB-1	20.70	6.546	0.00	108.39	0.0	1.000	0.000
DAB-2	16.83	5.454	58.86	97.24	411.5	0.897	0.323
DAB-3	14.18	4.841	99.17	82.81	700.9	0.764	0.550
DAB-4	11.92	4.136	133.45	67.32	911.7	0.621	0.716
DAB-5	10.78	3.591	150.81	58.16	984.5	0.537	0.773
DAB-6	9.63	3.295	168.35	49.37	1044.7	0.456	0.820
DAB-7	7.29	2.590	203.90	32.72	1107.7	0.302	0.869
DAB-8	4.42	1.560	247.46	17.07	1173.3	0.157	0.921
DAB-9	0.00	0.000	314.63	0.00	1274.0	0.000	1.000

TABLE 5.6   COMPARISON OF FINITE ELEMENT RESULTS WITH YIELD LINE SOLUTION FOR JOINT CAPACITIES UNDER BRANCH MOMENT

Joint No.	Yield Line Solution			F.E. Analysis	$\dfrac{M_u^*}{M_u}$
	M_{uf}^* (KN-m)	M_{uw}^* (KN-m)	M_u^* (KN-m)	M_u (KN-m)	
DB-1	46.7	87.0	133.7	103.1	1.30
DB-2	24.8	58.8	83.6	67.8	1.23
DB-3	19.8	46.6	66.4	58.1	1.14
DB-4	16.1	35.8	51.9	41.4	1.25
DB-5	21.7	59.2	80.9	77.5	1.04
DB-6	27.9	88.3	116.2	100.9	1.15
DB-7	24.8	58.8	83.6	70.1	1.19
DB-8	24.8	58.8	83.6	71.0	1.18
DB-9	14.9	43.0	57.9	52.1	1.11
DB-10	36.9	75.2	112.1	84.2	1.33
DB-11	51.5	91.9	143.4	108.4	1.32

TABLE 5.7 COMPARISON OF FINITE ELEMENT RESULTS WITH YIELD LINE SOLUTION
FOR JOINT CAPACITIES UNDER PUNCHING SHEAR

Joint	Yield Line Solution			F.E. Analysis	$\dfrac{P_u^*}{P_u}$
No.	P_{uf}^* (KN)	P_{uw}^* (KN)	P_u^* (KN)	P_u (KN)	
DA-1	351	1249	1600	1401	1.14
DA-2	223	1031	1254	1152	1.09
DA-3	199	920	1119	1091	1.03
DA-4	183	808	991	937	1.06
DA-5	193	1034	1227	1260	0.97
DA-6	203	1259	1462	1393	1.05
DA-7	223	1031	1254	1165	1.08
DA-8	223	1031	1254	1178	1.06
DA-9	135	762	897	909	0.99
DA-10	332	1304	1636	1326	1.23
DA-11	462	1581	2043	1756	1.16
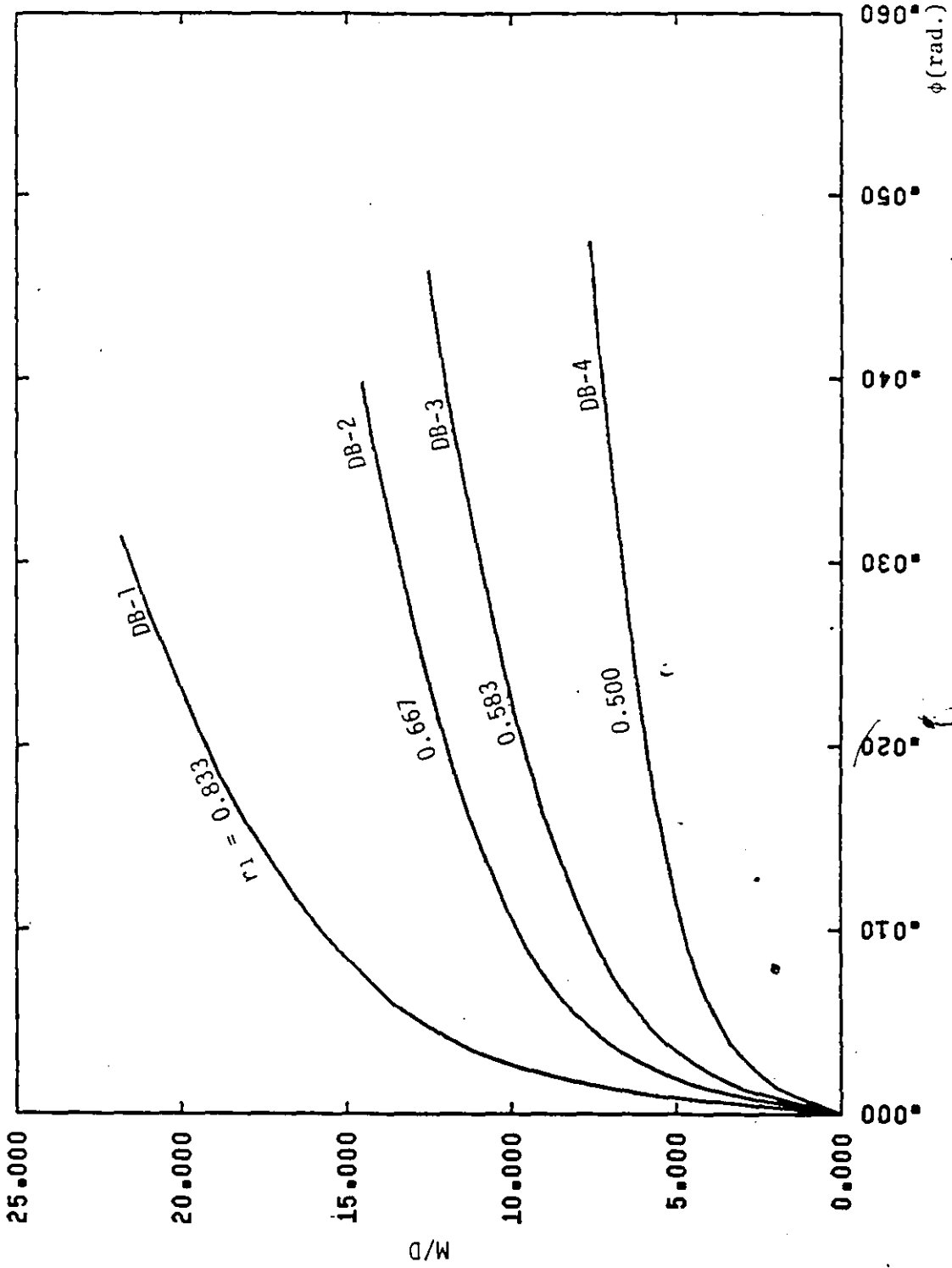
FIG.5.1   VARIATION OF PARAMETER $r_1 = b_1/2b_0$ (BRANCH MOMENT)
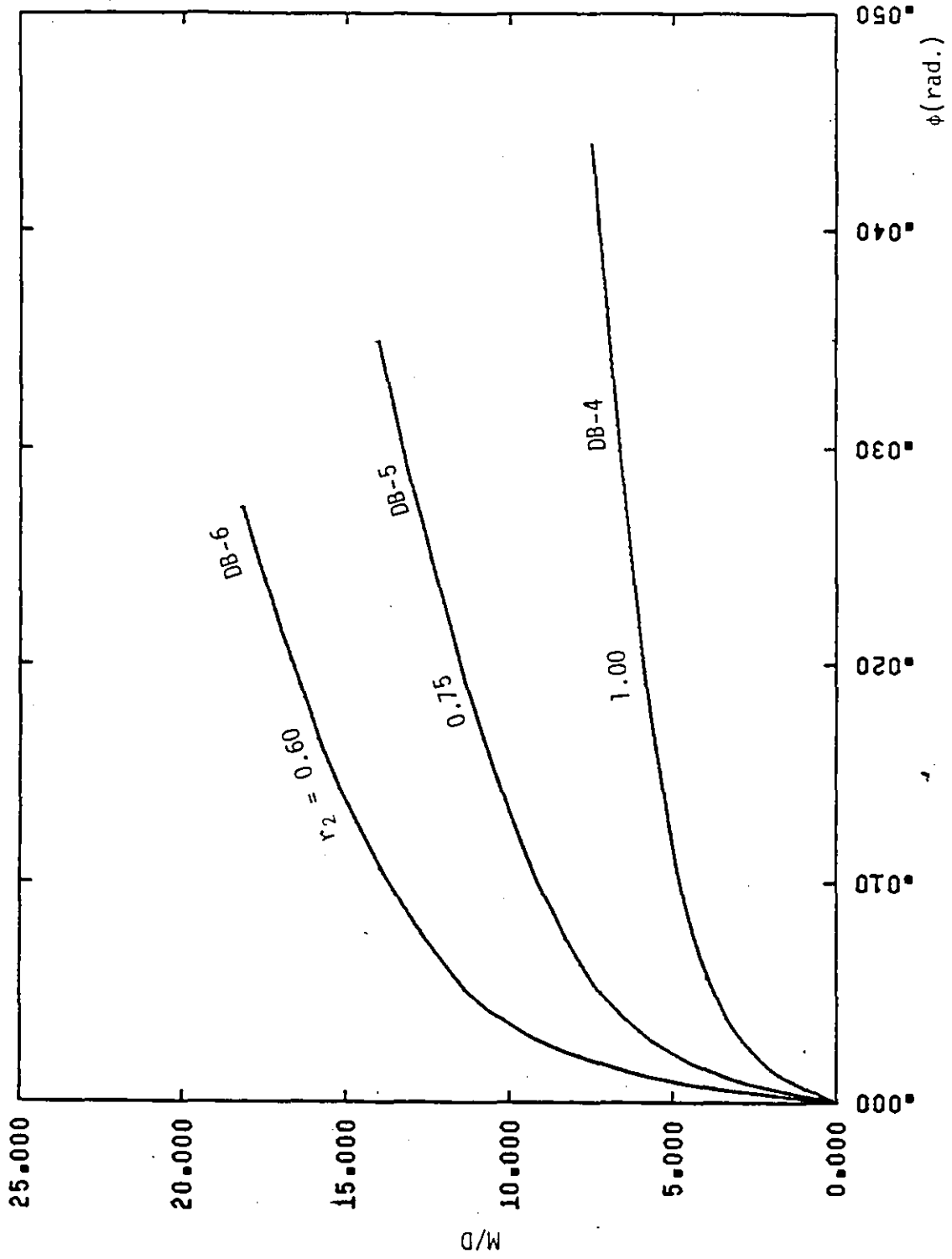
FIG. 5.2 VARIATION OF PARAMETER $r_2 = b_1/h_1$ (BRANCH MOMENT)
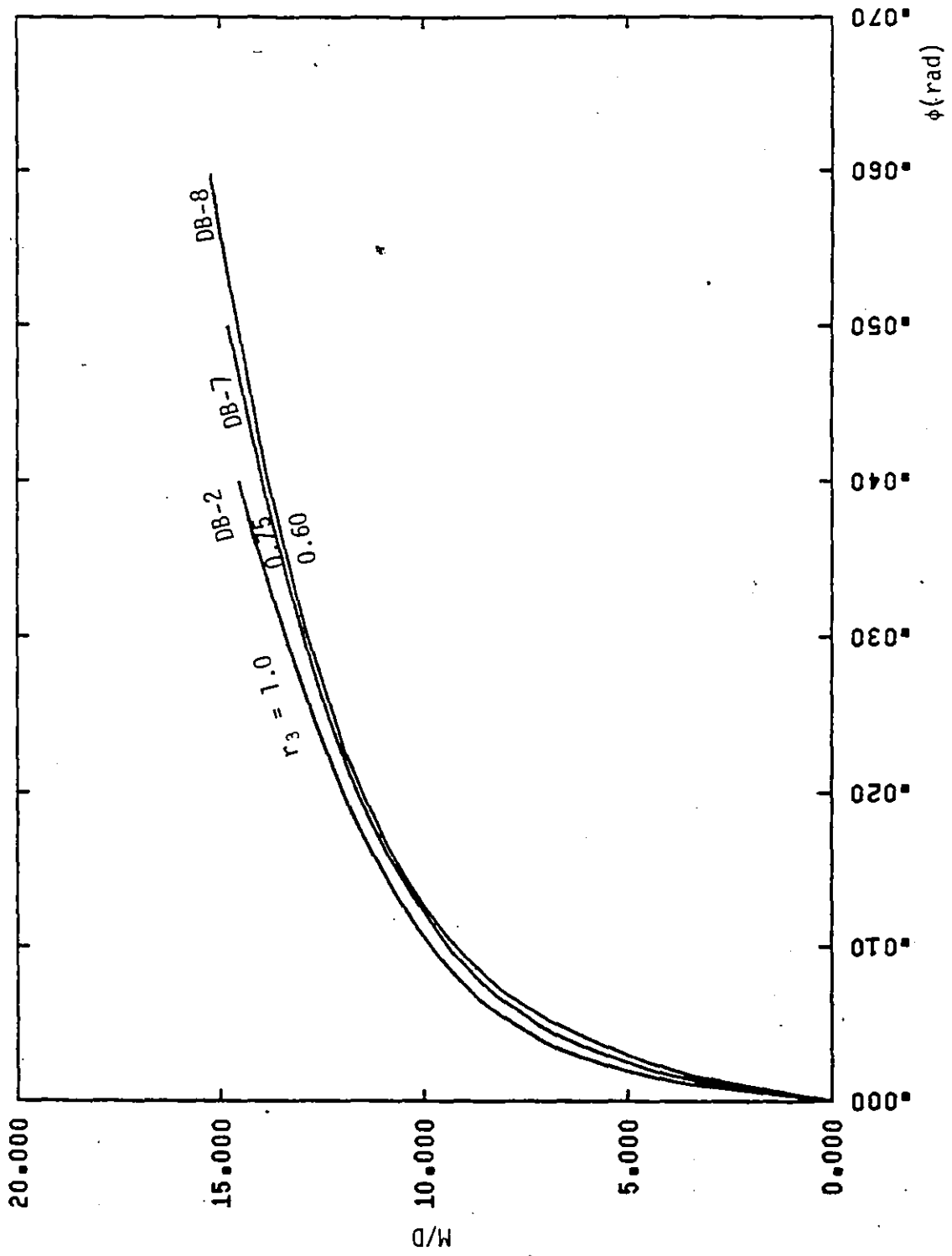
FIG. 5.3 VARIATION OF PARAMETER $r_3 = b_0/h_0$ (BRANCH MOMENT)
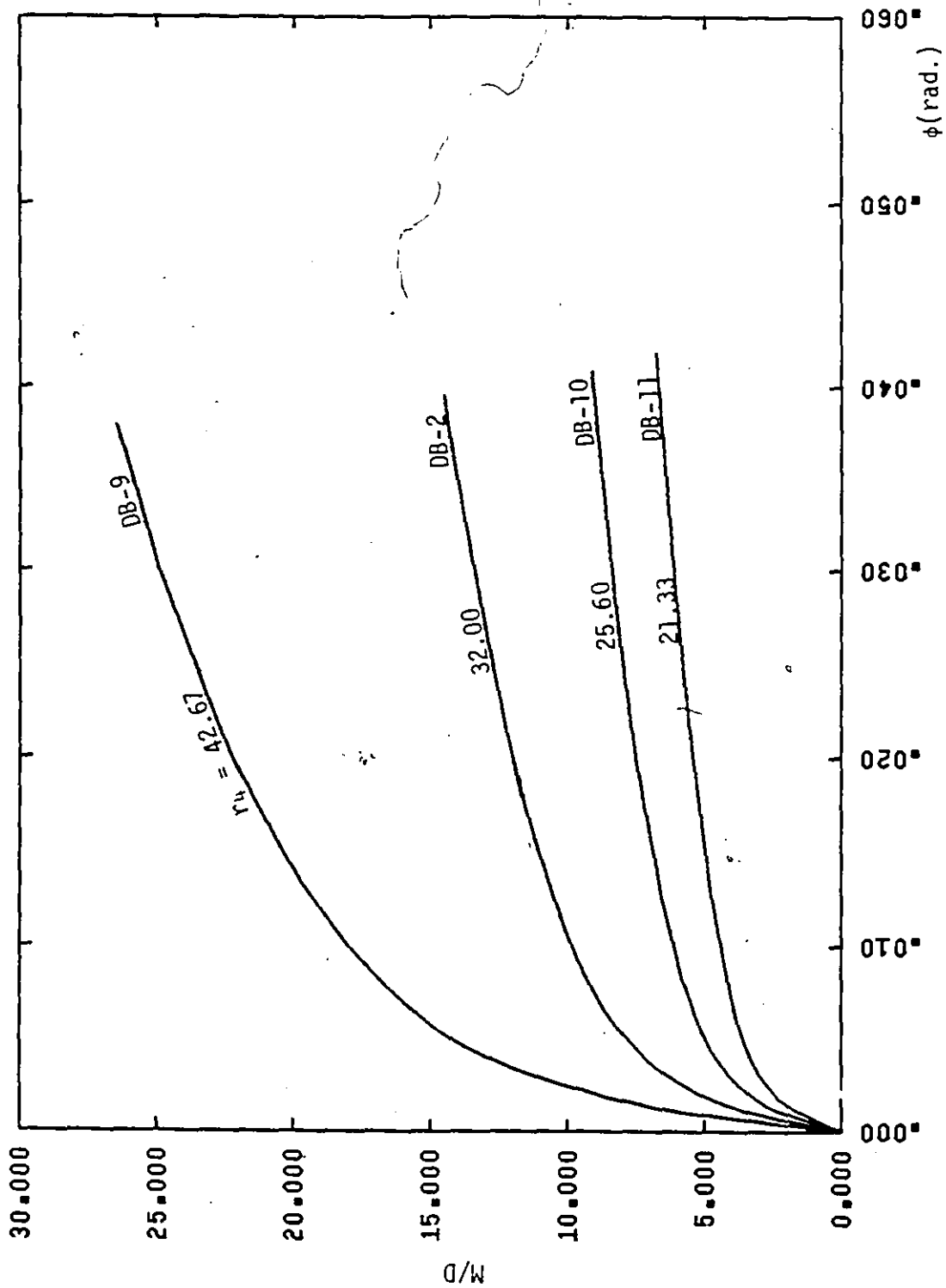
FIG. 5.4 VARIATION OF PARAMETER $r_4 = b_1/t_0$ (BRANCH MOMENT)
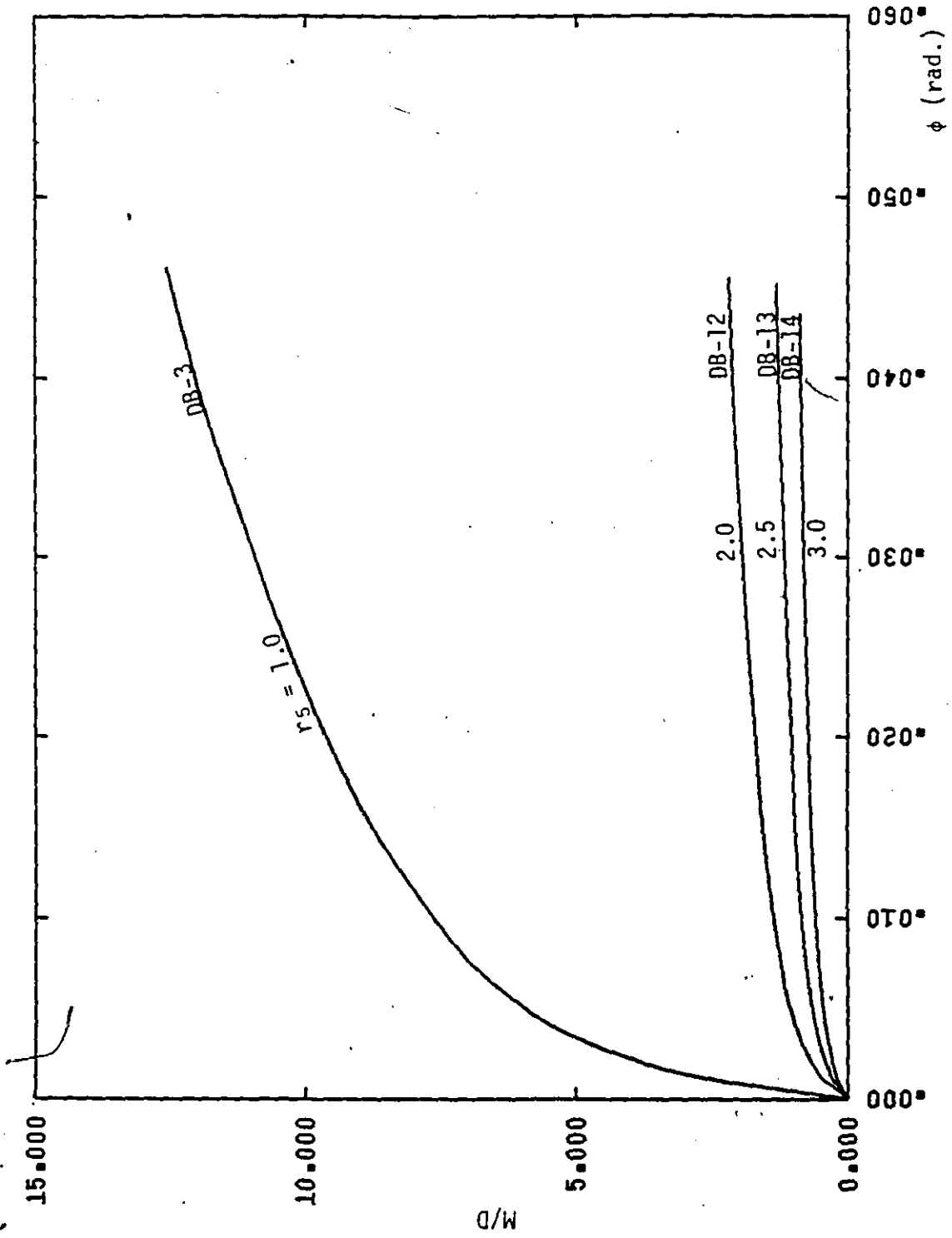
FIG. 5.5   VARIATION OF PARAMETER $r_5' = 1 + t_5'/t_0$ (BRANCH MOMENT)
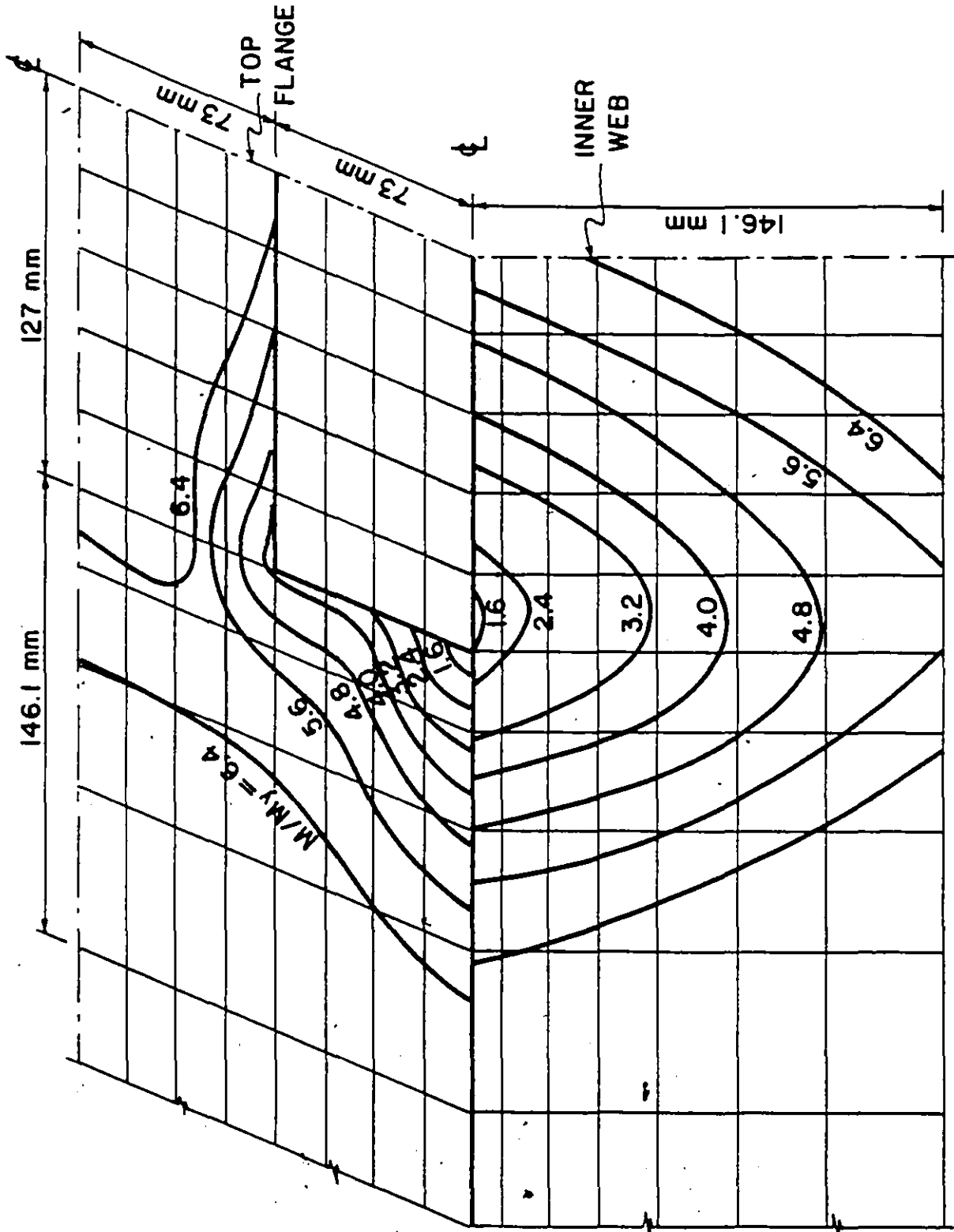
FIG. 5.6   PROGRESSION OF PLASTIC REGIONS IN JOINT DB-6
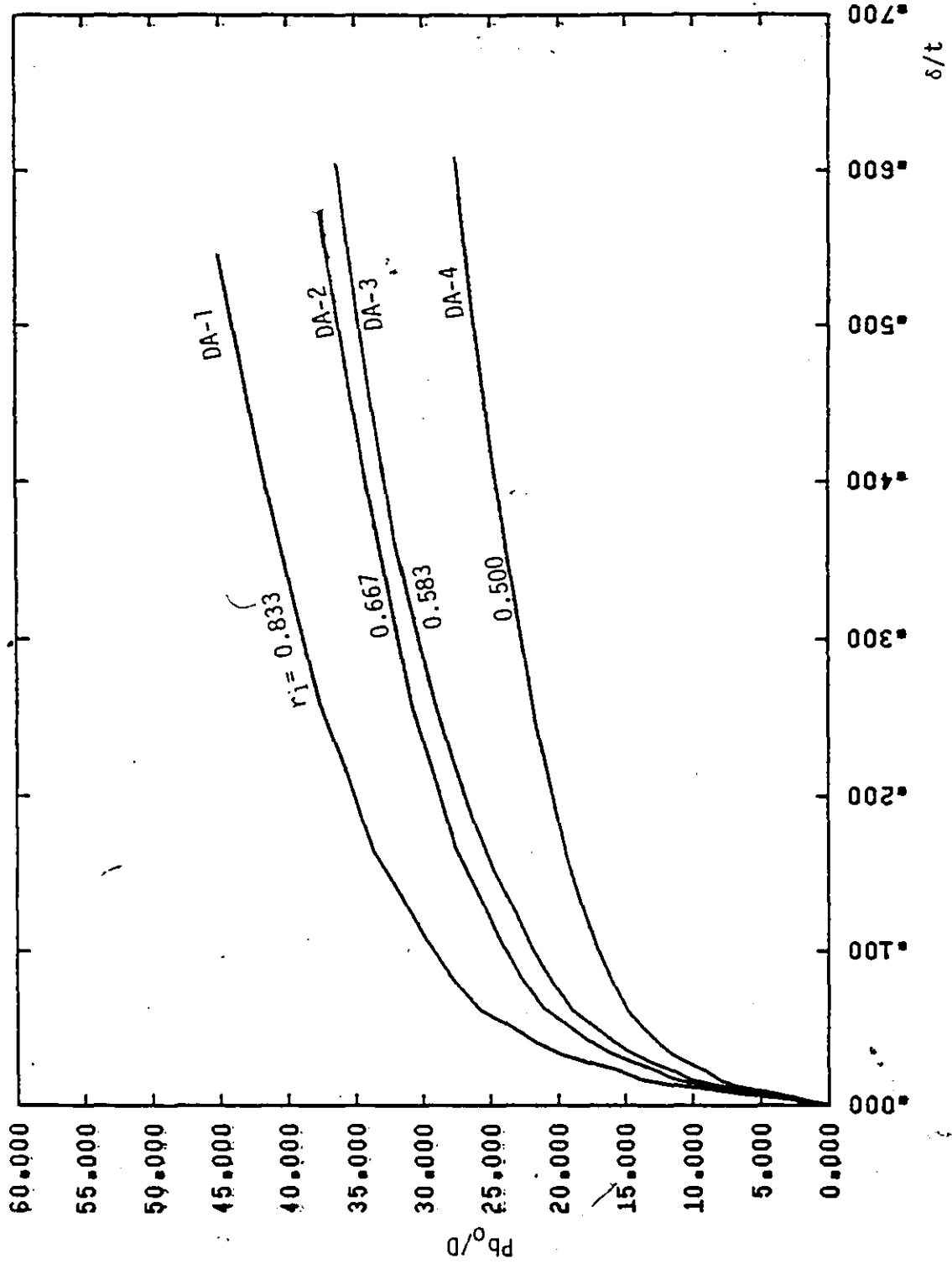
FIG. 5.7   VARIATION OF PARAMETER $r_1 = b_1/2b_0$ (PUNCHING SHEAR)
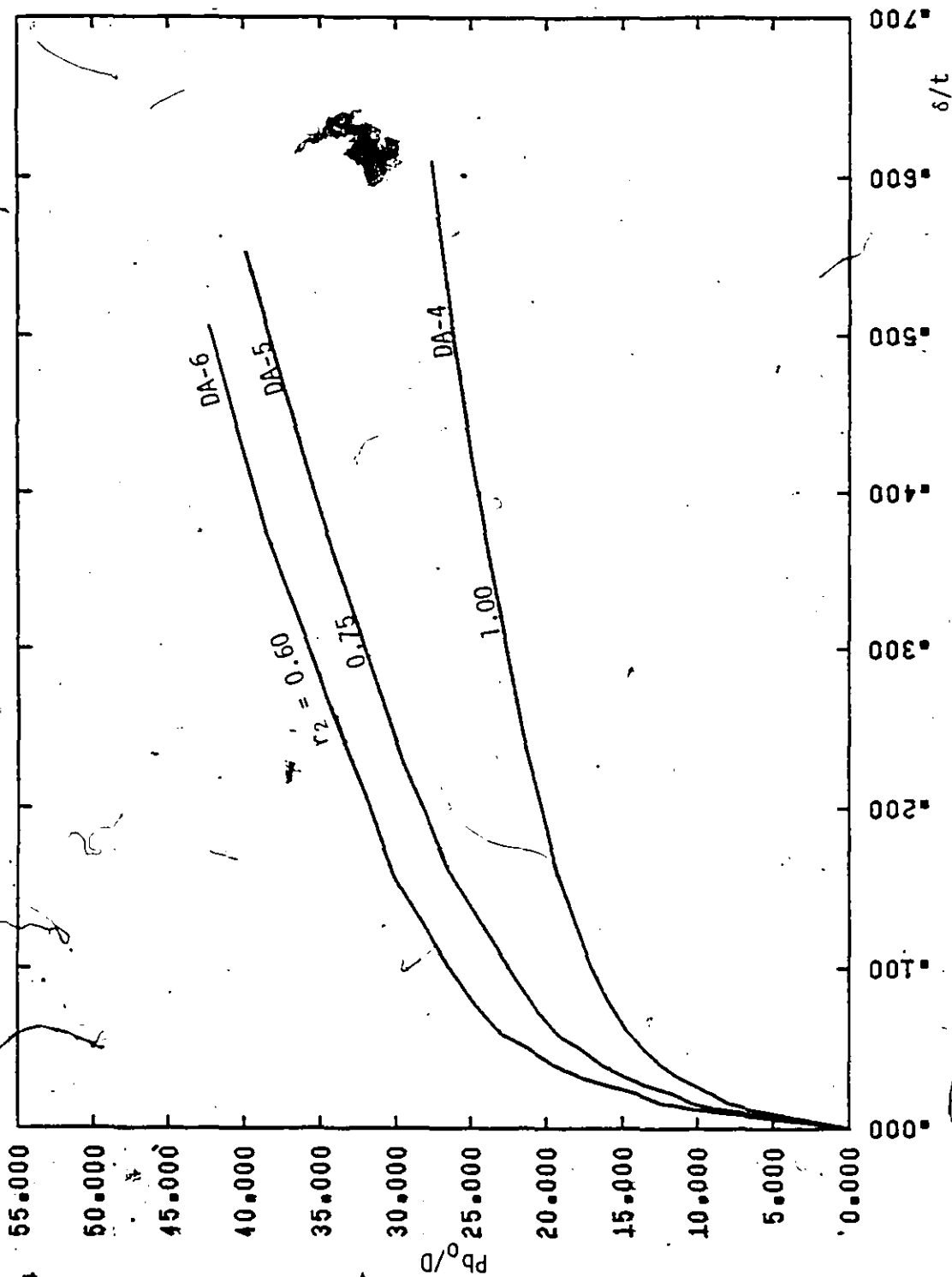
FIG. 5.8 VARIATION OF PARAMETER $r_2 = b_1/t_1$ (PUNCHING SHEAR)
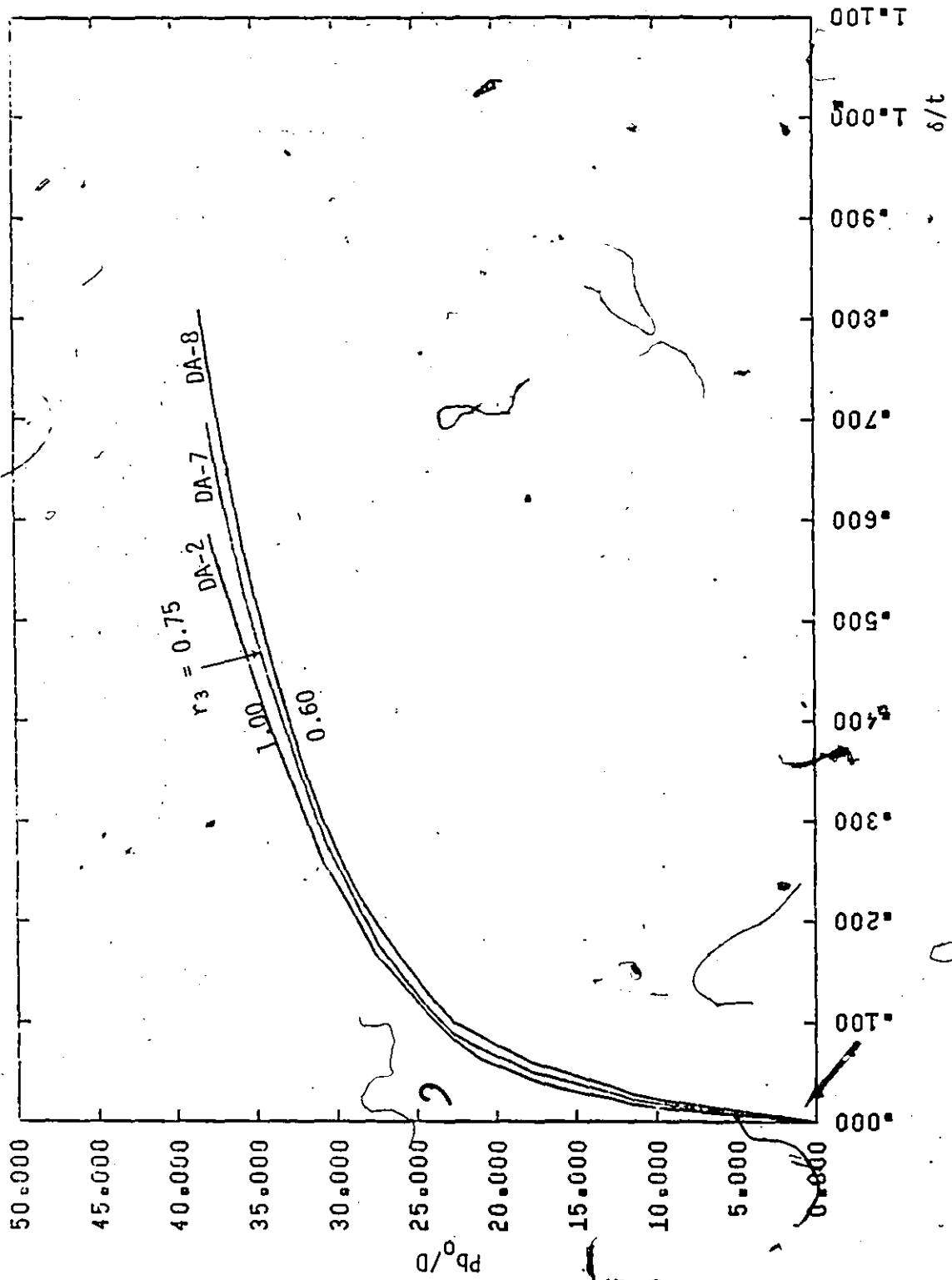
FIG. 5.9   VARIATION OF PARAMETER $r_3 = b_o/h_o$ (PUNCHING SHEAR)
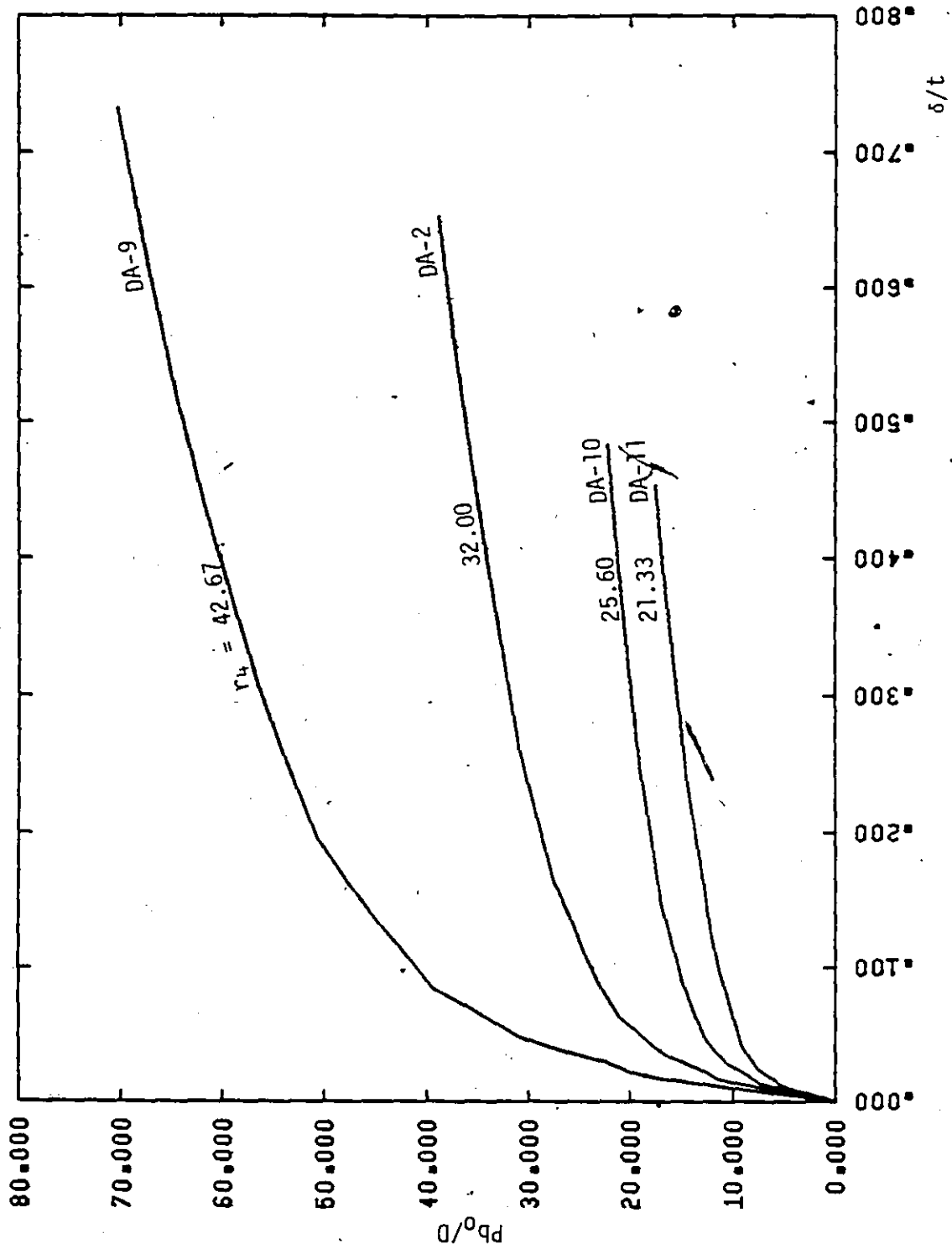
FIG. 5.10   VARIATION OF PARAMETER $r_4 = b_1/t_o$ (PUNCHING SHEAR)
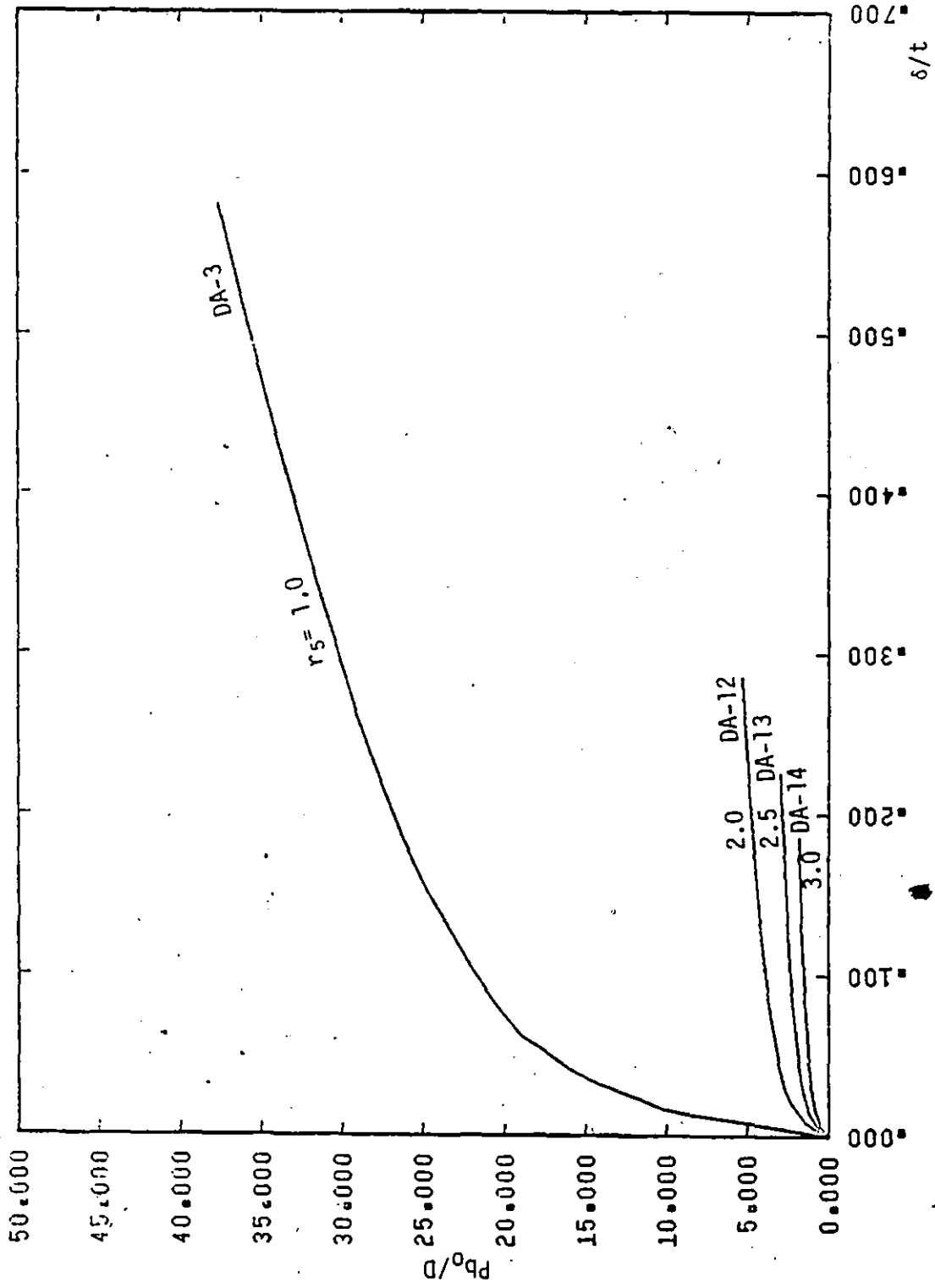
FIG 5.11   VARIATION OF PARAMETER $r_5 = 1 + t_s/t_o$ (PUNCHING SHEAR)
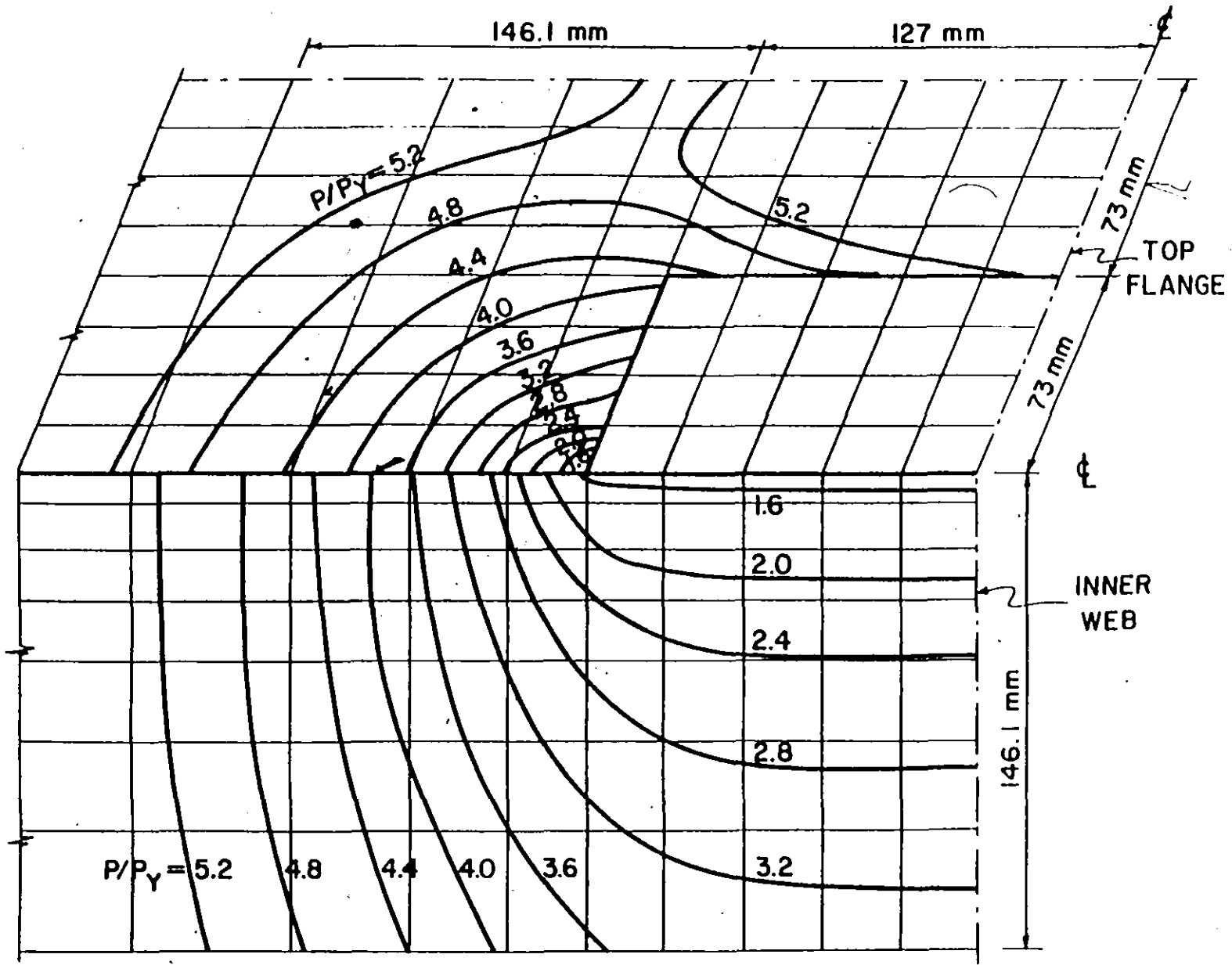
FIG. 5.12 PROGRESSION OF PLASTIC REGIONS IN JOINT DA-6
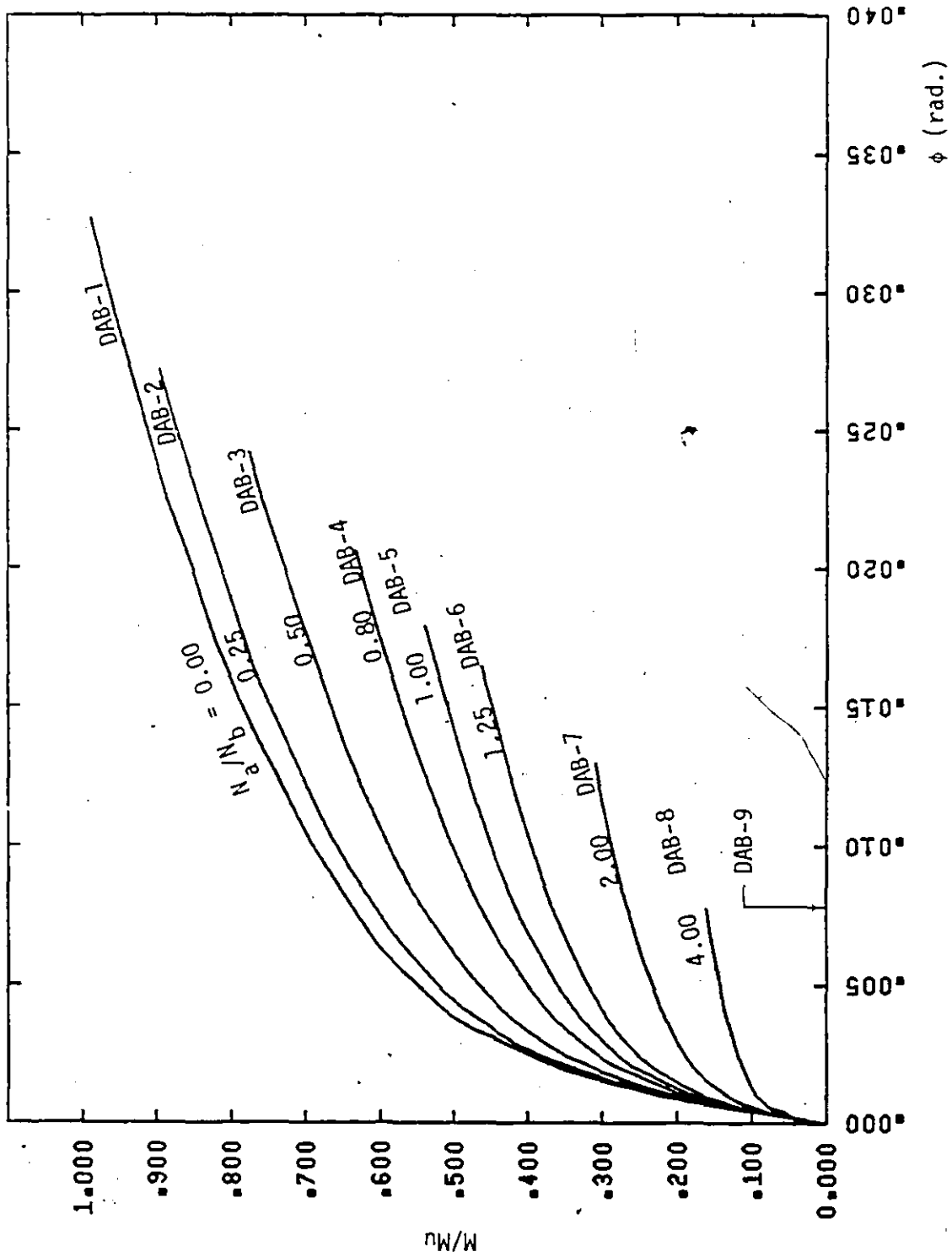
FIG. 5.13   NORMALIZED M-φ CURVES FOR DOUBLE CHORD JOINTS UNDER COMBINED LOADING

$$\left(\frac{P_m}{P_u}\right)^{\frac{5}{3}} + \left(\frac{M_m}{M_u}\right)^{\frac{5}{3}} = 1.0$$

$$\frac{P_m}{P_u} + 0.4\frac{M_m}{M_u} = 1.0$$
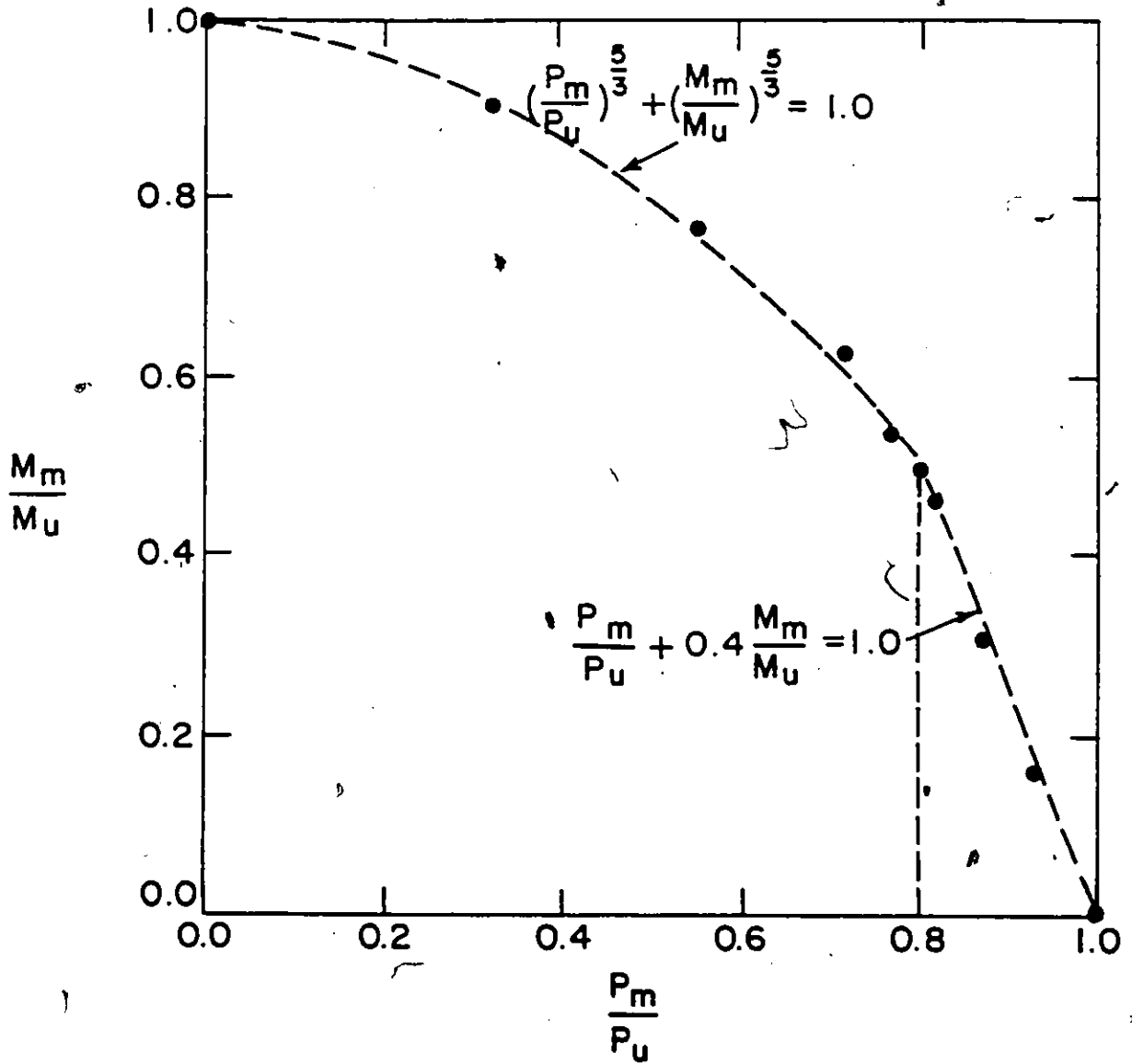
FIG. 5.14   INTERACTION ENVELOPE FOR DOUBLE CHORD JOINTS
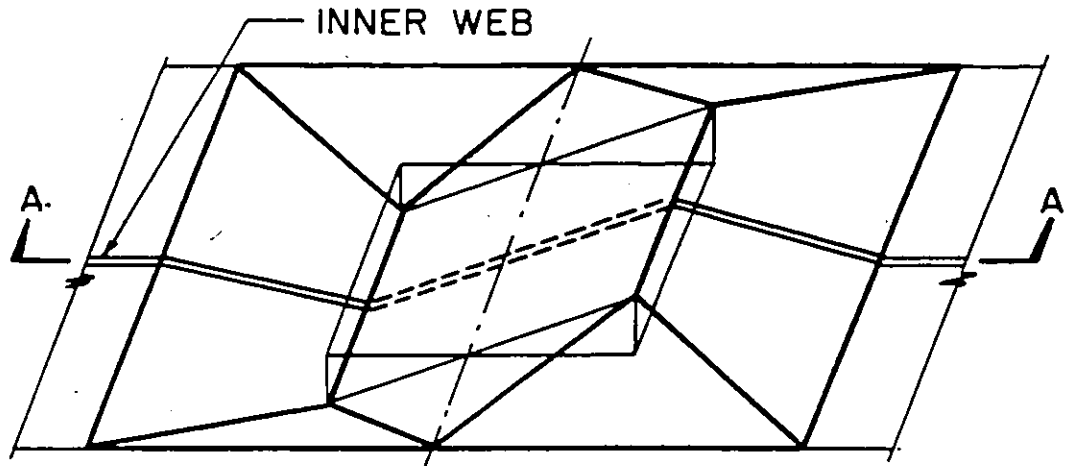
(a) FAILURE MECHANISM
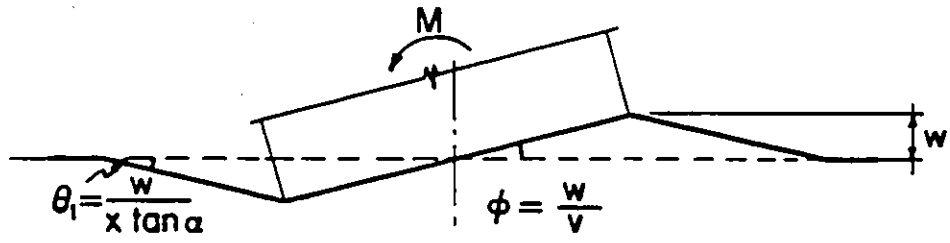
(b) SECTION A-A
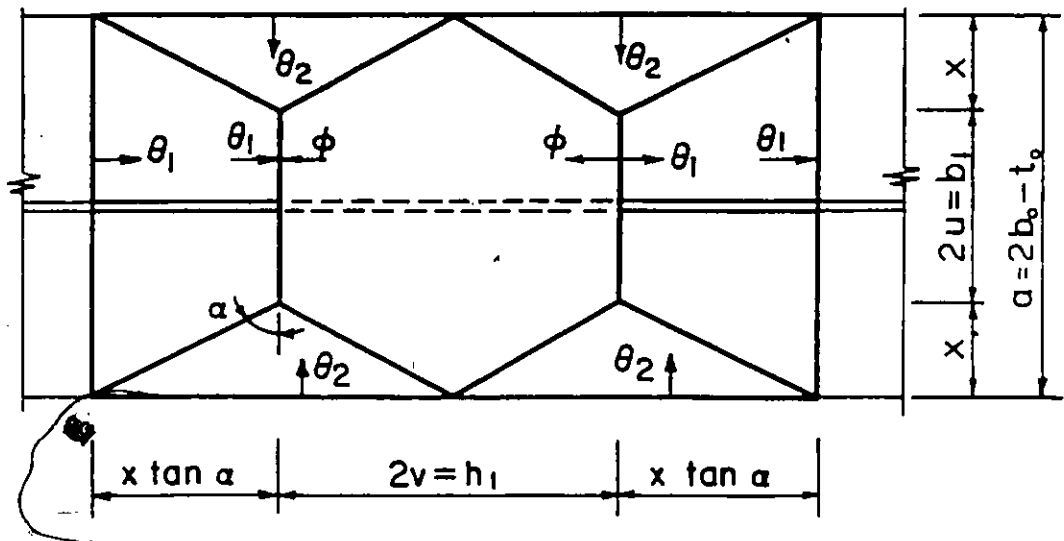
(c) PLAN

FIG. 5.15 FAILURE MECHANISM FOR DOUBLE CHORD JOINTS UNDER
BRANCH MOMENT

(a) FAILURE MECHANISM

(b) SECTION A-A
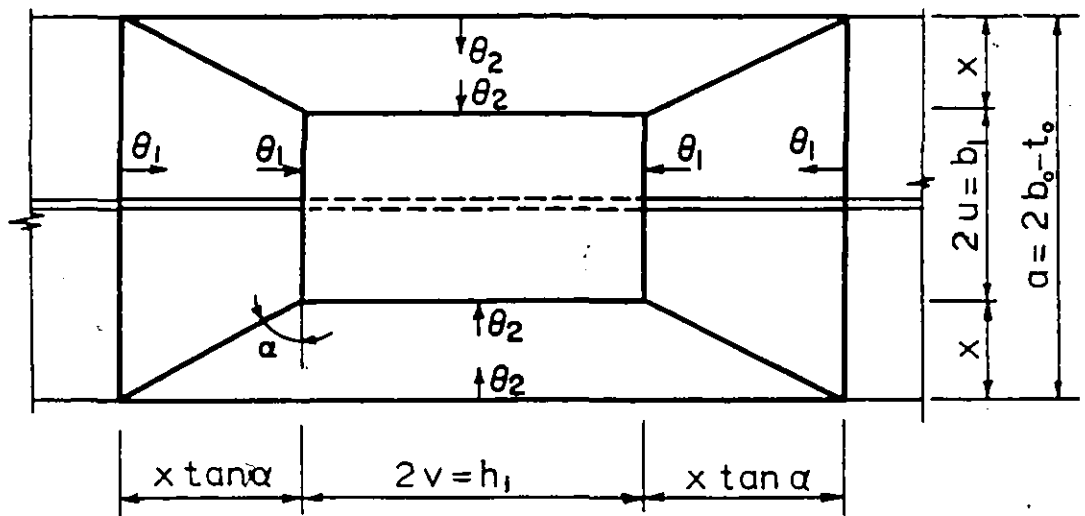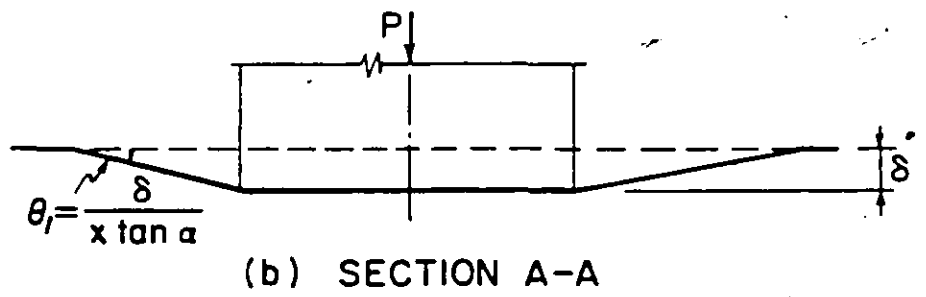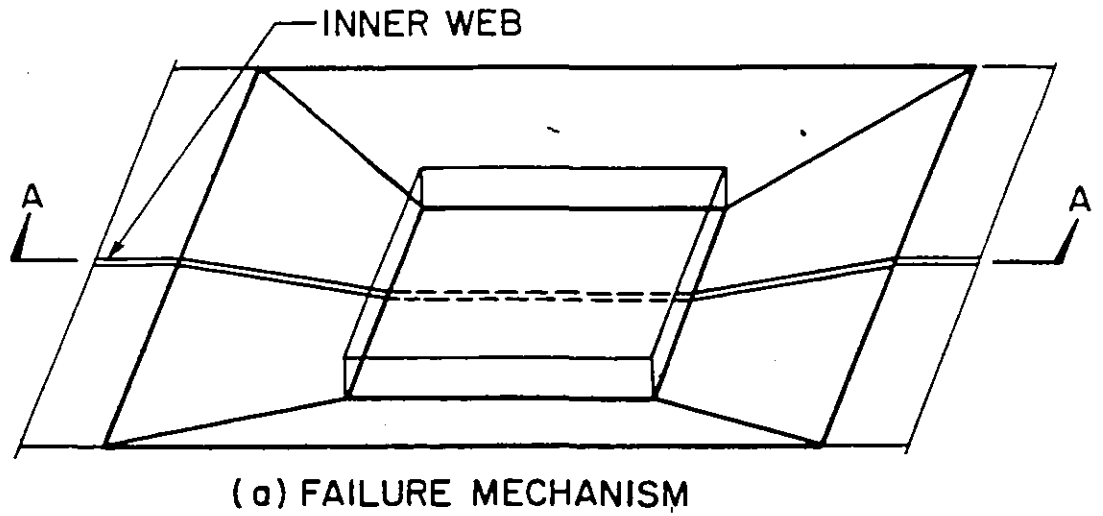
FIG. 5.16 FAILURE MECHANISM FOR DOUBLE CHORD JOINTS UNDER
PUNCHING SHEAR

CHAPTER 6

ANALYSIS OF SINGLE CHORD RHS T-JOINTS

6.1   Introduction

Single chord RHS T-joints are generally flexible and hence their stiffness and strength can have a significant effect on the overall behaviour of structures that employ this type of connection. This joint type can be assumed to behave rigidly when the branch and chord members are of the same width, according to reference [6]. However, an equal width joint requires a difficult butt weld to join the two members and means a higher cost of fabrication. Therefore, the web member should be 25 to 50 mm. narrower in width than the chord so that fillet welds can be used. A properly designed connection should be capable of transferring the branch forces to the chord without failure or unacceptable deformations. In heavily loaded Vierendeel trusses, some form of joint reinforcement is often necessary to develop the full-load capacity of the branch members.

In single chord RHS T-joints, various failure modes occur depending on the physical properties and the geometries of chord and branch members. These include flexural failure of chord flange plates, web crippling in chord members, local buckling of branch members and fracture in welds prior to developing full plastic moment in branch members. Kanatani et al. [14] concluded from an extensive experimental

study on RHS T-joints subject to moments, that flexural failure of the chord flange plate governs the joint strength when the ratio of branch width to width of flat portion of the chord flange is less than unity. It is this type of joint, then, that will be studied, using finite element analysis under different loading conditions. Analytical modelling of the joint and its material properties were presented earlier (Chapter 2).

Analyses of the single chord RHS joints were undertaken for branch moment or punching shear using the finite element mesh shown in Fig. 3.1. It will be noted that the mesh is finer in the regions of high stress gradients adjacent to the branch inclusion and becomes coarser away from this region. The purpose of this part of the research work was to provide useful information about the behaviour of this connection and to conduct a parametric study to formulate suitable design equations.

In the parametric study, the geometry of the connection was varied in order to study influence of the joint configuration on its performance. Five nondimensional parameters were selected to express variation in the joint geometry. They are defined for single chord joints as follows:

Width ratio; $r_1 = b_1/b_0$

Branch aspect ratio; $r_2 = b_1/h_1$

Chord aspect ratio; $r_3 = b_0/h_0$

Branch width-to-chord thickness ratio; $r_4 = b_1/t_0$

Stiffening plate parameter; $r_5 = 1 + t_s/t_0$.

As before, the length and width of the stiffening plate are considered as dependent variables and hence, the plate length h_s is taken as twice the branch height h_1 and its width b_s equal to the length of the flat portion of the top flange, i.e. $b_0 - 4t_0$.

In addition to the analyses mentioned above, the single chord joint behaviour was also investigated under combined loading. The finite element grid of Fig. 3.2 was used in this analysis and the results are presented in the form of an interaction envelope.

To obtain a predicted response, the loading was applied similar to that for the double chord joints, i.e. beyond the yield limit incre-ments of twenty percent of the yield load were utilized.

The results from the finite element analyses presented in this chapter will be employed in Chapter 7 to develop empirical formulae to aid in the design of single chord T-joints. These formulae will then be incorporated in an elasto-plastic analysis of Vierendeel trusses which employ such connections (Chapter 8).

6.2   Behaviour Under Branch Moment

A parametric study was conducted by analyzing fifteen joints under branch moment. These are designated SB-1 to SB-15. Dimensions of the chord and branch members of the joints as well as numerical values of the parameters are presented in Table 6.1. These joints were arranged in five groups, each of which was used to study the influence of a single parameter on the joint behaviour. The cases considered for a single parameter variation were grouped and indicated by underlining the numerical values of the corresponding parameter. Only one parameter was varied in each group (with the exception of the r_1 group) while holding the other parameters constant. In the r_1 group, both r_1 and t_4 varied and thus some provision had to be made to determine the influence of r_1 alone as will be explained later in Chapter 7. The selected values of each parameter cover the practical range of its variation.

It may be mentioned here that for all of the joints analyzed, the ratio of branch width to width of flat portion of the chord flange was less than 1.0. Hence, flexural failure of the chord flange, as predicted by the present approach, was expected to be the governing failure mode, as has been concluded experimentally [14].

Each joint was loaded incrementally well into the plastic range. The resulting incremental equations of equilibrium were solved iteratively until the prescribed tolerance of the determinant condition of one percent had been reached. Any remaining residual forces were added

to the next increment of the branch moment to prevent drifting of the response. Preliminary investigation had indicated that it is reasonable to consider that the joint has reached its limiting capacity when the joint rotation exceeds thirty five times the yield rotation. It is assumed that the geometric nonlinearities play a significant role after this level of deformation and hence the adopted theory of small deformations would no longer be appropriate.

Normalized moment-rotation curves for the analyzed joints were plotted in five groups, each representing variation of a single parameter, as shown in Figs. 6.1 to 6.5. Flexural rigidities D of the combined chord flange and the stiffening plate, if present, were used to normalize moments and are also given in Table 6.1. The predicted values of the yield moments M_Y, yield rotations ϕ_Y and moments M_u at $\phi = 35\phi_Y$ are given in Table 6.2. The joint flexural stiffness J is the slope of the tangent to the $M - \phi$ curve at any load level. Values of the elastic stiffness J_{EL} and the tangential stiffness J_T at limiting rotations are also given in Table 6.2.

It can be observed from Figs. 6.1 to 6.5 and Table 6.2 that, with the exception of chord aspect ratio r_3, the other parameters have a significant effect on the joint stiffness and strength. The curves in Fig. 6.3 indicated the same behaviour as has been reported for the double chord RHS T-joints in Section 5.2. The influence of r_3 is, however, small and can be neglected when standard RHS are analyzed. One can also conclude from the analytical results that the joints start to yield at an early stage of loading and sustain moments about six times

M_Y before attaining an extensive loss of stiffness. The tangential stiffness at ultimate moment reduces to about five percent of the initial elastic stiffness.

Progression of the plastic zones in the top flange and webs of the chord member is illustrated in Fig. 6.6 for one-quarter of joint SB-4. The same reasons, as explained for the double chord RHS T-joints in the previous chapter, also apply here for discontinuities of the contours at the interface between the top flange and the webs of the chord member. It can be observed from Fig. 6.6 that yielding initiates in the top flange at the four corners of the branch inclusion, whereas yielding of the webs does not start until the branch moment is about four times the yield value. Depth of the yielded zone in the webs at maximum moment is about one-third of the web depth. This depth of the yielded zone increases with higher width ratios b_1/b_0 due to the higher loads carried directly by the webs.

6.3 Behaviour Under Punching Shear

The same fifteen joints listed in Table 6.1 have also been analyzed under punching shear. The cases analyzed are designated here as SA-1 to SA-15. The parametric study was carried out in the same manner as for the branch moment loading cases. Each joint was loaded incrementally well into the plastic range. Tolerance of the determinant condition was again prescribed as one percent. Loading was terminated when the transverse deflection of the inclusion reached thirty five times the yield value.

Normalized load-deflection curves for these joints are plotted
in five groups, each representing the variation of a single geometric
parameter, as shown in Figs. 6.7 to 6.11. The ratio D/b_o was used to
normalize loads wherease deflections were normalized by the total thick-
ness $t = (t_0 + t_s)$ of the top flange and stiffening plate, if present.
The predicted values of yield load P_Y, yield deflection δ_Y and the ulti-
mate load P_u at $\delta = 35 \delta_Y$ are presented in Table 6.3. Also given in
Table 6.3 are the elastic axial stiffness C_{EL} and the tangential axial
stiffness C_T at limiting deflections. The joint axial stiffness is the
slope of the tangent to the P-δ curve. It may be concluded from the
results presented in Figs. 6.7 to 6.11 and Table 6.3 that all the geo-
metric parameters have a pronounced effect on the joint behaviour except
r_3. The results in Table 6.3 show that the depth of the chord members
has a small influence on the load capacity of the single chord RHS T-
joint. Patel et al. [5] arrived at the same conclusion experimentally
(see results for specimens B-5, LB-5, and L-5 in reference [5]). Hence,
the chord aspect ratio r_3 can be assumed to have negligible effect on
the joint behaviour under punching shear. It can also be concluded from
the results of Table 6.3 that the joint load capacity is about six times
the yield limit load. Furthermore, the tangential stiffness at the
ultimate load was reduced to about five percent of the elastic stiff-
ness. This indicates a large reserve of strength and stiffness in the
joint at the yield load level. Hence, it is extremely conservative to
limit the joint capacity to the yield load. Fig. 6.12 shows the pattern
of propagation of the plastic zone in a typical joint under punching
shear. The progression of plastic regions in the web and load-carrying

flange is shown for one-quarter of joint SA-4. Yielding of the flange, once again, is initiated at the points adjacent to the four corners of the branch inclusion. Yielding of the webs does not occur until, the load on the joint is about three times the yield load.

6.4   Behaviour Under Combined Loading

Joint SB-3 in Table 6.1 was analyzed for different combinations of branch moment and punching shear. The finite element mesh of Fig. 3.2 for one-half of the joint was employed in this analysis. Nine cases, designated SAB-1 to SAB-9 were considered. Different load combinations, ranging from pure branch moment for SAB-1 to pure punching shear for SAB-9, were prescribed by varying the ratio N_a/N_b, where N_a and N_b are as defined in Fig. 3.3. See Table 6.4 for the loading in each case.

The analytical moment-rotation curves for the nine cases are shown in Fig. 6.13 in a normalized form. The moments were normalized with respect to the ultimate moment M_u of case SAB-1 so that the maximum M/M_u would be equal to unity. The moment-rotation curve for joint SAB-9 (pure punching shear) coincides with the abscissa (rotation axis) due to absence of the branch moment. Loading was terminated when rotation ϕ (or deflection δ in case SAB-9) reached forty times the yield value ϕ_Y. This choice of limiting displacement was of no major consequence since the purpose here was to study the comparative strength under combined loading.

Results of the analyses are summarized in Table 6.5. The predicted maximum moments and punching shears under combined loading are designated M_m and P_m, respectively. The discrepancies in the results for SAB-1 and SAB-9 when compared to SB-3 and SA-3 results given in Tables 6.2 and 6.3, respectively, are again attributed to the different finite element mesh used and, also to different limits on displacements.

It can be observed from Fig. 6.13 and Table 6.5 that the presence of punching shear reduces the joint's branch moment capacity and vice-versa. Interaction between the two types of loadings can be described by an interaction envelope as shown in Fig. 6.14. The ratios M_m/M_u and P_m/P_u for the cases analyzed are given in Table 6.5. The maximum loads for each case are represented in Fig. 6.14 by a point. The interaction relationship can be expressed by the following equations.

$$\left(\frac{P_m}{P_u}\right)^{1.5} + \left(\frac{M_m}{M_u}\right)^{1.5} = 1.0 \quad ; \quad \frac{P_m}{P_u} < 0.70 \qquad (6.1)$$

and

$$\frac{P_m}{P_u} + 0.54\,\frac{M_m}{M_u} = 1.0 \quad ; \quad \frac{P_m}{P_u} > 0.70 \qquad (6.2)$$

Analytical formulae for M_u and P_u will be developed in Chapter 7. Knowing M_u and P_u for a given joint geometry, Equations 6.1 and 6.2 can

be used to predict the joint capacity under combined branch moment and
punching shear.

TABLE 6.1 PROPERTIES OF ANALYZED SINGLE CHORD T-JOINTS

Joint No.	Chord (RHS) $(h_0 \times b_0 \times t_0)$ (mm)	Branch (RHS) $(h_1 \times b_1)$ (mm)	t_s (mm)	$r_1 = b_1/b_0$	$r_2 = b_1/h_1$	$r_3 = b_0/h_0$	$r_4 = b_1/t_0$	$r_5 = 1 + \dfrac{t_s}{t_0}$	D * (KN-m)
SB-1	254.0×254.0×12.70	203.2×203.2	–	0.80	1.00	1.000	16.00	1.0	37.516
SB-2	254.0×254.0× 9.53	203.2×203.2	–	0.80	1.00	1.000	21.33	1.0	15.827
SB-3	254.0×254.0× 9.53	177.8×177.8	–	0.70	1.00	1.000	18.67	1.0	15.827
SB-4	254.0×254.0× 9.53	152.4×152.4	–	0.60	1.00	1.000	16.00	1.0	15.827
SB-5	254.0×254.0× 9.53	101.6×101.6	–	0.40	1.00	1.000	10.67	1.0	15.827
SB-6	254.0×254.0× 9.53	203.2×152.4	–	0.60	0.75	1.000	16.00	1.0	15.827
SB-7	254.0×254.0× 9.53	254.0×152.4	–	0.60	0.60	1.000	16.00	1.0	15.827
SB-8	254.0×254.0× 7.94	203.2×203.2	–	0.80	1.00	1.000	25.60	1.0	9.157
SB-9	254.0×254.0× 6.35	203.2×203.2	–	0.80	1.00	1.000	32.00	1.0	4.688
SB-10	254.0×254.0× 6.35	152.4×152.4	–	0.60	1.00	1.000	24.00	1.0	4.688
SB-11	254.0×254.0× 6.35	152.4×152.4	6.35	0.60	1.00	1.000	24.00	2.0	37.516
SB-12	254.0×254.0× 6.35	152.4×152.4	9.53	0.60	1.00	1.000	24.00	2.5	73.274
SB-13	254.0×254.0× 6.35	152.4×152.4	12.07	0.60	1.00	1.000	24.00	3.0	126.620
SB-14	304.8×254.0× 9.53	152.4×152.4	–	0.60	1.00	0.833	16.00	1.0	15.827
SB-15	381.0×254.0× 9.53	152.4×152.4	–	0.60	1.00	0.667	16.00	1.0	15.827

$$* D = \frac{Et^3}{12(1-\nu^2)}; \quad t' = t_0 + t_s, \quad E = 200,000 \text{ MPá}, \quad \nu = 0.30$$

TABLE 6.2   ANALYTICAL RESULTS FOR SINGLE CHORD T-JOINTS UNDER BRANCH
MOMENT

Joint	Yield Values			Values at $\phi=35\phi_Y$		$\dfrac{M_u}{M_T}$	$\dfrac{J_T}{J_{EL}}$
No.	M_Y (KN-m)	ϕ_Y $\times10^{-3}$(rad.)	$J_{EL}\times10^3$ (KN-m/rad)	M_u (KN-m)	$J_T\times10^2$ (KN-m/rad.)		
SB-1	15.56	0.828	18.79	107.31	11.42	6.90	0.061
SB-2	8.87	0.914	9.71	55.60	5.44	6.26	0.056
SB-3	5.31	1.468	3.62	33.01	1.98	6.21	0.055
SB-4	4.17	2.305	1.81	25.40	1.12	6.09	0.062
SB-5	3.12	2.971	1.05	20.15	0.45	6.46	0.056
SB-6	4.93	1.788	2.76	29.08	1.27	5.89	0.046
SB-7	5.40	1.347	4.01	32.24	2.28	5.97	0.057
SB-8	6.25	1.023	6.11	38.64	3.54	6.18	0.058
SB-9	4.13	1.216	3.40	24.95	1.83	6.04	0.054
SB-10	2.27	3.286	0.69	13.08	0.34	5.77	0.049
SB-11	5.44	2.157	2.52	31.55	1.33	5.80	0.053
SB-12	8.09	1.982	4.08	45.64	2.25	5.64	0.055
SB-13	11.07	1.848	5.99	61.06	3.47	5.52	0.058
SB-14	4.35	2.484	1.75	25.60	0.99	5.89	0.057
SB-15	4.50	2.711	1.67	25.72	0.98	5.68	0.059

1 KN-m = 8.851 Kip-in.

TABLE 6.3   ANALYTICAL RESULTS FOR SINGLE CHORD T-JOINTS UNDER PUNCHING
SHEAR

Joint	Yield Values			Values $\delta=50\delta_Y$			
No.	P_Y (KN)	δ_Y (mm)	$C_{EL}\times10^3$ (KN/mm)	P_u (KN)	$C_T\times10^2$ (KN/mm)	$\dfrac{P_u}{P_Y}$	$\dfrac{C_T}{C_{EL}}$
SA-1	143.7	0.033	4.35	1026	2.57	7.14	0.059
SA-2	115.1	0.064	1.80	755	1.01	6.56	0.056
SA-3	89.5	0.094	0.95	554	0.60	6.19	0.053
SA-4	66.0	0.157	0.42	395	0.25	5.98	0.060
SA-5	44.4	0.215	0.35	261	0.19	5.88	0.055
SA-6	75.4	0.150	0.50	431	0.27	5.72	0.053
SA-7	81.2	0.134	0.61	476	0.34	5.86	0.055
SA-8	81.8	0.071	1.15	523	0.67	6.39	0.058
SA-9	54.6	0.084	0.65	350	0.34	6.41	0.053
SA-10	37.9	0.213	0.18	211	0.09	5.57	0.049
SA-11	85.1	0.166	0.51	461	0.27	5.42	0.053
SA-12	115.0	0.149	0.77	631	0.42	5.49	0.054
SA-13	146.6	0.138	1.06	838	0.60	5.72	0.057
SA-14	65.3	0.176	0.37	385	0.21	5.90	0.056
SA-15	64.7	0.188	0.34	383	0.20	5.92	0.058

1 KN = 0.2248 Kips

1 KN/mm = 5.710 K/in.

TABLE 6.4   LOAD COMBINATIONS FOR SINGLE CHORD T-JOINTS
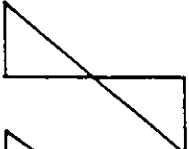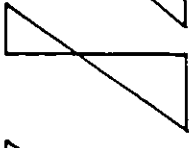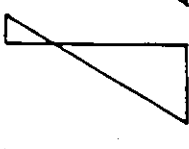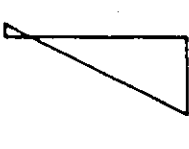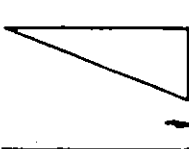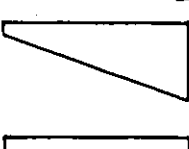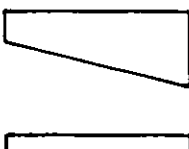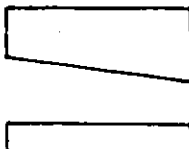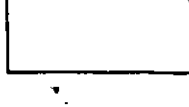
Case No.	Chord (RHS) $(h_0 \times b_0 \times t_0)$ (mm)	Branch (RHS) $(h_1 \times b_1)$ (mm)	N_a/N_b	Loading	Remarks
DAB-1	254.0×254.0×9.35	177.8×177.8	0.00		Pure Branch Moment
SAB-2	"	"	0.25		
SAB-3	"	"	0.50		
SAB-4	"	"	0.80		
SAB-5	"	"	1.00		
SAB-6	"	"	1.25		
SAB-7	"	"	2.00		
SAB-8	"	"	4.00		
SAB-9	"	"	∞		Pure Punching Shear

TABLE 6.5 ANALYTICAL RESULTS FOR SINGLE CHORD T-JOINTS UNDER COPMBINED
LOADING

Case	Yield Values			Values at $\phi = 40\phi_Y$ or $\delta = 40\delta_Y$			
No.	M_Y (KN-m)	ϕ_Y $\times 10^{-3}$ (rad.)	P_Y (KN)	M_m (KN-m)	P_m (KN)	$\dfrac{M_m}{M_u}$	$\dfrac{P_m}{P_u}$
SAB-1	5.85	1.635	0.00	39.10	0.0	1.000	0.000
SAB-2	4.82	1.349	20.33	34.45	145.3	0.882	0.292
SAB-3	4.10	1.147	34.56	29.46	248.6	0.754	0.500
SAB-4	3.47	0.973	46.85	23.73	320.3	0.608	0.644
SAB-5	3.15	0.884	53.15	20.92	353.0	0.536	0.709
SAB-6	2.82	0.793	59.55	17.92	378.0	0.459	0.759
SAB-7	2.15	0.606	72.65	12.38	417.7	0.317	0.839
SAB-8	1.32	0.374	88.93	6.68	450.6	0.171	0.905
SAB-9	0.00	0.000	104.52	0.00	498.1	0.000	1.000
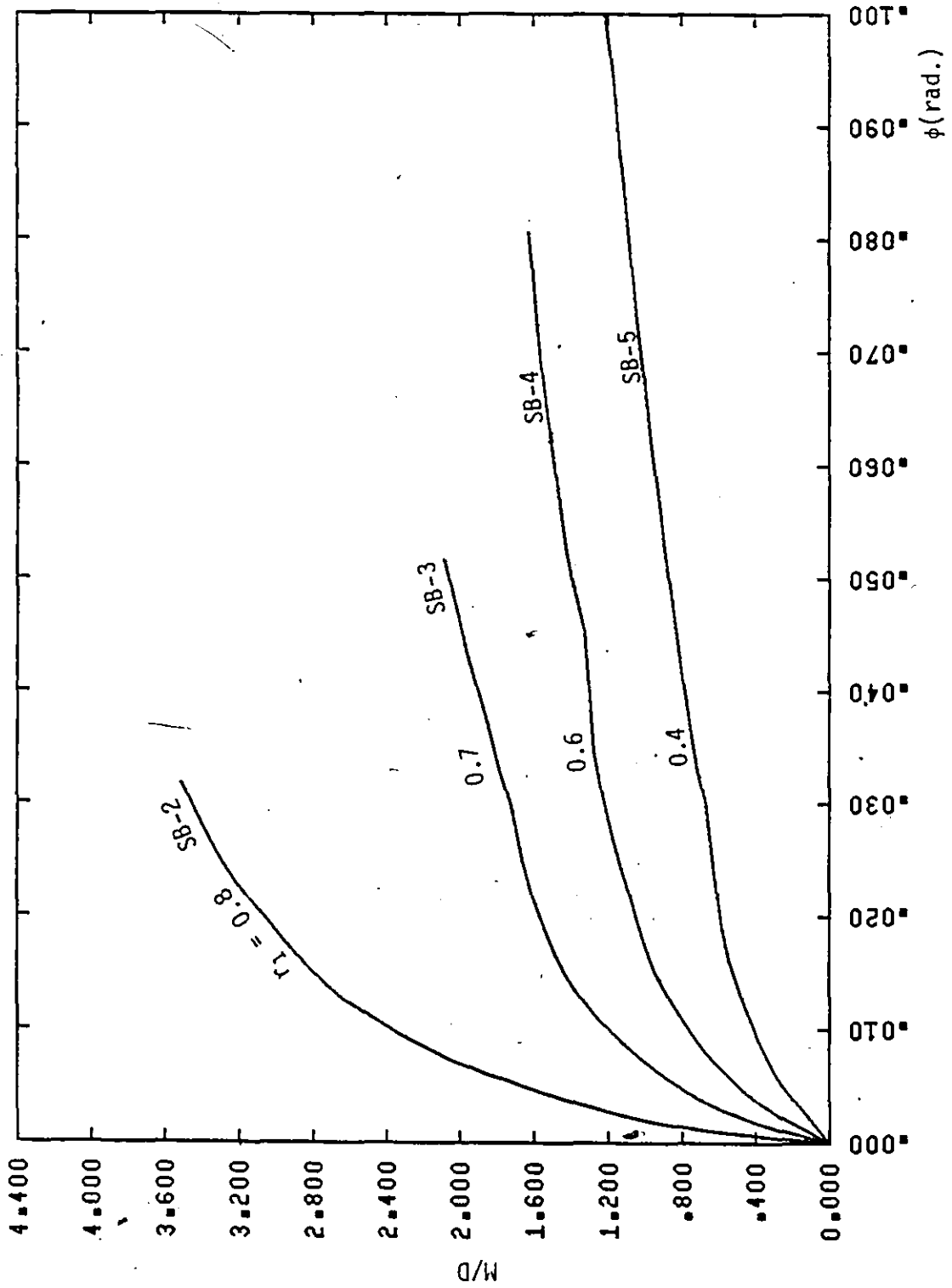
FIG. 6.1 VARIATION OF PARAMETER $r_1 = b_1/b_0$ (BRANCH MOMENT)
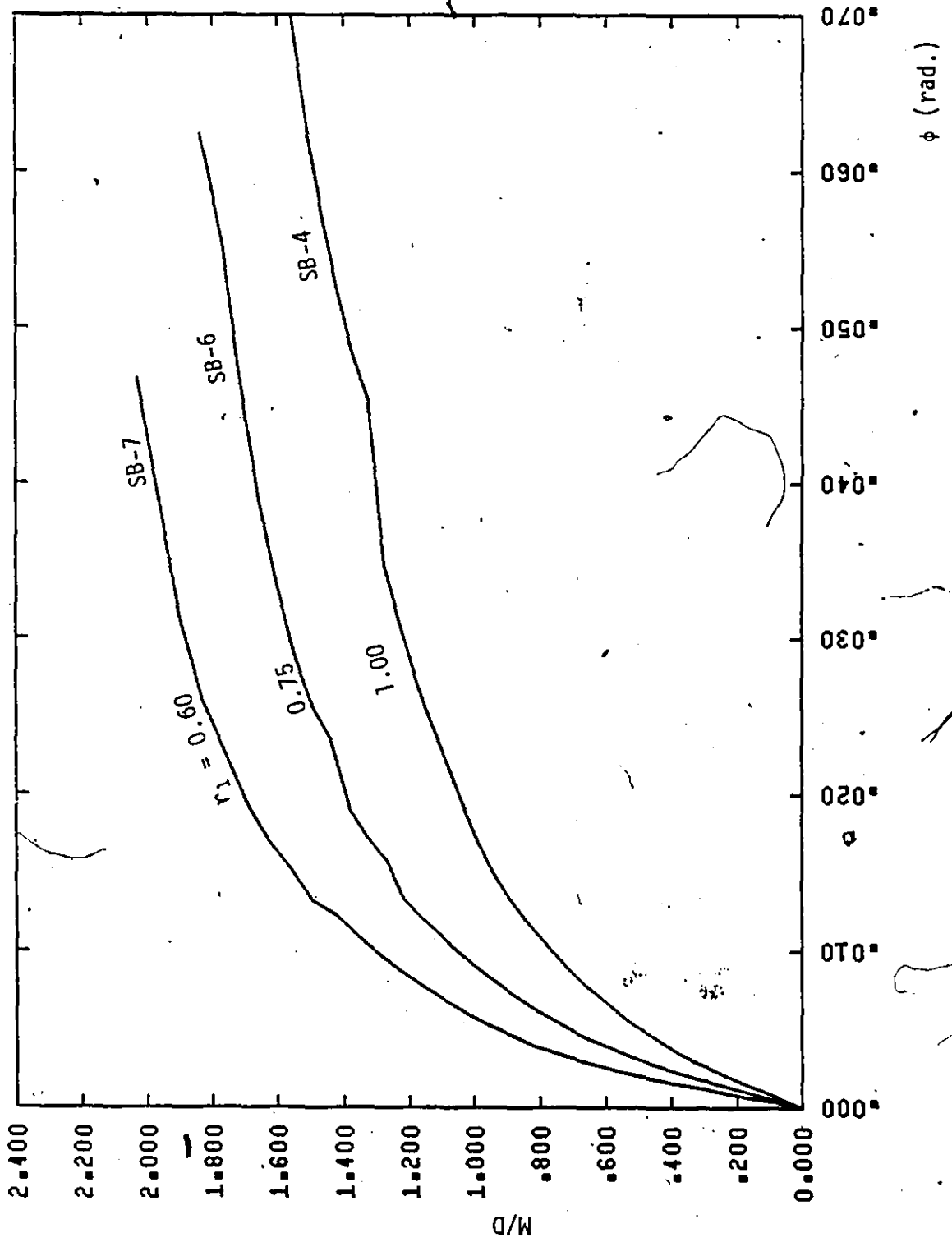
FIG. 6.2   VARIATION OF PARAMETER $r_2 = b_1/h_1$ (BRANCH MOMENT)
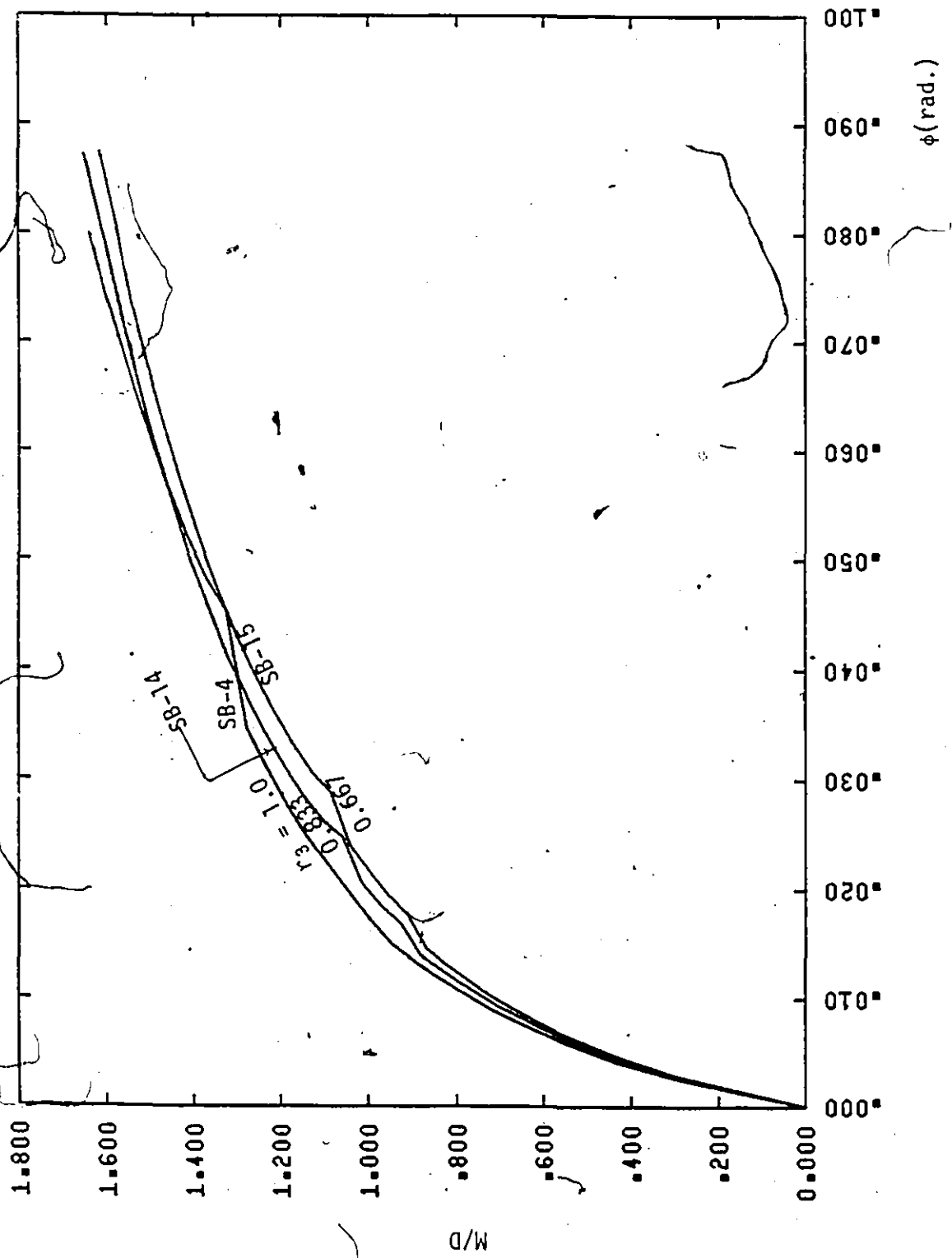
FIG. 6.3   VARIATION OF PARAMETERS $r_3 = b_0/h_0$ (BRANCH MOMENT)
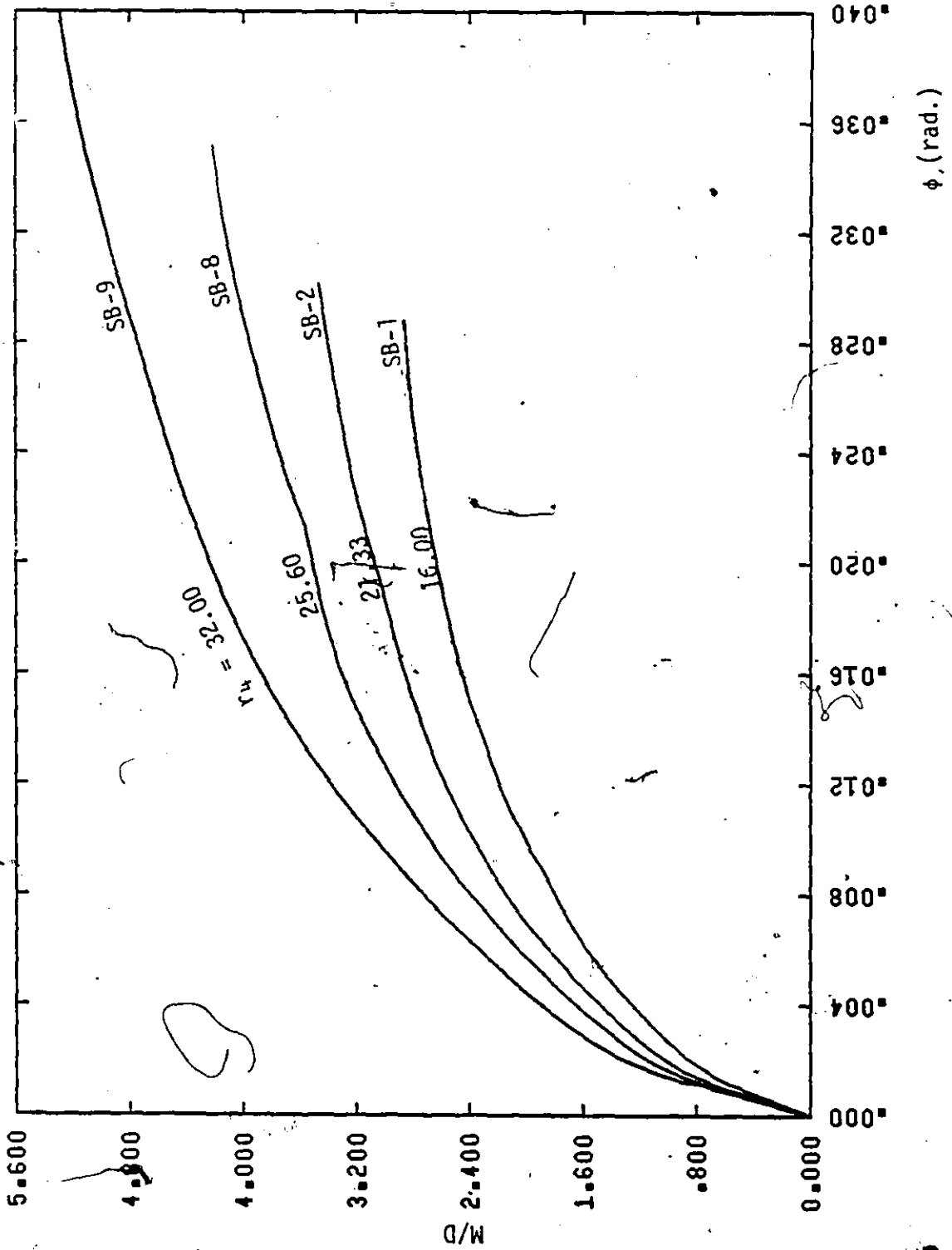
FIG. 6.4   VARIATION OF PARAMETER $r_4 = b_1/t_0$ (BRANCH MOMENT)
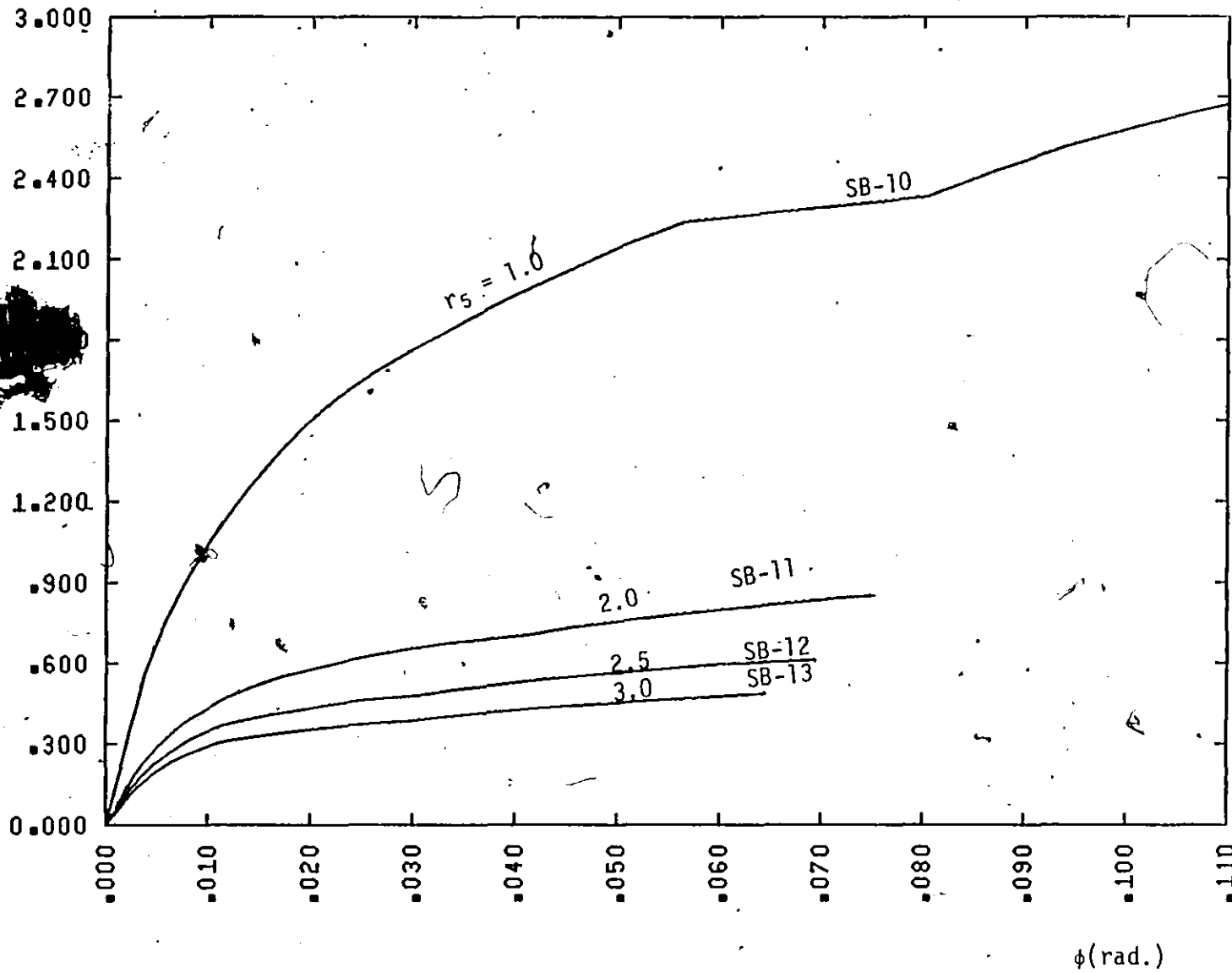
FIG. 6.5   VARIATION OF PARAMETER $r_5 = 1 + t_s/t_o$ (BRANCH MOMENT)
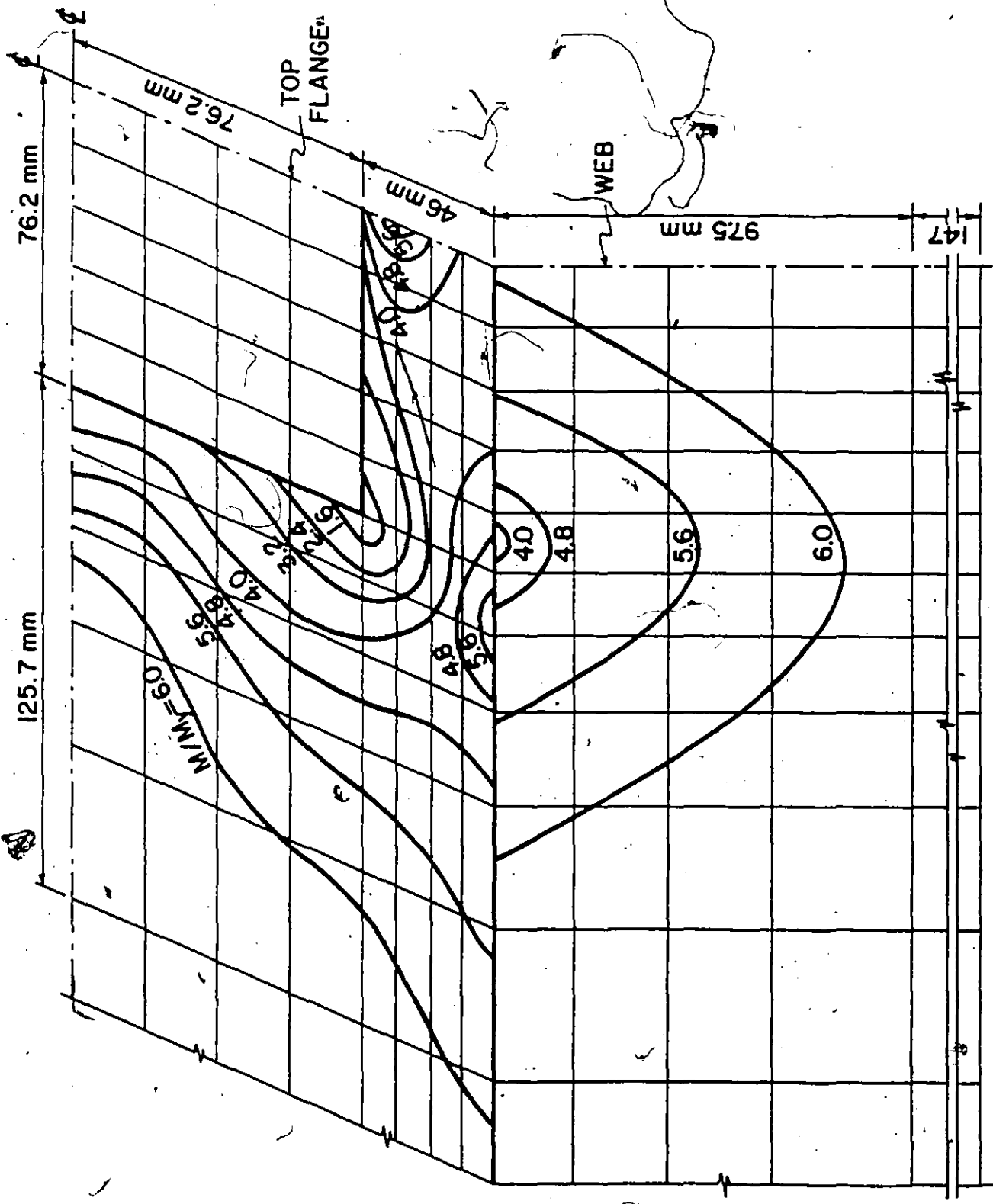
FIG. 6.6 PROGRESSION OF PLASTIC REGIONS IN JOINT SB-4
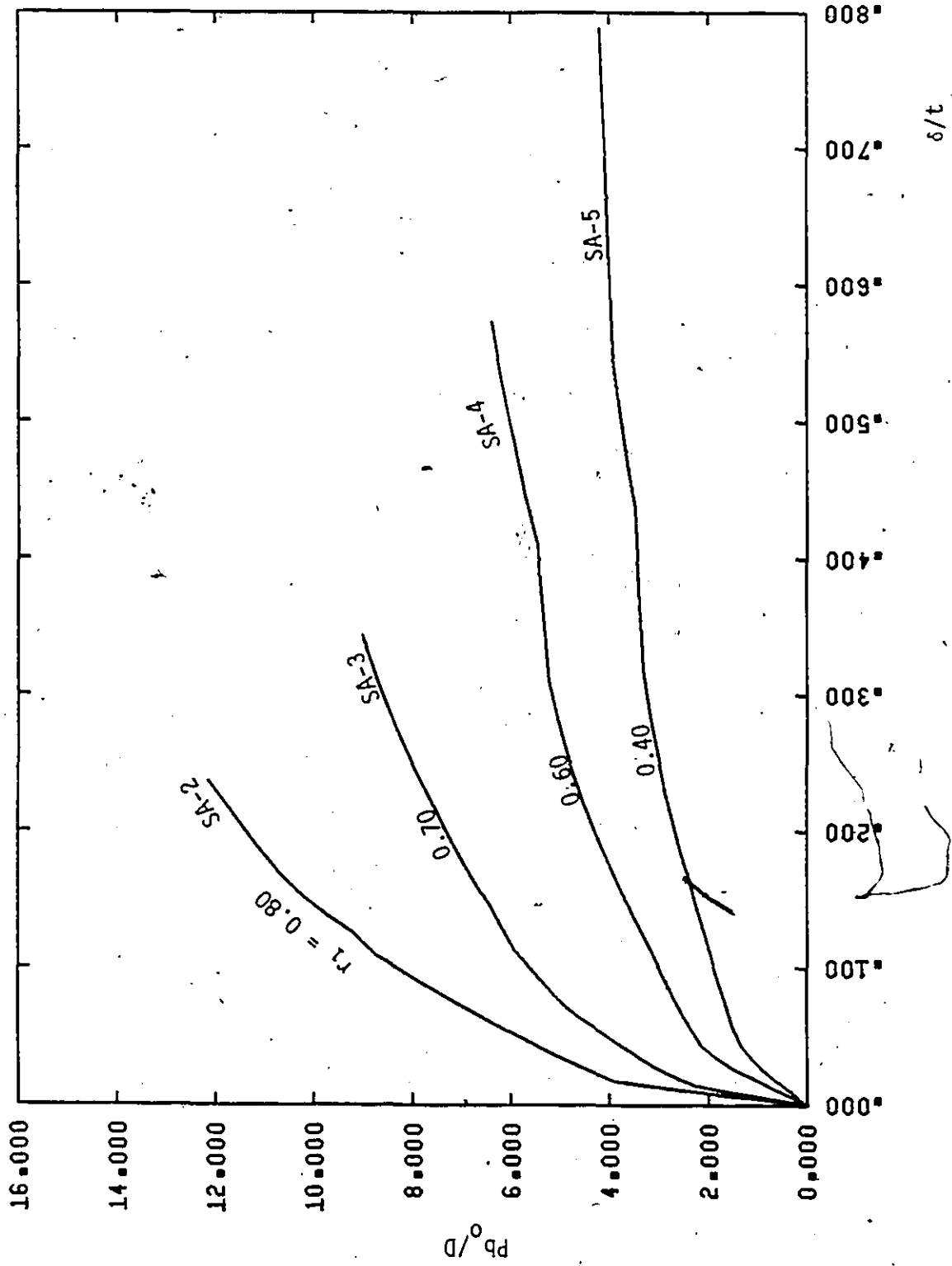
FIG. 6.7   VARIATION OF PARAMETER $r_1 = b_1/b_0$ (PUNCHING SHEAR)
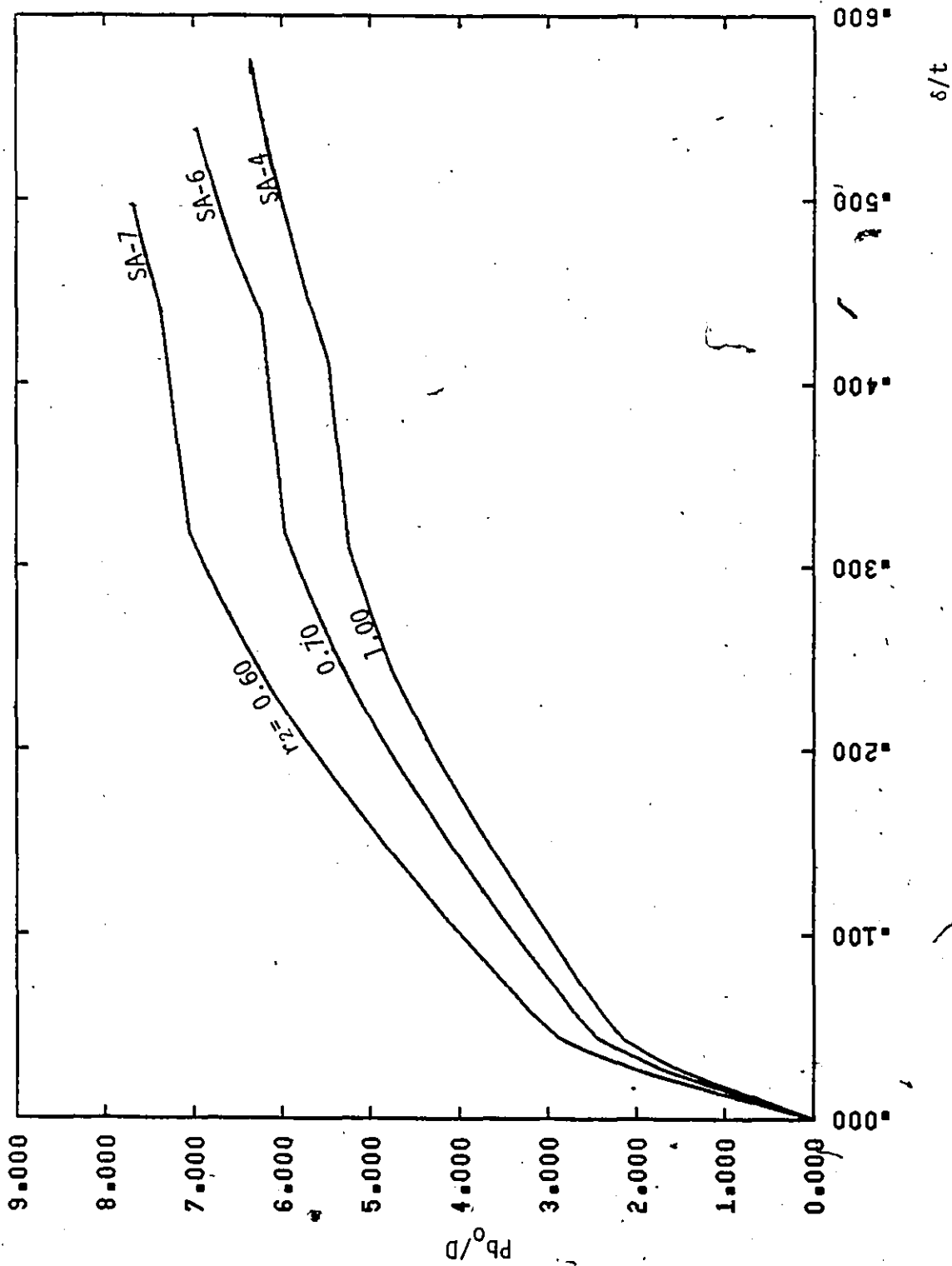
FIG. 6,8   VARIATION OF PARAMETER $r_2 = b_1/h_1$ (PUNCHING SHEAR)
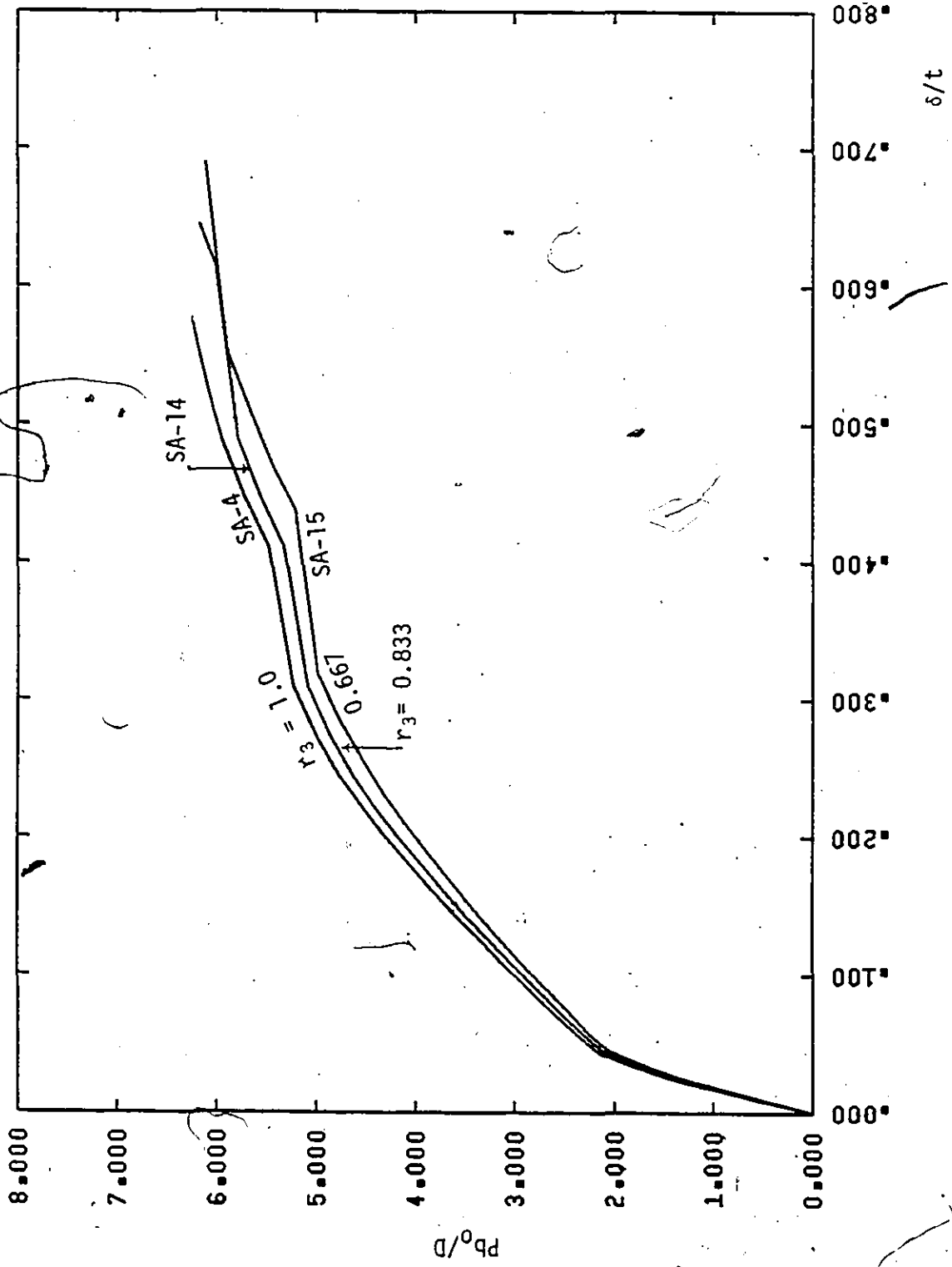
FIG. 6.9   VARIATION OF PARAMETER $r_3 = b_0/h_0$ (PUNCHING SHEAR)
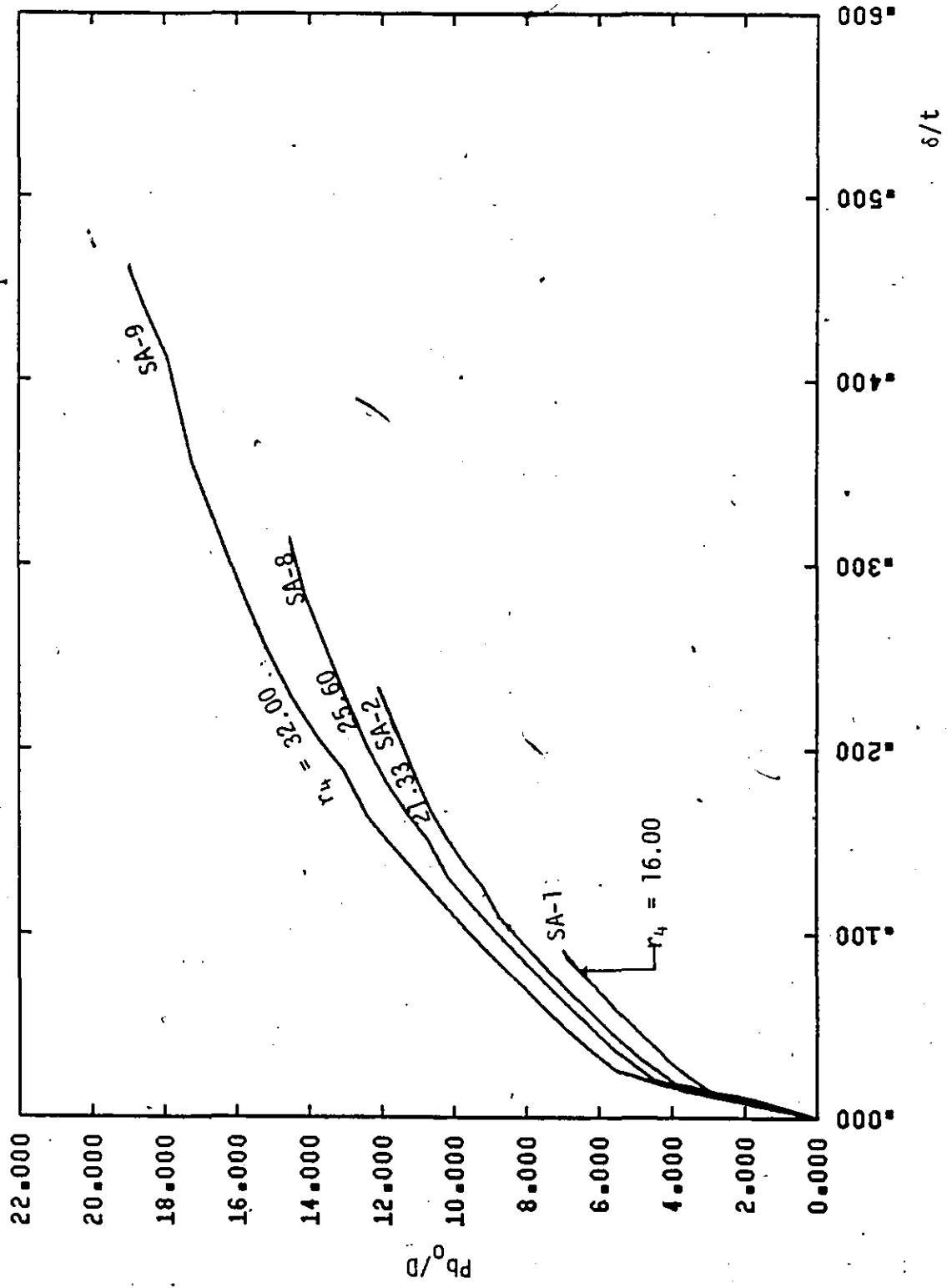
FIG. 6.10 VARIATION OF PARAMETER $r_4 = b_1/t_o$ (PUNCHING SHEAR)
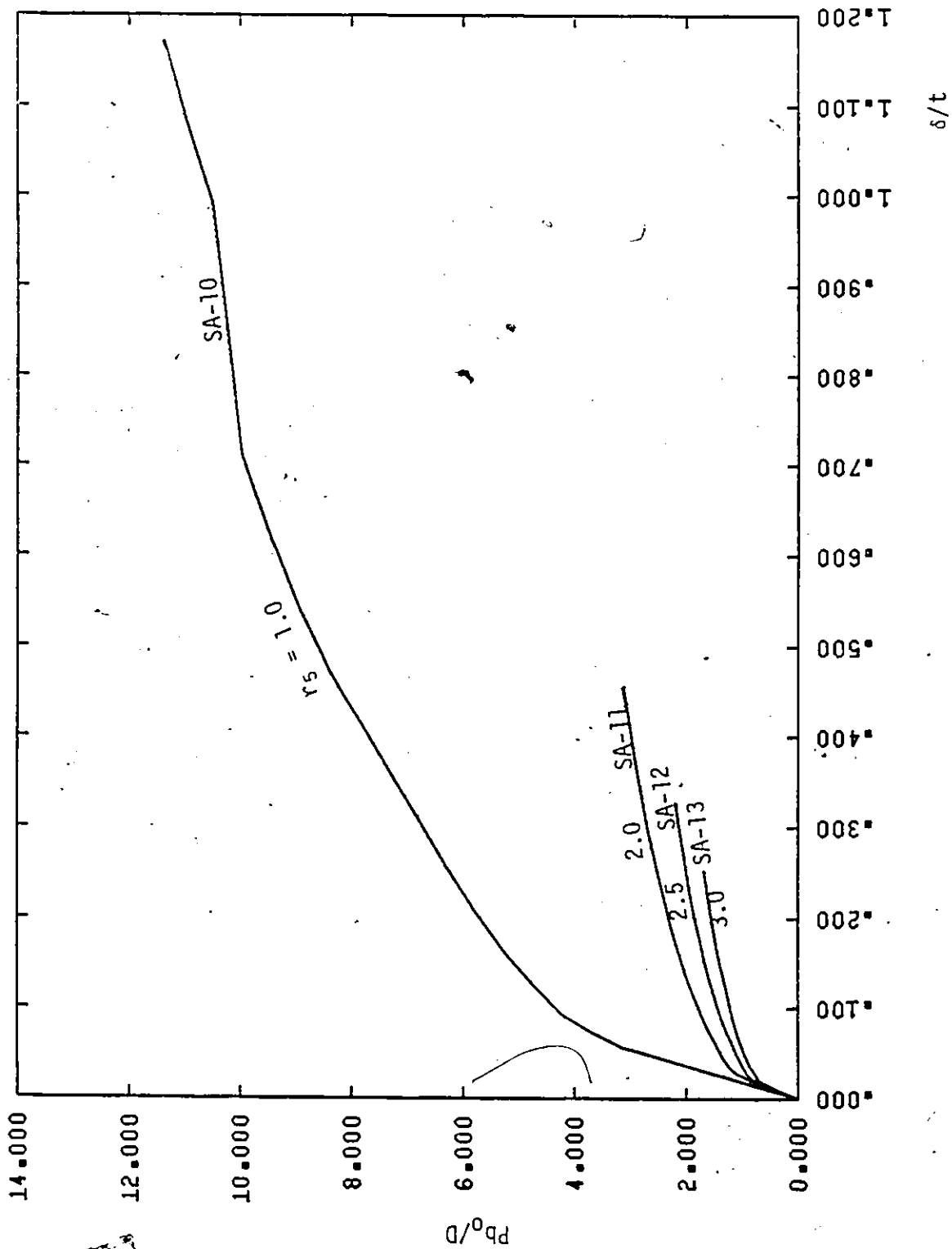
FIG. 6.11   VARIATION OF PARAMETER $r_5 = 1 + t_s/t_o$ (PUNCHING SHEAR)
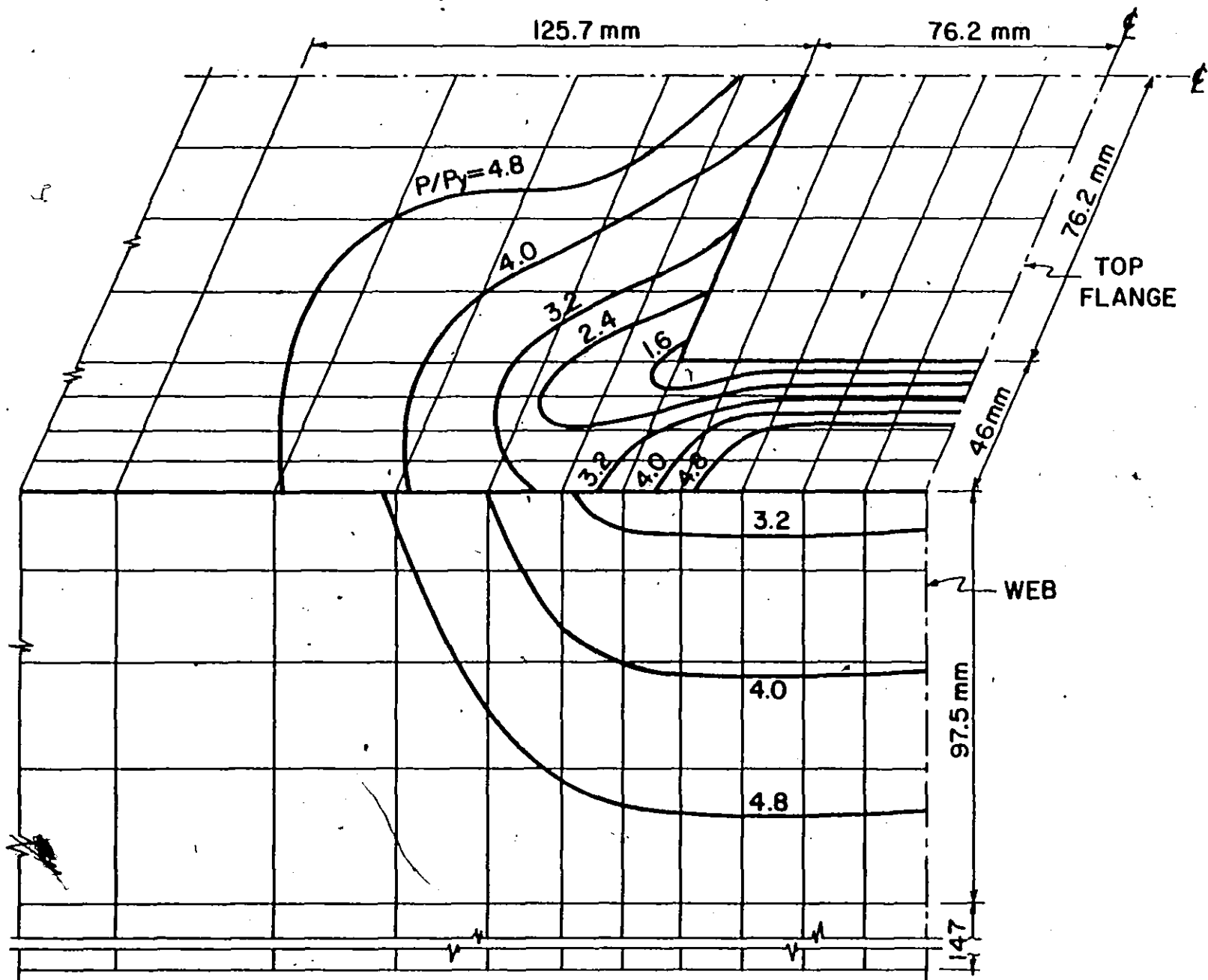
FIG. 6.12 PROGRESSION OF PLASTIC REGIONS IN JOINT SA-4
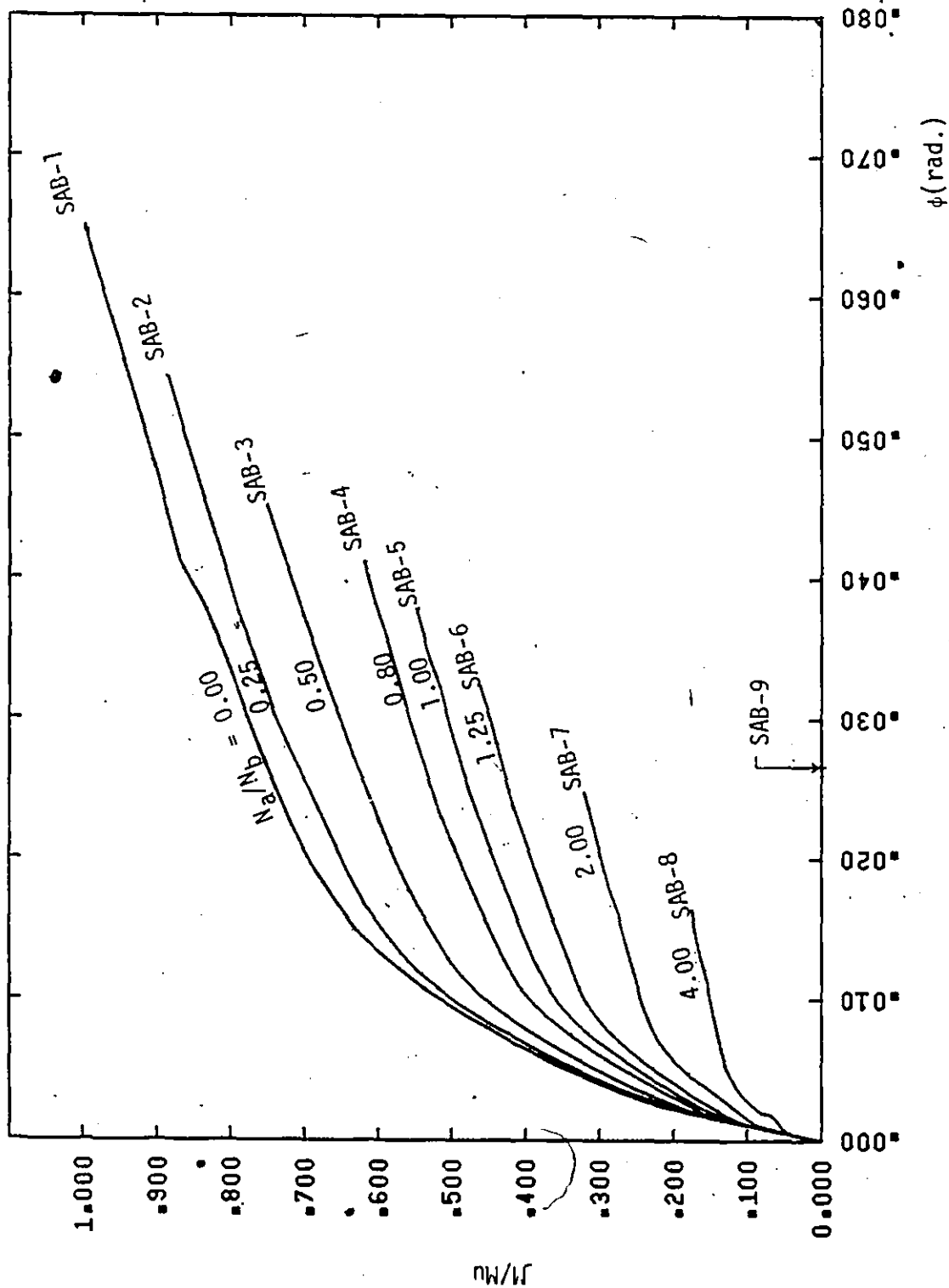
FIG. 6.13 NORMALIZED M-φ CURVES FOR SINGLE CHORD JOINTS UNDER COMBINED LOADING

$$\left(\frac{P_m}{P_u}\right)^{1.5} + \left(\frac{M_m}{M_u}\right)^{1.5} = 1.0$$

$$\frac{P_m}{P_u} + 0.54\frac{M_m}{M_u} = 1.0$$
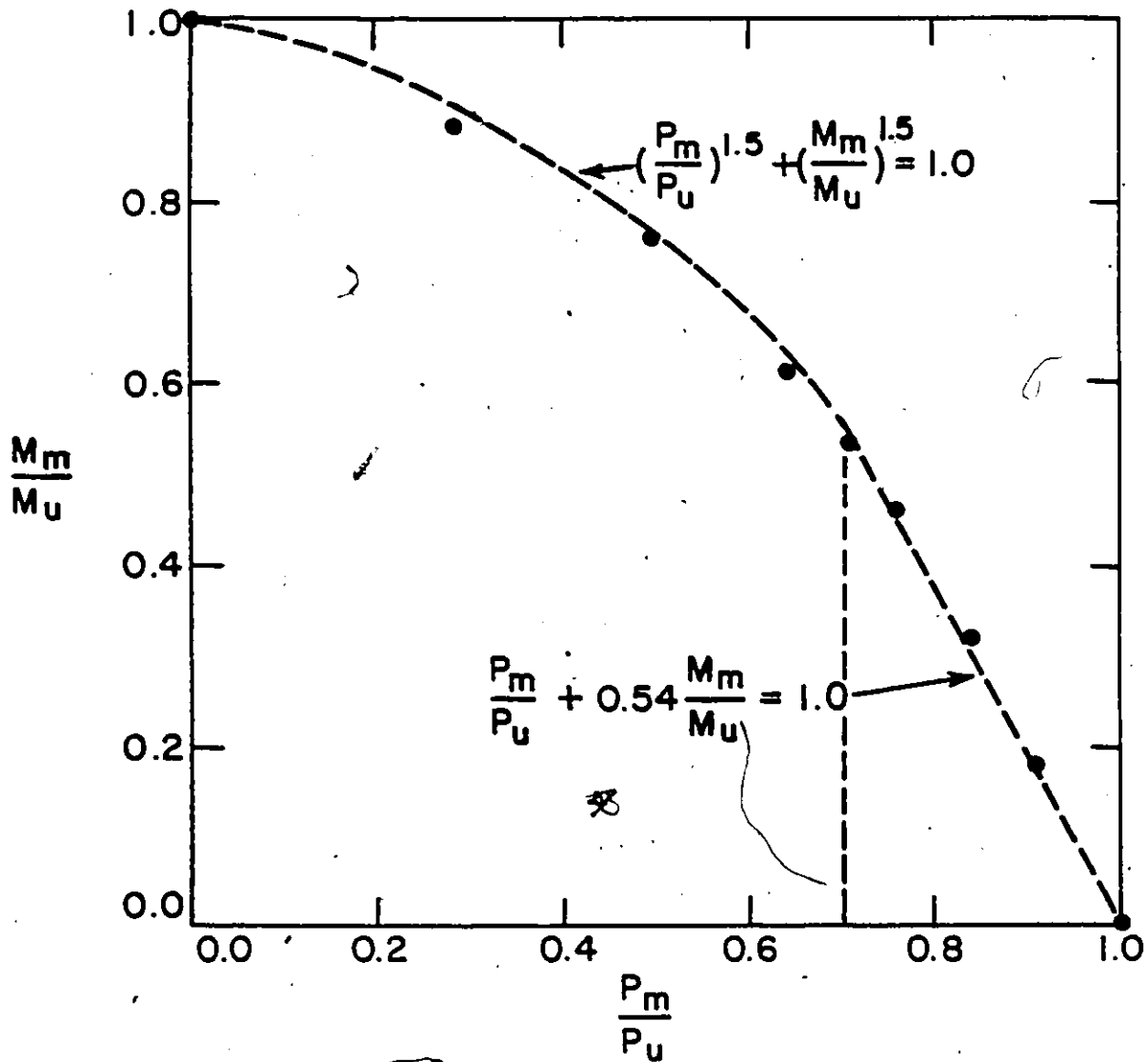
FIG. 6.14 INTERACTION ENVELOPE FOR SINGLE CHORD JOINTS

CHAPTER 7

STANDARDIZATION OF JOINT CHARACTERISTICS

7.1 . Introduction

The primary objective of this chapter is to develop analytical expressions describing the behaviour of the RHS T-joints in terms of their geometrical characteristics. Four sets of generalized expressions are developed; one for each of the two joint types (single or double chord) under either applied branch moment or punching shear. A curve-fitting technique is employed to derive non-dimensional load-deformation equations based on the parametric studies presented in Chapters 5 and 6. In addition, expressions for the joint stiffness and strength are obtained. Accuracy of the standardization formulae is tested against the earlier finite element results.

Furthermore, the joint behaviours, as predicted by the present analyses, are compared with experimental results and yield line solutions. The joint's stiffness and strength properties to be determined in the following sections will be incorporated into the analysis of single or double chord RHS Vierendeel trusses in Chapter 8.

7.2 Standardized Load-Deformation Curves

The standardization procedure involves the representation of the

load-deformation curves for all joints of a given type by a single function. The approach followed is somewhat similar to that reported in reference [20]. Considering joints under moment, this function is of the normalized form,

$$\phi = \sum_{i=1}^{\infty} C_i \left(\frac{RM}{D}\right)^i \qquad (7.1)$$

where ϕ, M and D are as defined earlier, C_i's are constants, and R is a dimensionless standardization factor dependent on the geometric parameters. The factor R is assumed to have the form

$$R = r_1^{a_1 + b_1 r_1} \cdot r_2^{a_2 + b_2 r_2} \cdots r_m^{a_m + b_m r_m} \qquad (7.2)$$

where r_j = the numerical value of the jth parameter; a_j and b_j are dimensionless constants which indicate the effect of the jth parameter on the moment-rotation relationship, while m is the total number of parameters. A linear exponent has been found to be the simplest function suitable for the problem at hand.

Since ϕ is an odd function of M/D, only terms involving odd powers of i appear in Equation 7.1. For this study, only three non-zero terms are included. Hence, Equation 7.1 takes the form

$$\phi = C_1 \left(\frac{RM}{D}\right) + C_2 \left(\frac{RM}{D}\right)^3 + C_3 \left(\frac{RM}{D}\right)^5. \qquad (7.3)$$

The factors a_j and b_j in Equation 7.2 can be evaluated by using a family of experimentally or analytically determined moment-rotation curves for joints for which all of the parameters are fixed except for one, as shown in Fig. 7.1. Suppose that a pair of curves, say 1 and 2, is selected. The relationship between normalized moments $(\frac{M}{D})_1$ and $(\frac{M}{D})_2$ for a fixed rotation φ is found from Equation 7.3 to be

$$\left(\frac{RM}{D}\right)^n_1 = \left(\frac{RM}{D}\right)^n_2, \quad n = 1, \ 3 \text{ and } 5. \tag{7.4}$$

Note that C_1, C_2 and C_3 are constant for all curves and only the $n = 1$ case need be considered for further manipulations. Substituting Equation 7.2 into Equation 7.4 and noting that only r_j varies, the following yields

$$r_{j1}^{(a_j + b_j r_{j1})} \left(\frac{M}{D}\right)_1 = r_{j2}^{(a_j + b_j r_{j2})} \left(\frac{M}{D}\right)_2 \tag{7.5}$$

where r_{j1} and r_{j2} are the numerical values of parameter r_j for joints 1 and 2, respectively.

Equation 7.5 can be rewritten in the form

$$a_j \ln(r_{j1}/r_{j2}) + b_j \ln\lfloor r_{j1}^{r_{j1}}/r_{j2}^{r_{j2}} \rfloor = \ln\lfloor \left(\frac{M}{D}\right)_2/\left(\frac{M}{D}\right)_1 \rfloor \tag{7.6}$$

which is a linear equation with two constants a_j and b_j. The derivation of Equation 7.6 is based on the assumption that only one parameter r_j varies. It was noted, however, in the parametric analyses presented in

Chapters 5 and 6 that the variation of parameter r_1 caused parameter r_4 to vary. As such, consider the case in which two parameters, one of which is dependent on the other, vary simultaneously. Suppose these two parameters are denoted by r_j and r_i, respectively, where r_j is dependent on r_i but not the reverse. Then Equation 7.6 is first used to calculate a_i and b_i. In order to determine the a_j and b_j values, Equation 7.4 gives

$$r_{i1}^{(a_i+b_i r_{i1})} \; r_{j1}^{(a_j+b_j r_{j1})} (\tfrac{M}{D})_1 = r_{i2}^{(a_i+b_i r_{i2})} \; r_{j2}^{(a_j+b_j r_{j2})} (\tfrac{M}{D})_2 \qquad (7.5a)$$

which can be rewritten in the form

$$a_j \ln(r_{j1}/r_{j2}) + b_j \ln\left[r_{j1}^{r_{j1}} / r_{j2}^{r_{j2}} \right] = \ln\left[(\tfrac{M}{D})_2 / (\tfrac{M}{D})_1 \right] + \ln p \qquad (7.6a)$$

where the value of p is known and is given by

$$p = r_{i2}^{(a_i+b_i r_{i2})} / r_{i1}^{(a_i+b_i r_{i1})} .$$

Therefore, the dependence of r_j or r_i only leads to a constant term (due to r_i) when determining the constants a_j and b_j. Equation 7.6 or 7.6a is used to calculate a_j and b_j values corresponding to several different rotations for each combination of analytical curves, such as 1 and 2, 1 and 3, 2 and 3, etc. The least squares curve fitting technique is then used to estimate the a_j and b_j values to be used in Equation 7.2.

The next step is to calculate the values of constants C_1, C_2 and C_3 in Equation 7.3 for each analytical curve again using the least square curve fitting technique. Finally the mean value of each constant is used in Equation 7.3 thus obtaining the standardized moment-rotation relationship for the particular joint type. Equation 7.3 may then be used to generate the moment-rotation curve for any joint configuration once the standardization factor R has been calculated from Equation 7.2.

The joint's tangential flexural stiffness J_T is defined as the slope of the $M - \phi$ curve. Hence from Equation 7.3,

$$J_T = \frac{dM}{d\phi} = (D/R)\left[C_1 + 3C_2 (\frac{RM}{D})^2 + 5C_3 (\frac{RM}{D})^4 \right]^{-1}. \qquad (7.7)$$

The elastic stiffness J_{EL} is obtained from Equation 7.7 when $M = 0$, i.e.

$$J_{EL} = D/(RC_1). \qquad (7.8)$$

Mathematically, the joint ultimate capacity M_u will be taken as that moment level at which the tangential stiffness becomes very small in comparison with the initial elastic stiffness. For a non-zero β (= J_T/J_{EL}), Equations 7.7 and 7.8 give

$$\left(\frac{1-\beta}{\beta}\right) C_1 - 3C_2 \left(\frac{RM_u}{D}\right)^2 - 5C_3 \left(\frac{RM_u}{D}\right)^4 = 0 \qquad (7.9)$$

which leads to the following unique real positive solution since C_1, C_2, C_3 and β are positive

$$M_u = \frac{D}{R} \left[\frac{-3C_2 + \sqrt{9C_2^2 + \frac{20(1-\beta)}{\beta} C_1 C_3}}{10\ C_3} \right]^{\frac{1}{2}} \qquad (7.10)$$

The joint capacity can be determined from Equation 7.10 for a given ratio for β. It should be noted that the solution for M_u in Equation 7.10 is based on a comparison of J_T with J_{EL} and not by taking $J_T = 0$.

In a similar manner, the standardized load-deflection curve for joints under punching shear is expressed as

$$\delta/t = \bar{C}_1 \left(\frac{\bar{R}b_o P}{D}\right) + \bar{C}_2 \left(\frac{\bar{R}b_o P}{D}\right)^3 + \bar{C}_3 \left(\frac{\bar{R}b_o P}{D}\right)^5 \qquad (7.11)$$

in which $\bar{R}$ is given by an expression similar to that for R. The quantities D/b_0 and t are used as normalizing factors for the punching shear P and deflection δ, respectively. Following the same procedure as outlined above for $M - \phi$ relationship, the joint tangential axial stiffness C_T is given by

$$C_T = \frac{dP}{d\delta} = (D/b_o \bar{R}) \left[\bar{C}_1 + 3\bar{C}_2 \left(\frac{\bar{R}b_o P}{D}\right)^2 + 5\bar{C}_3 \left(\frac{\bar{R}b_o P}{D}\right)^4 \right]^{-1} \qquad (7.12)$$

and the elastic stiffness C_{EL} by

$$C_{EL} = D/(b_o \bar{R} \bar{C}_1). \tag{7.13}$$

Consequently, the punching shear capacity P_u is given by the following expression

$$P_u = (\frac{D}{b_o \bar{R}})[\frac{-3\bar{C}_2 + \sqrt{9\bar{C}_2^2 + \frac{20(1-\bar{\beta})}{\bar{\beta}} \bar{C}_1 \bar{C}_3}}{10 \bar{C}_3}]^{\frac{1}{2}} \tag{7.14}$$

where $\bar{\beta} = C_T/C_{EL}$. Results of the parametric analyses were presented in Chapter 5 for double chord joints and in Chapter 6 for single chord joints. In each analysis, five non-dimensional geometric parameters, denoted r_1 to r_5, were considered. These were conceived to fully represent the joint configuration. It was found that all the parameters, except the chord aspect ratio r_3, have a significant effect on joint behaviour.

The forementioned standardization technique has been applied to both single and double chord RHS T-joints under either moment or punching shear. The formulas thus obtained for each joint type and loading are given in the following sections.

7.3   Generalized Formulae for Double Chord Joints Under Branch

Moment

The standardization procedure described in the preceeding sec-
tion has been applied to the analytical curves of Figs. 5.1 to 5.5.   The
resulting generalized moment-rotation curve is given by the following
equation

$$\phi = 0.617 \times 10^{-1}(\frac{RM}{D}) + 0.390 \times 10^3(\frac{RM}{D})^3 + 0.176$$

$$\times 10^6(\frac{RM}{D})^5 \tag{7.15}$$

where the standardization factor R is

$$R = r_1^{(-1.34+2.56r_1)} \; r_2^{(1.54+1.06r_2)} \; r_4^{(-1.58-0.0031r_4)}$$

$$\times \; r_5^{(2.75-0.13r_5)} . \tag{7.16}$$

Accuracy of the standardization procedure is illustrated in
Figs. 7.2 to 7.5, which show the normalized moment-rotation curves
generated by Equation 7.15 and the corresponding analytically obtained
curves reproduced from Figs. 5.1, 5.2, 5.4 and 5.5.   With few excep-
tions, the generalized formula was found to produce accurate moment-
rotation curves for analyzed connections.

In order to calculate the joint moment capacity (Equation 7.10), it is necessary to first define the corresponding relative tangential stiffness as given by the β ratio. Based on analytical results (see last column of Table 5.2) and available experimental data, the β ratio was taken as 0.015. Substituting this β ratio and C_1 to C_3 values from Equation 7.15 into Equation 7.10, the following expression for the joint moment capacity M_u is obtained.

$$M_u = 0.039 \frac{D}{R}. \tag{7.17}$$

The standardization factor R appears in Equation 7.17 and should be calculated by virtue of Equation 7.16 for the given joint configuration. In many instances, one or more parameters in Equation 7.16 become equal to unity and the computational effort in calculating R reduces. For example, both r_2 and r_5 are equal to unity for an unstiffened joint with a square branch member.

To test the validity of Equation 7.17, theoretical moment capacities of a number of joints were computed for which experimental capacities are known. Details and results of the four moment specimens, tested as part of this research program, have been reported in Chapter 4. All four specimens had their two chord members welded together at top and bottom edges along the central 305 mm. to simmulate the theoretical model used to derive the theoretical moment-rotation curves. A comparison between the theoretical capacities, M_u, adjusted to the actual chord yield strength, and the experimental values, $\bar{M}_u$, is presen-

ted in Table 7.1. The theoretical capacities obtained from Equation 7.17 are based on a 350 MPa chord yield strength. These values have been multiplied by the ratio between the actual and nominal yield strengths of the chord, assuming a linear variation in the vicinity of the nominal yield. Reasonable agreement was found between theoretical and experimental capacities as noted from Table 7.1.

Chidiac and Korol [7] reported test results of four T-joints using the same test apparatus shown in Fig. 4.2. Details and results of the tests are presented in Table 7.2. Specimens with similar geometries (T-1 and T-2 or T-3 and T-4) were identical except for chord member connecting welds both top and bottom.

The experimental moment capacities, $\bar{M}_u$, of the four specimens are compared with adjusted thoeretical values M_u in Table 7.3. It should be noted that specimens T-3 and T-4 failed due to branch flange buckling [7]. As such, results of these two specimens should be excluded when the validity of Equation 7.17 is examined. The theoretical capacity of joint T-1 was considerably higher than the experimental value due to an absence of chord welds in the tested joint.

Considering the results of joints M-1 to M-4 and T-2, the following expression relating the theoretical strength to the experimental strength is obtained.

$$M_u = 0.98 \,\bar{M}_u \pm 0.09 \,\bar{M}_u \qquad (7.18)$$

where the last term represents the standard deviation value. Examination of the theory has been based on very limited experimental data and is not conclusive. However, the correlation indicated by Equation 7.18 is satisfactory for design purposes. Graphical representation of Equation 7.17 and experimental capacities is given in Fig. 7.6 by a logarithmic plot.

A yield line solution for the joint strength has been outlined in section 5.5. Comparison of the yield line strength, M_u^*, with the theoretical strength, M_u, is presented in Table 7.4 for the analyzed joints DB-1 to DB-11. The two solutions correlate according to the following expression

$$M_u = 0.82 \ M_u^* \pm 0.08 \ M_u^* \qquad\qquad (7.19)$$

The yield line solution consistently predicts higher capacities but the discrepancy between the two solutions is relatively small as indicated by the standard deviation in Equation 7.19. Hence, the yield line solution given by Equation 5.8 can be used to predict the joint capacity after applying an appropriate scaling factor.

Further examination of the standardization equations presented in this section will be given in Chapter 8.

7.4   Generalized Formulae for Double Chord Joints Under Punching

Shear

The curve fitting procedure described in Section 7.2 was applied

again to the analytical load-deflection curves of Figs. 5.7 to 5.11 and

the following generalized equation was obtained

$$\delta/t = 0.123 \left(\frac{\bar{R}b_o P}{D}\right) + 0.982 \times 10^2 \left(\frac{\bar{R}b_o P}{D}\right)^3 + 0.516$$

$$\times 10^4 \left(\frac{\bar{R}b_o P}{D}\right)^5 \qquad \qquad (7.20)$$

where the standardization factor $\bar{R}$ is given as

$$\bar{R} = r_1^{(-0.14+2.38r_1)} \; r_2^{(0.12+1.26r_2)} \; r_4^{(-1.35-0.0031r_4)}$$

$$\times \; r_5^{(2.50-0.053r_5)} \qquad \qquad (7.21)$$

Accuracy of the standardization procedure is illustrated in

Figs. 7.7 to 7.10, which identifies the normalized load-deflection

curves generated by Equation 7.20 and the corresponding anaytically

obtained curves of Figs. 5.7, 5.8, 5.10 and 5.11. It can be seen that,

with few exceptions, correlation between generated and computed curves

is excellent.

The joint punching shear capacity is calculated using Equation 7.14 by substituting for $\bar{C}_1$, C_2 and $\bar{C}_3$ as given in Equation 7.20 and a small value for the $\bar{\beta}$ ratio. The following expression for the punching shear capacity P_u is obtained.

$$P_u = 0.150 \frac{D}{b_o \bar{R}} \tag{7.22}$$

The standardization factor $\bar{R}$ appears in Equation 7.22 and should be calculated from Equation 7.21 for the given joint configuration.

The theoretical joint capacities predicted by Equation 7.22 will now be compared with the experimental values for the punching shear tests reported in chapter 4. Details and results of the six test specimens are presented in Table 4.2. Since the analysis is based on a 305 mm inter-chord weld length, the results for specimens A-2, A-4, A-5 and A-6 only shall be considered in the comparison.

The capacities for the tested six joints are listed in Table 7.5. It is seen that the experimental ultimate loads of joints A-1 and A-3 are considerably lower than the predicted values. The theoretical capacities P_u for the other four specimens fall about evenly above and below the experimental capacities $\bar{P}_u$. The following relationship between P_u and $\bar{P}_u$ can be obtained from results of the latter four specimens

$$P_u = 1.02 \ \bar{P}_u \pm 0.14 \ \bar{P}_u \qquad\qquad (7.23)$$

where the last term represents the standard deviation value. The above comparison has been based on a small number of tests conducted as part of this research program. Hence, more experimental data is necessary to test the validity of Equation 7.22 more thoroughly. Graphical representation of Equation 7.22 and experimental load limit values are given in Fig. 7.11 by a logarithmic plot.

A yield line solution for the joint strength was developed in Section 5.6. Comparison of the yield line strength P_u^* with the theoretical strength P_u is presented in Table 7.6. Based on the results for the analyzed joints DA-1 to DA-11, the two solutions are found to correlate according to the following expression

$$P_u = 0.91 \ P_u^* \pm 0.04 \ P_u^* \qquad\qquad (7.24)$$

The yield line solution consistently predicts higher capacities but the discrepancy between the two solutions is small as indicated by the standard deviation in Equation 7.24. As such, Equation 5.15 can be used to predict the joint capacity provided that an appropriate scaling factor is applied.

In almost all practical situations, the joint will be subjected to both punching shear and moment. The behaviour of double chord joints under combined loading has been discussed in Section 5.4. The interac-

tion Equations 5.1 or 5.2 may be employed to calculate the reduced punching shear capacity P_m due to the presence of applied moment M_m, and vice-versa.

7.5   Generalized Formulae for Single Chord Joints Under Branch Moment

Results of the parametric analysis of single chord T-joints under moment were presented in Section 6.2. It was concluded that all geometric parameters considered in the analysis, with the exception of the chord aspect ratio r_3, have a significant effect on a joint's behaviour. In order to generalize the joint characteristics, the standardization procedure of Section 7.2 was applied to the analytical moment-rotation curves of Figs. 6.1 to 6.5. The generalized moment-rotation curve was found to be given by the following equation

$$\phi = 0.251 \times 10^{-2}(\frac{RM}{D}) + 0.465 \times 10^{-3}(\frac{RM}{D})^3 + 0.442$$

$$\times 10^{-4} (\frac{RM}{D})^5 \qquad\qquad (7.25)$$

while the standardization factor R is in the form

$$R = r_1^{(0.27-7.77r_1)} \; r_2^{(0.95-0.086r_2)} \; r_4^{(-0.45-0.0022r_4)}$$

$$\times \; r_5^{(1.56-0.094r_5)} \qquad\qquad (7.26)$$

A comparison between the moment-rotation curves generated by Equations 7.25 and 7.26 and the corresponding analytical curves is illustrated in Figs. 7.12 to 7.15 for the joints analyzed in Section 6.2. It can be concluded that Equation 7.25 is capable of generating the moment-rotation curves of analyzed joints with a good degree of accuracy.

An expression for the joint moment capacity is obtained from Equation 7.10 by substituting a small value for the β ratio (~ 0.004) and the values of C_1 to C_3 from Equation 7.25. The following expression for M_u is obtained:

$$M_u = 7.0 \frac{D}{R} \qquad (7.27)$$

It may be mentioned that the R factor as given in Equation 7.27 can be calculated for a given joint configuration very simply. Usually, one or more of the r parameters will be equal to unity which reduces computation. For example, an unreinforced connection with a square branch will have both r_2 and r_5 equal to unity.

The theoretical joint capacity as predicted by Equation 7.27 will now be compared with some of the available experimental data. Korol et al. [1] have reported the results of a number of tests on unequal width connections of square hollow sections. Details of the six unreinforced joint tests are given in Table 7.7. Also given are the R factors as calculated by Equation 7.26 and the flexural rigidities D of

the chord flanges. The experimental and theoretical joint capacities are compared in Table 7.8. The last column of the table gives the ratio of predicted to experimental moment capacity $(\frac{M_u}{\bar{M}_u})$ for each joint, where the theoretical value is calculated at the actual chord yield strength. It may be observed that the theoretical moment capacities agree closely with experimental values. As for the connections reinforced by a chord member top flange stiffener and reported in reference [1], direct comparison could not be made. The reason is that the stiffening plates in the tests had considerably different h_s/h_1 and b_s/b_1 ratios compared with those used in the parametric analysis defined in Section 6.1.

Table 7.9 gives the details of 16 specimens with square or rectangular branches tested by Kanatani et al. [14]. Table 7.10 shows the comparison between experimental and theoretical capacities, with the latter adjusted to the actual yield strength of the chord members. It can be noted that, with few exceptions, reasonable agreement exists.

Details of four joints tested by Redwood [2] are given in Table 7.11. The theoretical and test results for these joints are compared in Table 7.12.

For all of the 26 tests compared above, the predicted joint capacity M_u is linked to the experimental capacity $\bar{M}_u$ as follows

$$M_u = 1.00 \, \bar{M}_u \pm 0.16 \, \bar{M}_u. \tag{7.28}$$

Although the mean values of the predicted and experimental capacities are identical, a considerable scatter exists, as indicated by the last term of Equation 7.28. The discrepancy may be attributed to the inability of the model to accurately simulate the actual boundary conditions of the test setups. Furthermore, both residual stresses and large deformations have not been considered in the theoretical model of the joint. It is known that the joint undergoes considerable deformations prior to reaching its load limit.

However, the degree of accuracy indicated by Equation 7.28 is considered adequate for design purposes after applying an appropriate factor of safety to the predicted capacities given by Equation 7.27.

Equation 7.27 and experimental results for the 26 specimens can be represented graphically on a logarithmic plot as shown in Fig. 7.16. It may be observed that experimental capacities are about evenly distributed on both sides of the theoretical line.

From the foregoing discussion, it may be concluded that the generalized expressions for the joint characteristics provide a valid basis for assessment and design of these joints. Further examination of the theoretical results will be presented in Chapter 8.

7.6   Generalized Formulae for Single Chord Joints Under Punching Shear

A parametric analysis of single chord joints under punching shear was described in Section 6.3. Results of that analysis indicated that all geometric parameters considered, except the chord aspect ratio r_3, have a significant influence on behaviour. The standardization procedure described in Section 7.2 was employed to develop analytical expressions for the joint characteristics. By applying this procedure to the analytical curves of Figs. 6.7 to 6.11, the following relationship between punching shear and deflection is obtained

$$\delta/t = 0.678 \times 10^{-2} \left(\frac{\bar{R}b_oP}{D}\right) + 0.211 \times 10^{-3} \left(\frac{\bar{R}b_oP}{D}\right)^3$$

$$+ 0.135 \times 10^{-6}\left(\frac{\bar{R}b_oP}{D}\right)^5 \qquad (7.29)$$

where the standardization factor $\bar{R}$ is defined by

$$\bar{R} = r_1^{(0.067-6.62r_1)} \; r_2^{(1.17-1.05r_2)} \; r_4^{(-0.50+0.0008r_4)}$$

$$\times \; r_5^{(1.58-0.13r_5)} \qquad (7.30)$$

Equations 7.29 and 7.30 can be used to generate the load-deflection curve for a single chord joint of given configuration. The genera-

ted curves are in reasonably close agreement with the fitted curves as demonstrated in Figs. 7.17 to 7.20, where generated and computed curves for the fifteen joints, analyzed in Section 6.3, are compared.

Substituting the $\bar{C}$ values given in Equation 7.29 and a small value for the $\bar{\beta}$ ratio into Equation 7.14, the following expression is obtained for the joint capacity.

$$P_u = 16.0 \frac{D}{b_o \bar{R}} \qquad (7.31)$$

In order to gain confidence in the theoretical expressions given by Equations 7.29 to 7.31, the predicted joint capacity will be compared with experimental data. Details of thirteen joints reported in three separate experimental investigations are listed in Table 7.13. Also given are the $\bar{R}$ factors as calculated by Equation 7.30 and the flexural rigidities D of the chord flange. Experimental and theoretical joint capacities. are given in Table 7.14. Comparison between the predicted capacities, adjusted to the actual chord yield strength, and experimental values are shown in the last column. For all joints, correlation between predicted values P_u and experimental values $\bar{P}_u$ is given by the following relationship.

$$P_u = 0.98 \, \bar{P}_u \pm 0.12 \, \bar{P}_u \qquad (7.32)$$

The somewhat high discrepancy indicated by the last term of Equation

7.32 may be attributed to the same reasons given for the moment connections in the preceeding section. This degree of accuracy is, however, considered adequate for design purposes.

Equation 7.31 can be represented by a straight line on an R vs. $\frac{b_o P_u}{D}$ logarithmic plot as shown in Fig. 7.21. Experimental results are plotted as well on the same figure for comparison.

The preceding examination of the theoretical expressions developed herein suggests that they provide a valid basis for assessment and design of single chord RHS T-joints for which failure is governed by the strength of the chord's top flange. According to reference [14], this is the failure mode for all joints with width of branch members less than or equal to the flat width of the chord's mated flange, except for premature weld failure.

In almost all practical situations, the joint will be subjected to both punching shear and moment. The behaviour of single chord joints under combined loading has been discussed in section 6.4. The interaction Equations 6.1 or 6.2 may be employed to calculate the reduced punching shear capacity P_m due to the presence of applied moment M_m, and vice-versa.

TABLE 7.1   COMPARISON BETWEEN EXPERIMENTAL AND THEORETICAL MOMENT CAPACITIES FOR DOUBLE CHORD JOINTS

Specimen No.[a]	$R \times 10^{-2}$	D (KN-m)	M_u (KN-m)	$\overline{M}_u$[b] (KN-m)	$\dfrac{M_u}{\overline{M}_u}$
M-1	1.137	15.827	67.9	76.0	0.89
M-2	0.1612	4.688	97.9	107.3	0.91
M-3	0.5808	15.827	119.4	107.5	1.11
M-4	0.5593	15.827	124.0	125.8	0.99

(a)   See Table 4.1

(b)   "   "   4.3

TABLE 7.2   DETAILS AND RESULTS OF DOUBLE CHORD JOINTS TESTED BY CHIDIAC [7]

Specimen No.	Chord Member 2 RHS (mm)	Branch Member RHS (mm)	$b_1/2b_0$	b_1/h_1	b_1/t_0	Chord Yield Strength (MPa)	Ultimate Moment $\bar{M}_u$ (KN-m)	Weld Length Between Chords (mm)
T-1	152.4×152.4×6.35	254.0×152.4×7.13	0.500	0.600	24	370	87.0	-
T-2	152.4×152.4×6.35	254.0×152.4×7.13	0.500	0.600	24	347	102.0	305
T-3	152.4×152.4×6.35	177.8×127.0×4.78	0.417	0.714	20	377	50.8[a]	-
T-4	152.4×152.4×6.35	177.8×127.0×4.78	0.417	0.714	20	352	56.7[a]	305

(a)   Joints T-3 and T-4 failed due to branch flange buckling.

TABLE 7.3 COMPARISON BETWEEN EXPERIMENTAL [7] AND THEORETICAL MOMENT
CAPACITIES FOR DOUBLE CHORD T-JOINTS

Specimen No.	$R \times 10^{-2}$	D (KN-m)	M_u (KN-m)	$\bar{M}_u$ (KN-m)	$\dfrac{M_u}{\bar{M}_u}$
T-1	0.1786	4.688	108.2	87.0	1.24
T-2	0.1786	4.688	101.5	·102.0	1.00
T-3	0.4277	4.688	46.0	50.8	0.91
T-4	0.4277	4.688	43.0	56.7	0.76

TABLE 7.4   COMPARISON BETWEEN YIELD LINE AND THEORETICAL RESULTS FOR
DOUBLE CHORD T-JOINTS UNDER BRANCH MOMENT

Joint No.[a]	$R \times 10^{-2}$	M_u/D	$M_u^{\star}$[b] (KN-m)	$M_u^{\star}/D$	$\dfrac{M_u}{M_u^{\star}}$
DB-1	0.1612	24.19	133.7	28.52	0.85
DB-2	0.2558	15.25	83.6	17.83	0.86
DB-3	0.3565	10.94	66.4	14.16	0.77
DB-4	0.5428	7.18	51.9	11.07	0.65
DB-5	0.2773	14.06	80.9	17.26	0.81
DB-6	0.1786	21.84	116.2	24.79	0.88
DB-7	0.2558	15.25	83.6	17.83	0.86
DB-8	0.2558	15.25	83.6	17.83	0.86
DB-9	0.1394	27.98	57.9	29.27	0.96
DB-10	0.3969	9.83	112.1	12.24	0.80
DB-11	0.5593	6.97	143.4	9.09	0.77
DB-12	2.002	1.95	–	–	–
DB-13	3.288	1.19	–	–	–
DB-14	4.764	0.82	–	–	–

(a)   See Table 5.1

(b)   See Table 5.6

TABLE 7.5   COMPARISON BETWEEN EXPERIMENTAL AND THEORETICAL PUNCHING
SHEAR CAPACITIES FOR DOUBLE CHORD JOINTS

Specimen No. (a)	$\bar{R} \times 10^{-2}$	D (KN-m)	P_u (KN)	$\bar{P}_u$ (b) (KN)	$\dfrac{P_u}{\bar{P}_u}$
A-1	0.9969	15.827	1944	1412	1.38
A-2	0.9969	15.827	1806	1637	1.10
A-3	0.3845	4.688	1065	858	1.24
A-4	0.3845	4.688	1065	1255	0.85
A-5	0.3109	4.688	1771	1528	1.16
A-6	0.3664	4.688	1407	1465	0.96

(a) See Table 4.2

(b)   "   "   4.4

TABLE 7.6   COMPARISON BETWEEN YIELD LINE AND THEORETICAL RESULTS FOR DOUBLE CHORD T-JOINTS UNDER PUNCHING SHEAR

Joint No. (a)	$R \times 10^{-2}$	$\dfrac{P_u b_o}{D}$	P_u^*(b) (KN)	$\dfrac{P_u^* b_o}{D}$	$\dfrac{P_u}{P_u^*}$
DA-1	0.3155	44.37	1600	52.01	0.85
DA-2	0.3707	37.77	1254	40.77	0.93
DA-3	0.4290	32.63	1119	36.38	0.90
DA-4	0.5263	26.60	991	32.22	0.83
DA-5	0.3874	36.14	1227	39.89	0.91
DA-6	0.3364	41.62	1462	47.53	0.88
DA-7	0.3707	37.77	1254	40.77	0.93
DA-8	0.3707	37.77	1254	40.77	0.93
DA-9	0.2168	64.58	897	69.11	0.93
DA-10	0.5447	25.70	1636	27.23	0.94
DA-11	0.7348	19.05	2043	19.67	0.97
DA-12	2.255	6.21	–	–	–
DA-13	37558	3.73	–	–	–
DA-14	5.615	2.49	–	–	–

(a)   See Table 5.1

(b)   See Table 5.7

TABLE 7.7   DETAILS OF MOMENT CONNECTIONS TESTED BY KOROL ET AL. [1]

Specimen No.	Chord RHS $(h_0 \times b_0 \times t_0)$ (mm)	Branch RHS $(h_1 \times b_1 \times t_1)$ (mm)	r_1	r_2	r_4	R	D (KN-m)
1	152.4×152.4×4.76	127.0×127.0×6.35	0.833	1.0	26.67	0.5835	1.978
2(P)	152.4×152.4×4.76	127.0×127.0×6.35	0.833	1.0	26.67	0.5835	1.978
3	254.0×254.0×9.53	152.4×152.4×4.76	0.600	1.0	16.00	2.455	15.827
4(P)	254.0×254.0×9.53	152.4×152.4×4.76	0.600	1.0	16.00	2.455	15.827
5	152.4×152.4×6.35	127.0×127.0×6.35	0.833	1.0	20.00	0.7058	4.688
6(P)	152.4×152.4×6.35	127.0×127.0×6.35	0.833	1.0	20.00	0.7058	4.688

Notes: 1.   (P) = prepared butt weld (other specimens fillet welded)

2.   Failure mode in all tests was chord flange yielding.

TABLE 7.8 COMPARISON BETWEEN EXPERIMENTAL (KOROL ET AL.) AND THEORETICAL RESULTS

Specimen No.	Experimental			Theoretical		$M_u/\bar{M}_u$
	Chord Yield Strength σ_Y(MPa)	Ultimate Moment $\bar{M}_u$(KN-m)	$\bar{M}_u/D$	Ultimate Moment M_u(KN-m)	M_u/D	
1	396.4	28.7	14.51	26.9	13.60	0.94
2(P)	390.2	25.2	12.74	26.5	13.38	1.05
3	405.5	50.5	3.19	52.3	3.30	1.04
4(P)	410.9	55.4	3.50	53.0	3.35	0.96
5	369.6	45.4	9.68	49.1	10.51	1.08
6(P)	363.4	47.3	10.09	48.3	10.30	1.02

TABLE 7.9   DETAILS OF MOMENT CONNECTIONS TESTED BY KANATANI ET AL. [14]

Specimen No.	Chord RHS $(h_o \times b_o \times t_o)$ (mm)	Branch RHS $(h_1 \times b_1 \times t_1)$ (mm)	r_1	r_2	r_4	R	D (KN-m)
S1		100×100×2.3	0.500		16.67	3.016	
S2		100×100×6.0	0.500		16.67	3.016	
S3	200×200×6.0	125×125×3.2	0.625	1.0	20.83	1.915	3.956
S4		125×125×6.0	0.625		20.83	1.915	
S5		150×150×4.5	0.750		25.00	0.9736	
S9		100×100×6.0	0.500		11.11	3.909	
S11	200×200×9.0	125×125×6.0	0.625	1.0	13.89	2.438	13.352
S13		175×175×6.0	0.875		19.44	1.145	
S15	200×200×12.0	100×100×6.0	0.500	1.0	8.33	5.984	31.648
S21	150×150×6.0	100×100×6.0	0.667	1.0	16.67	1.859	3.956
R3		203×152×6.4	0.760	0.749	25.33	0.7089	
R4	200×200×6.0	254×152×6.4	0.760	0.598	25.33	0.5764	3.956
R5		350×150×6.0	0.750	0.429	25.00	0.4496	
R7		203×152×6.4	0.76	0.749	16.89	0.9169	
R8	200×200×9.0	254×152×6.4	0.76	0.598	16.89	0.7468	13.352
R9		350×150×6.0	0.75	0.429	16.67	0.5729	

Note: Failure mode of all joints, except S13, R7, R8 and R9, was chord flange yielding. Failure mode of joints S13, R7, R8 and R9 was weld fracture.

TABLE 7.10 COMPARISON BETWEEN EXPERIMENTAL (KANATANI ET AL.) AND THEORETICAL RESULTS.

Specimen No.	Experimental			Theoretical		$\dfrac{M_u}{\bar{M}_u}$
	Chord Yield Strength σ_Y(MPa)	Ultimate Moment $\bar{M}_u$(KN-m)	$\bar{M}_u/D$	Ultimate Moment M_u(KN-m)	M_u/D	
S1		11.1	2.81	10:1	2.54	0.91
S2		14.1	3.56	10.1	2.54	0.72
S3	383	17.8	4.50	15.8	4.00	0.89
S4		21.2	5.36	15.8	4.00	0.75
S5		34.4	8.70	31.1	7.87	0.90
S9		30.4	2.28	23.2	1.74	0.76
S11	340	39.3	2.94	37.2	2.79	0.95
S13		66.7	5.00	79.3	5.94	1.19
S15	378	31.8	1.00	40.0	1.26	1.26
S21	392	19.8	5.01	16.7	4.22	0.84
R3		41.4	10.47	42.7	10.81	1.03
R4	383	49.9	12.61	52.6	13.29	1.05
R5		70.3	17.77	67.4	17.04	0.96
R7		85.2	6:38	99.0	7.42	1.16
R8	340	125.4	9.39	121.6	9.11	0.97
R9		163.2	12.22	158.5	11.87	0.97

TABLE 7.11   DETAILS OF MOMENT CONNECTIONS TESTED BY REDWOOD [2]

Specimen No.	Chord RHS $(h_0 \times b_0 \times t_0)$ (mm)	Branch RHS $(h_1 \times b_1 \times t_1)$ (mm)	r_1	r_2	r_4	R	D (KN-m)
1		88.9×88.9×4.94	0.700	1.0	18.67	1.501	
2		69.9×69.9×4.18	0.550	1.0	14.67	3.000	1.978
3	127.0×127.0×4.76	63.5×63.5×4.18	0.500	1.0	13.33	3.540	
4		47.6×47.6×4.18	0.375	1.0	10.00	4.510	

TABLE 7.12   COMPARISON BETWEEN EXPERIMENTAL (REDWOOD) AND THEORETICAL RESULTS

Specimen No.	Experimental			Theoretical		$\dfrac{M_u}{\bar{M}_u}$
	Chord Yield Strength σ_Y(MPa)	Ultimate Moment $\bar{M}_u$(KN-m)	$\bar{M}_u/D$	Ultimate Moment M_u(KN-m)	M_u/D	
1		6.83	3.45	6.54	3.31	0.96
2	248.2	2.89	1.46	3.27	1.65	1.13
3		2.40	1.21	2.77	1.40	1.15
4		1.49	0.75	2.18	1.10	1.46

TABLE 7.13 DETAILS OF TESTED PUNCHING SHEAR SINGLE CHORD CONNECTIONS

Reference	Specimen No.	Chord RHS ($h_o \times b_o \times t_o$) (mm)	Branch RHS ($h_1 \times b_1 \times t_1$) (mm)	r_1	r_2	r_4	$\bar{R}$	D (KN-m)
	B-3	50.8×152.4×4.76	101.6× 50.8×6.35	0.333	0.50	10.67	2.095	
	B-4	50.8×152.4×4.76	101.6× 76.2×6.35	0.500	0.75	16.00	2.197	
Patel et al. [5]	B-5	50.8×152.4×4.76	101.6×101.6×6.35	0.667	1.00	21.33	1.329	1.978
	L-4	152.4×152.4×4.76	76.2×101.6×6.35	0.667	1.33	21.33	1.244	
	L-5	152.4×152.4×4.76	101.6×101.6×6.35	0.667	1.00	21.33	1.329	
	1		88.9×88.9×4.94	0.700	1.00	18.67	1.233	
Redwood [2]	2	127.0×127.0×4.76	69.9×69.9×4.18	0.550	1.00	14.67	2.283	1.978
	3		47.6×47.6×4.18	0.375	1.00	10.00	3.443	
	1		50.8×50.8	0.571	1.00	13.33	2.255	
Mee [3]	2	88.9×88.9×3.81	3.81×38.1	0.429	1.00	10.00	3.367	1.013
	3		25.4×25.4	0.286	1.00	6.67	3.848	

TABLE 7.14   COMPARISON BETWEEN EXPERIMENTAL AND THEORETICAL RESULTS FOR SINGLE CHORD JOINTS UNDER PUNCHING SHEAR

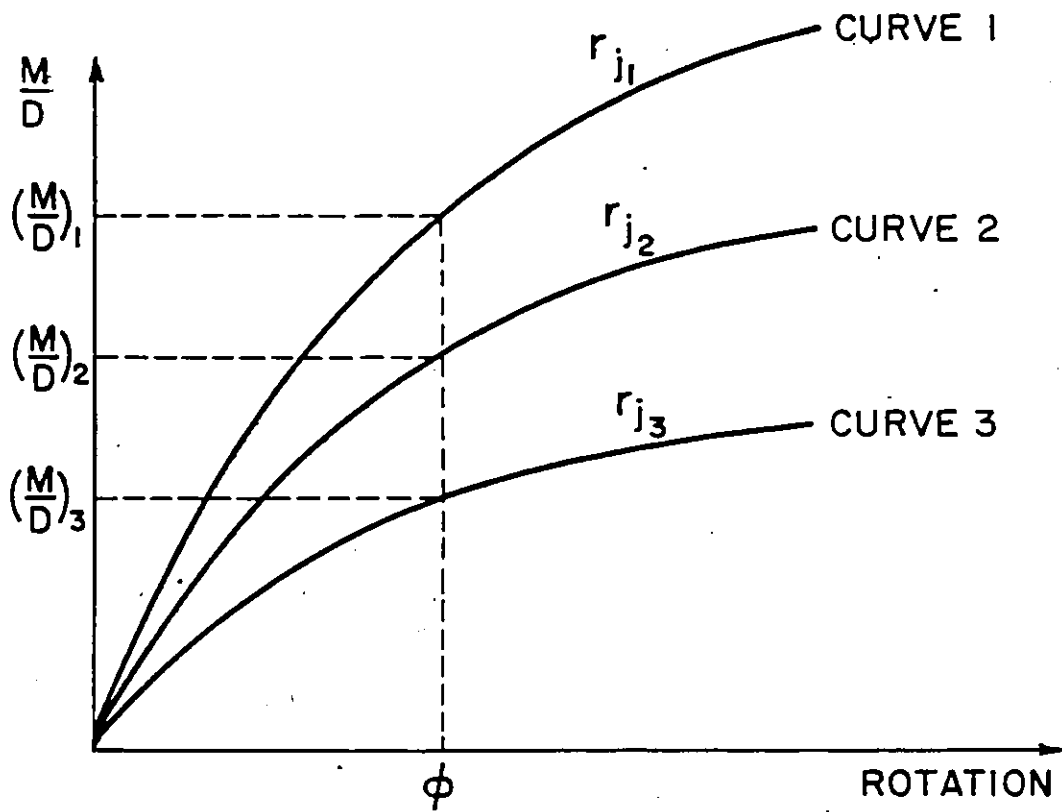| Reference	Specimen No.	Experimental			Theoretical		$\dfrac{P_u}{\bar{P}_u}$
		Chord Yield Strength σ_Y(MPa)	Ultimate Load $\bar{P}_u$(KN)	$\dfrac{\bar{P}_u b_o}{D}$	Ultimate Load P_u(KN)	$\dfrac{P_u b_o}{D}$	
	B-3		57.0	4.93	70.3	5.42	1.23
	B-4		72.2	5.56	67.0	5.16	0.93
Patel et al. [5]	B-5	248.2	118.2	9.11	110.8	8.54	0.94
	L-4		98.4	7.58	118.4	9.12	1.20
	L-5		109.5	8.44	110.8	8.54	1.01
	1		151.0	9.70	143.3	9.20	0.95
Redwood [2]	2	248.2	87.8	5.64	77.4	4.97	0.88
	3		53.7	3.45	51.3	3.30	0.96
	1		69.7	6.12	63.7	5.59	0.9ⱽ
Mee [3]	2	275.8	51.3	4.50	42.7	3.74	0.83
	3		38.7	3.40	37.3	3.28	0.96

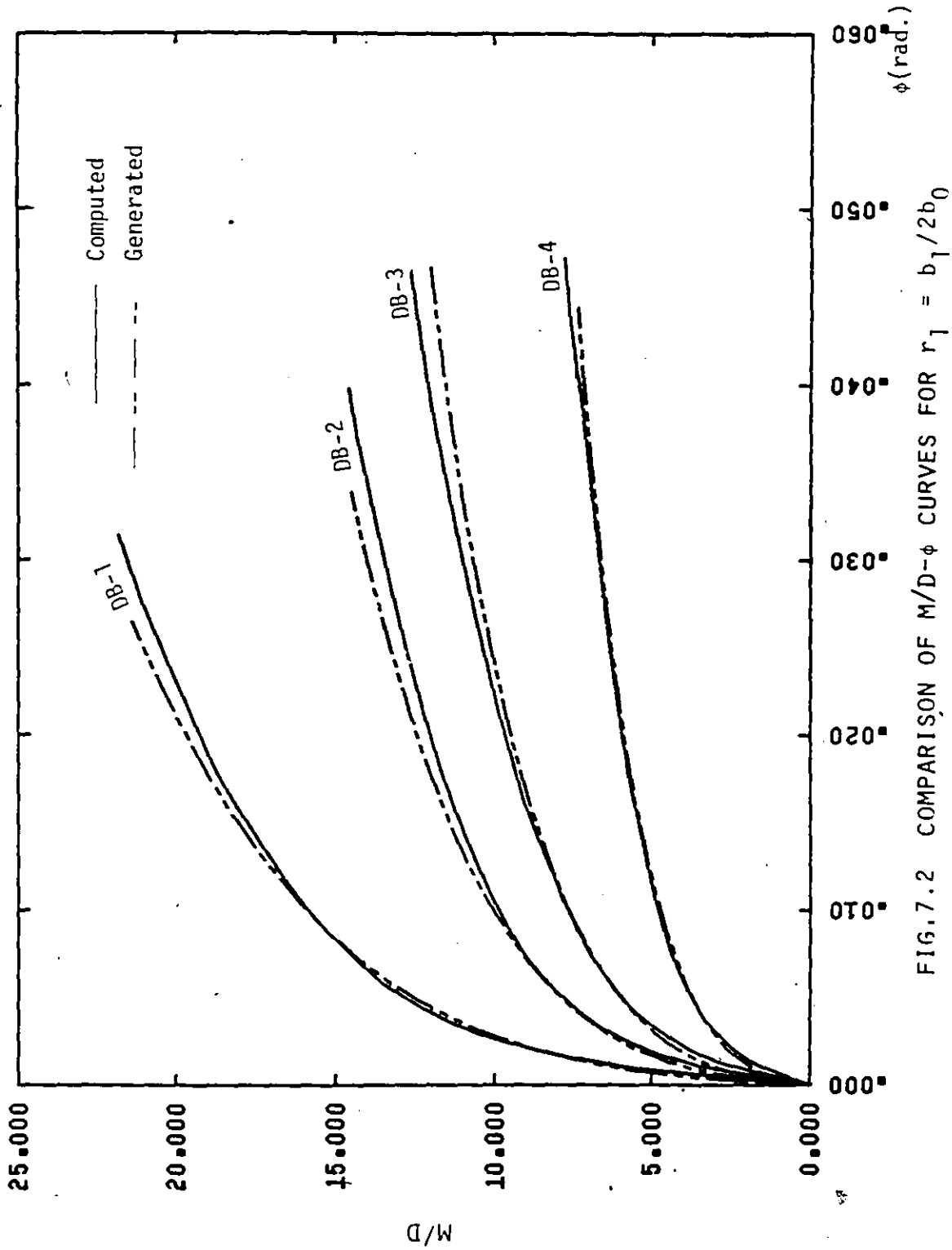FIG. 7.1   FAMILY M/D-ϕ CURVES FOR CONNECTIONS WITH DIFFERENT r_j VALUES

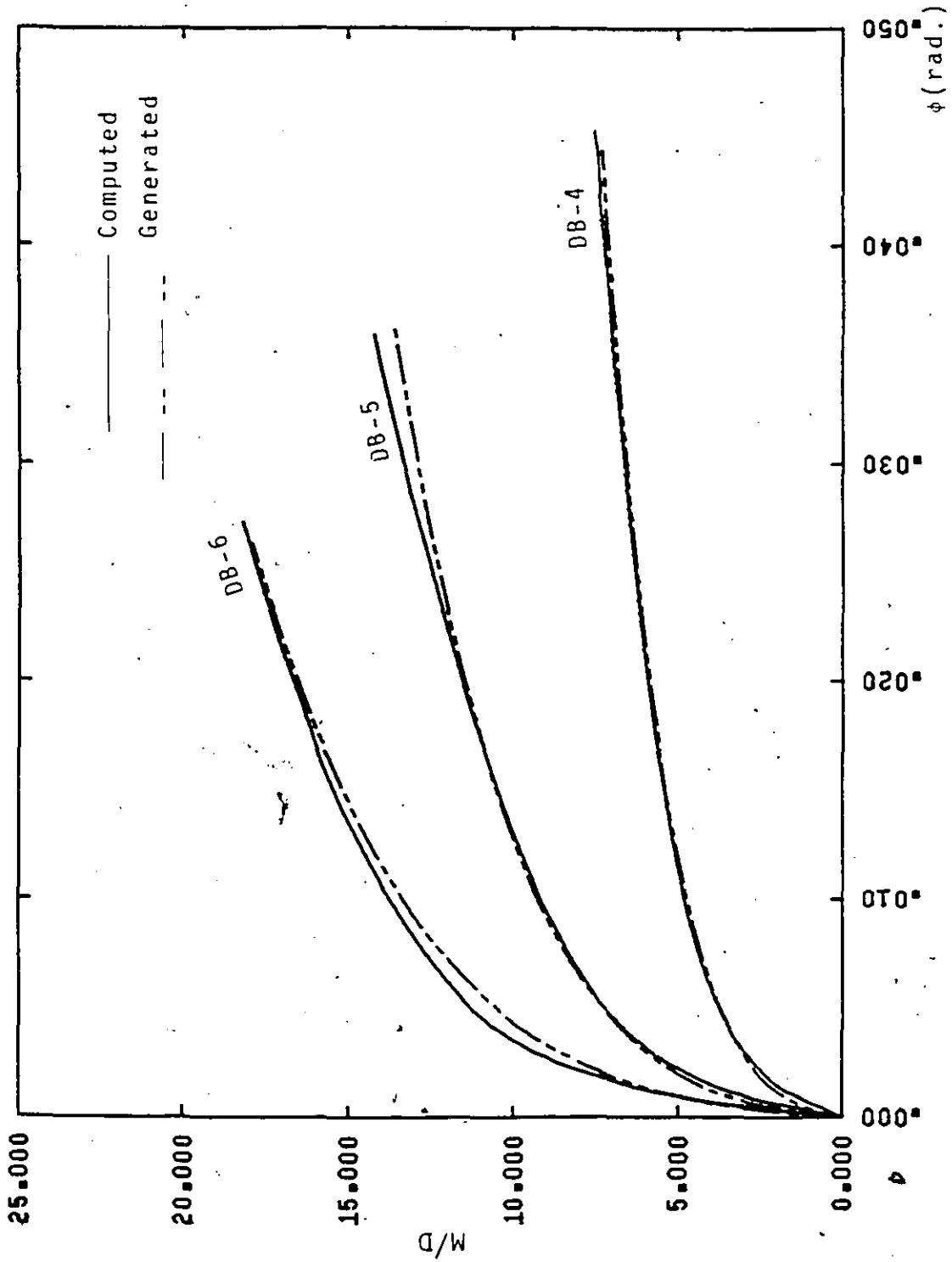FIG.7.2 COMPARISON OF M/D-ϕ CURVES FOR $r_1 = b_1/2b_0$

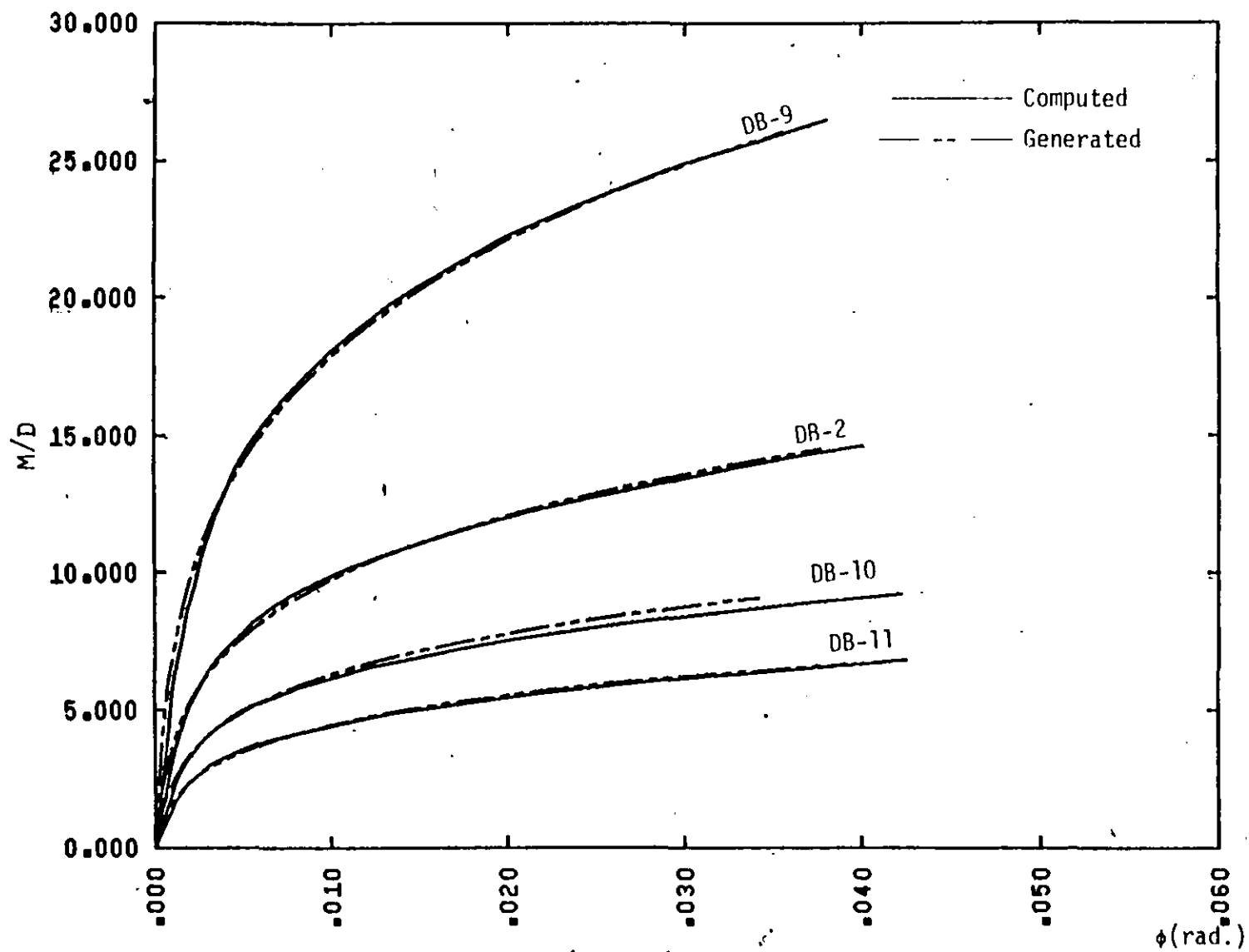FIG. 7.3   COMPARISON OF M/D-ϕ CURVES FOR $r_2 = b_1/h_1$

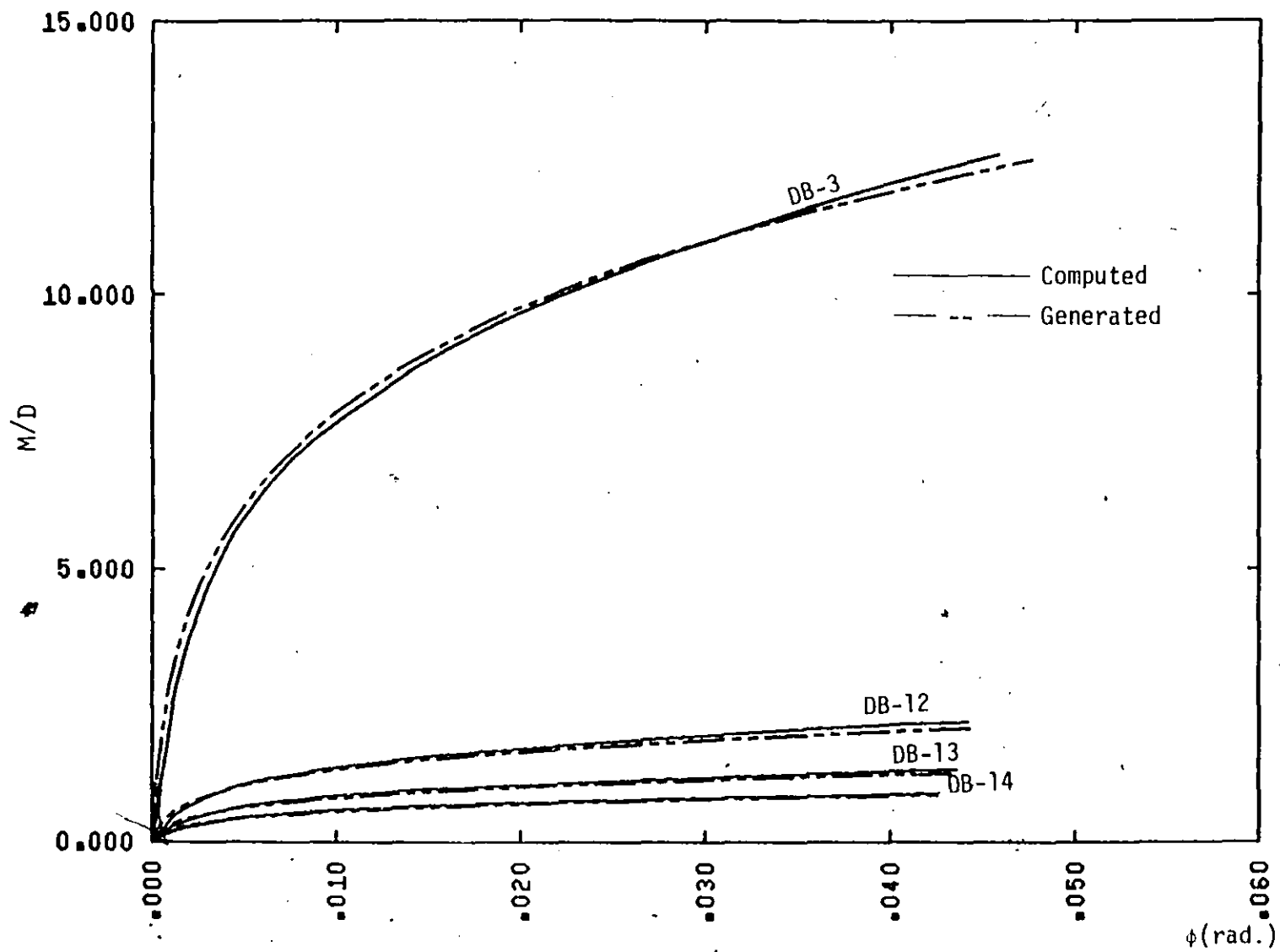FIG.7.4 COMPARISON OF M/D-ϕ CURVES FOR $r_4 = b_1/t_0$

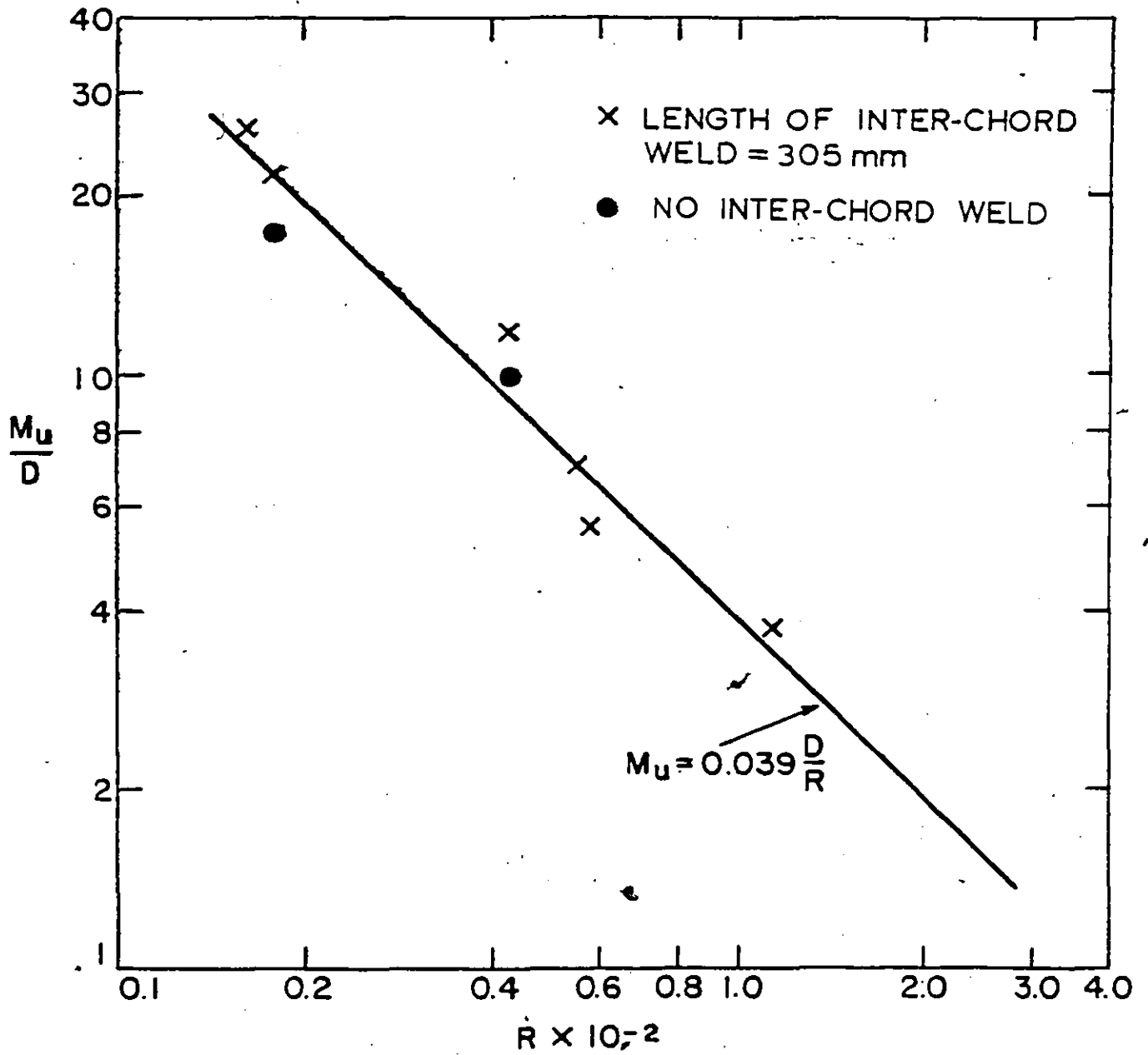FIG. 7.5   COMPARISON OF M/D-φ CURVES FOR $r_5 = 1 + t_s/t_o$

FIG. 7.6   COMPARISON BETWEEN THEORETICAL AND EXPERIMENTAL CAPACITIES FOR DOUBLE CHORD JOINTS UNDER BRANCH MOMENT

FIG. 7.7 COMPARISON OF Pb_0/D-δ/t CURVES FOR $r_1 = b_1/2b_0$

FIG. 7.8 COMPARISON OF $Pb_0/D-\delta/t$ CURVES FOR $r_2 = b_1/h_1$

FIG. 7.9. COMPARISON OF Pb_0/D–δ/t CURVES FOR $r_4 = b_1/t$

FIG. 7.10 COMPARISON OF $Pb_0/D-\delta/t$ CURVES FOR $r_5 = 1+t_s/t_0$

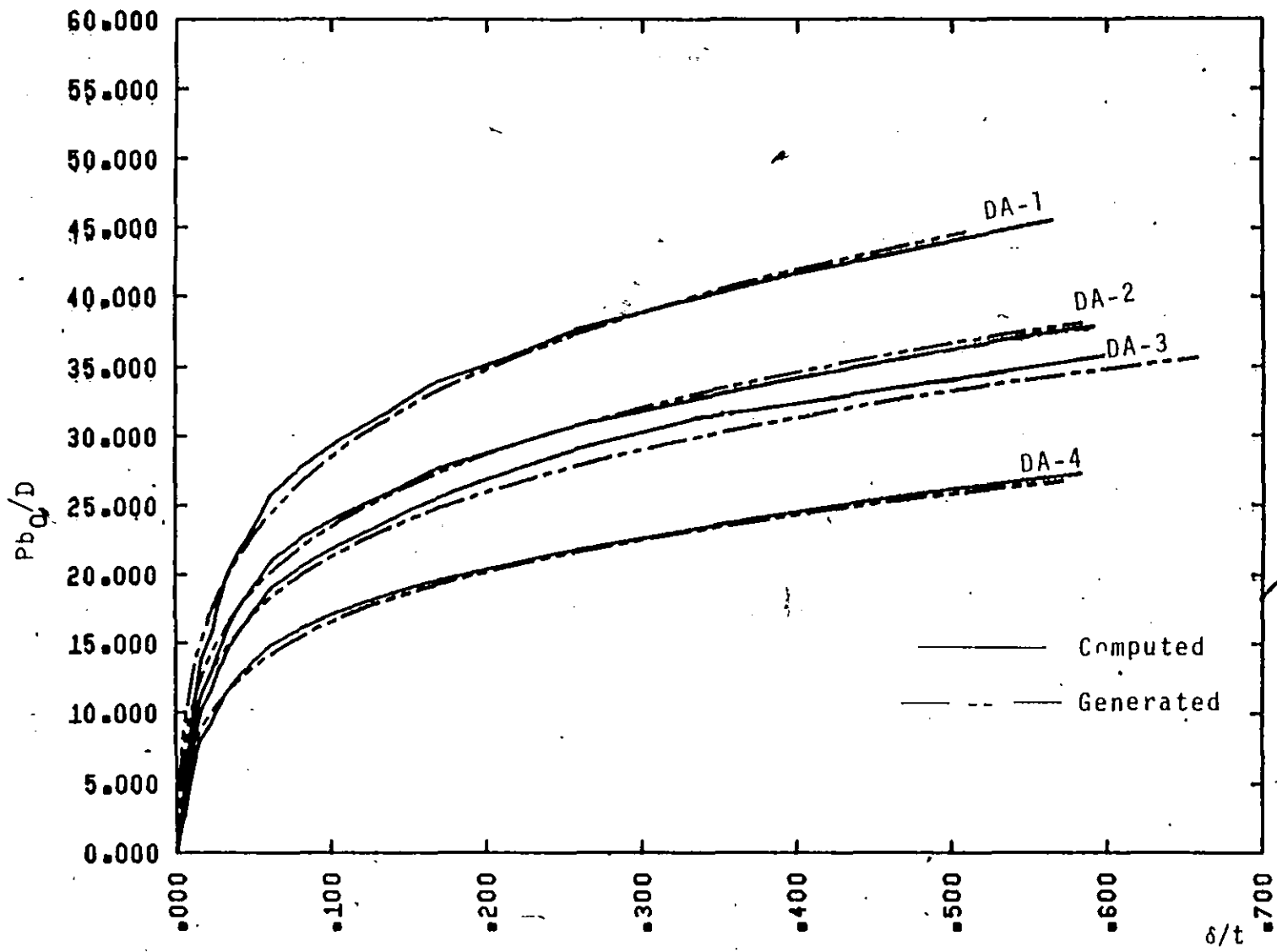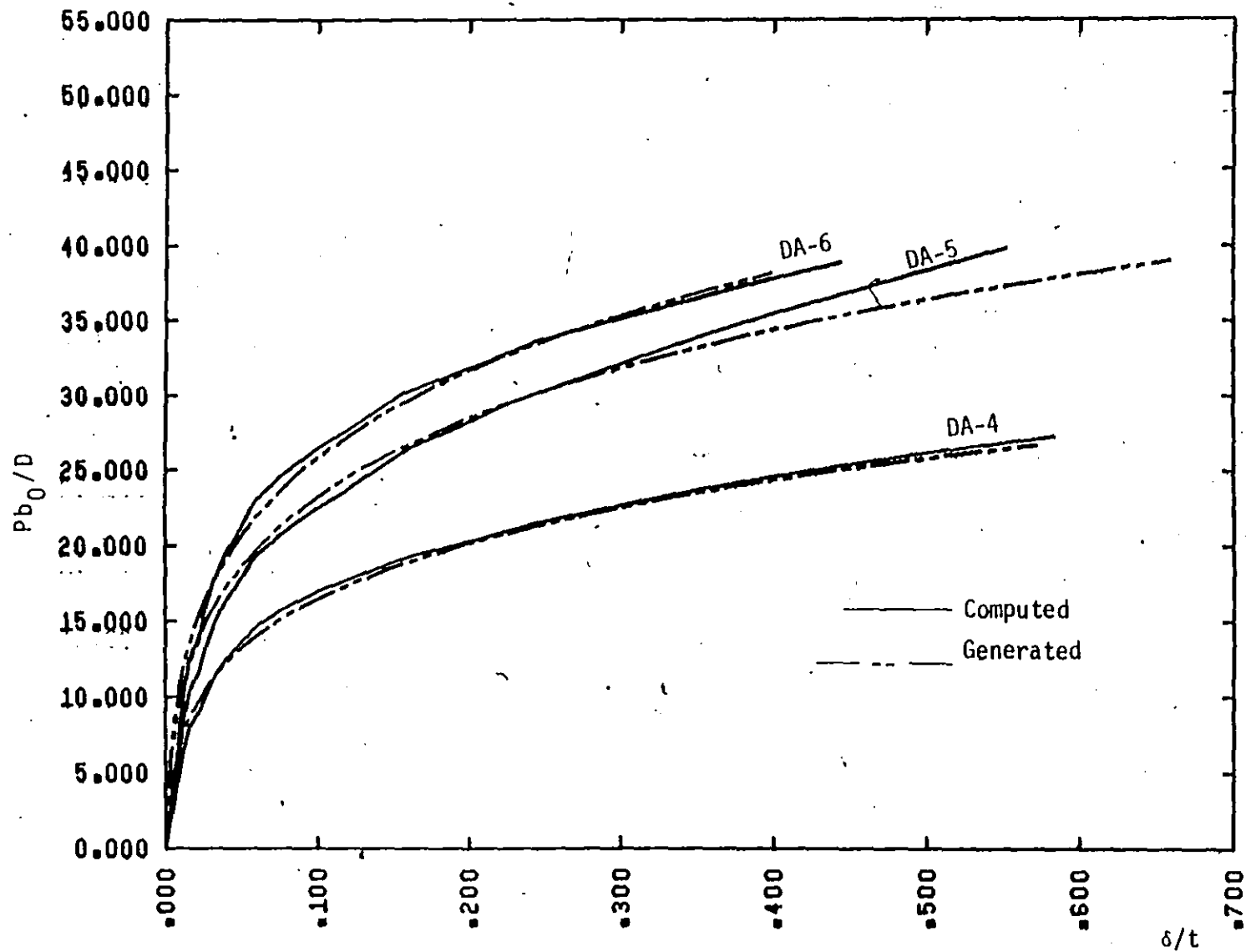FIG. 7.11   COMPARISON BETWEEN THEORETICAL AND EXPERIMENTAL CAPACITIES FOR DOUBLE CHORD JOINTS UNDER PUNCHING SHEAR

FIG. 7.12 COMPARISON OF M/D -- φ CURVES FOR $r_1 = b_1/b_0$
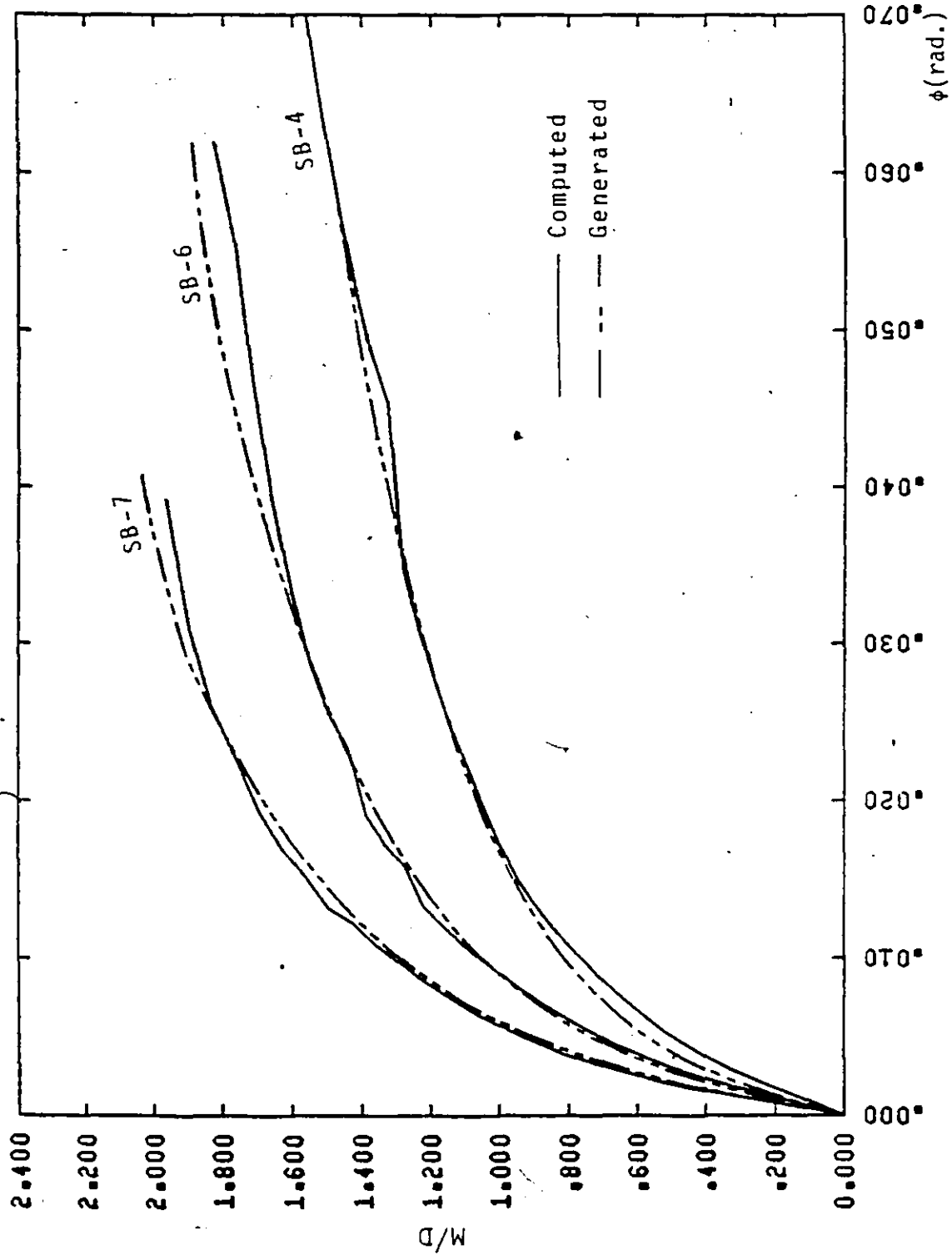
FIG. 7.13 COMPARISON OF M/D - ϕ CURVES FOR $r_2 = b_1/h_1$
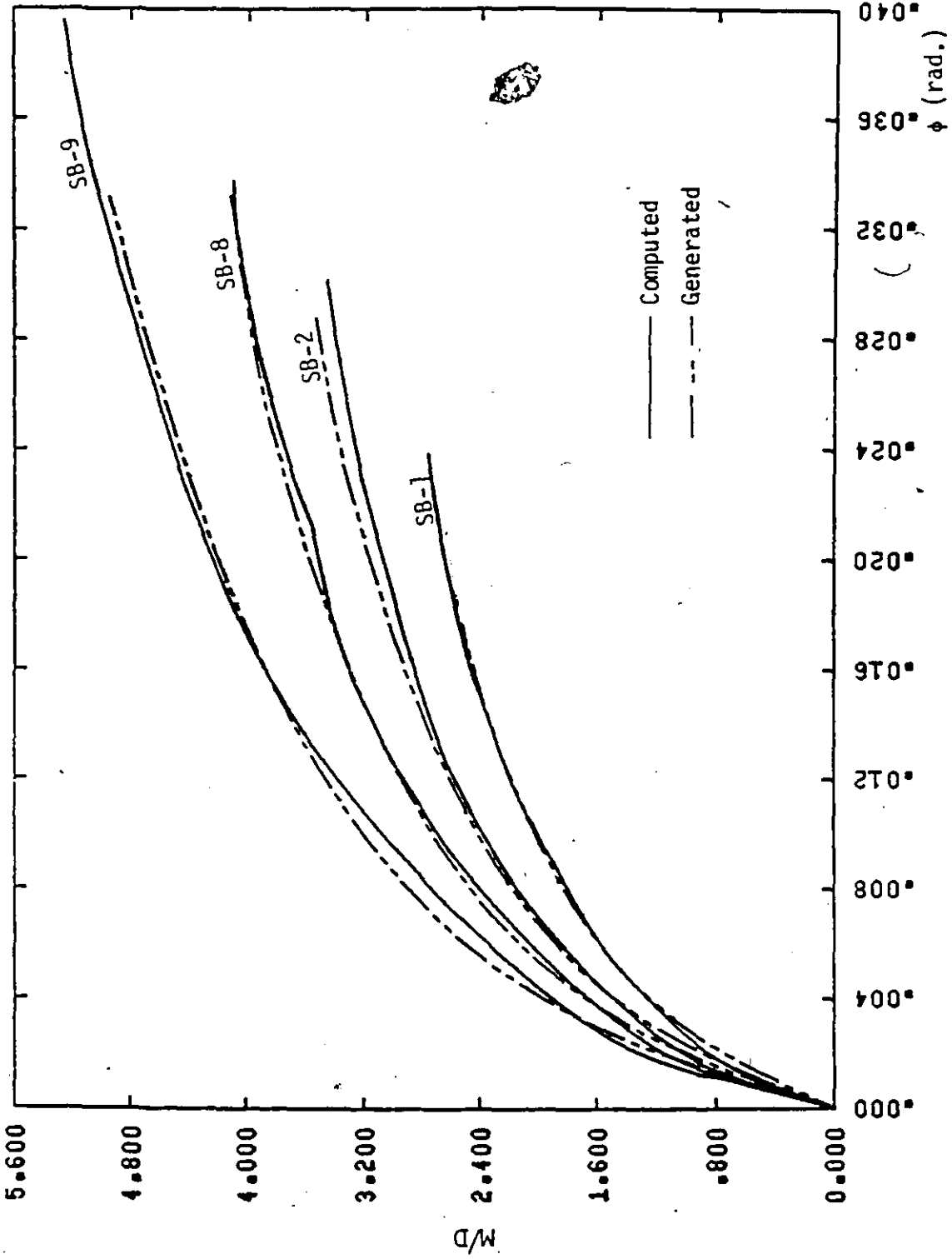
FIG. 7.14   COMPARISON OF M/D - ϕ CURVES FOR $r_4' = b_1/t_0$
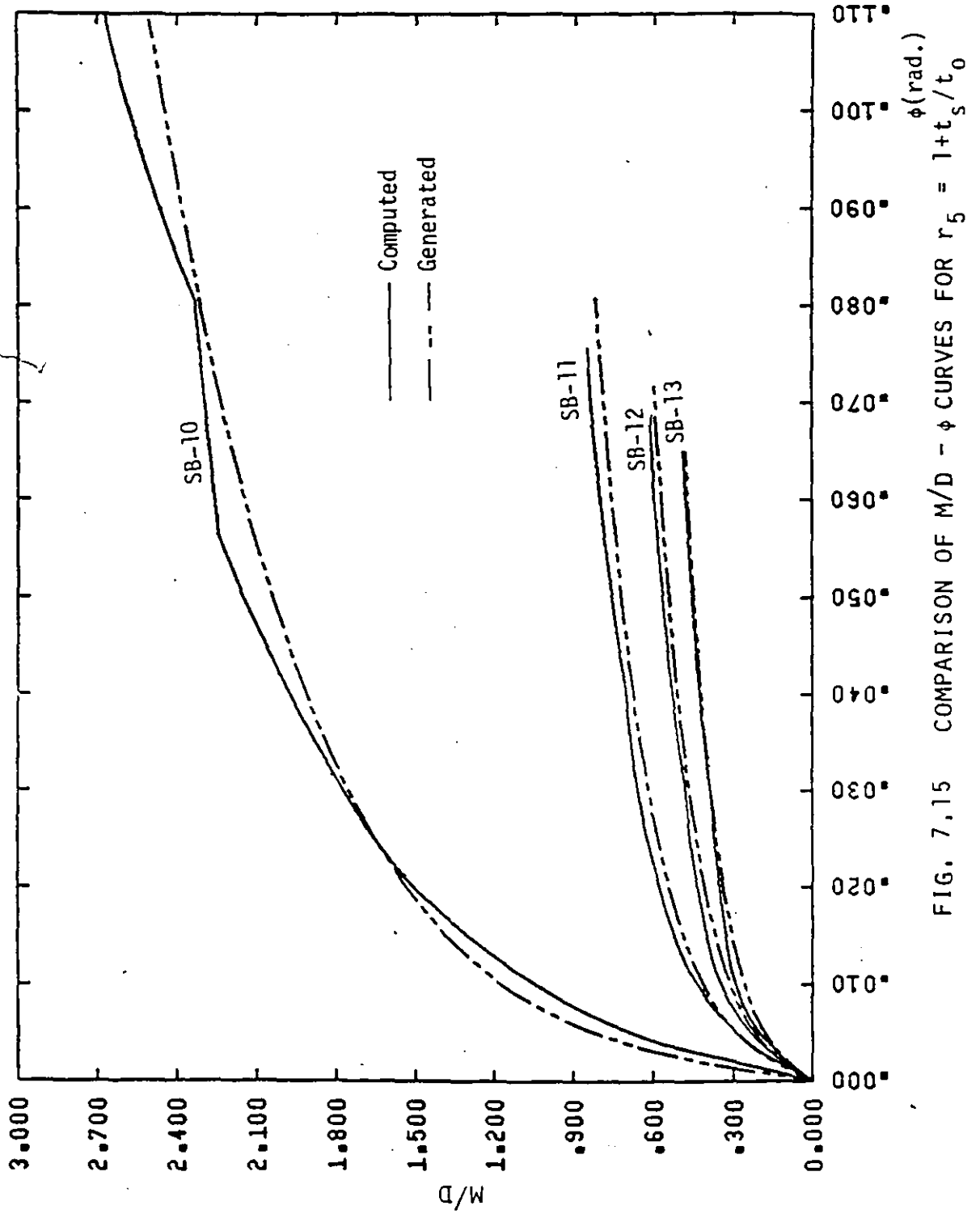
FIG. 7.15 COMPARISON OF M/D – φ CURVES FOR $r_5 = 1 + t_s/t_0$
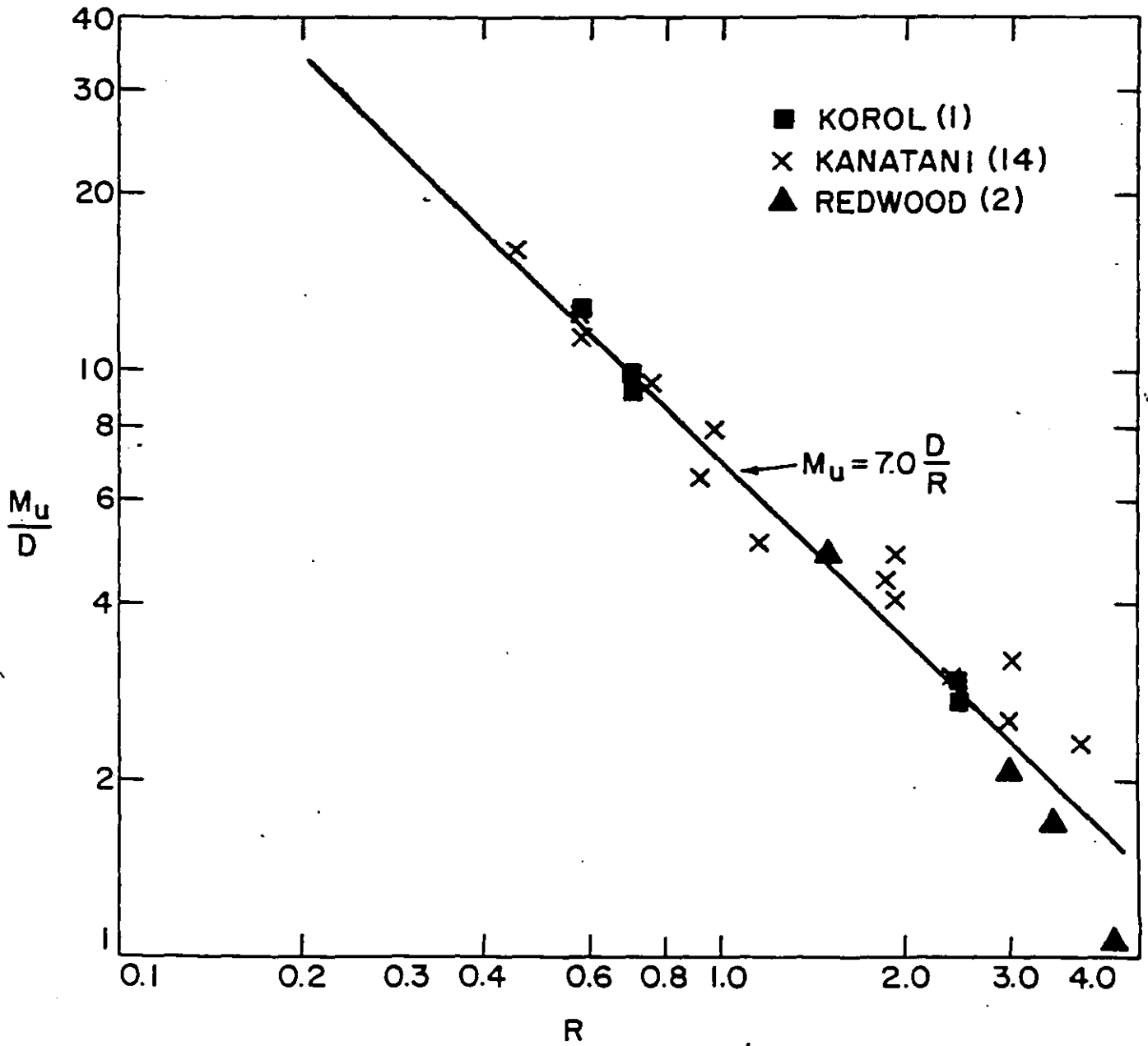
FIG. 7.16   COMPARISON BETWEEN THEORETICAL AND EXPERIMENTAL CAPACITIES OF SINGLE CHORD JOINTS UNDER BRANCH MOMENT
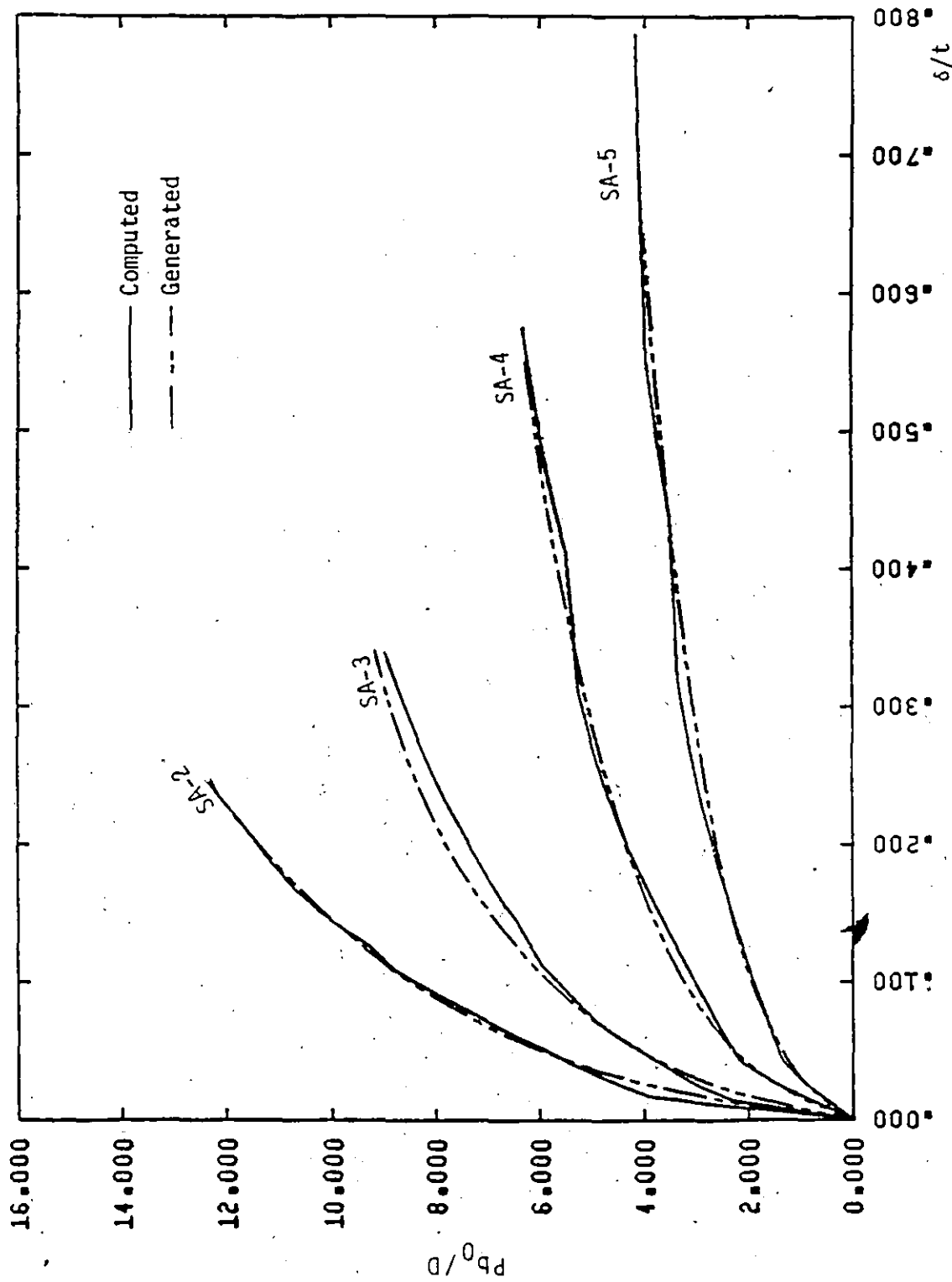
FIG 7.17 COMPARISON OF $Pb_0/D - \delta/t$ CURVES FOR $r_1 = b_1/b_0$
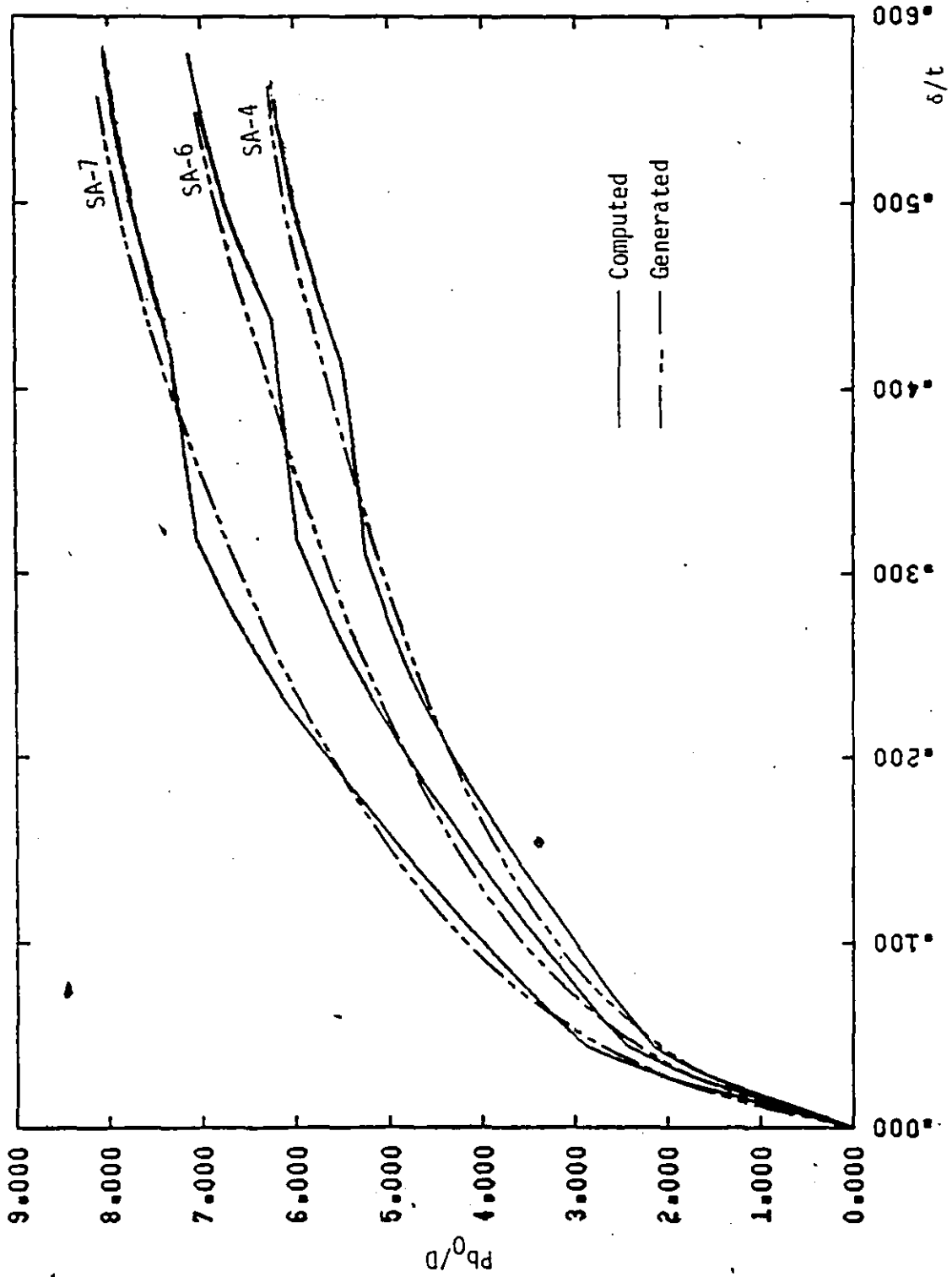
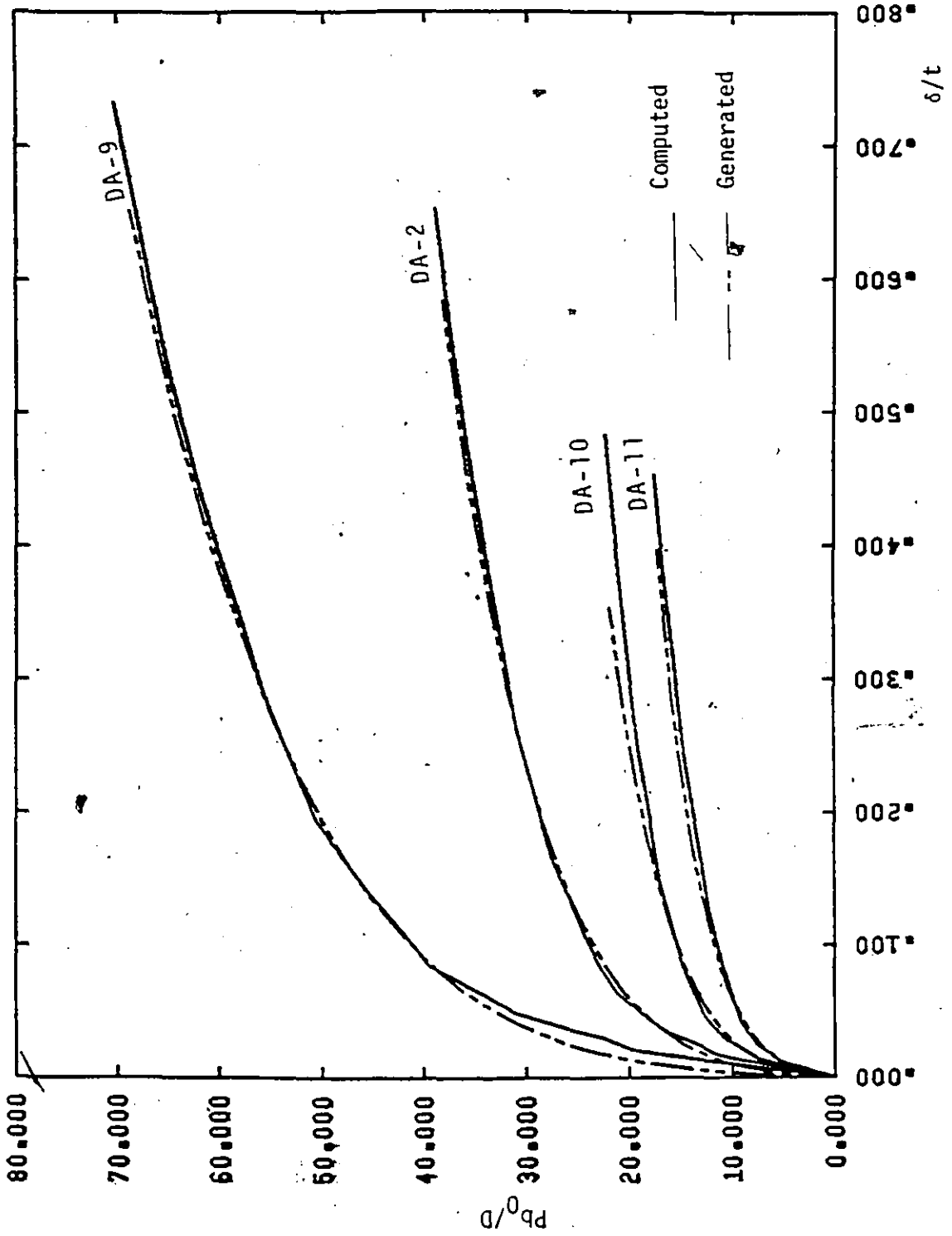FIG. 7.18 COMPARISON OF $Pb_0/D - \delta/t$ CURVES FOR $r_2 = b_1/h_1$
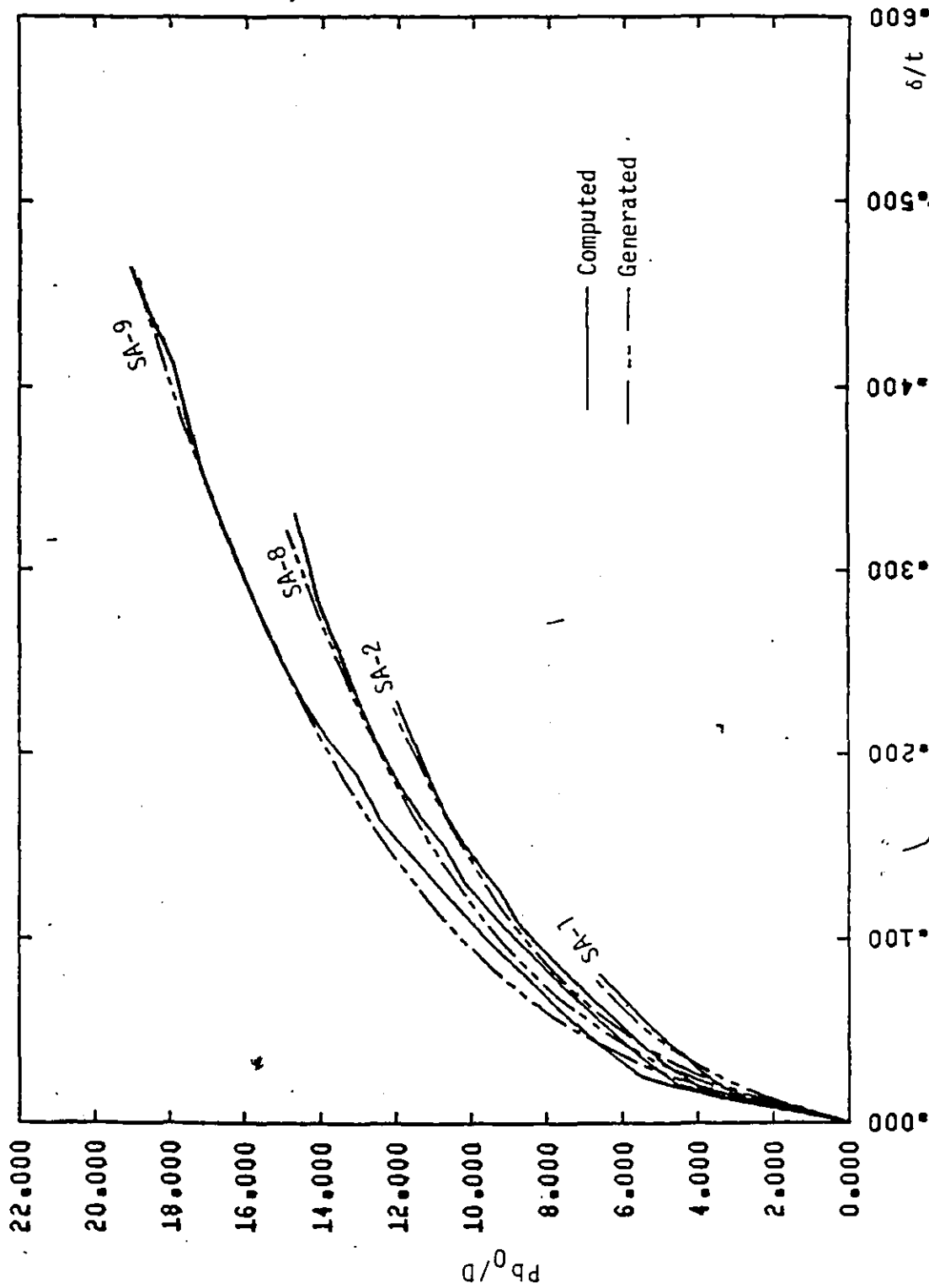
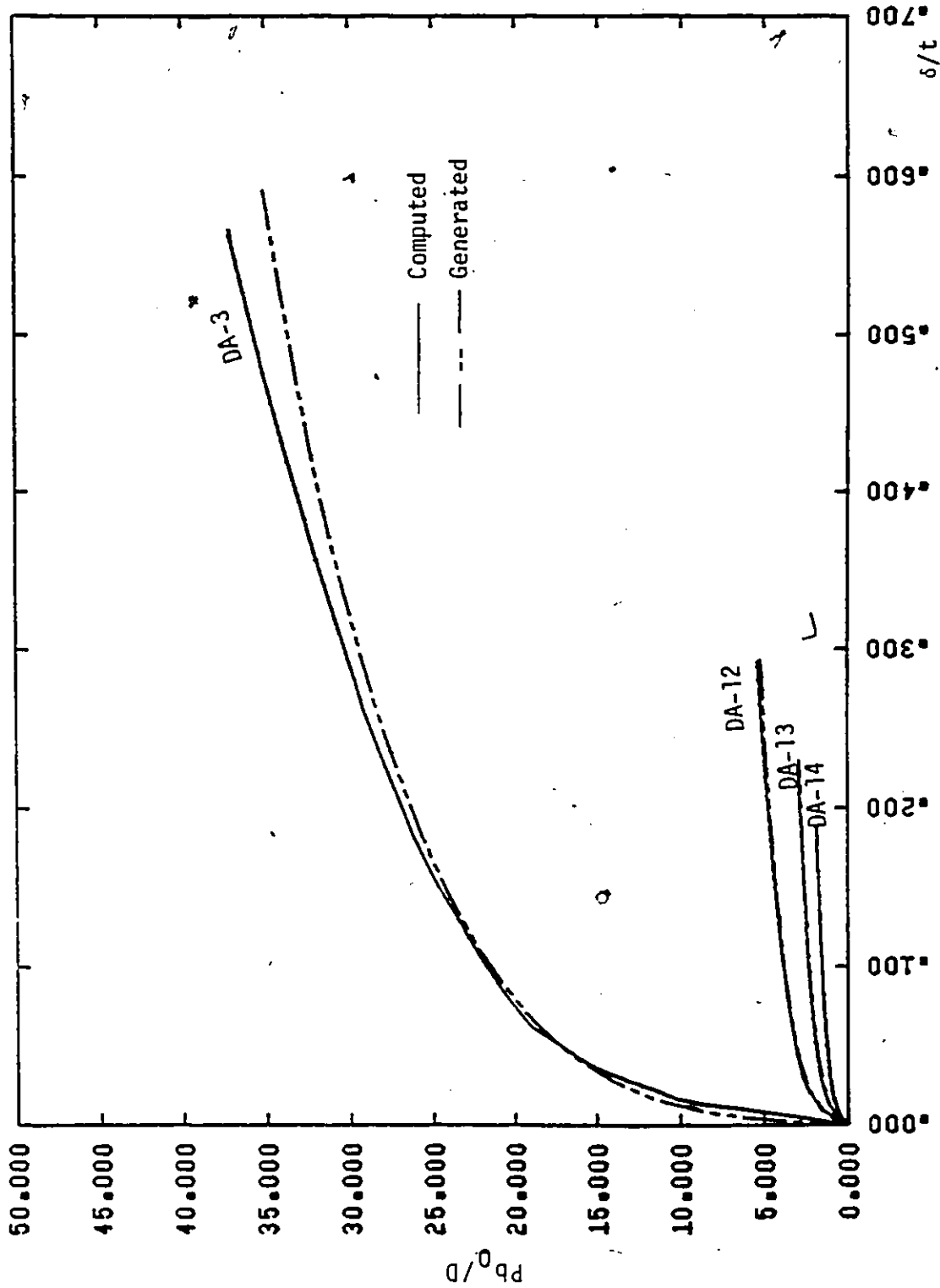FIG. 7.19 COMPARISON OF $Pb_0/D - \delta/t$ CURVES FOR $r_4 = b_1/t_0$
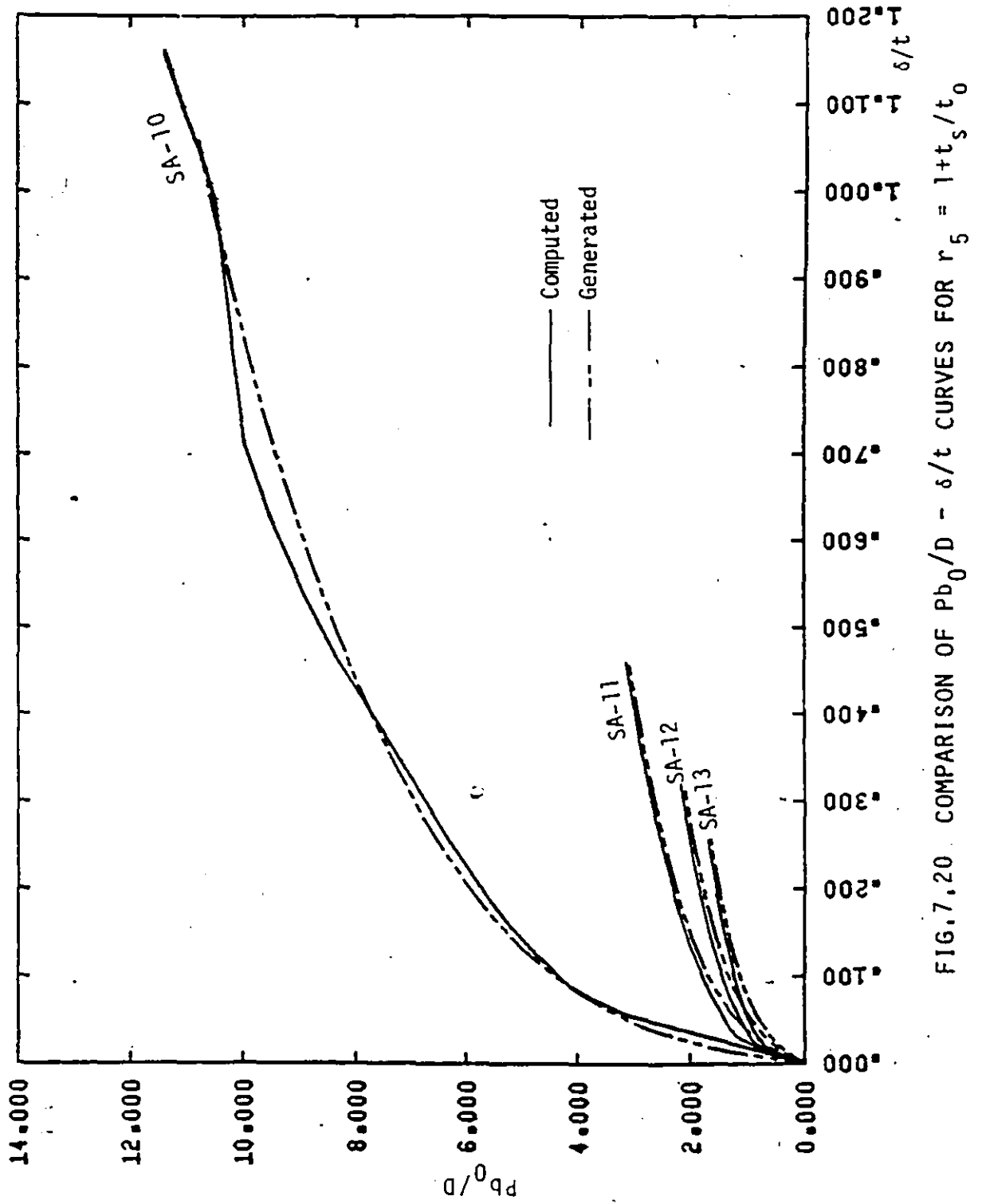
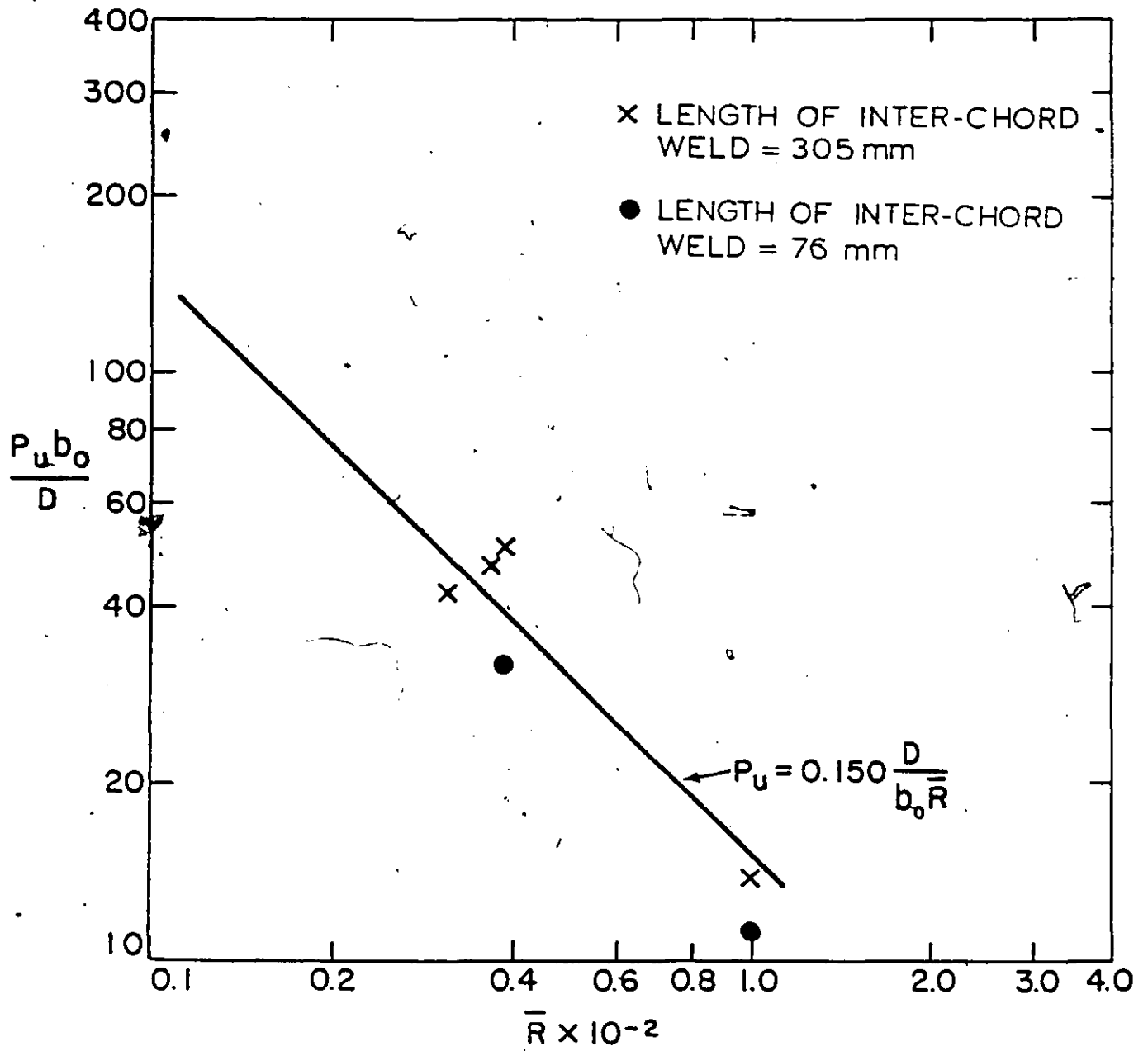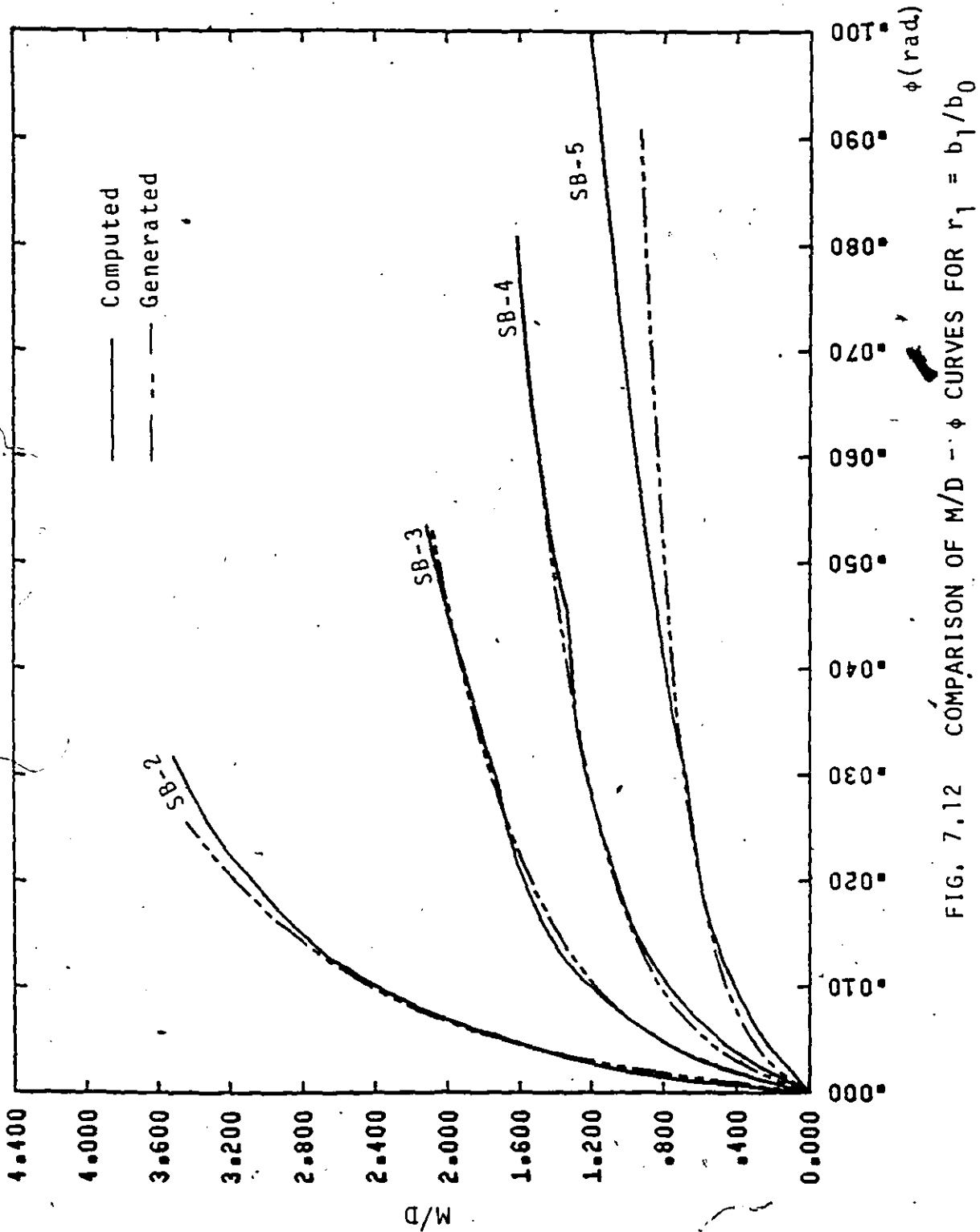FIG.7.20 COMPARISON OF $Pb_0/D - \delta/t$ CURVES FOR $r_5 = 1 + t_s/t_0$
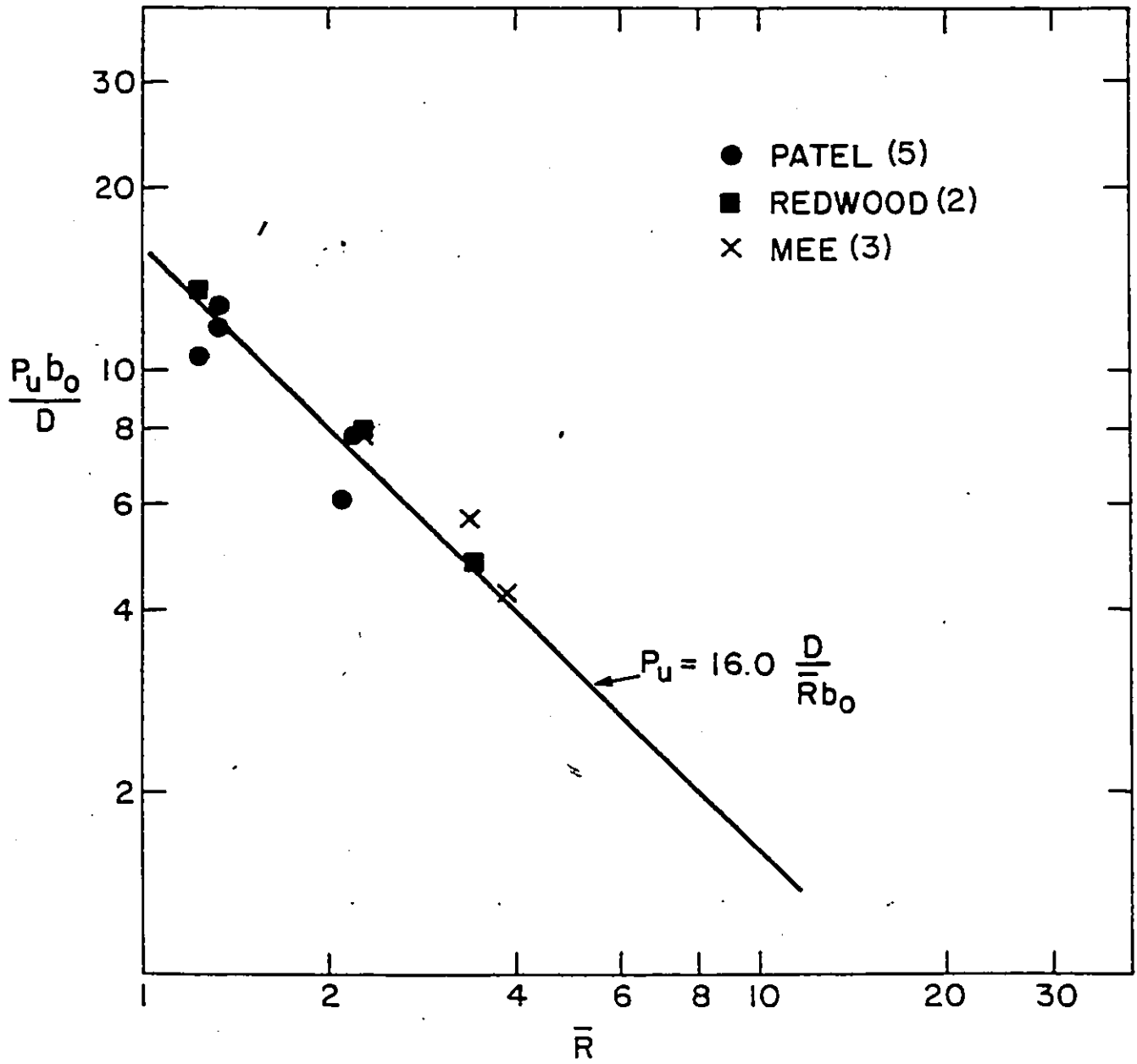
FIG. 7.21 COMPARISON BETWEEN THEORETICAL AND EXPERIMENTAL CAPACITIES FOR SINGLE CHORD JOINTS UNDER PUNCHING SHEAR

CHAPTER 8

ANALYSIS OF RHS VIERENDEEL TRUSSES

8.1   Introduction

        Members in a Vierendeel truss are subject to predominately
bending action.   This type of structure, then, is susceptible to rela-
tively high bending stresses since axial forces play a less significant
role in distributing the forces.

        Joints in a Vierendeel truss, such as shown in Fig. 8.1 (a) must
possess enough rotational stiffness to render a stable load-carrying
structure.   Futhermore, when a truss consists of rectangular hollow
section (RHS) members, the joints are usually flexible.   In such cases,
the joints may have a significant effect on the truss behaviour even if
they are able to develop the moment capacity of the connected members.

        In this chapter, a number of Vierendeel trusses with different
joint configurations are analyzed.   Uncoupled, nonlinear rotational and
translational springs are introduced at the branch-to-chord connections
to simulate the joint flexibilities, as shown in Fig. 8.1 (b).   The
standardized equations, presented in Chapter 7 for double and single
chord joints, are used to define the stiffness and strength characteris-
tics of the model springs.

An analysis that employs the finite element method and incorporates material nonlinearities in both members and joints is introduced. The Newton-Raphson method, as presented in Chapter 3, is employed again to solve the nonlinear problem incrementally. The computer program written for the present study has the capability of static analysis of any plane frame which can be modelled by one-dimensional straight elements and whose material obeys the Von-Mises yield criterion with an associative flow rule for strain-hardening as presented in Section 3.5. Different aspects of the finite elment formulation are presented in the following sections.

8.2 Finite Element Modelling of Rectangular Hollow Section (RHS) Members

Numerical integration is used to évaluate the element matrices in the finite element formulation of the nonlinear problem at hand. Each RHS member is divided into a number of beam elements of different lengths according to the expected stress gradients. A typical beam element is shown in Fig. 8.2 (a). Nodal degrees of freedom are axial displacement u, transverse displacement w and rotation Θ. Hence, both axial and bending actions are considered in the formulation.

The tangential stiffness matrix (K_T) is written in the standard form as

$$[K_T] = \int_V [B]^T \ [\bar{E}] \quad [B] \ dV \qquad (8.1)$$
$$(6\times6) \qquad (6\times1) \ (1\times1) \ (1\times6)$$

where $\bar{E}$ is the modulus of elasticity E or the tangential modulus E_T and [B] is the strain matrix relating the longitudinal strain to nodal displacements, i.e.,

$$[\varepsilon] = [B] \ [\delta_e] \qquad (8.2)$$
$$1\times1 \quad (1\times6) \ (6\times1)$$

$$[B] = \ < -\frac{1}{\ell}, \ -\frac{6z}{\ell^2}(1-2\xi), \ \frac{2z}{\ell}(2-3\xi), \ \frac{1}{\ell},$$

$$-\frac{6z}{\ell^2}(1-2\xi), \ \frac{2z}{\ell}(1-3\xi) > \qquad (8.3)$$

$$\{\delta_e\}^T = \ < u_1 \ \ w_1 \ \ \theta_1 \ \ u_2 \ \ w_2 \ \ \theta_2 \ >. \qquad (8.4)$$

In order to simplify integration of Equation 8.1 numerically, the double or single chord RHS is transformed into an equivalent I-section. The equivalent I-section dimensions are related to the original double and single RHS chords as follows (see Fig. 8.2(b))

For double RHS: $b = b_0$, $h = h_0/2$, $t = t_0$, $t_1 = 2t_0$
For single RHS: $b = b_0/2$, $h = h_0/2$, $t = t_0$, $t_1 = t_0$.

This renders a simpler geometric input for the computer program. Integration in the z-direction is carried out using three point Gauss

quadrature within each of the flanges and web of the equivalent section, as illustrated in Fig. 8.2 (b) because of the abrupt changes in the cross-section shape. Three point integration scheme is also employed to integrate along the element length in the x-direction. Hence, a total of 27 integration points are used to evaluate the element stiffness matrix. Equation 8.1 can then be integrated numerically by the following equation;

$$[K_T]_{(6\times6)} = \ell \cdot (h-t) \cdot t_1 \sum_{i=1}^{3} \sum_{j=1}^{3} W_i W_j \left[f(\xi_i, z_j) \right]$$

$$+ \frac{1}{2} \ell \cdot b \cdot t \sum_{i=1}^{3} \sum_{j=1}^{3} W_i W_j \left[f(\xi_i, z_j') \right]$$

$$+ \frac{1}{2} \ell \cdot b \cdot t \sum_{i=1}^{3} \sum_{j=1}^{3} W_i W_j \left[f(\xi_i, z_j'') \right] \qquad (8.5)$$

where

$$W_i = 5/9, \ 8/9, \ 5/9$$

$$\xi_i = 0.5 - \sqrt{0.15}, \ 0.5, \ 0.5 + \sqrt{0.15}$$

$$z_i = -2(h-t)\sqrt{0.15}, \ 0.0, \ 2(h-t)\sqrt{0.15}$$

$$z_i' = -h-t(\frac{1}{2} + \sqrt{0.15}), \ h-t/2, \ h-t(\frac{1}{2} - \sqrt{0.15})$$

$$z_i'' = -h+t(\frac{1}{2} + \sqrt{0.15}), \ -h+t/2, \ -h+t(\frac{1}{2} - \sqrt{0.15})$$

$$\lfloor f(\xi_i, z_j)\rfloor = \lfloor B(\xi_i, z_j)\rfloor^T \lfloor \bar{E}(ij)\rfloor \lfloor B(\xi_i, z_j)\rfloor \qquad (8.6)$$
$$(6\times 6) \qquad (6\times 1) \qquad (1\times 1) \qquad (1\times 6)$$

$\bar{E}(ij)$ is equal to E or E_T depending on the stress level at the integration point (ξ_i, z_j). Equation 8.5 permits calculating the element stiffness matrix to within 1% error.

8.3   Finite Element Modelling of Vierendeel Truss Joints

To account for the flexibility of joints in the analysis of Vierendeel trusses the branch member is assumed to be connected to the chord member through springs as shown schematically in Fig. 8.1. Rotational stiffness of the joint is modelled by a rotational spring S_r, whereas the axial stiffness is incorporated through a translational spring S_t. A typical joint spring element is shown in Fig. 8.3 (a).

Under an applied branch moment M, the spring S_r undergoes a rotation ϕ and its tangential stiffness J_T will be given by the slope of the M-ϕ curve, as illustrated in Fig. 8.3(b). Similarly, the spring S_t undergoes a deflection δ under an applied force P and its tangential stiffness C_T will be given by the slope of the P-δ curve, as shown in Fig. 8.3 (c). Standardized equations for J_T and C_T were developed in Chapter 7 for both single and double chord RHS T-joints and are implemented in the present analysis. The incremental equations of equilibrium of the spring element can be written in the following matrix form:

$$\begin{Bmatrix} \Delta P_1 \\ \Delta M_1 \\ \Delta P_2 \\ \Delta M_2 \end{Bmatrix} = \begin{bmatrix} C_T & 0. & -C_T & 0 \\ 0 & J_T & 0 & -J_T \\ -C_T & 0 & C_T & 0 \\ 0 & -J_T & 0 & J_T \end{bmatrix} \begin{Bmatrix} \Delta w_1 \\ \Delta \Theta_1 \\ \Delta w_2 \\ \Delta \Theta_2 \end{Bmatrix} \qquad (8.7)$$

or in a simpler form as

$$\{\Delta R^S\} = [K_T^S] \{\Delta \delta_e^S\} \qquad (8.8)$$

where $\{\Delta R^S\}$ and $\{\Delta \delta_e^S\}$ are vectors of incremental nodal forces and displacements, respectively and $[K_T^S]$ is the tangential stiffness matrix of the spring element. Equation 8.7 implies that the rotational and translational springs are uncoupled. Numerical results to follow do indicate validity of this assumption.

8.4   Solution Procedure

It may be observed that the finite element formulation presented in Chapter 3 for analysis of RHS joints and that of the Vierendeel trusses here are analogous in many respects. While the former employs two-dimensional rectangular plate elements and boundary spring elements, the latter employs one-dimensional beam elements and joint spring elements. In addition, both analyses incorporate material nonlinearities through the same yield and strain-hardening criteria. The Newton-Raphson solution scheme will be used again to solve the present nonlinear problem

incrementally.   Steps of the solution technique have been presented in

Section 3.5.   The same solution procedure can easily be adopted for the

analysis of Vierendeel trusses employing one dimensional elements.

To start the analysis of a Vierendeel truss, an arbitrary load

is applied and the elastic system is solved for displacements, strains

and stresses.   These internal actions are then scaled so that the most

highly stressed point in the structure (a member or a joint spring) just

yields.   The corresponding load is then the yield load.   Additional

loads are applied in increments proportional to the yield load.   For

each load increment, the incremental equations of equilibrium are solved

iteratively and the global stiffness matrix is updated after each iter-

ation.   Equilibrium is considered to be satisfied when the difference

between the determinants of two consecutive stiffness matrices is within

one percent, the specified tolerance.   The unbalanced loads are added to

the next load increment and the solution process is repeated.   A stiff-

ness or deflection criterion can be specified to define failure and thus

cause termination of the analysis.   In the following sections, numerical

examples,   illustrating   some   applications   of   the   analysis   procedure

above, are presented.

8.5   Vierendeel Trusses with RHS Members

It is valuable from a practical point of view to gain some

insight into the influence of the RHS joint configuration on the overall

behaviour of a framed structure.   A comprehensive investigation of the

problem is, however, beyond the scope of the present work.   Hence, only

a few cases of Vierendeel trusses with a fixed geometry have been anal-
yzed.

The geometry of the trusses analyzed is shown in Fig. 8.4 (a).
Each truss is simply supported at both ends and consists of six 2.5 m ×
3 m bays. A total load, W, acting on the upper deck is represented by
the equivalent joint loads as shown. Each truss member is modelled by
six beam elements of decreasing lengths toward the joints at both ends,
as shown in Fig. 8.4 (b).

Two double chord trusses, denoted DCT1 and DCT2, and two single
chord trusses, denoted SCT1 and SCT2, are considered. Each truss is
analyzed for two conditions namely, rigid joints (RJ) and flexible
joints (FJ). Member sizes of chords and branches are listed in Table
8.1 for all trusses. Member sizes are chosen such that the plastic
moment capacities of chords and branches of DCT1 and DCT2 are approxi-
mately equal to those of SCT1 and SCT2, respectively. Thus, the behav-
iour of cases DCT1-RJ and DCT2-RJ should be comparatively similar to
those of cases SCT1-RJ and SCT2-RJ, respectively. Furthermore, the
width ratios r_1 for the joints of trusses DCT1 and DCT2 are equal or
approximately equal to those of trusses SCT1 and SCT2 to allow for com-
parison between flexibly-connected double and single chord trusses.

Material of the trusses is assumed to be structural steel with
the same properties as given in Section 2.4. When analyzing the
rigidly-connected trusses, all load increments, applied after initial
yielding, were chosen as five percent of the yield load. Yielding of

these trusses progresses rapidly and hence the loads must be applied in small increments to obtain enough points for the load-deflection curves. On the other hand, size of the load increments applied to the flexibly-connected trusses has been taken as twenty percent of the yield load.

8.5.1   Response of Rigidly-Connected Trusses

The joints of these trusses are assumed to behave rigidly, i.e., the framing angle between the branch and chord members does not change as load is applied to the truss. Hence, the joints will have no effect on the truss behaviour.

The applied load W versus the central deflection δ are plotted in Figs. 8.5 and 8.6 for the two double chord and two single chord trusses, respectively. The deflection δ is taken as that of the central joint on the bottom chord of the truss (joint A in Fig. 8.4). Loading on each truss is terminated when its current stiffnes reduces to about ten percent of the elastic stiffness value. The convergence of the incremental solution becomes relatively slow as stiffness falls below this limiting value.

The loads and deflections at both the yield and limiting levels are listed in Table 8.2. Also presented are the elastic stiffness S_{EL} and the ratio W_u^r/W_Y of ultimate to yield loads. It can be seen that the results for trusses DCT1-RJ and SCT1-RJ and for trusses DCT2-RJ and SCT2-RJ are only slightly different. This is expected because of the

choice of member sizes as explained before. It may also be observed that the maximum load, based on the failure criterion, is only about twice the yield load.

Results of the present analysis in the elastic range have been found to agree exactly with the results obtained by using an independently developed frame analysis program [24]. In addition, the truss capacities as predicted here are also compared with the upper bound capacities predicted by plastic analysis of the trusses. Although each of the two approaches is based on a different theory, the relative comparison is, nevertheless, useful. The plastic analysis is presented in Appendix C. The predicted upper bound capacities, W_u^{*r}, of the four trusses are shown by horizontal lines in Figs. 8.5 and 8.6. They are somewhat higher than the finite element capacities for the weaker trusses but lower for the stronger trusses. Nevertheless, the difference between the two solutions is less than 20% in all cases.

8.5.2   Response of Flexibly-Connected Trusses

Flexibilities of the joints are incorporated in the analysis via Equation 8.7. The load versus central deflection curves are presented in Figs. 8.7 and 8.8 for the double and single chord trusses, respectively. Since all joints in each truss have the same configuration, they have equal initial rotational stiffness, J_{EL}. As the load is applied gradually, rotational stiffnesses of the joints at top and bottom of the end branches (joints B in Fig. 8.4 (a)) deteriorate most rapidly but

are followed closely by joints at ends of the second branches (points C). Each truss is assumed to have reached its capacity when the rotational stiffness of joints B reduces to two percent of the elastic value; i.e., when $J_T/J_{EL} = 0.02$. On the other hand, the axial stiffness of all joints, except joints B, remain elastic throughout the loading history whereas that of joints B reduces to about sixty percent of the elastic stiffness. The effect of axial stiffness of joints will be discussed in Subsection 8.5.4.

The truss capacities, W_u^{*f}, as obtained from plastic analysis of flexibly-connected trusses, are also shown in Figs. 8.7 and 8.8 by horizontal lines. The plastic (mechanism) solution is given in Appendix C. With the exception of truss SCT1-FJ, agreement between the two solutions is reasonable.

Results of the analyses are summarized in Table 8.3. Listed are the loads W and central deflections δ at the yield level and at the limiting condition $J_T = 0.02 \ J_{EL}$ where J_T is for joints B in Fig. 8.4 (a) as explained above. It can be concluded from W_u^f/W_Y ratios given in Table 8.3 that the trusses possess considerable reserve strength beyond initial yielding.

Another important conclusion can be drawn from comparing the behaviour of double and single chord trusses. It was observed in the previous section that, when the joints are treated as rigid, the respective double and single chord trusses (DCT1 and SCT1, or DCT2 and SCT2)

have similar stiffness and strength characteristics. When the inherent joint flexibilities are taken into account, however, the double chord trusses show superior qualities. The load capacities, W_u^f, of trusses DCT1-FJ and DCT2-FJ are about two and half times the capacities of trusses SCT1-FJ and SCT2-FJ, respectively. Approximately the same ratio applied also to the elastic stiffness of the trusses. The superior behaviour of double chord trusses is attributed to the fact that double chord joints are much stiffer than single chord joints. This is apparent from comparing the elastic rotational stiffness S_{EL} of the two types of joints, as shown in Table 8.3.

8.5.3 Effect of Joint Flexibility on Truss Load Capacity

When designing a Vierendeel truss, it is desirable to make the joints strong enough to transfer the maximum member forces without failure or excessive deformations. This can be achieved if the joint capacity is at least equal to the plastic moment capacity of the weaker of the connected members. It is assumed here that the truss will not fail prematurely due to an overall or localized buckling.

Moment capacities M_u of joints of each truss are listed in Table 8.4. The M_u values are calculated via Equations 7.17 and 7.26 for double chord and single chord joints, respectively. Also given are the ratios of M_u and the smaller plastic moment M_{pc} or M_{pb} of the chord and branch members. For all cases, the joint capacity is (deliberately) less than the smaller of the member plastic moment capacities. Hence,

the capacity of each truss is governed by the strength of its joints rather than members. This is apparent from W_u^f/W_u^r ratios given in Table 8.4. It can be observed that some correlation exists between W_u^f/W_u^r ratios and the governing M_u/M_{pc} or M_u/M_{pb}. Although the joint config-urations (as defined by the joint parameters in Table 8.1) in trusses DCT1 and SCT1 or DCT2 and SCT2 are closely similar, the moment capaci-ties of the double chord joints are considerably higher. This of course is due to direct transfer of a large portion of the branch forces through the middle webs of the double chords as has been seen in section 5.5.

From the foregoing discussion, it is clear that a Vierendeel truss will have the same load capacity as a rigidly-connected truss if each of its joints is designed to develop the full capacity of the con-nected members. A stiffening, plate, welded to the mated flange of the chord member, is probably the most efficient and economical strengthen-ing device of the joints. The minimum thickness t_s of stiffening plates required to develop full capacities of rigidly connected trusses are given in Table 8.4. However, from a stiffness point of view, the response would still be more flexible for a Vierendeel truss with flexible joints than the one with rigidly connected joints.

8.5.4   <u>Effect of Joint Axial Stiffness</u>

The rotational and axial stiffnesses of RHS joints have been assumed to be uncoupled, as implied by Equation 8.7. Now the validity of this assumption is tested. It was noted in Subsection 8.5.2 that the

axial (punching shear) stiffness of all joints, with the exception of the end joints (joints B in Fig. 8.4 (a)), remain elastic throughout the loading history; whereas those of joints B reduce to about sixty percent of the elastic value. This is because joints in a Vierendeel Truss are subject to predominately bending action with less significant axial forces.

In order to assess the effect of axial stiffness of the joints on behaviour of a Vierendeel truss, the four trusses were re-analyzed assuming the joints to have an infinite axial stiffness. This is accomplished by giving C_T in Equation 8.7 a very large value, say 10^8 KN/mm. The resulting load-deflection curves for the double and single chord trusses were compared with the previously obtained curves in Figs. 8.9 and 8.10. The difference between each associated pair of curves is virtually imperceptible and can be neglected. This observation can be explained through interaction envelopes of the joints. These envelopes are given in Figs. 5.14 and 6.14 for the double and single chord joints, respectively. As the moment and punching shear on the joint increase gradually, the loading path follows a line starting from the origin and intersects the envelope at a point with a small P_m/P_u value. Hence, the axial stiffness remains within or close to the elastic limit and the displacement due to punching shear is negligible. Therefore, a very large axial stiffness will not introduce any significant errors as seen from Figs. 8.9 and 8.10.

TABLE 8.1   DETAILS OF VIERENDEEL TRUSSES

Case No.	Chord Members $(h_o \times b_o \times t_o)$ (mm)	Branch Members $(h_1 \times b_1 \times t_1)$ (mm)	Chord Plastic Moment M_{pc} (KN-m)	Branch Plastic Moment M_{pb} (KN-m)	Joint Parameters			
					r_1	r_2	r_4	r_5
DCT1-RJ & DCT1-FJ	2RHS 152.4×152.4×9.53	RHS 152.4×152.4× 6.35	192.5	68.0	0.500	1.0	16.00	1.0
DCT2-RJ & DCT2-FJ	2RHS 152.4×152.4×9.53	RHS 254.0×254.0× 6.35	192.5	197.3	0.833	1.0	26.67	1.0
SCT1-RJ & SCT1-FJ	RHS 254.0×254.0×6.35	RHS 127.0×127.0× 9.53	197.3	64.5	0.500	1.0	20.00	1.0
SCT2-RJ & SCT2-FJ	RHS 254.0×254.0×6.35	RHS 203.2×203.2×10.3	197.3	191.1	0.800	1.0	32.00	1.0

TABLE 8.2   RESULTS OF RIGIDLY-CONNECTED VIERENDEEL TRUSSES

| Case No.	Yield Values			Values at $S_T=0.10 \ S_{EL}$		
	W_y (KN)	δ_Y (mm)	$S_{EL}=W_Y/\delta_Y$ (KN/mm)	W_u^r (KN)	δ_u (mm)	W_u^r/W_Y
DCT1-RJ	182	71.0	2.57	419	397	2.30
DCT2-RJ	438	64.2	6.83	775	255	1.77
SCT1-RJ	202	80.2	2.52	449	381	2.22
SCT2-RJ	459	63.5	7.23	778	260	1.69

TABLE 8.3   RESULTS OF FLEXIBLY-CONNECTED VIERENDEEL TRUSSES

| Case No.	Yield Values			Values at $J_T = 0.02 J_{EL}$			$\dfrac{W_u^f}{W_Y}$
	W_Y (KN)	δ_Y (mm)	$S_{EL} = W_Y/\delta_Y$ (KN/mm)	$J_{EL} \times 10^6$ (KN-mm/rad)	W_u^f (KN)	δ_u (mm)	
DCT1-FJ	29.3	13.2	2.22	22.6	223	238	7.61
DCT2-FJ	74.3	12.7	5.85	69.6	561	290	7.55
SCT1-FJ	8.9	10.0	0.89	0.671	80.6	125	9.06
SCT2-FJ	21.3	11.2	1.90	3.01	196	230	9.20

TABLE 8.4   EFFECT OF JOINT FLEXIBILITY ON TRUSS LOAD CAPACITIES

Truss No.	Capacity, M_u (KN-m)	$\dfrac{M_u}{M_{pc}}$ or $\dfrac{M_u}{M_{pb}}$	W_u^f/W_u^r	Minimum t_s (mm)[a]
DCT1	54.3	0.800	0.532	6.5
DCT2	167.6	0.871	0.724	3.5
SCT1	11.8	0.183	0.180	11.0
SCT2	52.9	0.277	0.252	7.5

[a]Minimum thickness of stiffening plate required to develop the full truss. capacity, W_u^r.
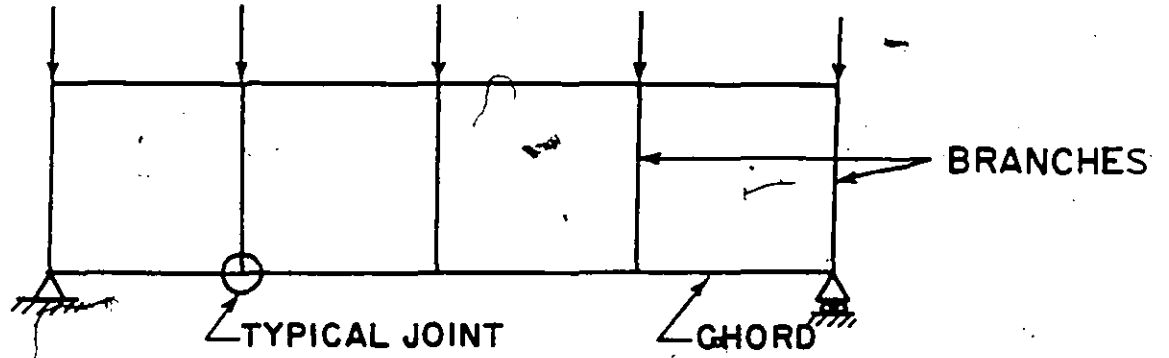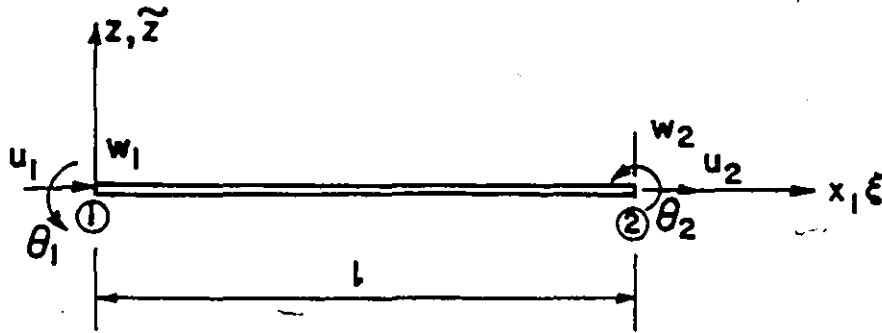
(a) VIERENDEEL TRUSS
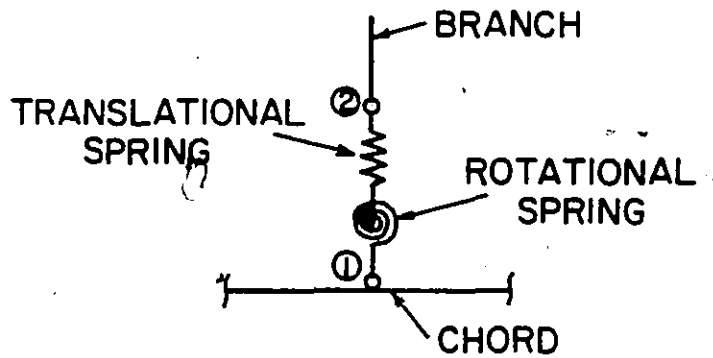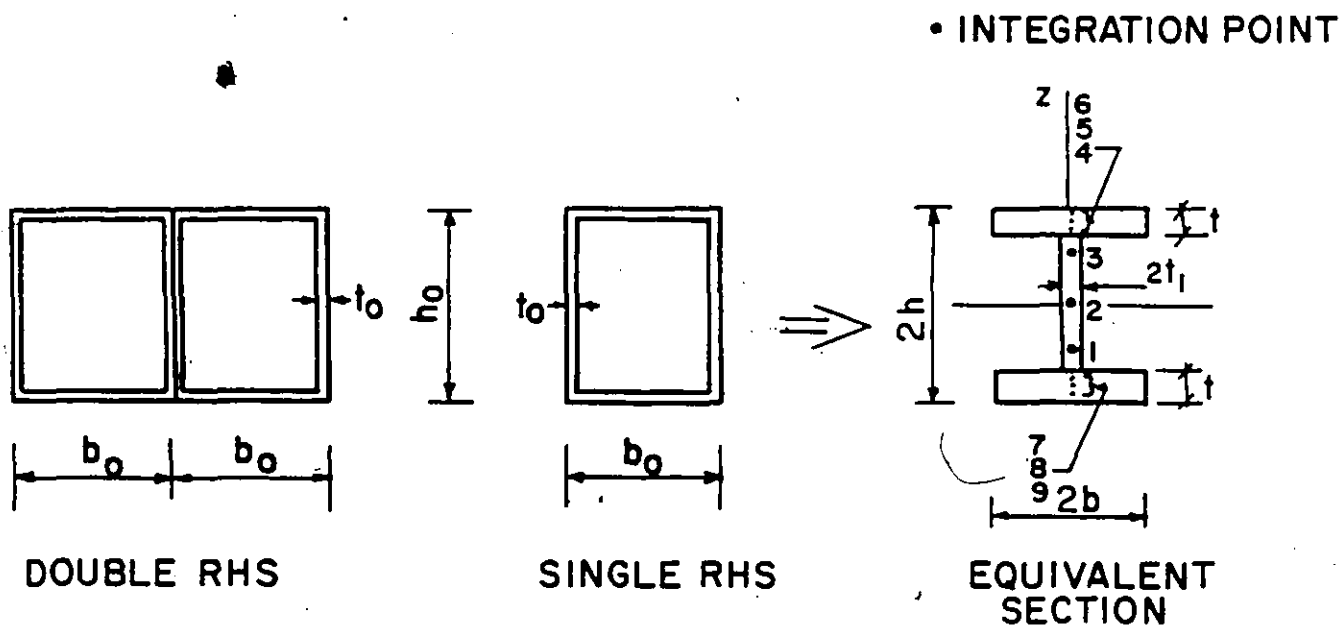

(b) IDEALIZED JOINT

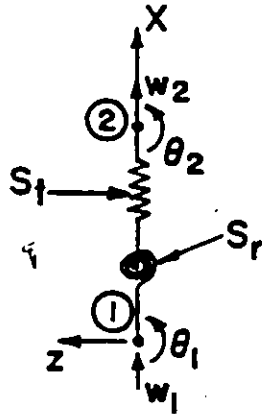FIG. 8.1 JOINT IDEALIZATION IN RHS VIERENDEEL TRUSSES

(a) TYPICAL BEAM ELEMENT

• INTEGRATION POINT

DOUBLE RHS   SINGLE RHS   EQUIVALENT SECTION
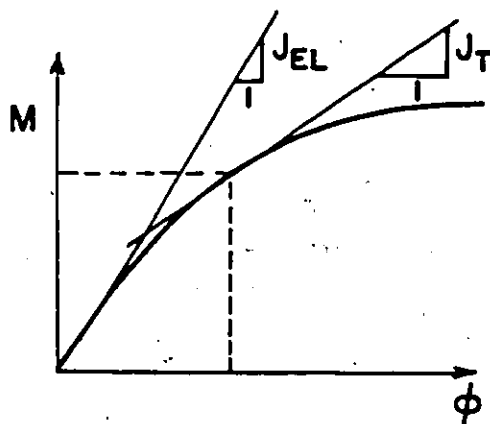
(b) EQUIVALENT SECTION

FIG. 8.2 MEMBER IDEALIZATION IN RHS VIERENDEEL TRUSSES

(a) JOINT SPRING ELEMENT

(b) M−φ CURVE FOR
    ROTATION SPRING S_r
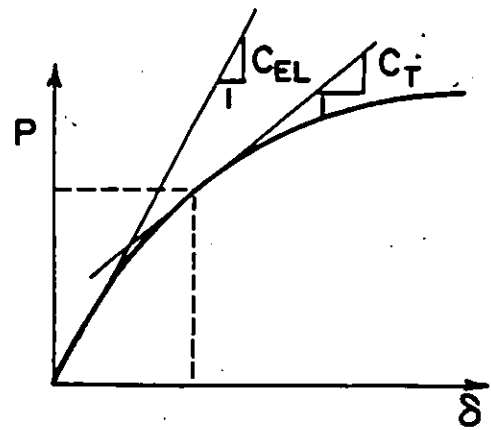
(c) P−δ CURVE FOR
    TRANSLATIONAL SPRING
    S_t

FIG. 8.3 CHARACTERISTICS OF SPRING ELEMENTS
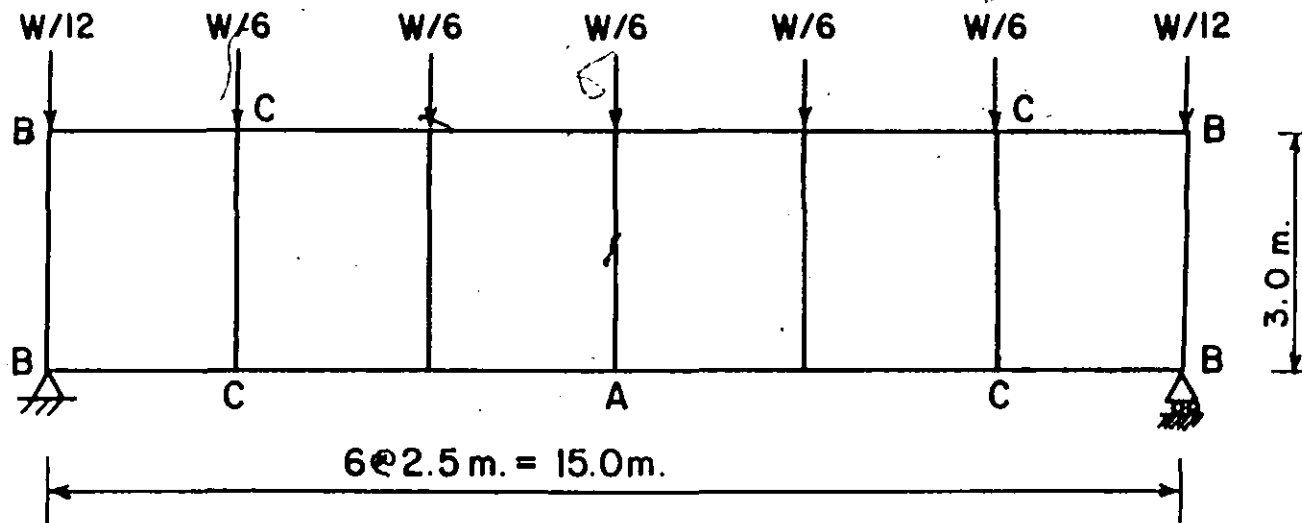
(a) GEOMETRY AND LOADING
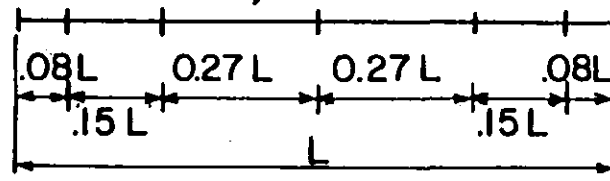
(b) DIVISION OF A TYPICAL TRUSS MEMBER INTO SIX ELEMENTS.

FIG. 8.4 DETAILS OF VIERENDEEL TRUSSES

FIG. 8.5 LOAD-DEFLECTION CURVES FOR DOUBLE CHORD TRUSSES (RIGID JOINTS)

FIG. 8.6 LOAD-DEFLECTION CURVES FOR SINGLE CHORD TRUSSES (RIGID JOINTS)

FIG. 8.7 LOAD-DEFLECTION CURVES FOR DOUBLE CHORD TRUSSES (FLEXIBLE JOINTS)

FIG. 8.8 LOAD-DEFLECTION CURVES FOR SINGLE CHORD TRUSSES (FLEXIBLE JOINTS)
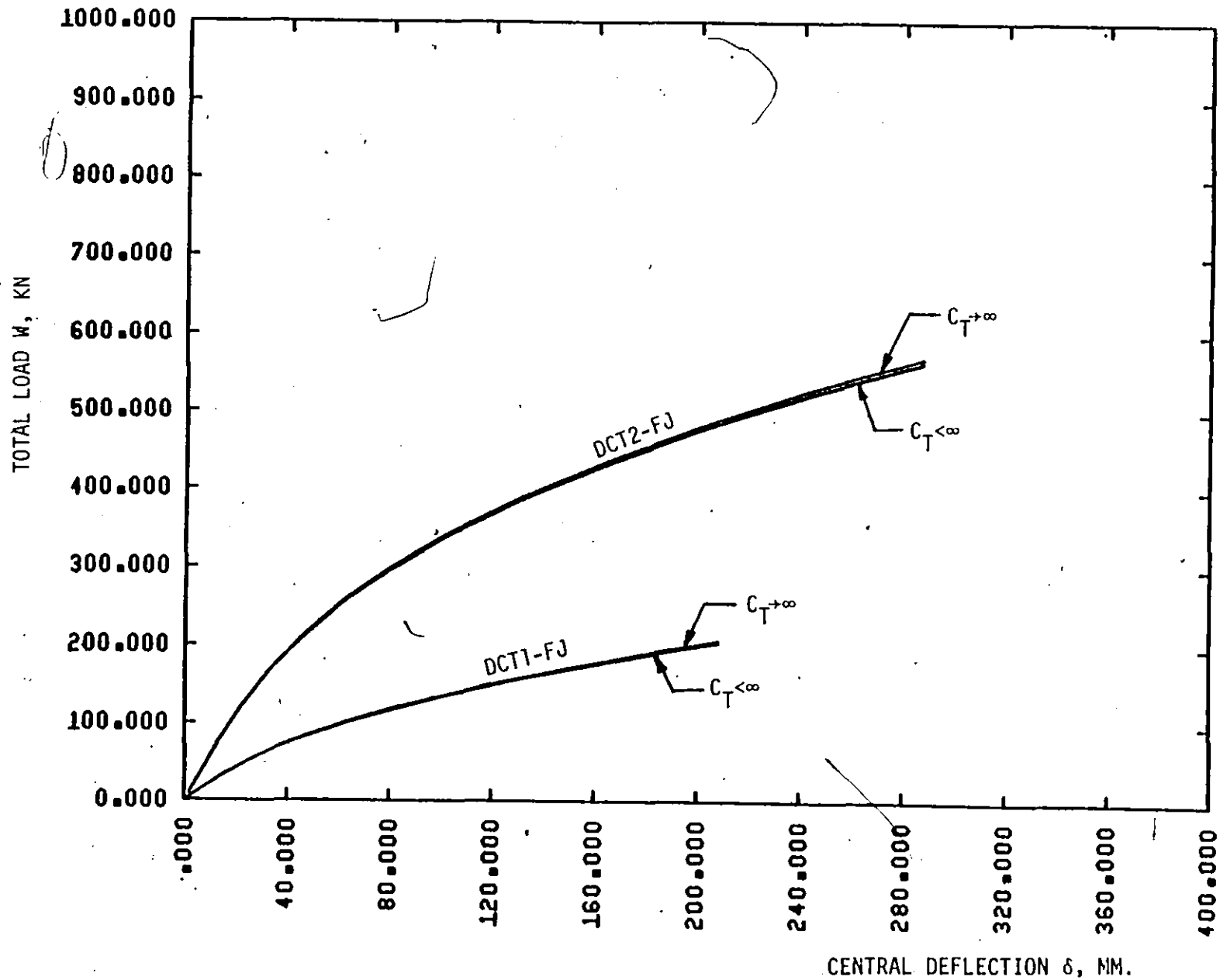
FIG. 8.9   EFFECT OF AXIAL STIFFNESS ON BEHAVIOUR OF DOUBLE CHORD TRUSSES
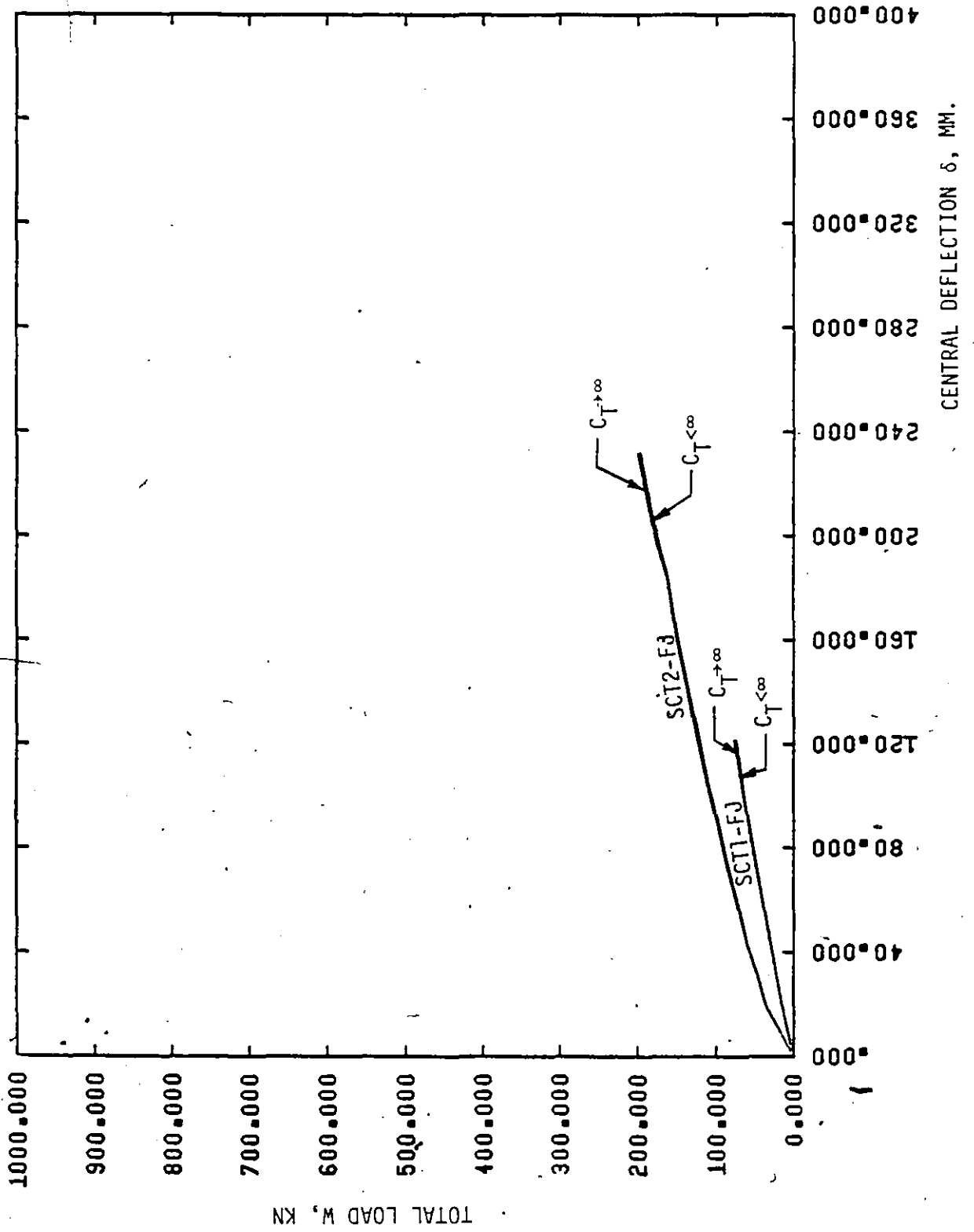
FIG. 8.10 EFFECT OF AXIAL STIFFNESS ON BEHAVIOUR OF SINGLE CHORD TRUSSES

CHAPTER 9

SUMMARY AND CONCLUSIONS

9.1 Summary and Conclusions

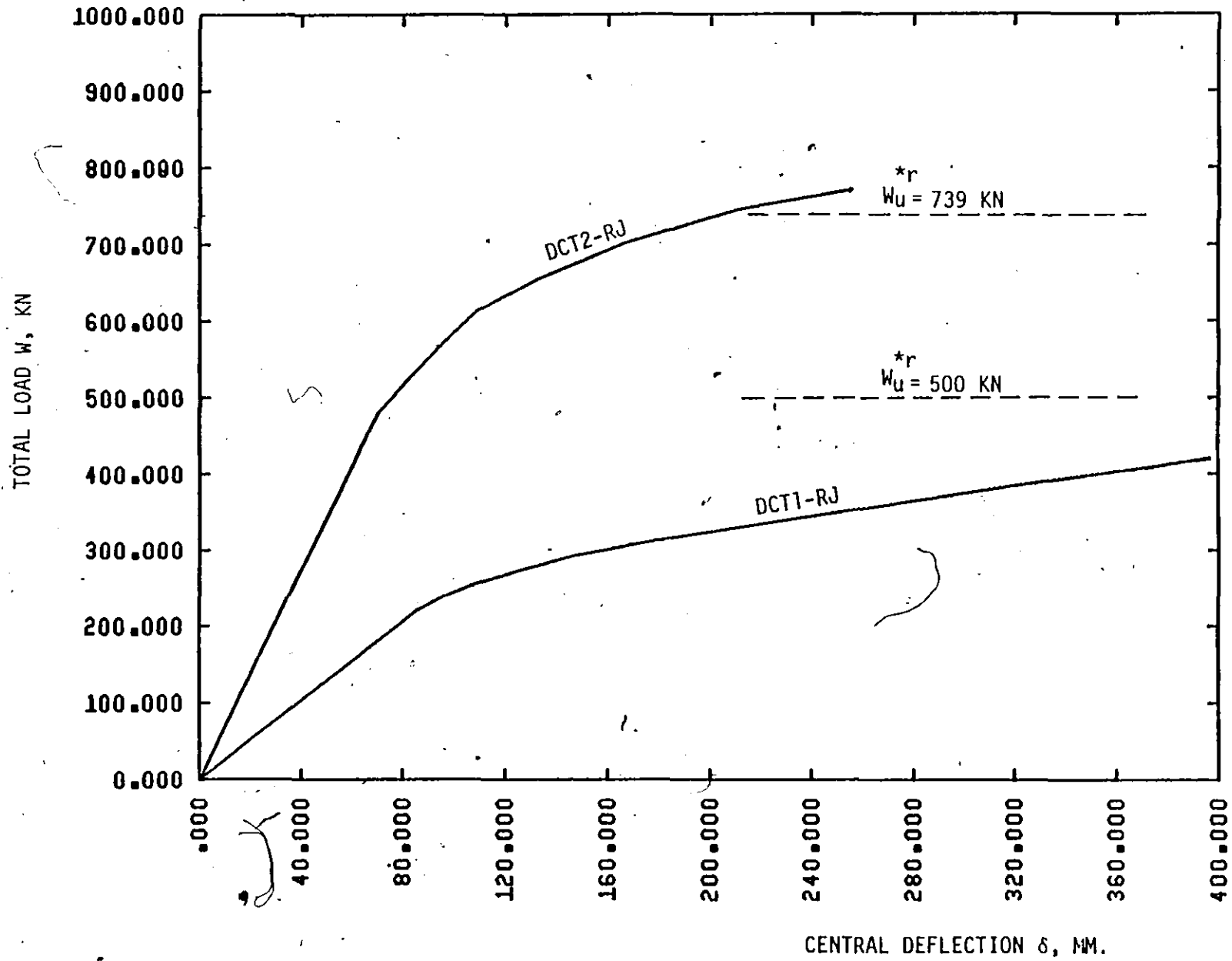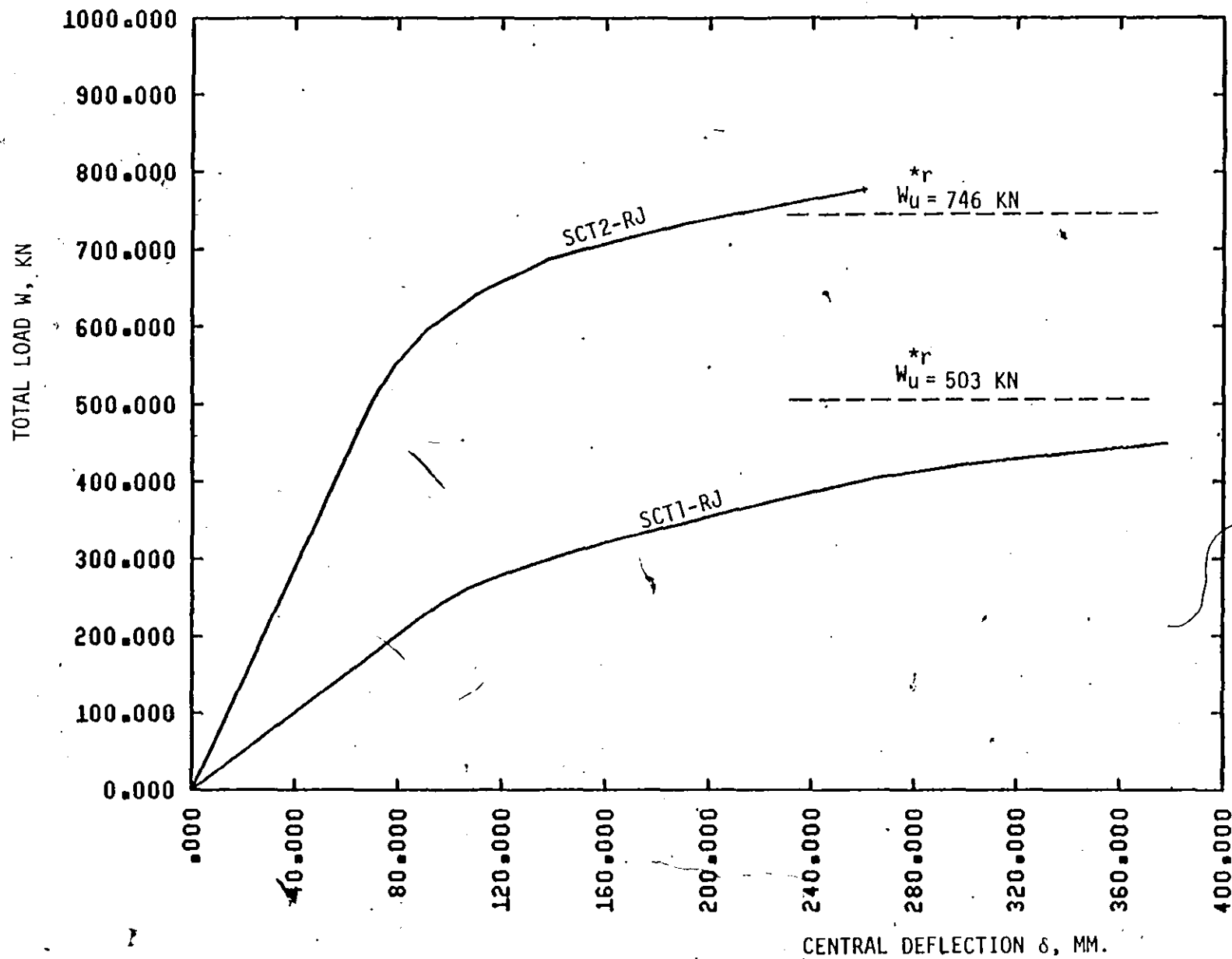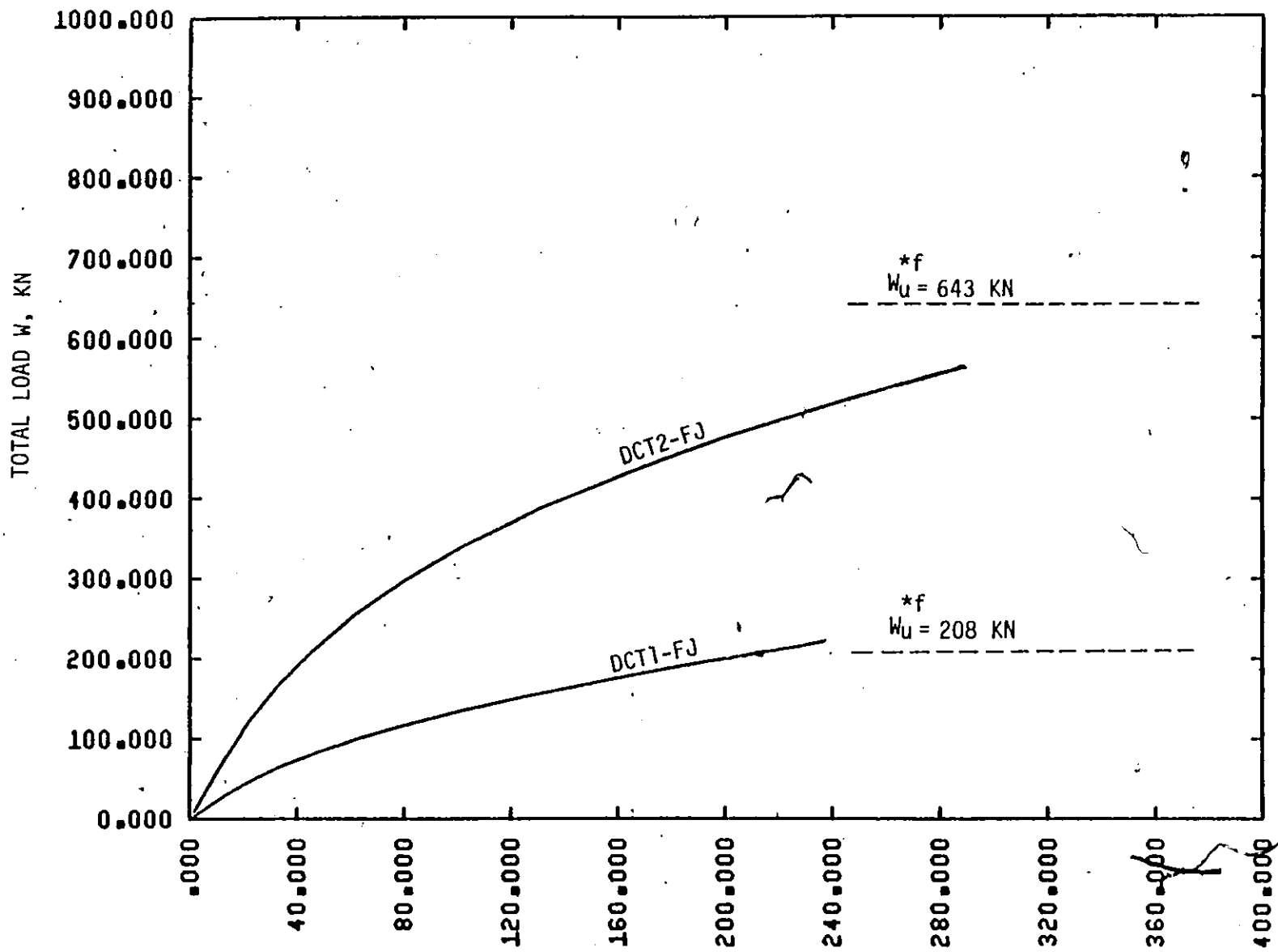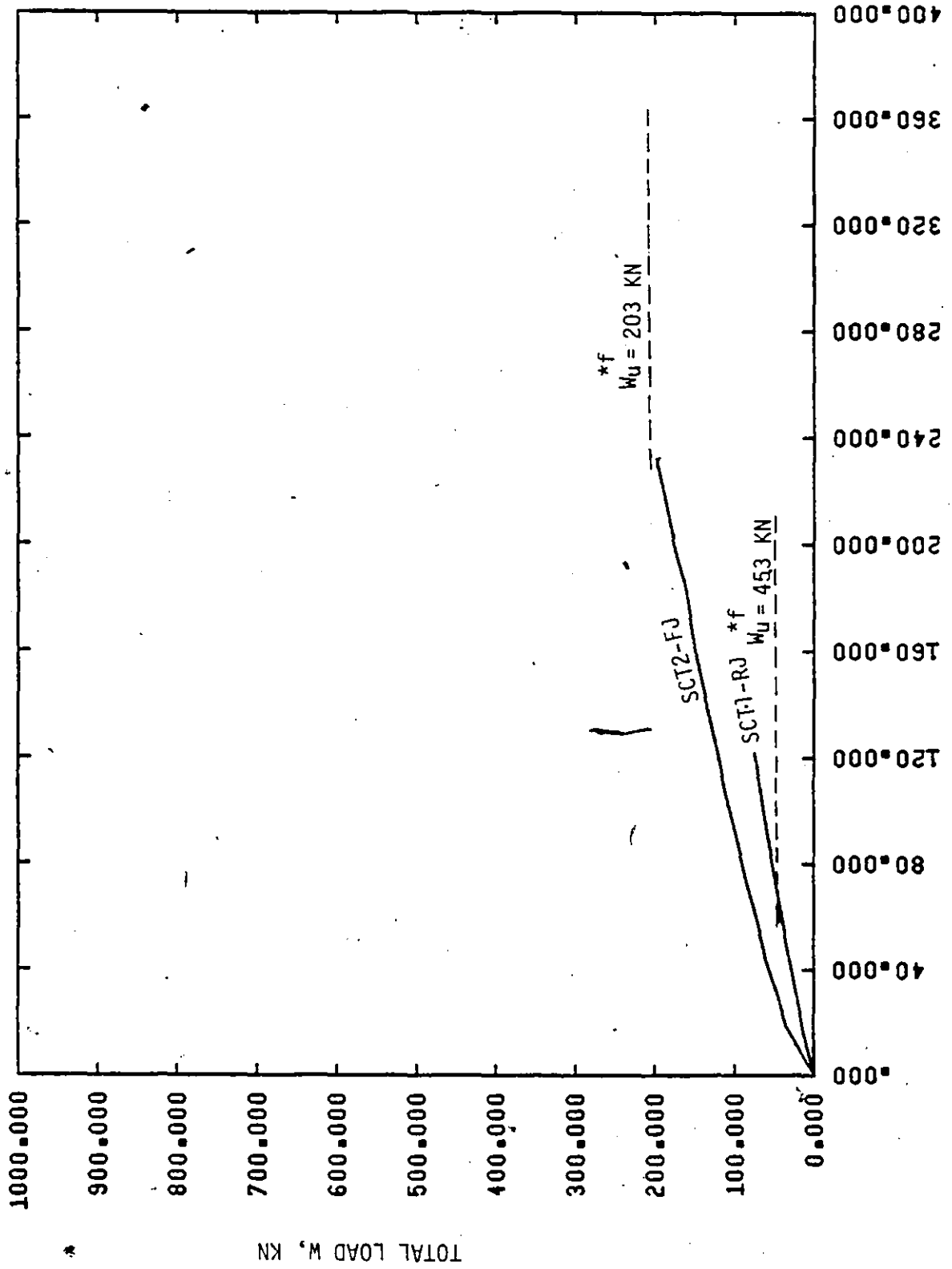The main objective of this investigation was to develop an analytical model for double chord RHS T-Joints in steel that would be computationally efficient and yet capable of simulating the behaviour as accurately as possible. By giving appropriate consideration to the modelling scheme, it was possible to extend this model to include single chord RHS T-joints as well.

The models involve idealization of a joint's connecting flange of the chord member as a thin plate restrained along the longitudinal edges by coupled translational and rotational springs. The restraining effect of these edge (or boundary) springs is equivalent to that provided by the webs and bottom flange. The models also incorporate material nonlinearities of the joint material that is presumed to be homogeneous and isotropic. Its constitutive relations can be adequately described by the Von-Mises yield criterion and the associated strain-hardening rule [8]. Furthermore, deformations are assumed small and hence geometric nonlinearities are neglected. This latter assumption is generally satisfactory in the practical range of deformations for metallic structures.

Three types of finite elements are used for the finite element approximation of the joint models. The four node-rectangular elements, with both membrane and bending degrees of freedom, are employed in defining the mesh for the top flange plate. A beam-column element is used to define the U-frame comprised of the webs and bottom flange of the RHS. The boundary spring element is developed to incorporate the boundary springs in the finite element analysis.

The joint models developed were then used to carry out parametric analyses of both double and single chord RHS T-joints, subjected to branch moment, punching shear or a combination of both. Under the first two types of loading, five nondimensional geometric parameters were considered. These parameters are thought to fully describe different joint configurations inlcuding those with flange plate stiffeners. Under combined loading, the parametric analyses considered different ratios of applied branch moment and punching shear. Results of each parametric study were presented as the load-displacement ($M-\phi$ or $P-\delta$) curves in a nondimensional form and in terms of interaction curves.

The experimental part of this investigation involved the testing of ten double chord RHS T-joints, four of which were under branch moment and the other six under punching shear. The results of these tests, in addition to the four moment tests reported in reference [7], were used to examine results of the analytical model for double chord joints.

A standardization procedure was developed to express the results

of the parametric analyses in equation form. This allows expressing the behaviour of a given joint type and loading in terms of a nondimensional standardization factor. This factor encompasses the influence of all shape parameters that were found to have a significant effect on the joint behaviour. The predicted joint capacities, based on the standardization procedure, were compared with documented test results as well as results of the tests performed as part of the present study. The predicted values are in very good agreement with the experimental results for both double and single chord connections under either branch moment or punching shear. The standard deviation in all cases was within sixteen percent of the experimental values.

. It may be emphasized that the model for the double chord joint has the capabilty of incorporating different interchord connection conditions. The standardized functions for the joint are based on the analysis of joints possessing interchord welds at both top and bottom. The length of these welds was taken as 305 mm (12 inches), centrally located about the joint centerline. Experimental as well as analytical results show that the joints possessing the interchord welding have greater strength and stiffness than those not so treated. Hence, it is recommended that the individual chords should be welded together near the joint to form a composite section.

Another aspect of this investigation was to employ the yield line method in developing upper bound solutions for the branch moment or punching shear capacity of double chord RHS T-joints. The upper bound capacities have been found to be consistently higher than those obtained

from the finite element solution as well as the generated equations. Discrepancies are, however, small as was observed in Chapters 5 and 7. Hence, it can be concluded that the yield line solutions reported in Chapters 5 and 6 may be used to predict the capacities of double chord RHS T-joints after applying an appropriate reduction factor.

The standardized joint stiffness and strength formulae were incorporated into an elasto-plastic finite element analysis of Vierendeel trusses composed of single and double chord RHS members. The main purpose of this analysis was to study the effect of joint flexibilities on the overall response of such trusses. Furthermore, this model was also employed to carry out a comparison of stiffness and strength characteristics for Vierendeel trusses consisting of double chord RHS members and equivalent single chord RHS members.

A number of important conclusions can be drawn from the analysis of Vierendeel trusses in which the joint behaviour is defined by the standardized M-ϕ and P-δ functions mentioned above. It was found that the truss behaviour is governed by the rotational rigidity of its joints. The axial (punching shear) rigidity of the joints, on the other hand, does not affect the truss behaviour in any significant manner. This phenomenon is easily explained by the load transfer mechanism in a Vierendeel truss where the members are subjected to predominately bending ac. This type of structure is susceptible to very high end member stresses since axial forces play an insignificant role in distributing the load. In order to develop the full anticipated capacity of the truss, its joints must be capable of transferring the maximum end

moments in the connected members without excessive deformation. The addition of a chord flange stiffening plate is an efficient way to considerably enhance the strength of the joints, and consequently of the truss.
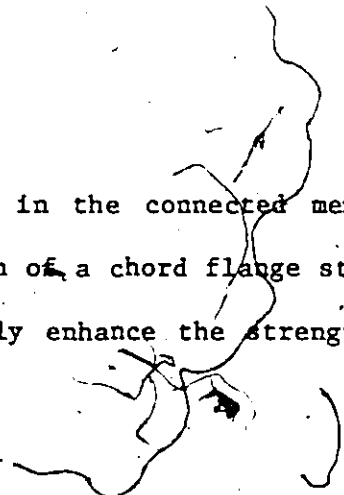
The proposed formulae, describing the behaviour of double chord RHS T-joints, are listed in Table 9.1 for easy reference. The table includes the standardized load-deformation ($M-\phi$ or $P-\delta$) function; the standardization constant, R or $\bar{R}$, the tangential stiffness, J_T or C_T, the elastic stiffness, J_{EL} or C_{EL}, and the joint capacity, M_u or P_u, under branch moments or punching shears, respectively. Also given are the upper bound capacities, M_u^* or P_u^* as obtained from a yield line solution. The interaction equations, defining reduced capacities, M_m and P_m, under combined loading, are also listed. The corresponding formulae for single chord joints are presented in Table 9.2. Formulae for the upper bound capacities are however excluded and can be found in other references such as [5] and [12].

The double chord T-type connection exhibits superior qualities to the equivalent single chord connection. A greater joint stiffness and higher moment capacity can be expected from the double chord connection. This is mainly due to the presence of the inner webs of the chord member which directly transfer a large portion of the branch loads through membrane action. The yield line solution indicates that about seventy five percent of the double chord strength is provided by the inner webs. In the case of single chord connections, the branch loads

are transferred mainly by flexural action of chord's top flange plate. However, as the width ratio of the joint approaches unity, an increasing portion of the load is resisted directly by the chord's outer webs.

9.2   Suggestions for Future Research

In order to further our knowledge about the behaviour of RHS T-connections, additional experimental and analytical research is required. The following areas are suggested for future research:

(1)   additional tests on double chord RHS T-joints under branch moment or punching shear,

(2)   tests on single and double chord RHS T-joints under combined loading,

(3)   tests on RHS Vierendeel trusses,

(4)   incorporation of large deformations in the joint models in order to predict failure modes,

(5)   extension of the joint models to analyze the behaviour of single and double chord RHS joints of the N and K-types.

As more experimental data become available, validity of the theoretical models, such as the ones developed here, can be examined further or improved to reflect the actual behavioural characteristics of the structures considered.

TABLE 9.1   SUMMARY OF FORMULAE FOR DOUBLE CHORD RHS T-JOINTS

Loading Type	Formulae	Equation Number
	$\varphi = 0.617 \times 10^{-1} (\frac{RM}{D}) + 0.390 \times 10^3 (\frac{RM}{D})^3 + 0.176 \times 10^6 (\frac{RM}{D})^5$	7.15
	$R = r_1^{(-1.34+2.56r_1)} \quad r_2^{(1.54+1.06r_2)} \quad r_4^{(-1.58-0.0031r_4)}$	
	$\times \quad r_5^{(2.75-0.13r_5)}$	7.16
Branch	$J_T = (D/R)/\lfloor 0.617 \times 10^{-1} + 0.117 \times 10^4 (\frac{RM}{D})^2 + 0.88 \times 10^6 (\frac{RM}{D})^4 \rfloor$	7.7
Moments	$J_{EL} = 16.2 \; D/R$	7.8
	$M_u = 0.039 \; D/R$	7.17
	$M_u^* = t_0 h_1 \sigma_Y \lfloor \frac{h_1}{2}(1+\frac{2t_0}{a-b_1}) + \frac{at_0}{2h_1} + \sqrt{2at_0(1+\frac{2t_0}{a-b_1})} \rfloor$	5.8
	$\delta/t = 0.123(\frac{\bar{R}b_0 P}{D}) + 0.982 \times 10^2 (\frac{\bar{R}b_0 P}{D})^3 + 0.516 \times 10^4 (\frac{\bar{R}b_0 P}{D})^5$	7.20
	$\bar{R} = r_1^{(-0.14+2.38r_1)} \quad r_2^{(0.12+1.26r_2)} \quad r_4^{(-1.35-0.0031r_4)}$	
	$\times \quad r_5^{(2.50-0.053r_5)}$	7.21
Punching	$C_T = (D/\bar{R}b_0)/\lfloor 0.123 + 0.295 \times 10^3 (\frac{\bar{R}b_0 P}{D})^2 + 0.258 \times 10^5 (\frac{\bar{R}b_0 P}{D})^4 \rfloor$	7.12
Shear	$C_{EL} = 8.13 \; D/\bar{R}b_0$	7.13
	$P_u = 0.150 \; D/\bar{R}b_0$	7.22
	$P_u^* = 2t_0 \sigma_Y \lfloor h_1(1+\frac{t_0}{a-b_1}) + \sqrt{2at_0(1+\frac{2t_0}{a-b_1})} \rfloor$	5.15
Combined Moment and	$(\frac{P_m}{P_u})^{5/3} + (\frac{M_m}{M_u})^{5/3} = 1.0, \qquad \frac{P_m}{P_u} < 0.80$	5.1
Punching Shear	$(\frac{P_m}{P_u}) + 0.40 \frac{M_m}{M_u} = 1.0, \qquad \frac{P_m}{P_u} > 0.80$	5.2

$r_1 = b_1/2b_0, \quad r_2 = b_1/h_1, \quad r_4 = b_1/t_0, \quad r_5 = 1+t_s/t_0, \quad a = 2b_0 - t_0, \quad D = Et^3/12(1-\nu^2), \quad t = t_0 + t_s$

TABLE 9.2   SUMMARY OF FORMULAE FOR SINGLE CHORD RHS T-JOINTS

Loading Type	Formulae	Equation Number
Branch Moment	$\phi = 0.251 \times 10^{-2}(\frac{RM}{D}) + 0.465 \times 10^{-3}(\frac{RM}{D})^3 + 0.442 \times 10^{-4}(\frac{RM}{D})^5$	7.24
	$R = r_1^{(0.27-7.77r_1)} \; r_2^{(0.95+0.86r_2)} \; r_4^{(-0.45-0.0022r_4)}$	7.25
	$\times \; r_5^{(1.56-0.94r_5)}$	7.16
	$J_T = (D/R)/\lfloor 0.251 \times 10^{-2} + 0.14 \times 10^4 (\frac{RM}{D})^2 + 0.221 \times 10^{-3}(\frac{RM}{D})^4 \rfloor$	7.7
	$J_{EL} = 398.4 \; D/R$	7.8
	$M_u = 7.0 \; D/R$	7.26
	$\delta/t = 0.678 \times 10^{-2}(\frac{\bar{R}b_0 P}{D}) + 0.211 \times 10^{-3}(\frac{\bar{R}b_0 P}{D})^3 + 0.135 \times 10^{-6}(\frac{\bar{R}b_0 P}{D})^5$	7.28
	$\bar{R} = r_1^{(0.067-6.62r_1)} \; r_2^{(17.1-1.05r_2)} \; r_4^{(-0.50-0.000r_4)}$	7.29
	$\times \; r_5^{(1.58-0.13r_5)}$	
Punching Shear	$C_T = (D/\bar{R}b_0)/\lfloor 0.678 \times 10^{-2} + 0.633 \times 10^{-3}(\frac{\bar{R}b_0 P}{D})^2 + 0.675 \times 10^{-6}(\frac{\bar{R}b_0 P}{D})^4 \rfloor$	7.12
	$C_{EL} = 147.5 \; D/\bar{R}b_0$	7.30
	$P_u = 16.0 \; D/\bar{R}b_0$	7.22
Combined Moment and Punching Shear	$(\frac{P_m}{P_u})^{1.5} + (\frac{M_m}{M_u})^{1.5} = 1.0, \qquad \frac{P_m}{P_u} < 0.70$	6.1
	$(\frac{P_m}{P_u}) + 0.54 \frac{M_m}{M_u} = 1.0, \qquad \frac{P_m}{P_u} > 0.70$	6.2

$r_1 = b_1/2b_0, \; r_2 = b_1/h_1, \; r_4 = b_1/t_0, \; r_5 = 1 + t_s/t_0, \; a = 2b_0 - t_0, \; D = Et^3/12(1-2^2), \; t = t_0 + t_s$

APPENDIX A

SHAPE FUNCTIONS FOR THE RECTANGULAR PLATE ELEMENT

$$N_{p1} = (1-\xi)(1-n)$$

$$N_{p2} = \xi(1-n)$$

$$N_{p3} = \xi n$$

$$N_{p4} = (1-\xi)n$$

$$N_{b1} = 1-\xi n-(3-2\xi)\xi^2(1-n)-(1-\xi)(3-2n)n^2$$

$$N_{b2} = (1-\xi)n(1-n)^2 b$$

$$N_{b3} = -\xi(1-\xi)^2(1-n)a$$

$$N_{b4} = (3-2\xi)\xi^2(1-n)+\xi n(1-n)(1-2n)$$

$$N_{b5} = \xi n(1-n)^2 b$$

$$N_{b6} = (1-\xi)\xi^2(1-n)a$$

$$N_{b7} = (3-2\xi)\xi^2 n-\xi n(1-n)(1-2n)$$

$$N_{b8} = -\xi(1-n)n^2 a$$

$$N_{b9} = (1-\xi)\xi^2 na$$

$$N_{b10} = (1-\xi)(3-2n)n^2+\xi(1-\xi)(1-2\xi)n$$

$$N_{b11} = - (1-\xi)(1-n)n^2 b$$

$$N_{b12} = -\xi(1-\xi)^2 na$$

APPENDIX B

DERIVATION OF WORK EQUATIONS FOR YIELD LINE SOLUTION OF

DOUBLE CHORD RHS T-JOINTS

B.1   Internal Work Due to Branch Moment

Assume that the branch member is given a virtual rotation ϕ that causes formation of a plastic failure mechanism shown in Fig. 5.15(a). The yield line pattern for the top flange plate of double chord member is shown in Fig. 5.15(c). At failure the top flange is divided into seven rigid planes, connected together and to the outer webs by yield lines. Angle α defines the extent of the yielded zone. In order for the failure mechanism to take place, the inner webs are assumed to yield in their planes by stretching or indenting without bulging, as shown in Fig. 5.15(b).

The interal work required to form a yield line in the flange plate is given by the plastic moment capacity, multiplied by the yield line length and the rotation angle along a perpendicular to the yield line. To simplify calculations, the yield lines and their rotations are resolved in the longitudinal and transverse directions of the joint. Thus the contribution to internal work, W_{If} of the top flange, is (see Fig. 5.15(c)) given by:

$$W_{If} = M_p \left\{ 4(x \cdot \tan \alpha + 2v + x \cdot \tan \alpha)\Theta_2 + 4a \cdot \Theta_1 + 2a \cdot \phi \right\}.$$

Noting that $M_p = t_o^2 \cdot \sigma_Y/4$, $\Theta_1 = w/x \cdot \tan \alpha$, $\Theta_2 = w/x$ and $\phi = w/v$, then

$$W_{If} = \frac{t_o^2 \cdot \sigma_Y}{4} \left\{ \frac{8w}{v} (v + x \cdot \tan \alpha) + \frac{4w \cdot a}{x \cdot \tan \alpha} + \frac{2a \cdot w}{v} \right\}.$$

The internal work, W_{Iw}, due to inner webs, is given by the yield line force per unit length $(2t_o \cdot \sigma_Y)$ multiplied with the deformation area (see Fig. 5.15(b)), and results in the following equation

$$W_{Iw} = 2t_o \cdot \sigma_Y \left\{ w(v + x \cdot \tan \alpha) \right\}.$$

B.2   Internal Work Due to Punching Shear

The branch member is given a virtual punching shear displacement δ which will cause a plastic failure mechanism such as shown in Fig. 5.16(a). Failure will occur due to "dishing" action in the top flange and in-plane indentation of the inner webs.

Following the same procedure outlined in the preceding section, the internal work W_{If}, due to the top flange is calculated as

$$W_{If} = M_p \left\{ 4(x \cdot \tan \alpha + 2v + x \cdot \tan \alpha)\Theta_2 + 4a \cdot \Theta_1 \right\}.$$

Substituting for $M_p = t_o \cdot \sigma_Y/4$, $\Theta_1 = \delta/x \tan \alpha$ and $\Theta_2 = \delta/x$, then

$$W_{If} = \frac{t_o^2 \cdot \sigma_Y}{4} \left\{ \frac{8\delta}{x} (v + x \cdot \tan \alpha) + \frac{4a \cdot \delta}{x \cdot \tan \alpha} \right\}.$$

Also, the internal work W_{Iw} done due to the innter webs is given by the following expression

$$W_{Iw} = 2t_o \cdot \sigma_Y \{x \cdot \tan \alpha \cdot \delta + 2v \cdot \delta\}.$$

APPENDIX C

PLASTIC ANALYSIS OF VIERENDEEL TRUSSES

The plastic analysis (upper bound) solution for the 6-bay truss of Fig. 8.4 (a) is presented in this appendix. The truss is externally determinate but there are 18 internal redundants, 3 per bay. Therefore, there must be 16 elementary mechanisms. Ten of these are joint mechanisms. Of the remaining six mechanisms, three are shown in Fig. C.1 as mechanisms (a) or (b), (c) and (d). Mechanisms (e) to (i) are possible combined mechanisms.

The plastic moments of the chord and branch members are denoted M_{pc} and M_{pb}, respectively. First, consider the case where the truss capacity is not governed by the joints, i.e., the joint capacity M_u is greater than both M_{pc} and M_{pb}. In this case, a failure mechanism occurs when enough plastic hinges form in the members rather than the joints.

Applying the principle of virtual work to each mechanism (see reference [21] for details), the following equations for the truss capacity W_u^{*r} are obtained (see Fig. C.1).

Mechanism (a):

$$\frac{W_u^{*r}}{6} (1+2+3+4+5) \cdot \theta L = 24 \, M_{pc} \cdot \theta$$

Hence $\quad W_u^{*r} = \dfrac{9.6 \, M_{pc}}{L}$ (C.1)

Mechanism (b):

$$\frac{W_u^{*r}}{6} (1+2+3+4+5) \cdot \theta L = (12 \, M_{pc} + 12 \, M_{pb}) \cdot \theta$$

Hence $\quad W_u^{*r} = \dfrac{4.8}{L} (M_{pc} + M_{pb})$ (C.2)

Mechanism (c):

$$\frac{W_u^{*r}}{6} (1+2+3+4-1) \cdot \theta L = 24 \, M_{pc} \cdot \theta$$

Hence $\quad W_u^{*r} = \dfrac{16 \, M_{pc}}{L}$ (C.3)

Mechanism (d):

$$\frac{W_u^{*r}}{6} (1+2+3-2-1) \cdot \theta L = 24 \, M_{pc} \cdot \theta$$

$$\text{or} \quad W_u^{*r} = \frac{48 \, Mp_c}{L} \tag{C.4}$$

Mechanism (e)

$$\frac{W_u^{*r}}{6} (1+2+3+4+5) \cdot \theta L = (24 \, M_{pc} + 8Mp_b)\theta$$

$$\text{or} \quad W_u^{*r} = \frac{3.2}{L} (3M_{pc} + 3M_{pb}) \tag{C.5}$$

Mechanism (f):

$$\frac{W_u^{*r}}{6} (1+2+3+4+5) \cdot \theta L = (20 \, M_{pc} + 12 \, M_{pb})\theta$$

$$\text{or} \quad W_u^{*r} = \frac{1.6}{L} (5 \, M_{pc} + 3 \, M_{pb}) \tag{C.6}$$

Mechanism (g):

$$\frac{W_u^{*r}}{6} (1+2+3+4+2) \cdot \theta L = (16\ M_{pc} + 8\ M_{pb})\theta$$

$$\text{or} \quad W_u^{*r} = \frac{4}{L} (2\ M_{pc} + M_{pb}) \tag{C.7}$$

Mechanism (h):

$$\frac{W_u^{*r}}{6} (1+2+3+4+2) \cdot \theta L = (8\ M_{pc} + 16\ M_{pb})\theta$$

$$\text{or} \quad W_u^{*r} = \frac{4}{L} (M_{pc} + 2\ M_{pb}) \tag{C.8}$$

Mechanism (i):

$$\frac{W_u^{*r}}{6} (1+2+3+2+1) \cdot \theta L = (6\ M_{pc} + 18\ M_{pb})\theta$$

$$\text{or} \quad W_u^{*r} = \frac{4}{L} (M_{pc} + 3\ M_{pb}) \tag{C.9}$$

The least value of W_u^{*r} as evaluated from Equations C.1 to C.9 is the correct upper bound capacity. The predicted capacities of the four rigidly-connected trusses analyzed before are given in Table C.1. Also given is the governing mechanism in each case.

When the joint capacity M_u is less than both M_{pc} and M_{pb}, plastic hinges will form at the joints rather than in the members. The capacity W_u^{*f} of the flexibly-connected trusses is thus obtained by replacing M_{pc} and M_{pb} by M_u in each expression of Equations C.1 to C.9. It is found that mechanisms (a) or (b), with plastic hinges forming at the joints, govern. The truss capacity in this case is given by

$$W_u^{*f} = \frac{9.6 \, M_u}{L}. \tag{C.10}$$

The upper bound capacities of the four flexibly-connected trusses as predicted by Equation C.10 are also given in Table C.1.

Table C.1 Upper Bound Capacities of Vierendeel Trusses

Case No.	Truss Capacity W_u^{*r} (KN)	Governing Mechanism	Case No.	Truss Capacity W_u^{*f} (KN)	Governing Mechanism
DCT1-RJ	500	(b)	DCT1-FJ	208	(a) or (b)
DCT2-RJ	739	(a)	DCT2-FJ	643	(a) or (b)
SCT1-RJ	503	(b)	SCT1-FJ	45.3	(a) or (b)
SCT1-RJ	746	(b)	SCT2-FJ	203	(a) or (b)

W/12 W/6 W/6 W/6 W/6 W/6 W/12

GEOMETRY AND
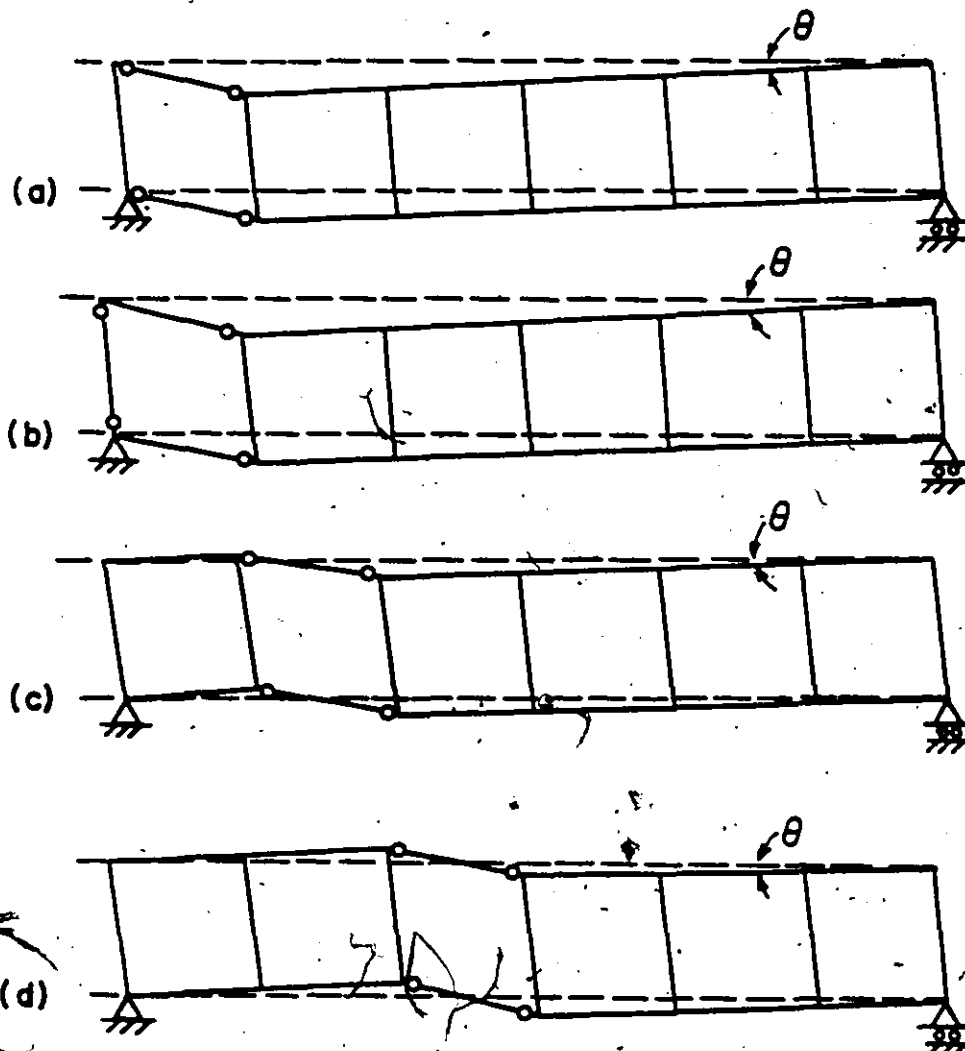LOADING

H

MECHANISM (a)

θ

(b)

θ

(c)

θ

(d)

θ
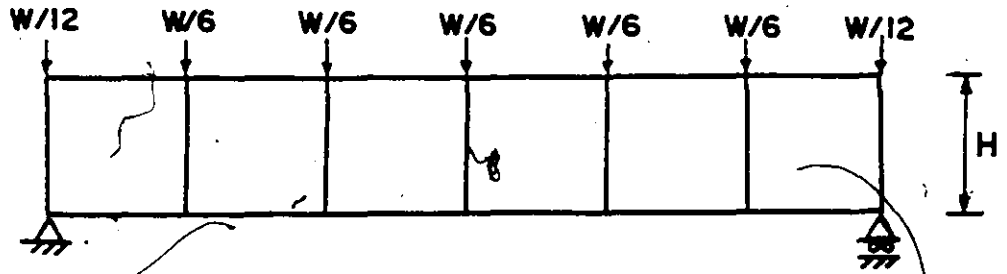
FIG. C.1 POSSIBLE FAILURE MECHANISMS FOR VIERENDEEL TRUSSES
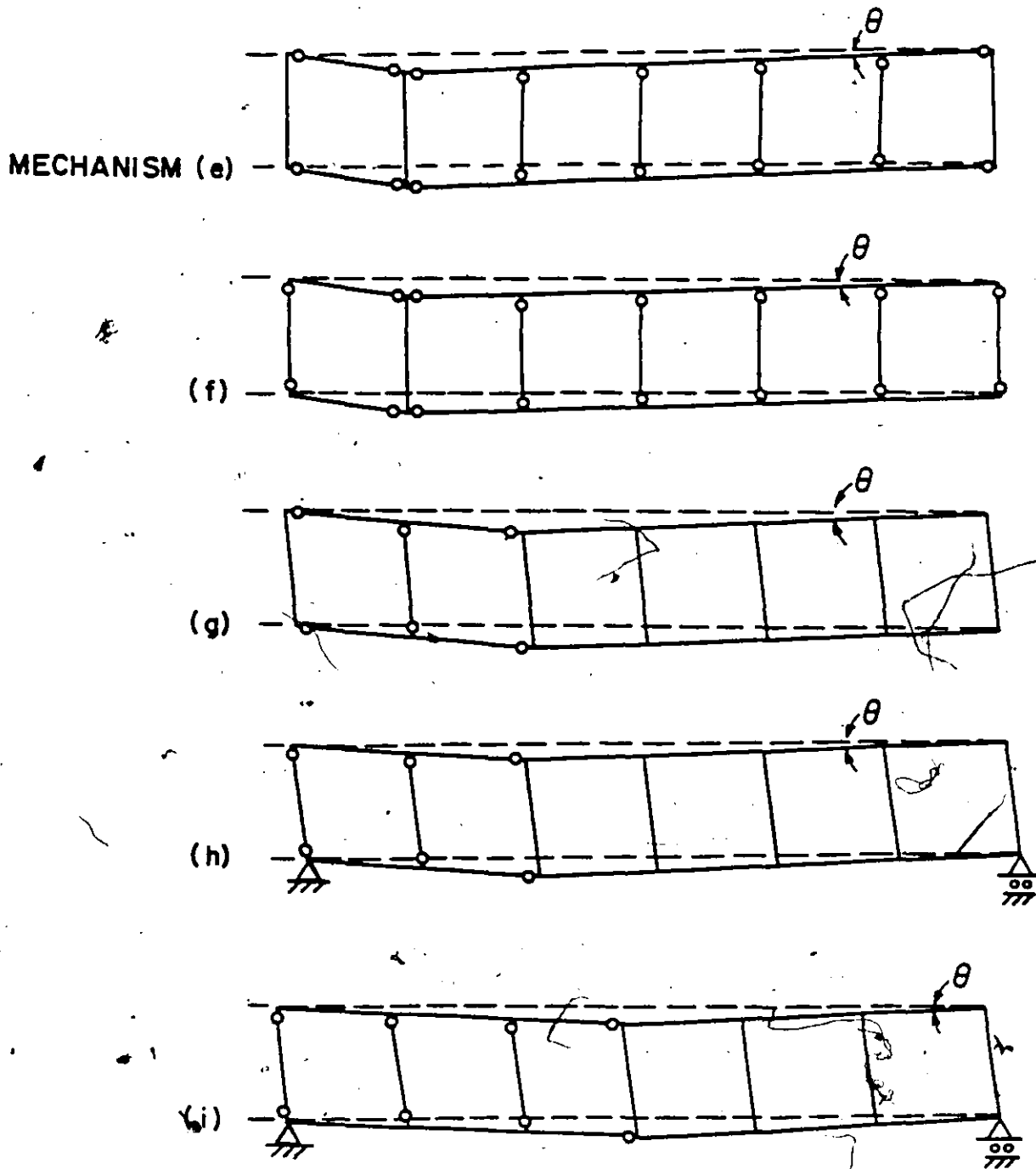
FIG. C.1 (Cont'd.) POSSIBLE FAILURE MECHANISMS FOR VIERENDEEL TRUSSES

BIBLIOGRAPHY

[1]   Korol, R.M., El-Zanaty, M. and Brady, F.J. "Unequal Width Connec-
       tions of Square Hollow Sections in Vierendeel Trusses", Can.
       J. Civ. Eng., Vol. 4, No. 2, pp. 190-201 (1977).

[2]   Redwood, R.G. "The Behaviour of Joints Between Rectangular Hollow
       Structural Members", Civ. Eng. and Public Works Review, Vol.
       60, No. 711, pp. 1463-1469 (1965).

[3]   Mee, B.L. "The Structural Behaviour of Joints in Rectangular
       Hollow Sections", Ph.D. Thesis, University of Sheffield
       (1969).

[4]   Mang, F. "Fatigue Strength of Welded HSS Joints", International
       Symposium on HSS, Toronto (sponsored by CIDECT), May (1977).

[5]   Patel, N.M., Graff, W.J. and White, A. "Punching Shear Character-
       istics of RHS Joints", ASCE National Struct. Eng. Mtg., San
       Francisco, April (1975).

[6]   Korol, R.M. and Mansour, M. "Theoretical Analysis of Haunch-
       Reinforced T-Joints in Square Hollow Sections", Can. J. Civ.
       Eng., Vol. 6, No. 4, pp. 601-609 (1979).

[7]   Chidiac, M.A. and Korol, R.M. "Rectangular Hollow Section Double-
       Chord T-Joints", J. of the Struct. Div. ASCE., Tech. Note
       105(STB), pp. 1717-1721, (1979).

[8]   Zienkiewicz, C.C. "The Finite Element Method", McGraw-Hill Publi-
       shers, 1977.

[9]   Dym, C.L. and Shames, I.H. "Solid Mechanics, a Variational
       Approach", McGraw-Hill Publishers (1973).

[10]   Brady, F.J. "An Experimental Investigation of Unequal Width HSS
       Moment Connections for Vierendeel Trusses", M. Eng. Thesis,
       McMaster University (1974).

[11]   Jubb, J.E. and Redwood, R.G. "Design of Joints to Box Sections",
       The Institution of Structural Engineers, Conference on Indus-
       trial Building and the Structural Engineer, May, 1966.

[12]   Mouty, J. "Theoretical Prediction of Welded Joint Strength",
       International Symposium on HSS, Toronto, Canada, May, 1977.

[13]   Stanton, E.L. and Schmidt, L.A. "A Discrete Element Stress and
       Displacement Analysis of Elastoplastic Plates", AIAA Journal,
       July, 1970.

[14]   Kanatani, H. and Fujiwara, K. "Bending Tests on T-Joints of RHS
       Chord and RHS or H-Shape Branch", CIDECT Programme 5AF,
       March, 1981.

[15] Redwood, R.G. "The Bending of a Plate Loaded Through a Rigid Rectangular Inclusion." Int. J. of Mech. Sciences, Vol. 7, pp. 421-430, 1965.

[16] Mansour, M.H. "Theoretical Analysis of T-Joints in Hollow Structural Sections", M.Eng. Thesis, McMaster University, 1978.

[17] Galambos, T.V. "Structural Members and Frames", 1978.

[18] Struik, J.H.A. "Applications of Finite Element Analysis to Nonlinear Plane Stress Problems", Ph.D. Dissertation, Lehigh University, 1972.

[19] Przemieniecki, J.S. "Theory of Matrix Structural Analysis McGraw-Hill Book Company, N.Y., 1968.

[20] Frye, M.J. and Morris, G.A. "Analysis of Flexibly Connected Steel Frames", Can. J. Civ. Eng., Vol. 2, 1975.

[21] Hodge, P.G., Jr., "Plastic Analysis of Structures", McGraw-Hill Publishers, New York, 1959.

[22] El-Hifnawy, L. "Elasto-Plastic Finite Element Analysis of Rectangular Hollow Section T-Joint", M. Eng. Thesis, McMaster University (1980).

[23] Korol, R.M., Mitri, H. and Mirza, F.A. "Plate Reinforced Square Hollow Section T-Joints of Unequal Widths, Can. J. Civ. Eng., Vol. 9, 1982.

[24] Mirza, F.A. "Finite Element Method and Basic Finite Element Computer Programs", Graduate Course Notes, McMaster University, Civil Eng. Department, 1979-1980.

[25] Mirza, F.A., Shehata, A.A. and Korol, R.M. "Modelling of Double Chord Rectangular Hollow Section T-Joints by Finite Element Method", Computer and Structures, Vol. 15, No. 2, 1982.

[26] Mirza, F.A., Korol, R.M. and Shehata, A.A. "Elasto-Plastic Analysis of Double Chord T-Joints by Finite Element Method", Submitted to CANCAM'83.

[27] Cook, R.D., "Concepts and Applications of Finite Element Analysis", John Wiley and Sons Inc., 1974.